AFRL-AFOSR-VA-TR-2017-0066

SYNTHESIS, CHARACTERIZATION AND MODELING OF
FUNCTIONALLY GRADED MULTIFUNCTIONAL HYBRID
COMPOSITES FOR EXTREME ENVIRONMENTS

Dimitris Lagoudas
TEXAS ENGINEERING EXPERIMENT STATION COLLEGE STATION
1470 WILLIAM D FITCH PKY
COLLEGE STATION, TX 77843-3577

04/04/2017
Final Report

Air Force Research Laboratory
AF Office Of Scientific Research (AFOSR)/RTA1

REPORT DOCUMENTATION PAGE

Form Approved
OMB No. 0704-0188

The public reporting burden for this collection of information is estimated to average 1 hour per response, including the time for reviewing instructions, searching existing data sources, gathering and maintaining the data needed, and completing and reviewing the collection of information. Send comments regarding this burden estimate or any other aspect of this collection of information, including suggestions for reducing the burden, to Department of Defense, Executive Services, Directorate (0704-0188). Respondents should be aware that notwithstanding any other provision of law, no person shall be subject to any penalty for failing to comply with a collection of information if it does not display a currently valid OMB control number.
PLEASE DO NOT RETURN YOUR FORM TO THE ABOVE ORGANIZATION.

1. REPORT DATE *(DD-MM-YYYY)* 04-04-2017	2. REPORT TYPE Final Performance	3. DATES COVERED *(From - To)* 15 Sep 2009 to 14 Mar 2015

4. TITLE AND SUBTITLE
SYNTHESIS, CHARACTERIZATION AND MODELING OF FUNCTIONALLY GRADED
MULTIFUNCTIONAL HYBRID COMPOSITES FOR EXTREME ENVIRONMENTS

5a. CONTRACT NUMBER

5b. GRANT NUMBER
FA9550-09-1-0686

5c. PROGRAM ELEMENT NUMBER
61102F

6. AUTHOR(S)
Dimitris Lagoudas

5d. PROJECT NUMBER

5e. TASK NUMBER

5f. WORK UNIT NUMBER

7. PERFORMING ORGANIZATION NAME(S) AND ADDRESS(ES)
TEXAS ENGINEERING EXPERIMENT STATION COLLEGE STATION
1470 WILLIAM D FITCH PKY
COLLEGE STATION, TX 77843-3577 US

8. PERFORMING ORGANIZATION REPORT NUMBER

9. SPONSORING/MONITORING AGENCY NAME(S) AND ADDRESS(ES)
AF Office of Scientific Research
875 N. Randolph St. Room 3112
Arlington, VA 22203

10. SPONSOR/MONITOR'S ACRONYM(S)
AFRL/AFOSR RTA1

11. SPONSOR/MONITOR'S REPORT NUMBER(S)
AFRL-AFOSR-VA-TR-2017-0066

12. DISTRIBUTION/AVAILABILITY STATEMENT
DISTRIBUTION A: Distribution approved for public release.

13. SUPPLEMENTARY NOTES

14. ABSTRACT
A novel hybrid materials structure is proposed in this MURI to enable the design of next generation highspeed,
long-range, high-altitude aerospace vehicles with sensing and remaining life prognosis
capabilities. This vision is carried into the research objective, which is to develop multifunctional,
functionally graded hybrid composite (FGHC) systems with integrated sensing capabilities for extreme
environments. The hybrid concept is based on a ceramic thermal/environmental barrier layer, followed by a
graded ceramic/metal composite layer that finally transitions to a high temperature polymer matrix
composite with integrated SHM sensors. The research thrust areas are designed to enable the
development of reliable, damage tolerant, lightweight structures with excellent thermal management and
self-healing capability.

15. SUBJECT TERMS
COMPOSITES, ENVIRONMENTS

16. SECURITY CLASSIFICATION OF:			17. LIMITATION OF ABSTRACT	18. NUMBER OF PAGES	19a. NAME OF RESPONSIBLE PERSON TILEY, JAIMIE
a. REPORT	b. ABSTRACT	c. THIS PAGE			
Unclassified	Unclassified	Unclassified	UU		19b. TELEPHONE NUMBER *(Include area code)* 703-588-8316

Standard Form 298 (Rev. 8/98)
Prescribed by ANSI Std. Z39.18

DISTRIBUTION A: Distribution approved for public release.

SYNTHESIS, CHARACTERIZATION AND MODELING OF FUNCTIONALLY GRADED MULTIFUNCTIONAL HYBRID COMPOSITES FOR EXTREME ENVIRONMENTS

(MURI 09) AWARD NO. FA-9550-09-1-0686
FINAL PERFORMANCE REPORT

Sept 14, 2009 - March 14, 2015

TEXAS A&M UNIVERSITY
Dimitris Lagoudas-Director
Paul Cizmas, Ibrahim Karaman, Ozden Ochoa,
Miladin Radovic, J.N. Reddy, John Whitcomb

UNIVERSITY OF ILLINOIS AT URBANA-CHAMPAIGN
Philippe Geubelle, Nancy Sottos, Scott White

UNIVERSITY OF MICHIGAN
Dan Inman, Nakhia Goulbourne

VIRGINIA POLYTECHNIC INSTITUTE AND STATE UNIVERSITY
Gary Seidel

STANFORD UNIVERSITY
Fu-Kuo Chang

UNIVERSITY OF DAYTON RESEARCH INSTITUTE
Khalid L. Lafdi

January 31, 2015

1

Table of Contents

EXECUTIVE SUMMARY

A novel hybrid materials structure is proposed in this MURI to enable the design of next generation high-speed, long-range, high-altitude aerospace vehicles with sensing and remaining life prognosis capabilities. This vision is carried into the research objective, which is to develop multifunctional, functionally graded hybrid composite (FGHC) systems with integrated sensing capabilities for extreme environments. The hybrid concept is based on a ceramic thermal/environmental barrier layer, followed by a graded ceramic/metal composite layer that finally transitions to a high temperature polymer matrix composite with integrated SHM sensors. The research thrust areas are designed to enable the development of reliable, damage tolerant, lightweight structures with excellent thermal management and self-healing capability.

The research team in over the course of this project was composed of **fourteen faculty members**, **thirty-seven graduate students (**nineteen graduated in the last five years and eighteen will graduate until Spring 2016**), seven post-docs**, **and nineteen undergraduate students**. Over the last 5 years we have (1) published or submitted for publishing **sixty-eight peer reviewed journal publications**, (2) published **seventy-one conference proceeding papers,** (3) presented **one-hundred and nineteen conference papers**, and **(4) submitted one patent application**, We have continued or expanded our collaborations with colleagues at a number of national laboratories (e.g. AFRL RX and RB) and other academic institutions, on a number of topics - especially on joining PMC composites to the GCMeC.

We used web-based tools extensively to facilitate communication; our MURI web site, a Google Groups, and Google Docs to exchange information and news. SABA Centra Web conferencing tool was the mainstay for the webinars for all students and PIs to share their activities. In addition to individual on-site campus meetings among the local research team, we had formal full PI team telecon-webcons and informal ones between individual PIs as needed. Herein the synopsis of technical highlights of the project are presented.

Hybrid Multifunctional Composite Processing and Characterization:

First, with respect to the MAX phases, substantial effort has been undertaken with respect to both manufacturing and characterization. For instance, SPS samples based on commercial, high-purity, and elemental powders have been produced. Including a Ti_2AlC specimen with the highest yet produced UCS. The additional of Mn into Cr_2AlC compositions has also been studied to produce a potentially high corrosion resistant material. In terms of characterization, a number of macroscopic and microscopic experiments have been performed. For instance, the impact of grain size on the strength of specimens has been thoroughly investigated. Detailed investigations utilized RUS have also been performed to identify three distinct regimes of dissipative behavior in the MAX phase response corresponding to different combinations of deformation and damage accumulation mechanisms. Additionally, high-temperature experiments investigating the brittle to ductile transition have been performed. High-strain rate and DIC experiments have also been performed. The latter has shown the importance of combinations of intergranular and intragranular deformations play on the overall behavior of the composite which have been analyzed via some modeling approaches

A number of steps have also been undertaken in terms of composite characterization. First, the unique shape memory behaviors of the MAX-SMA composites have been further explored – specifically with respect to their damping and actuation behaviors. The damping behaviors have been shown to be remarkable, yielding dissipated energies an order of magnitude more than Mg/Ti_3SiC_2 composites. For their actuation behavior, the contribution of the different constituents to the irrecoverable composite deformation and effective two-way behaviors have also been studied. Importantly, substantial effort has also been placed on studying the interfaces of these systems. Through both compositional characterization and nanoindentation, the various elastic properties of the interfaces have been studied and have been shown to result in strong interfaces. In terms of manufacturing, multilayer $NiTi/Ti_3SiC_2/NiTi$ systems have been produced, along with

3

porous Ti_2AlC specimens. Novel Ti_2AlC/AA6061 composites have also been produced via melt-infiltration of the latter materials. The results properties of these composites have also been characterized.

The characteristics of interfaces of PMC/Ti and PMC/SMA have also been studied through experimental and numerical means. Double cantilever beams tests of both material systems have been performed to identify their fracture toughness. Additionally, continuum level modeling via FEA have also been performed on such systems and have shown for instance, that there is less than 1% mode-mixity in asymmetric DCB Ti-PMC interfaces. Through collaboration with the sensors team, SHM sensors have been inserted into these interfaces and their capabilities studied through experimental and numerical means. Finally, in moving beyond continuum scale modeling, MD simulations have also been performed to study the adhesion work and traction separation capabilities of EPON862/TiO_2 systems with an eye towards subsequent design of interfaces.

At the PMC level, a series of composites have been developed incorporating cooling microchannels in both polymer matrix and NiTi-polymer matrix systems. In addition to studying their cooling capabilities, the mechanical performance via tensile tests (showing limited degradation due to the presence of channels). A series of tests in which PMCs have been subject to thermomechical loading conditions (via externally applied heating and four point bending apparatus) have also been performed to identify their capabilities under higher temperatures. The cooling performance and preferential configurations of the NiTi-PMC composites have also been studied and identified. Additionally, the interface-based generalized finite element method (IGFEM), developed as part of this work, has also been used to study a variety of loadings and channel dispersion to identify optimal configurations.

Multiscale Computational Models:

To build upon the results of the materials teams, a number of issues have been addressed by constructing a series of models to study the response of the material systems involved. First, microstructurally informed finite element models of various elements of the GCMeC have been constructed. Specifically, the NiTi-Ti_3SiC_2 system has been used to create representations and study the thermal properties of these composites in good agreement with experiments and highlighting the impact of the reaction layers. Additionally, models of the NiTi-Ti_2AlC system have been constructed and used to study the inelastic response of the SMA-MAX systems subject to thermomechanical loading. This model, and some smaller RVE models, has been used to study various microstructural features. More recently, a new constitutive model for the MAX phases considering the various mechanisms present to study the response of these materials. At the PMC level, the damage response of has been studied through a variety of multiscale models. For instance, random and hexagonal RVEs have been studied with respect to their damage and failure performance. It was shown that utilizing truly random microstructures can be essential in accurately determining material properties and a reduced order predictive model framework for damage modeling was also developed. The developed models were also used to study the NiTi-Ti_3SiC_2 interfaces when subjected to four point bend tests.

At the structural level, a number of models have been constructed for the efficient analysis of the FGHC structure. First, the new structural shell elements were constructed and used to study functionally graded materials subject to various thermal-mechanical loadings. In terms of the dynamic characteristics, surrogate modeling was used to study and determine the properties of the FGHC – including the effects of the microchannels. Finally, the above referenced PMC models were also integrated into new aeroelastic coupled fluid-structural models. The developed framework (highly parallel in compilation) was used to study the dynamic aerothermoelastic response of the FGHC under hypersonic loading conditions.

Dynamic response and In-situ SHM:

The in-situ SHM capabilities of the FGHC focused on two primary areas – the piezoresistivity of "fuzzy" fibers with CNTs and high temperature piezoelectric sensors. With respect to the

4

former, fuzzy fibers were grown and their applicability as sensors was demonstrated experimentally and numerically. In terms of the material response, it was shown that CNTs could serve as thermal insulators as the impedance decreases with nano-additives concentration. Mechanically, low CNT concentrations were shown to improve responses but higher concentrations (20%) proved to be a detriment. A series of multiscale models were also developed to explore the source of the piezoresistive effect associated by CNTs. These models incorporated a series of mechanical response incorporating damage at various scales and distinguished between electron hopping and inherent piezoresistivity. Importantly, the role of damage in terms of disrupting electron paths was shown and the critical importance of electron hopping in strain and damage sensing identified. At the larger scale, high temperature piezoelectric transduces were developed and integrated into sensor networks. The potential of these sensors as high-temperature sensors was experimentally demonstrated. For use and integration as mentioned above, these sensors were miniaturized and validated.

1. RESEARCH THRUST AREA: DEVELOPMENT & FABRICATION

Develop a multifunctional FGHC that will consist of multiple layers, starting from a ceramic thermal barrier layer, and followed by a graded ceramic/metal composite (GCMeC) layer that finally transitions to a high-temperature polymer matrix composite (PMC). We will develop Actively-Cooled PMCs (AC-PMC) using microvascular cooling functionality on commercially available PMCs, High-Temperature PMCs (HT-PMC) based on polyimide matrices, and combination of both. Structural health monitoring will be introduced through the incorporation of networked sensor/actuator arrays, and its development will interrelate closely to modeling and characterization efforts.

1.1 GRADED CERAMIC/METAL COMPOSITES

RESEARCH TEAM MEMBERS
PIs: Dr. Miladin Radovic and Dr. Ibrahim Karaman
Graduate Students: Huili Gao, Rogelio Benitez, Ankush Kothalkar, and Liangfa Hu
Undergraduate Student: Morgan O'Neil

COLLABORATORS:
Dr. Scott White (University of Illinois at Urbana-Champaign)
Anthony Coppola (a MURI student at University of Illinois at Urbana-Champaign)
Dr. Junuthula N. Reddy (Texas A&M University)
Dr. Feifei Cheng (a MURI student graduated from Texas A&M University, now at Intel)
Dr. Nakiah Goulbourne (University of Michigan)
Dr. Arun Shukla (University of Rhode Island)
Dr. Gweneale Proust (University of Sydney)
Dr. Elizabeth Hoffman (Savanah river National Laboratory)

TECHNICAL ACCOMPLISHMENTS
1.1.1.   Characterization of Ti$_2$AlC
1.1.1.1.   Room Temperature Mechanical Properties ofTi$_2$AlC

The mechanical properties of high purity Ti$_2$AlC samples prepared by Spark Plasma Sintering (SPS) from powders synthesized at Texas A&M were investigated via quasi-static compression testing and compared to those from commercially available Ti$_2$AlC (Figure1.1.1). The results show that high purity Ti$_2$AlC has an average Ultimate Compressive Strength (UCS) of 1038 and the samples made from commercial powder shows UCS of 1260 MPa, the highest ever reported for Ti$_2$AlC. Note however, that latter exhibits a less desirable brittle-like behavior, while all other

5

samples, including high-purity Ti$_2$AlC, show pseudo-plastic behavior prior to failure. A careful examination of the sample's microstructure, confirmed that the UCS of Ti$_2$AlC MAX phase is grain size dependent, and specifically follows Hall Petch behavior whereby the strength of the sample increases with a reduction in grain size (Figure 1.1.2). Note that the effect of grain size prevails even with intermetallic impurities in the 17 vol. %. It was therefore concluded that the superb UCS observed during this investigation were obtained not by the reduction in intermetallic impurities but by the mitigation of grain growth that resulted from the fast processing times obtained by SPS.
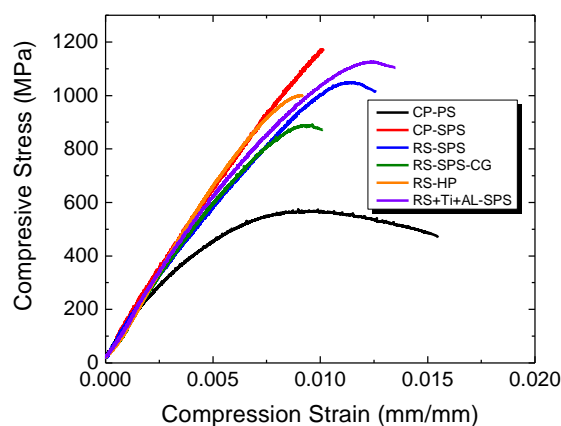

Figure 1.1.1: Compressive stress-strain behavior of Ti$_2$AlC MAX phase. "CP" denotes samples from Commercial Powder, while "RS" denotes samples from high-purity reactive sintering produced at Texas A&M.
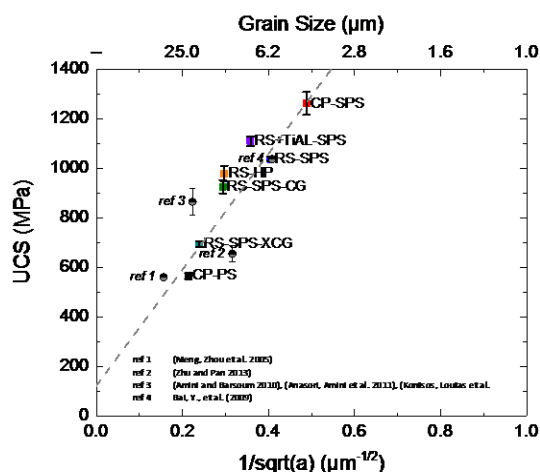

Figure 1.1.2: Ultimate Compressive Strength (UCS) of Ti$_2$AlC MAX phase as a function of the square root of grain size indicating Hall Petch relationship. Also included are data from other studies on Ti$_2$AlC.

1.1.1.2.   *High Temperature Mechanical Properties of Ti$_2$AlC*

The mechanical properties of Ti$_2$AlC up to 1100°C were studied in compression under quasi-static loading. For this study, four types of samples were chosen. To understand the effect of grain size, high-purity coarse and fine grain microstructure were tested and to understand possible effects of impurities, samples commercially available in bulk and from commercially available powders were also tested. Representative true stress-strain curves of high-purity fine-grain Ti$_2$AlC

6

shown in (Figure 1.1.3) are also indicative of the behavior of all samples tested. At low temperatures, (700°C and below) the samples exhibit high strengths and slight quasi-plastic behavior, while at higher temperatures the strength decreases and the quasi-plastic deformation increases, indicative of their Brittle-to-Plastic (BTP) transition. Note, all samples tested at 1000°C and 1100°C did not fail, instead the tests were stopped and barreling of samples was observed. The peak compressive true strengths for all samples were summarized in (Figure 1.1.4). Note the grain size effect is most pronounce below the BTP transition and by 1100°C the peak strength seems to converge for all samples at about 300 MPa, except for the fine grain sample from commercial powders whose peak strength is just shy of 200 MPa. For comparison, data from 718 Inconel also for compression at comparable strain rates is presented. Note peak values of Inconel are in the range of the fine grain MAX phase at 750°C and by 900°C and above, all the MAX phases, regardless of grain size or impurity, exhibit higher strengths than Inconel 718.
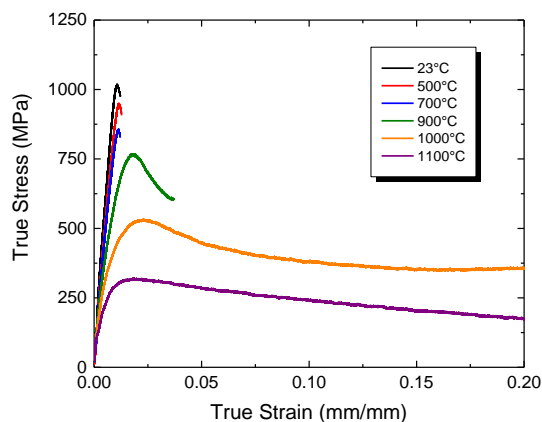

Figure 1.1.3: True ultimate compressive strength (UCS) of high purity fine-grainTi$_2$AlC MAX phase at various temperatures. Note that the testing was stopped for samples tested at 1000 and 1100 °C due to limit of extensometer and therefore the samples did not fail.
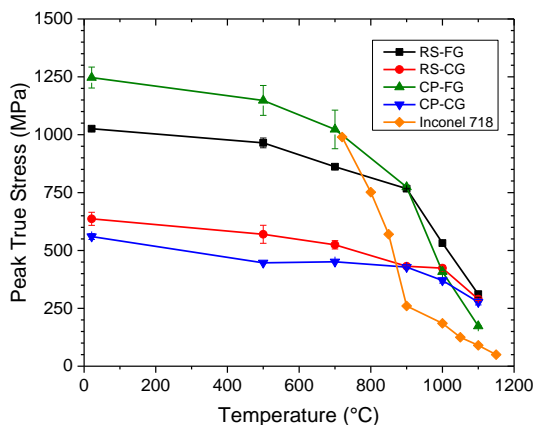

Figure 1.1.4: Summary of the average peak true stress and its standard deviation in compression for all Ti$_2$AlC MAX phase samples tested at various temperatures and Inconel 718 from literature for comparison.

7

1.1.1.3. *Hysteresis and Damage Accumulation in Ti$_2$AlC*

The hysteretic behavior of Ti$_2$AlC MAX phase was studied via cyclic compressive loading at 0.5 Hz. To investigate the effect on grain size on the hysteretic behavior, high-purity samples were heat treated to promote grain growth. In addition, the results were compared to commercially available Ti$_2$AlC in bulk and sintered from commercial powders by Spark Plasma Sintering. The energy dissipation per unit cycle of stress per unit volume plotted as a function of maximum applied stress squared (Figure 1.1.5). The sample made from commercial powder (CP-SPS-FG) has the finest grain size and shows the least energy dissipation followed by the high-purity samples which exhibit increasing energy dissipation with grain size. Note, however, that the maximum applied stress decreases with increasing grain size, as previously discussed, however the energy dissipation is higher at the same stress magnitude for samples with larger grain size.

To get a more in depth understanding of the hysteretic behavior and possible damage accumulation during cyclic loading, Resonant Ultrasound Spectroscopy (RUS) was performed. By performing small incremental steps in stress and monitoring the changes in the elastic properties, the precise moment of initiation and subsequent accumulation of microcracks in Ti$_2$AlC could be determined and their effects onto the hysteretic behavior investigated. In short three regions of hysteresis were observed in high-purity Ti$_2$AlC (Figure 1.1.6). At very low stresses, the energy dissipation quickly increases with maximum applied stress, the elastic modulus remains constant, and permanent deformation increases rapidly indicating that hysteresis in this region, does not cause large scale damage and is indicative of that caused by reversible dislocation pile ups. At the second regime, or higher stresses, the energy dissipation depends linearly on the maximum applied stress squared, as indicated by the incipient kinking model. In this range, a subtle decrease in elastic modulus indicates some minor damage, but the reduced rate of irrecoverable strain, indicates this is stable and is attributed to the small voids between grains that are necessary for incipient kinking to occur. At the last hysteretic regime, a deviation of the expected linear dependence of energy dissipation to higher values, along with a pronounce drop in elastic modulus indicates that the microscopic damage, possibly in the form of microcracks occurs. It is expected that energy dissipation from friction of between microcracks adds to the dissipation from incipient kinking, resulting in the larger than expected values of energy dissipation. It was therefore concluded that damage accumulation in MAX phases can be monitored by nondestructive techniques, namely RUS.
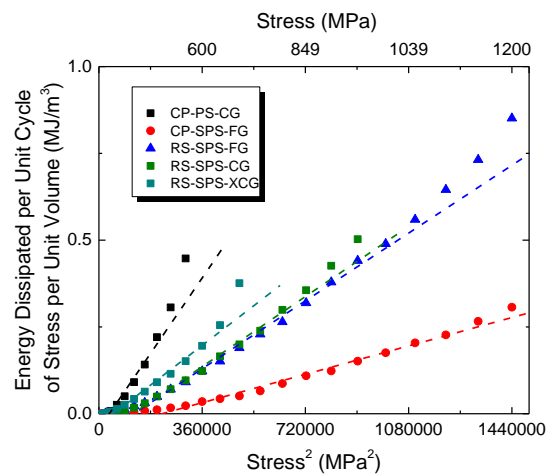

Figure 1.1.5: Summary of the Energy Dissipation of Ti$_2$AlC with various microstructures as a function of maximum applied stress squared. In dashed lines is the linear dependence of energy dissipation on maximum applied stress squared as proposed by the incipient kinking model.
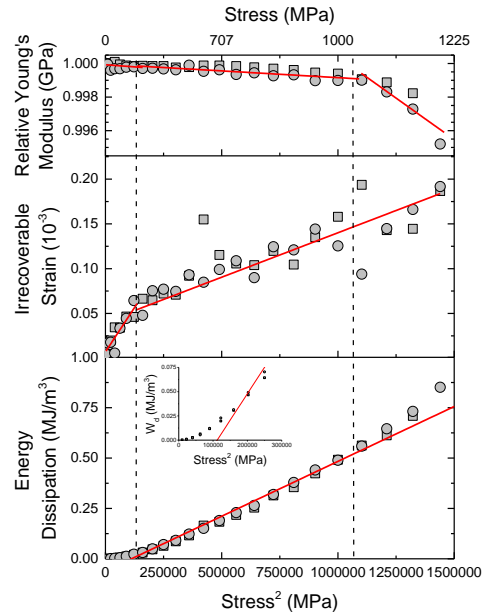
Figure 1.1.6: Summary of cyclic compression loading complemented by Resonant Ultrasound Spectroscopy (RUS). The top plot shows the change in elastic modulus, the middle plot shows the permanent deformation after the first load-unload cycle, and the bottom shows the energy dissipation; all results are for high-purity Ti_2AlC fine grain as a function of maximum applied stress squared.

1.1.2. Characterization of NiTi-MAX Composites and Interfaces
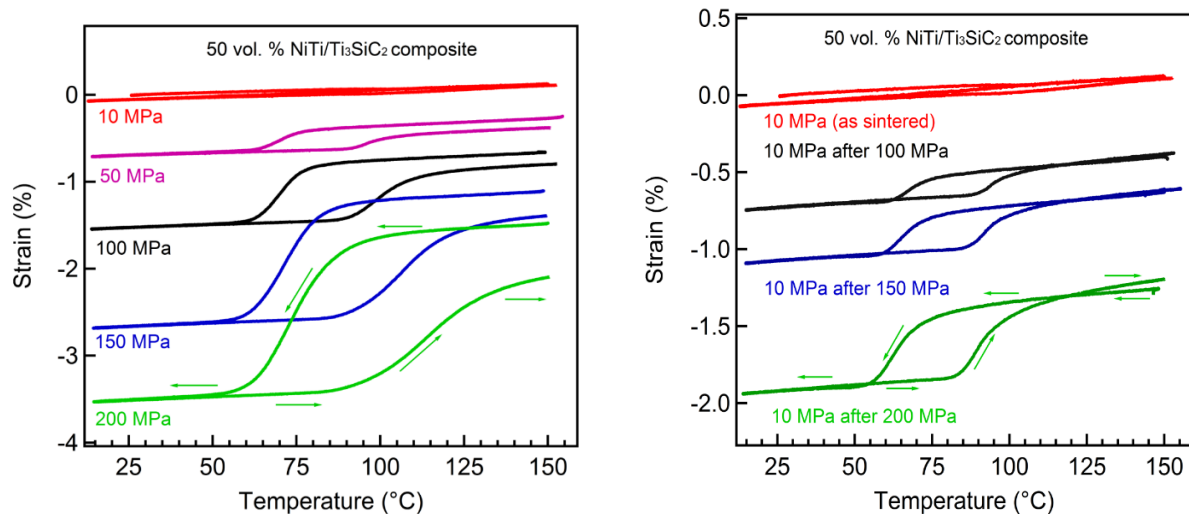### *1.1.2.1. Thermomechanical Characterization of Composites*

Figure 1.1.7: (a) Strain versus temperature plots under increasing compressive stress for the composite, (b) Evolution of two way shape memory effect (TWSME) with increasing compressive bias stresses during prior thermo-mechanical cycling for the composite

9

Figure 1.1.7 (a) and (b) show strain versus temperature plots under increasing compressive stress and two way shape memory effect respectively, for the composite. Compressive TWSM strains are observed for both the composite and the NiTi and are found to increase with stress, similar to transformation strains. The transformation strains increase with the applied stresses for pure NiTi and the composite as shown in Figure 1.1.8 (a). Smaller transformation strains are observed in the composite as compared to pure NiTi due to the following reasons: first, the composite has less than 50 vol. % of pure transformable NiTi; secondly, the stress experienced by the NiTi phase in the composite is less than the applied external stress because the stiffer Ti_3SiC_2 phase carries most of the stress; and lastly, the Ti_3SiC_2 phase puts a constraint on the amount of detwinning occurring by not allowing the martensite to detwin in order to maintain the compatibility across the interfaces.

Irrecoverable strains increase with increasing the applied stresses due to higher transformation induced plasticity and amount of retained martensite, as observed in Figure 1.1.8 (a). Interestingly, the irrecoverable strains for the composite is very close to that of pure NiTi, even after having large difference in the transformation strains, at each stress value. The ratio of the irrecoverable to transformation strains of the composite and pure NiTi at each stress provides a better comparison for the reversibility of the martensitic transformation in the composite and the pure NiTi (Figure 1.1.8 (b)). This ratio is much higher for the composite than that of pure NiTi which suggests that more factors are contributing towards the irrecoverable strain in the composite than those mentioned above for pure SMAs (NiTi). Irrecoverable strain in the composite is arguably a sum of two contributions: irrecoverable strain in NiTi and irrecoverable strain in Ti_3SiC_2. Irrecoverable strain in NiTi can be further categorized into two parts: one caused by dislocations and retained martensite in NiTi, irrespective of the presence of Ti_3SiC_2 around it; second caused by generation of dislocations and retained martensite due to the presence of Ti_3SiC_2 in the NiTi region, especially closer to the interface between NiTi and Ti_3SiC_2. Irrecoverable strain in Ti_3SiC_2 could be due to dislocation glide in individual grains and their bending or kinking. Some of the irrecoverable strain in Ti_3SiC_2 can possibly come from delamination, that does not propagate, but remains contained within the grain.
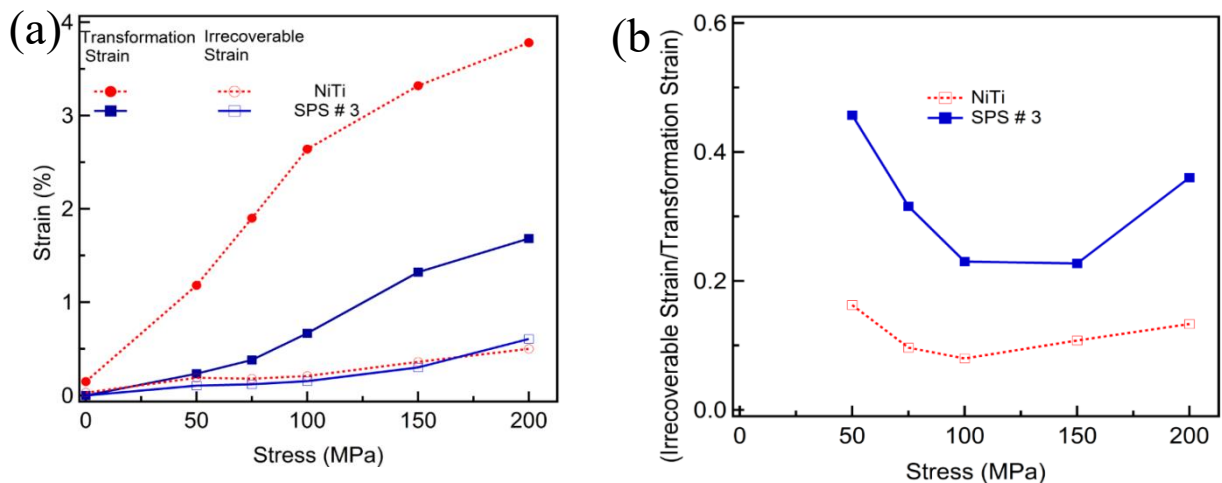

Figure 1.1.8: (a) Evolution of the transformation (solid)) and irrecoverable (hollow) strains with increasing compressive stresses for the composite (blue color) and its comparison with that of pure NiTi (red color), and (b) comparison of the ratio of irrecoverable to transformation strains of the composite with that of pure NiTi at different compressive stresses.

10
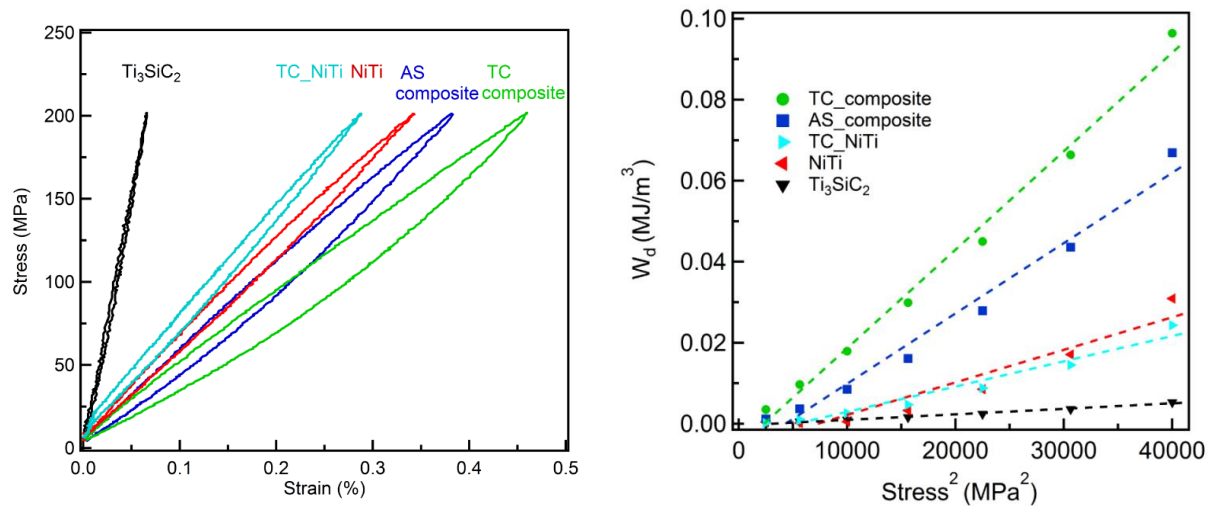
1.1.2.2. Energy Dissipation in Composites

Figure 1.1.9: (a) Engineering stress-strain loops at 200 MPa for each material, namely pure NiTi, fully dense pure Ti$_3$SiC$_2$, thermo-mechanically cycled (TC) pure NiTi, as-sintered (AS) and thermo-mechanically cycled (TC) composites, and (b) Energy dissipation per unit volume per loading-unloading cycle (W$_d$) as a function of maximum applied stress squared for each material, namely pure NiTi, fully dense pure Ti$_3$SiC$_2$, TC pure NiTi, AS and TC composites.

Both the as-sintered (AS) and thermo-mechanically cycled (TC) composites, show fully reversible, closed, non-linear hysteretic stress-strain loops when loaded in compression. Figure 1.1.9 (a) shows one representative engineering stress-strain loop at 200 MPa for each material, namely fully dense pure Ti$_3$SiC$_2$, pure NiTi, TC pure NiTi, AS and TC composites. The energy dissipation is the highest for the TC composite followed by AS composite, pure NiTi, TC pure NiTi and fully dense pure Ti$_3$SiC$_2$. To compare the energy dissipation capacity at varying stress levels for different materials, the energy dissipation (W$_d$) is plotted as a function of maximum stress squared in Figure 1.1.9 (b). On plotting W$_d$ as a function of σ^2 for the pure NiTi and NiTi/Ti$_3$SiC$_2$ composites, a linear dependence is observed where all the straight lines have an R^2 value > 0.96 except for pure NiTi which has a value of 0.91. The highest slope and thereby the highest dissipation, (W$_d$), is observed at all stress values for the TC composite followed by AS composite. At 200 MPa applied stress, W$_d$ in the TC composite is eighteen times larger than that of fine grain (FG) fully dense pure Ti$_3$SiC$_2$ and three times larger than pure NiTi. In AS composite, W$_d$ is thirteen times larger than that of FG fully dense pure Ti$_3$SiC$_2$ and two times larger than that observed in pure NiTi. W$_d$ in the TC composites is higher by an order of magnitude when compared to Mg/Ti$_3$SiC$_2$ composites at similar stresses.

This increase is due to the following reasons: First, higher stress experienced by the Ti$_3$SiC$_2$ phase due to difference in elastic moduli of NiTi and Ti$_3$SiC$_2$ phases which lead to higher damping in the Ti$_3$SiC$_2$ phase; second, damping due to hysteretic movement of twins and twin boundaries in NiTi phase; third, newly formed twins and twin boundaries in the NiTi phase near the interface region due to relaxation of residual stresses in the composite; and lastly, the presence of porosity.

1.1.2.3. NiTi-MAX Interfaces

Figure 1.1.10 shows the cross sectional views of the microstructure of NiTi-Ti$_3$SiC$_2$ interface after diffusion bonding at 800, 900 and 1000°C for 1, 5 and 10 hours. All the

11

microstructural images are shown on the X-Y plot where the X-axis is the bonding time and the Y-axis the bonding temperature. In all the micrographs in Figure 1.1.10, the lighter region on the left is equiatomic NiTi and the dark grey region on the right is Ti_3SiC_2. In between the two, the interface is marked with vertical dotted red lines to denote the start and end of the reaction layer in the interface. The numbers on each of the image are the lengths of the horizontal black lines which represents the average interface thickness. Successful bonding has been observed for all conditions except at 800°C for 1 hour.
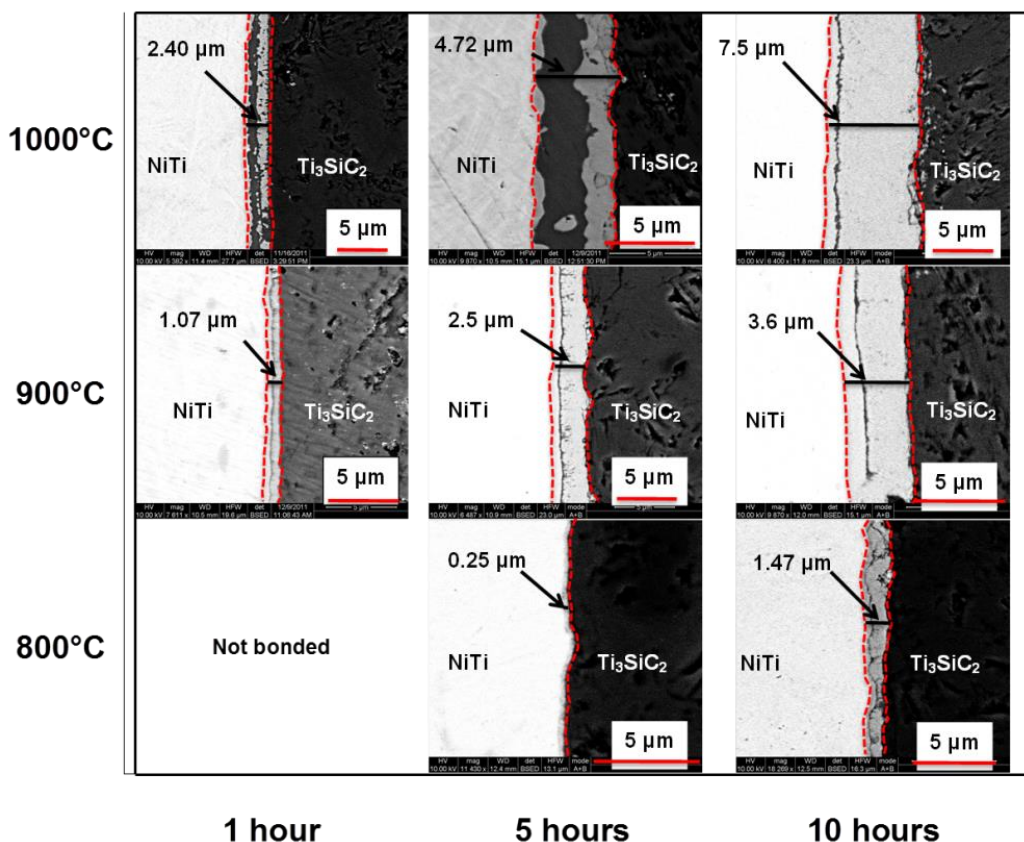
Figure 1.1.10: Microstructural evolution of the NiTi-Ti$_3$SiC$_2$ interface with time and temperature obtained by SEM. Red (dotted) line indicates the start and end of the interface region between NiTi and Ti$_3$SiC$_2$. Numbers shown in each of the micrographs are the thickness of the interface as indicated by the black horizontal line on each image in the interface region.

Figure 1.1.11 shows the distribution of different phases in the NiTi-Ti$_3$SiC$_2$ interface for the condition of 1000°C, 5 hours, obtained using Electron Back Scatter Diffraction analysis. It confirmed and substantiated the formation of Ti$_2$Ni, Ti$_5$Si$_3$ and NiTiSi reaction phases in the interface, inferred from the results of earlier quantitative analysis and Ni-Ti-Si ternary phase diagram. Figure 1.1.11 (a) shows the backscattered electron image of the NiTi-Ti$_3$SiC$_2$ interface formed at 1000°C, 5 hours, marked with area A from where the phase map shown in Figure 1.1.11 (b) is obtained using EBSD. Clearly, the interface has a structure of NiTi / Ti$_2$Ni / Ti$_5$Si$_3$ / NiTiSi / Ti$_3$SiC$_2$. TiC phases are detected in the Ti$_3$SiC$_2$ phase and also along the boundary between NiTiSi and Ti$_3$SiC$_2$. Small amount of TiC is expected to form as a result of Si de-intercalation and as Ti$_3$SiC$_2$ phase usually contains few percent impurities in the form of TiC.
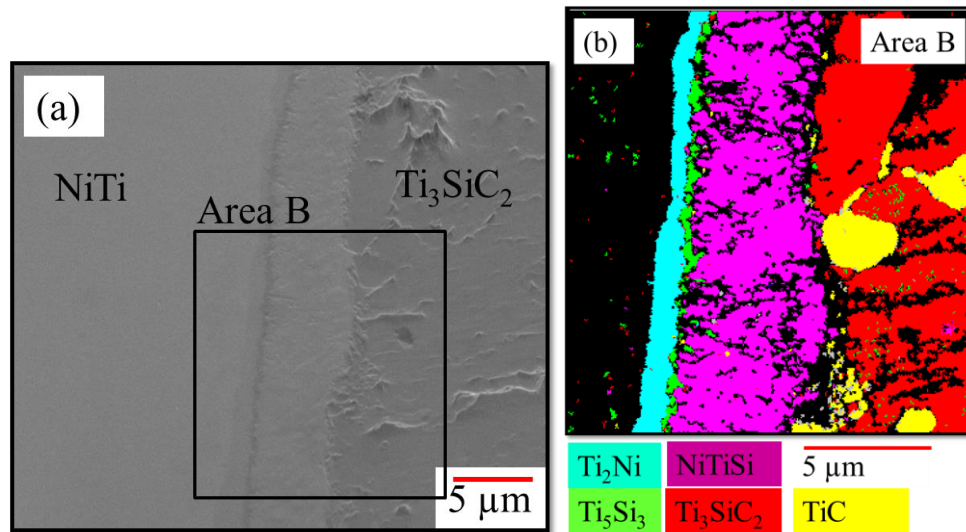
12

Figure 1.1.11: Images of the NiTi-Ti$_3$SiC$_2$ interface for the bonding condition of 1000°C, 10 hours (a) BSE image, and (b) Electron backscattered diffraction (EBSD) phase map of the area B marked in (a) showing the distribution of the reaction phases, Ti$_2$Ni (light blue),), Ti$_5$Si$_3$ (green) and NiTiSi (pink) and in the interface. Also shown are TiC (yellow) and Ti$_3$SiC$_2$ (red).
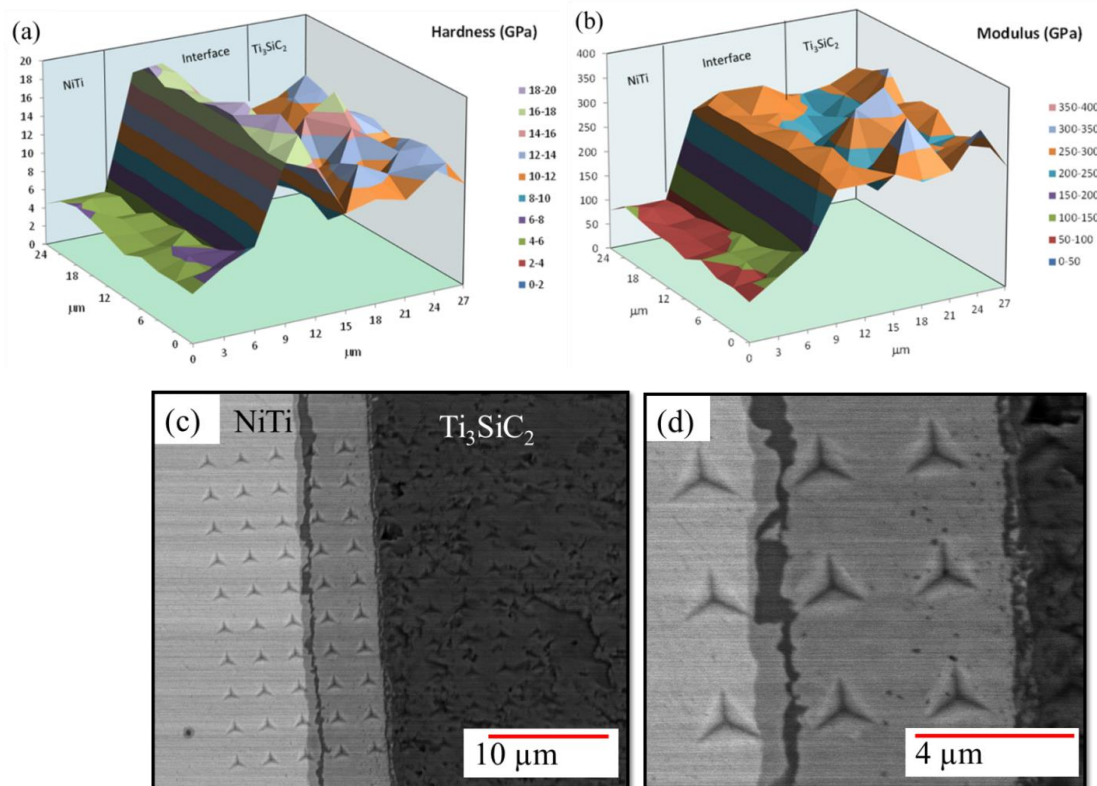

Figure 1.1.12: 3-dimensional plot of the (a) hardness in GPa and (b) elastic modulus in GPa, obtained using nanoindentation across the NiTi-Ti$_3$SiC$_2$ interface for the bonding condition of 1000°C, 5 hours. (c) BSE image of the locations of the indents where the plots in (a) and (b) were generated and (d) high magnification BSE image showing indents in different reaction phases.

13

Figure 1.1.12 (a) and (b) show 3-dimensional plots of the hardness and elastic modulus, respectively, obtained using nano-indentation across the NiTi-Ti$_3$SiC$_2$ interface for the bonding condition of 1000°C, 5 hours. A grid of 100 indents (10 x 10) each separated by a distance of 3 µm is made across the interface as shown in Figure 1.1.12 (c). High magnification BSE image shows the indents in different reaction phases (Figure 1.1.12 (d)). Indents lie partially in NiTi, interface and Ti$_3$SiC$_2$. Hardness of the reaction zone in the interface is higher than that observed for both NiTi and Ti$_3$SiC$_2$. An average hardness of 17.55 ± 0.95 GPa is obtained for the interface as compared to 5.44 ± 0.73 GPa for NiTi and 11.86 ± 1.80 GPa for Ti$_3$SiC$_2$. Elastic modulus of the reaction zone is higher than NiTi and close to that of Ti$_3$SiC$_2$. An average elastic modului of 278.68 ± 10.02 GPa is obtained for the interface as compared to 91.62 ± 11.16 GPa for NiTi and 263.21 ± 31.89 GPa for Ti$_3$SiC$_2$. Most of the indents within the interface lie in the NiTiSi phase which is responsible for the increased hardness as compared to the individual components.
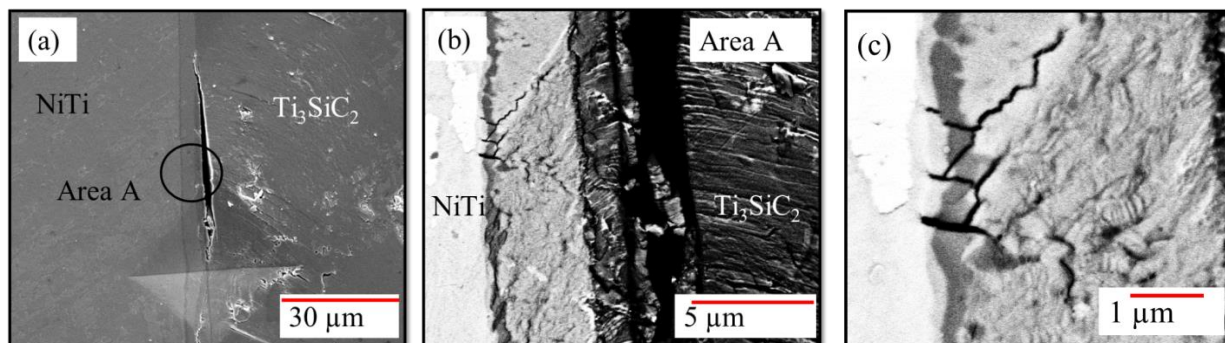

Figure 1.1.13: (a) Secondary electron (SE) image of the indent obtained during Vickers micro-hardness tests at a load of 0.3 kg on the NiTi-Ti$_3$SiC$_2$ interface bonded at 1000°C, 1 hour. (b) Backscattered electron (BSE) image of the "Area A" marked in Figure (a), (c) High magnification BSE image of the zigzag crack pattern obtained in the interface as shown in Figure (b).

Vickers micro-hardness test is used to obtain indents on/near the NiTi-Ti$_3$SiC$_2$ interface and investigate whether any cracks initiate and/or propagate near the interface. Any further quantitative analysis of these results is difficult to perform as most of the indents are larger than the interface thickness for most of the bonding conditions. As the interface thickness is in the order of few microns compared to the indent size which is in the range of tens of microns, the indents lie partially in NiTi, interface and Ti$_3$SiC$_2$ regions. Interestingly for few cases, cracks near the NiTi-Ti$_3$SiC$_2$ interface are observed around the indents. When the indent was oriented, so that its diagonal lies along the interface between the two phases, some corner cracks that propagate along the interface were observed. For example, Figure 1.1.13 (a) shows an indent obtained at a test load of 0.3 kg in the NiTi-Ti$_3$SiC$_2$ interface for the bonding condition of 1000°C, 1 hour. A large (~ 60 µm) crack initiates very close to the NiTi-Ti$_3$SiC$_2$ interface and propagates between Ti$_3$SiC$_2$ and interfacial reaction layer, and partially through Ti$_3$SiC$_2$. Some damage in the form of delamination is observed near the corners and edges of the indent on the Ti$_3$SiC$_2$ side. Figure 1.1.13 (b) shows a BSE image of the area marked as "Area A" in Figure 1.1.13 (a). Apart from the large crack, small cracks and crack patterns are also observed in the NiTi-Ti$_3$SiC$_2$ interface. These sub-cracks branch from the large crack in Ti$_3$SiC$_2$ and stop at the interface as it is depicted in Figure 1.1.13 (c) that shows a high magnification BSE image of the zigzag crack pattern obtained in the interface. The zigzag crack pattern and crack branching in the interface (Figure 1.1.13 c) is unlike straight crack paths commonly observed in typical brittle materials. The common phenomena of cracks originating elsewhere and terminating at the interface, as well as their torturous propagation path in the interface suggests the formation of a strong interface between bulk NiTi and Ti$_3$SiC$_2$ components at these temperatures, regardless of the fact that

14

interfacial reaction layer has higher hardness and, in some locations, stiffness than parent phases. Nevertheless, more quantitative testing such as interracial fracture toughness tests is needed to characterize and effectively comment on the mechanical properties of the NiTi-Ti_3SiC_2 interface.

1.1.3. Processing of Pure MAX Phase Powder and Bulk

OBJECTIVES:
(i) Processing of high-purity MAX phase powder from elemental powders through vacuum tube furnace and acid-rinse method
(ii) Processing of high-density and high-purity MAX phase samples from commercial powders and elemental powders through Spark Plasma Sintering

1.1.3.1. Processing of Fully Densified MAX phase from Commercial Powders

High-density Ti_2AlC and Ti_3SiC_2 samples were sintered at 1300°C and 1325°C for 15min from commercial powders by Spark Plasma Sintering system, respectively. However, SEM images shows that significant secondary intermetallics, approximately 18 vol. % $TiAl_x$ and ~6 vol. % $TiSi_x$, were present in bulk fully dense Ti_2AlC and Ti_3SiC_2 samples, respectively, after sintering from commercial powders. With collaboration of Dr. Nakiah Goulbourne in Michigan University and Dr. Arun Shukla in University of Rhode Island, the constitutive behavior and fracture toughness of commercial Ti_2AlC and Ti_3SiC_2 samples under dynamic thermo-mechanical loading were investigated in detail.

1.1.3.2. Processing of High-purity MAX Phase Powders

Herein, to minimize the effect of secondary intermetallics and improve the high temperature mechanical behavior, high-purity Ti_2AlC powder was fabricated from the elemental powders. The process of high-purity Ti_2AlC powder was as followed. The porous Ti_2AlC sample was firstly synthesized from 1.05Ti + 1.05Al + 0.95TiC at 1400°C for 4hrs through pressureless sintering. Then high-purity Ti_2AlC powder was milled from the porous sample The microstructure and morphology of pure Ti_2AlC powder are shown as Figure 1.1.14. It indicates the high-purity Ti_2AlC MAX powder was firstly successfully fabricated with only ~4%TiAl. In the next section, we studied the quasi-static and cyclic mechanical characterization on the high-purity Ti_2AlC powder.

As typical Cr_2AlC MAX phases exhibit the most corrosion resistance and high temperature resistance. With doping of Mn element, the mechanical behavior shall be improved without damage of Cr_2AlC characteristics. Therefore, high-purity $(Cr_{0.9}Mn_{0.1})_2AlC$ powder was fabricated for high temperature and corrosion resistance application. The processing was as followed. Firstly, bulk $(Cr_{0.9}Mn_{0.1})_2AlC$ MAX phase was fabricated through SPS from elemental powders. Then raw $(Cr_{0.9}Mn_{0.1})_2AlC$ powder was drilled from the bulk sample and acid-rinsed to get the - high-purity powder. The rinse solution was 10 vol% of acid mixture of $1HNO_3$:$1HCl$:$1HF$. The microstructure and morphology of high-purity $(Cr_{0.9}Mn_{0.1})_2AlC$ powder after acid-rinse was shown as Figure 1.1.14. Vickers hardness test indicates the hardness of $(Cr_{0.9}Mn_{0.1})_2AlC$ increases from 4.1 GPa for pure Cr_2AlC to 5GPa with substituting of Mn on Cr site. We are working on studying corrosion resistance and magnetic behavior of high-purity $(Cr_{0.9}Mn_{0.1})_2AlC$ MAX phase.

1.1.3.3. Synthesis of Bulk High-purity MAX Phase from Elemental Powders

High-purity Ti_2AlC, Ti_3AlC_2 and Ti_3SiC_2 samples were also successfully synthesized and densified by Spark Plasma Sintering in one-step process from elemental powders. Near single
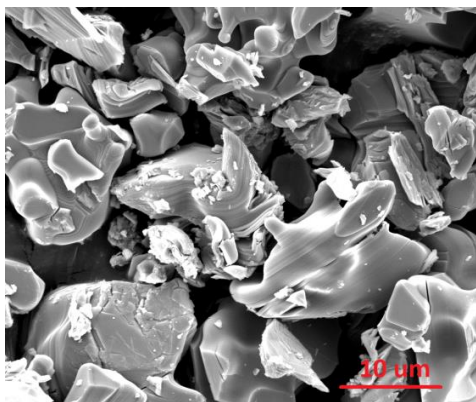
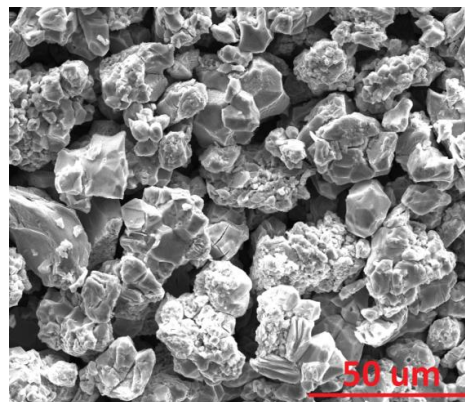**Figure 1.1.14: Secondary electron SEM image of pure Ti$_2$AlC powder.**

Figure 1.1.15: Secondary electron SEM image of pure (Cr$_{0.9}$Mn$_{0.1}$)$_2$AlC powder after acid rinse.

phase Ti$_2$AlC (with 5 vol% TiAl) and Ti$_3$AlC$_2$ were fabricated from Ti, Al and TiC powders at 1450°C and 1510°C for 15mins, respectively. The resultant microstructure and morphology of Ti$_2$AlC and Ti$_3$AlC$_2$ are shown in Figure 1.1.15. Room temperature mechanical characterization such as hardness and compressive strength were investigated on fully-dense and high-purity Ti$_2$AlC and Ti$_3$AlC$_2$. The ultimate compressive strengths of Ti$_2$AlC and Ti$_3$AlC$_2$ were about 1200 ± 50 and 1087 ± 58 MPa, respectively. All specimens did not exhibit obvious plastic deformation and fractured abruptly. The fracture strength of Ti$_2$AlC was higher than any value reported in literature. In the future, we are looking forward to processing large quantities of pure bulk MAX phase samples for thermal and mechanical characterization in Texas A&M University, as well in Dr. Goulbourne's and Dr. Shukla's Lab. And high-purity Ti$_3$SiC$_2$ samples was also made from Ti, Si, and TiC at 1580°C for 15mins under pressure of 50MPa. The back scattering SEM image was shown in Figure 1.1.16. The mapping shows that the dark phase was poor of Si element (TiC impurity), indicating there was ~7 vol% TiC impurity. We are working on polishing the recipe of fabrication of bulk Ti$_3$SiC$_2$ MAX phase samples from elemental powders through Spark Plasma Sintering.
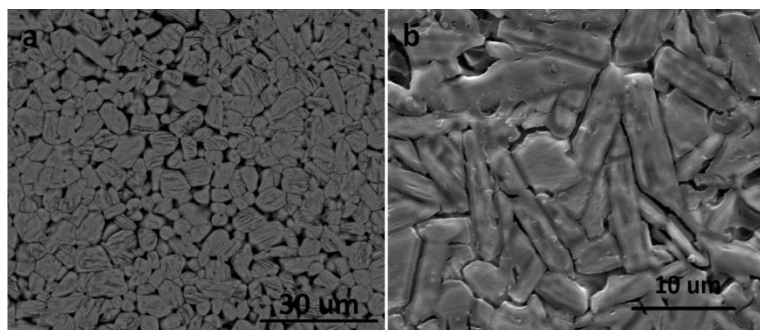

Figure 1.1.15: Backscatering electron SEM image of Ti$_2$AlC (a) and Ti$_3$AlC$_2$ (b) synthesized from the elemental powders.
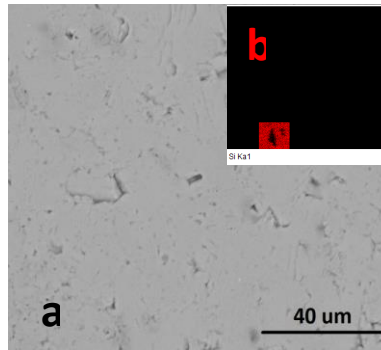
16

Figure 1.1.16: Backscatering electron SEM image of Ti$_3$SiC$_2$ (a) synthesized from the elemental powders and Si-element mapping of (b)

1.1.4. Graded Ceramic/Metal Composites (GCMeC)

OBJECTIVES:
(iii) Fabricate NiTi/MAX phase composites using spark plasma sintering (SPS) and melt infiltration and characterize their structural, thermal and mechanical properties.
(iv) Fabricate a multifunctional FGHC that will consist of multiple layers, starting from a ceramic thermal barrier layer, and followed by a graded ceramic/metal composite (GCMeC) layer that finally transitions to a high-temperature polymer matrix composite (PMC).
(v) Develop Actively-Cooled PMCs (AC-PMC) using microvascular cooling functionality on commercially available PMCs, High-Temperature PMCs (HT-PMC) based on polyimide matrices, and combination of both.

TECHNICAL ACCOMPLISHMENTS
1.1.4.1. Multilayer Composites
A multilayer hybrid composite (Figure 1.1.17) consisting of three layers, Ti$_3$SiC$_2$, NiTi/Ti$_3$SiC$_2$ composite, and NiTi, respectively, was prepared from a bulk Ti$_3$SiC$_2$ disk, NiTi/Ti$_3$SiC$_2$ powder mixture, and NiTi powder using SPS. During the preparation, powder consolidation and joining of different layers simultaneously took place.

Significant difference of the processing temperatures of the components, however, makes the joining a challenging process. Specifically, the composite in Figure 1.1.17 was prepared at 960 °C, that is, the sintering temperature of NiTi. However, the sintering of Ti$_3$SiC$_2$ requires much higher temperatures. To overcome the problem, a fully-dense, bulk disk of Ti$_3$SiC$_2$, instead of powder, was used. Meanwhile, to enhance the bonding between the Ti$_3$SiC$_2$ and the NiTi/Ti$_3$SiC$_2$ composite, the bonding surface of Ti$_3$SiC$_2$ was sand blasted prior to joining. More importantly, the same technique could apply for joining the NiTi to the PMC, where PMC has a much lower processing temperature.

1.1.4.2. Metal/MAX Phase Composites Fabricated by SPS-assisted Infiltration
In addition to powder metallurgy, infiltration is another technique to prepare ceramic metal composite. In some cases, infiltration is more effective than powder metallurgy with respect to minimizing two-phase reactions. Meanwhile, the ceramic that normally requires a higher sintering temperature than the metal can be sintered prior to infiltration to avoid incomplete sintering in that case where the ceramic-metal powder mixture was sintered. Therefore, an infiltration technique based on SPS is developed to process metal/MAX phase composites.
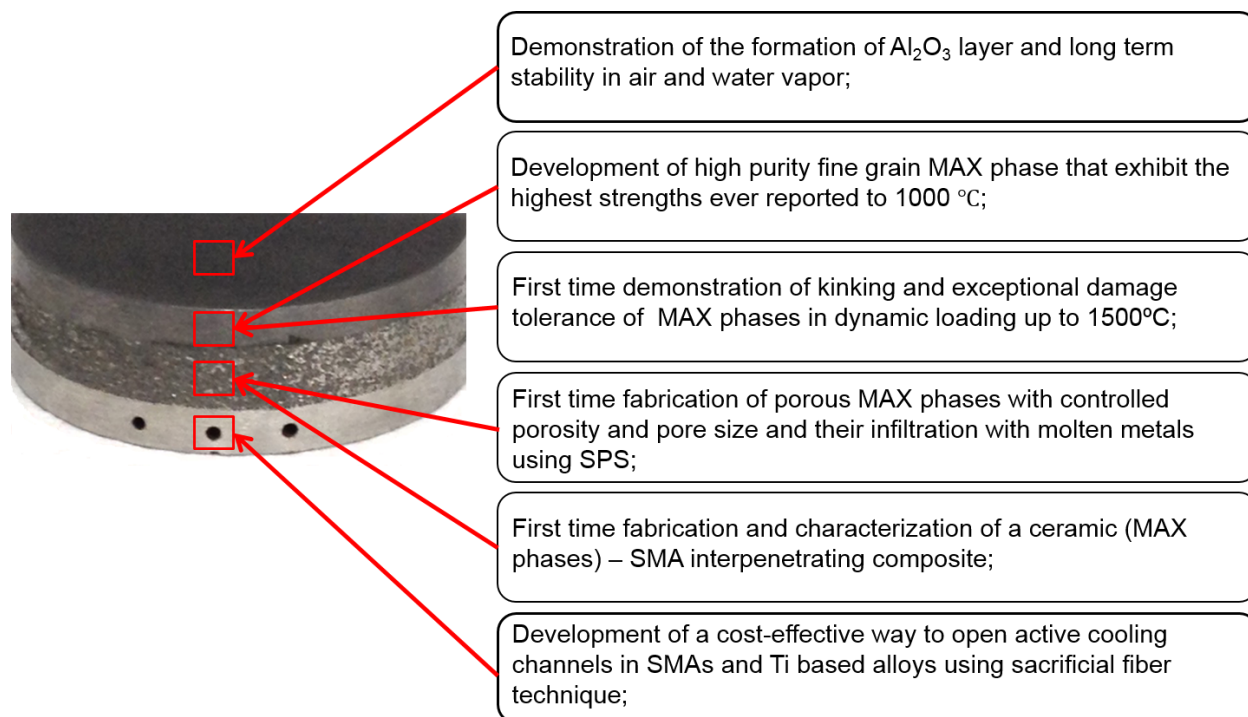
17

Demonstration of the formation of Al_2O_3 layer and long term stability in air and water vapor;

Development of high purity fine grain MAX phase that exhibit the highest strengths ever reported to 1000 ℃;

First time demonstration of kinking and exceptional damage tolerance of MAX phases in dynamic loading up to 1500℃;

First time fabrication of porous MAX phases with controlled porosity and pore size and their infiltration with molten metals using SPS;

First time fabrication and characterization of a ceramic (MAX phases) – SMA interpenetrating composite;

Development of a cost-effective way to open active cooling channels in SMAs and Ti based alloys using sacrificial fiber technique;

Figure 1.1.17: An optical image of a hybrid composite consisting of three layers of Ti_3SiC_2, NiTi with microchannels, and $NiTi/Ti_3SiC_2$ composite.

A Ti_2AlC foam with 40 vol.% porosity and 355–500 μm particle size (Figure 1.1.18 (a)–(c)) was prepared as a preform for infiltration. It is clearly shown that the interconnected, open pores are homogeneously dispersed in the Ti_2AlC, while some closed pores can be found on the struts of the foam due to incomplete sintering during the pressureless sintering. Meanwhile, Figure (c) illustrates clearly the strong connectivity of Ti_2AlC grains on the struts of the foam. The strong network of grains is critical to obtain high mechanical strength of porous preform, which turned into the struts of the composite after infiltration.

The Ti_2AlC foam was then infiltrated with aluminum alloy 6061 (AA6061). Figure 1.1.18 (d)–(f) show an optical image and the microstructure of the $AA6061/Ti_2AlC$ composite. The AA6061 infiltration occurred dominantly in the open pores, and volume fractions of the components in the final composites, e.g. ceramic phase, metallic phase, open and closed pores, are tunable by adjusting the initial porosities in the ceramic preform.

Figure 1.1.19 shows a phase map and four element maps, namely Ti, Al, C, and O, of the composite with interpenetrating phase sizes of 167–545 μm. Both identified and unidentified phases are color coded in the phase map. 82.0 % of all phases were identified, and 18.0 % were not identified. The identified phases include Ti_2AlC, Ti_3AlC_2, Al, $TiAl_3$, and Al_2O_3. Al_2O_3 is present in both ceramic and metallic phase regions. The Al_2O_3 in the ceramic phase region most likely comes from the raw materials, whereas the Al_2O_3 in the metallic phase region most likely results from surface oxidation. The unindexed, black regions have three possible sources. First, the black dots with sizes of approximately 10 μm in the Ti_2AlC region are pores. Second, the black dots with sizes less than 1 μm at interfacial area are unidentified because of the height difference between Al and Ti_2AlC. The height difference was generated during polishing, because Al and Ti_2AlC have different wear rates, and some shadow areas prevented the scattering of the electrons in these areas. Third, the black, straight lines with lengths of 50–150 μm are scratches, which were introduced by polishing. A significant amount of $TiAl_3$, i.e. 7.3 %, was identified at either the interfacial region or the ceramic phase regions. The $TiAl_3$ in the interfacial region forms

18

a "ring" surrounding the Al phase and separating it from the ceramic phases. A comparison between the phase map and a SEM image of the Ti_2AlC foam suggests that the locations of the $TiAl_3$ at the ceramic phase region are formerly the pores on the ceramic walls where molten Al could reach and react with Ti_2AlC during the infiltration process.
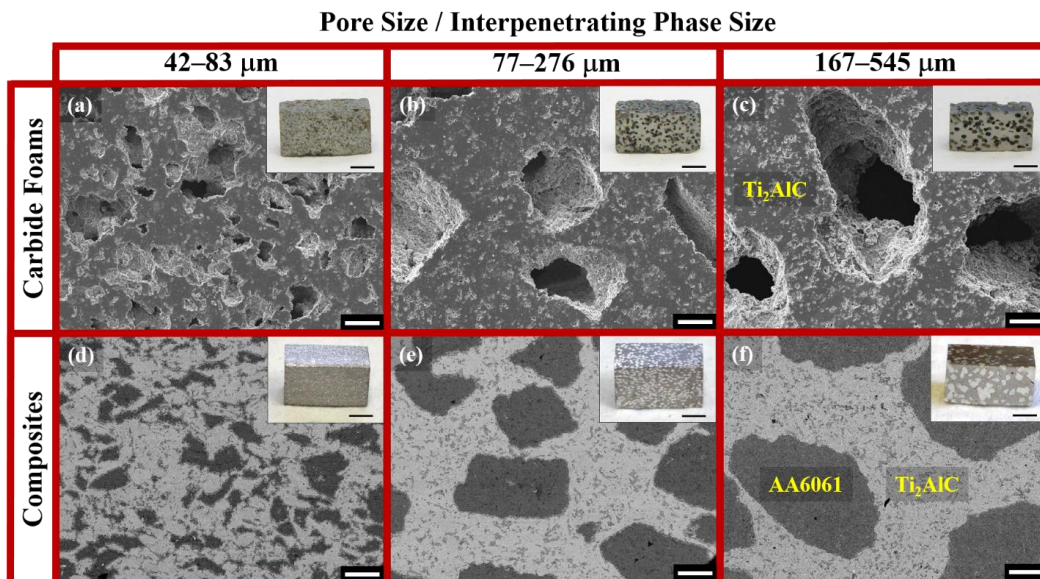

Figure 1.1.18: SEM images of Ti$_2$AlC foams with different pore sizes fabricated using NaCl particles as pore formers; the ranges of the pore size are (a) 42–83 μm, (b) 77–276 μm, and (c) 167–545 μm. All three foams were fabricated using the same volume fraction (40 vol.%) of the NaCl particles. The infiltration of these three foams with AA6061 resulted in AA6061/Ti$_2$AlC composites with different interpenetrating phase sizes: (d) 42–83 μm, (e) 77–276 μm, and (f) 167–545 μm; the interpenetrating phase size are formerly pore size in the foams before infiltration. Insets show photographs of both the foams and the composites after electrical discharge machining to dimensions of 3.5 mm × 3.5 mm × 7 mm. Scale bars in optical photograph: 2mm. Scale bars in the SEM images: 100 μm. Scale bars in the photographs: 2 mm.

Figure 1.1.20 (a) shows the compressive stress-strain curves of a 27%AA6061/Ti$_2$AlC composite, a solution heat treated (SHT) AA6061, and a Ti$_2$AlC foam. SHT AA6061 is more comparable with the condition of aluminum alloy in the composite. The ultimate strength of the composite is 1095 MPa, which is about 7 times that of the Ti$_2$AlC foams (150 MPa) and about 10 times the yield strength of the SHT AA6061 (110 MPa). Figure 1.1.20 (b) shows that the specific strength, i.e., compressive/yield strength divided by density, of the composite is 335 MPa•cm^3/g, which is about 5 times that of the Ti$_2$AlC foam (62 MPa•cm^3/g), 3 times that of the peak aged (PA) AA6061 (115 MPa•cm^3/g), 6 times that of previously reported value of the Ti$_3$AlC$_2$/Al composite (55 MPa•cm^3/g), and 5 times the yield strength of the SHT AA6061 (41 MPa•cm^3/g). Post-testing analysis of fracture surfaces (now shown here) shows evidences of the crack propagation resistance in the composite. Figure 4(c) shows typical compressive stress-strain curves of the composites and PA AA6061 at 25 ºC and at 400 ºC. Note that AA6061 creeps at 400 ºC, which is approximately 0.7 times the melting point of aluminum. The ultimate strength of the composites at 400 ºC (800 MPa) is approximately 14 times the yield strength of AA6061 at 400 ºC (58 MPa) and is even 2.5 times the yield strength of AA6061 at room temperature (300 MPa).
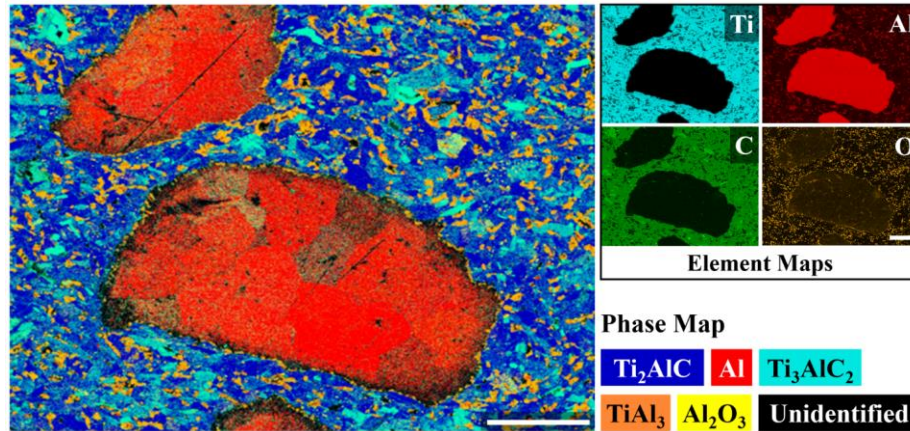
19

Figure 1.1.19: A phase map and four element maps, namely Ti, Al, C, and O, of the AA6061/Ti$_2$AlC composite with interpenetrating phase sizes of 167–545 μm. Both identified and unidentified phases are color coded in the phase map; 82.0 % of all phases were identified, and 18.0 % were not identified. The identified phases include Ti$_2$AlC, Ti$_3$AlC$_2$, Al, TiAl$_3$, and Al$_2$O$_3$; the percent of each phase is listed in Table 2. Scale bars: 100 μm.
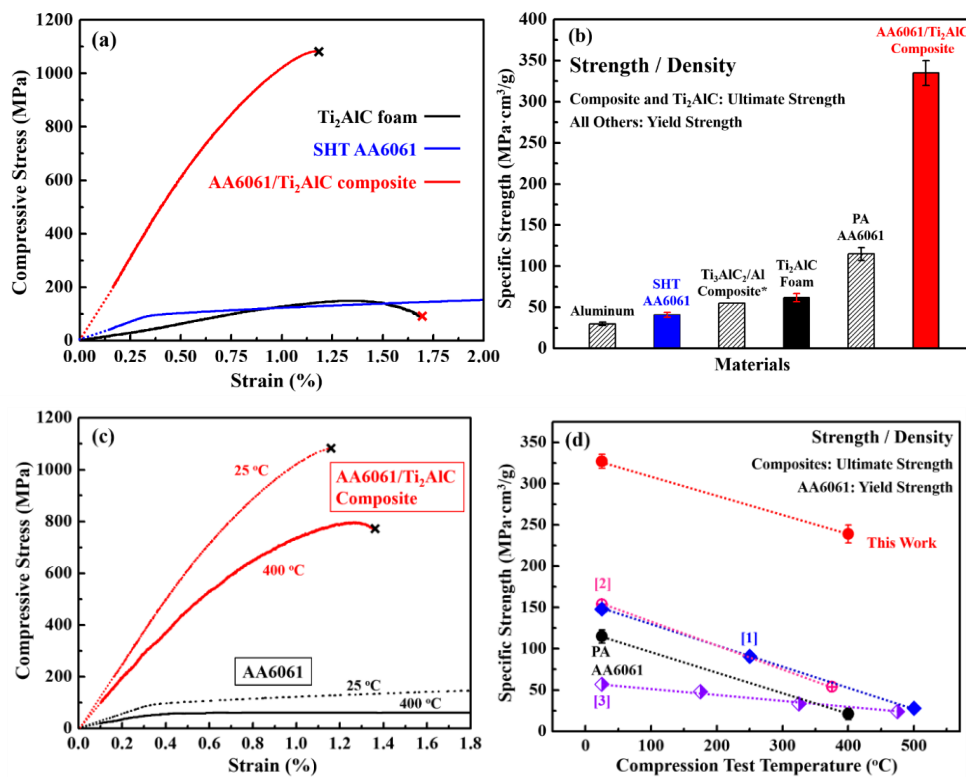
Figure 1.1.20: (a) Typical compressive stress-strain curves of a 27%AA6061/Ti$_2$AlC composite, a solution heat treated (SHT) AA6061, and a Ti$_2$AlC foam. (b) Specific strength of the AA6061/Ti$_2$AlC composites, the peak aged (PA) AA6061, and the Ti$_2$AlC foam, the Ti$_3$AlC$_2$/Al composites, the solution heat treated AA6061, and pure aluminum. (c) Compressive stress-strain curves of the 27%AA6061/Ti$_2$AlC composites and AA6061 at 25 °C and 400 °C. (b) Specific strength as a function of compression test temperature for the 27%AA6061/Ti$_2$AlC composites from the present study (red curve), Ti$_3$AlC$_2$/Al composites (blue curve [1]), B$_4$C/Al composites (pink curve [2]), Al$_2$O$_3$/Al composites (purple curve [3]), and PA AA6061 (black curve).

20

1.1.4.3. SMA/MAX Phase Composites Fabricated by Powder Metallurgy

It has been shown that the $NiTi/Ti_3SiC_2$ composite with the most fraction of active (shape memory) component has a relative density of 86%. Therefore, it is worthy to investigate if a higher density could be achieved without losing the active component.

One factor that plays an important role in the densification during SPS is sintering pressure. Holding the sample at a significantly higher pressure, however, requires a much stronger die set than the graphite one, which has already been used at extreme pressures. A WC die set was used as a replacement of graphite die set to achieve pressures as high as 300 MPa, that is, three times of the capability of the graphite die set. Figure 1.1.21 shows the relative density, differential scanning calorimeter (DSC) curves, and microstructure of $NiTi/Ti_3SiC_2$ composites SPSed at 960 °C for 8 min using different sintering pressures. It is clearly shown that using higher sintering pressure significantly improves the densification of the $NiTi/Ti_3SiC_2$ composites with active (shape memory) components.
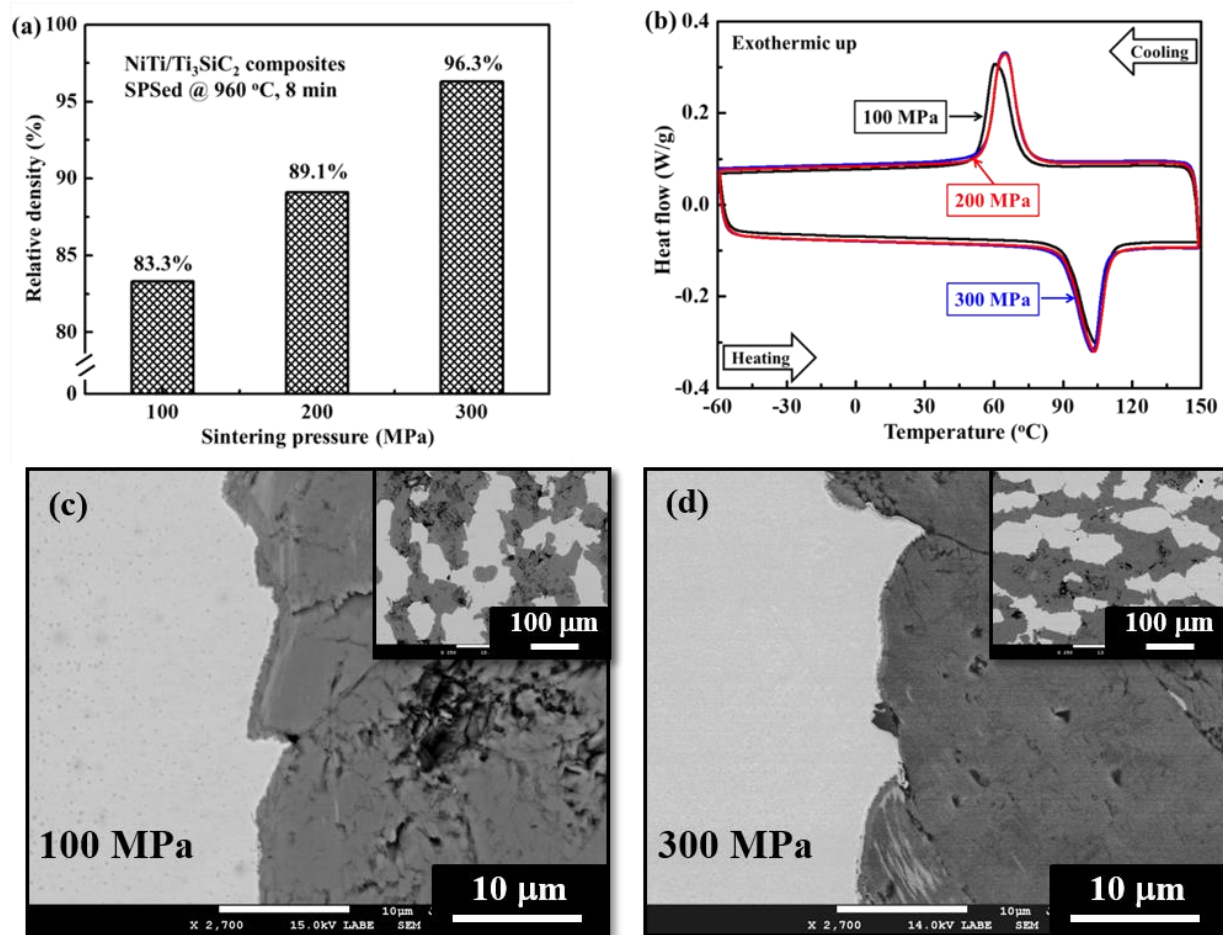
Figure 1.1.21: Effect of sintering pressure on (a) density, (b) DSC curves, and (c~d) microstructure of the $NiTi/Ti_3SiC_2$ composites.

An accurate measurement of the thermo-physical properties of shape memory alloy (SMA)/MAX phase composites is essential for modeling and predicting their thermal performance in high-temperature structural applications. Therefore, the thermal diffusivity and specific heat at constant pressure of the $NiTi/Ti_3SiC_2$ composite were measured in a range from room temperature

21

to as high as 1224 K, and thus the corresponding thermal conductivity was calculated. To validate the measurement results, a survey of data for the thermal diffusivity, specific heat, and thermal conductivity of monolithic NiTi and Ti_3SiC_2 was carried out. To predict the thermal conductivity of this composite and compare with the experimental data, finite element (FE) modeling on a micromechanics based representative volume element (RVE) was also carried out.
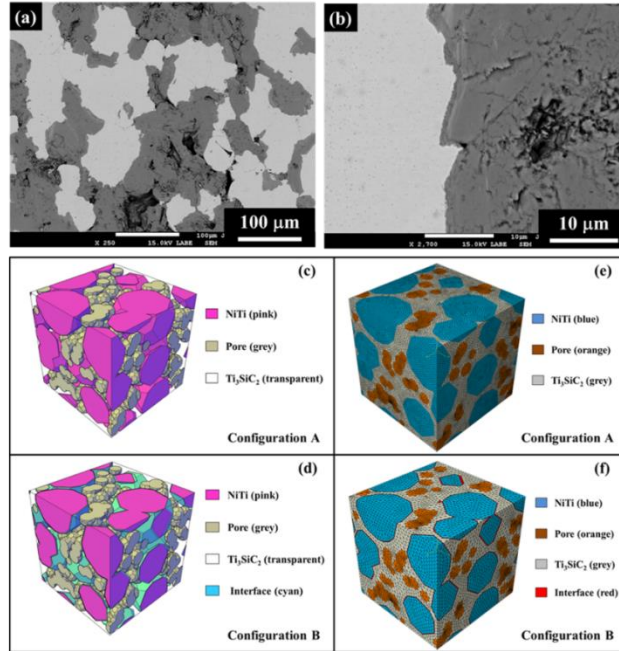

Figure 1.1.22: Back scattered SEM images showing (a) phase distribution and morphology, and (b) interface. 3-D RVEs of the NiTi/Ti_3SiC_2 composite: (c) in configuration A, grey represents pore, pink NiTi, and transparent Ti_3SiC_2; (d) in configuration B, grey represents pore, pink NiTi, transparent Ti_3SiC_2, and cyan interface; (e) FE meshes on the configuration A RVE; and (f) FE meshes on the configuration B RVE.
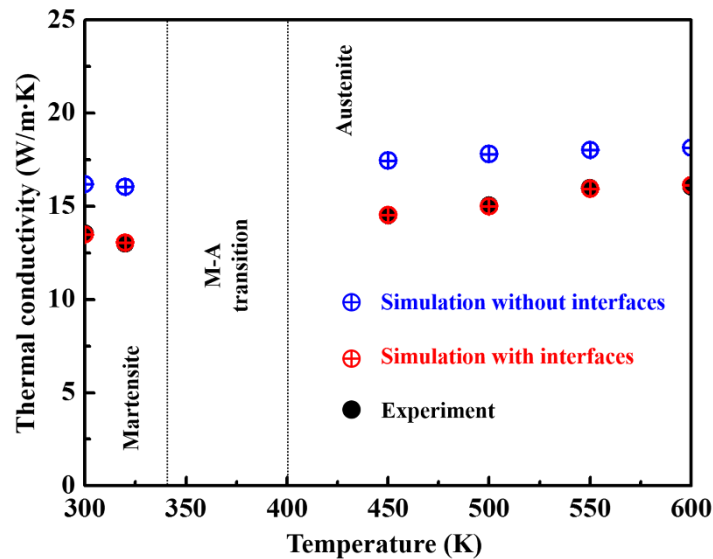
Figure 1.1.23: Temperature-dependent thermal conductivity of the NiTi/Ti_3SiC_2 composite as a function of temperature: simulation and experimental results. Simulations results based on both configuration A and B are shown.

Two 3-D representative volume elements (RVEs), configurations A and B, are generated based on the micrographs of the composites (Figure 1.1.22 (a) and (b)). In addition to the two constitutive phases, the configuration A considers only porosity, whereas the configuration B considers both porosity and interfaces, as shown in Figure 6(c) and (d), respectively. Figure 1.1.23 shows the comparison of simulation with experimental results for the two configurations. The discrepancy between the measured data and the modeling predictions indicates that the presence of interfaces, besides porosity, may play an important role in thermal transport.

The computational framework developed in this study offers a tool to provide insight into the effective thermal properties of the interface layer, which are difficult to determine experimentally.

1.1.4.4. *NiTi with Microchannels*
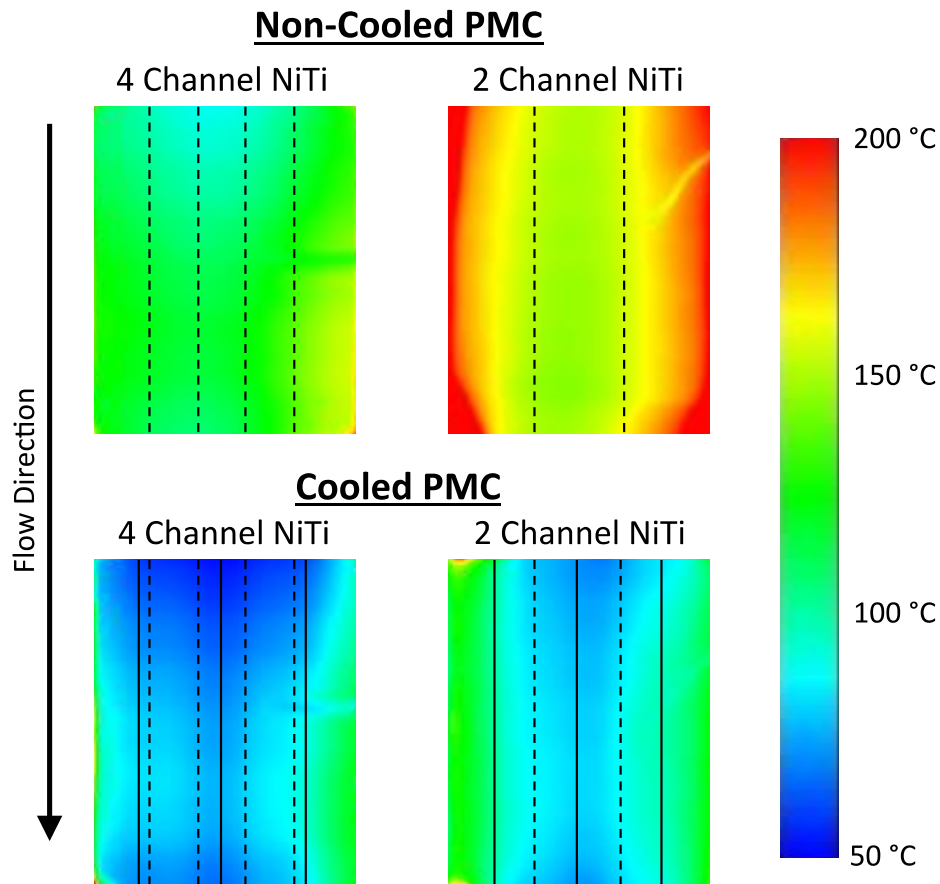
Figure 1.1.24: Free surface temperature profiles from the IR camera for each of the four test configurations. The approximate location of the channels are marked on each image, with the NiTi channels shown as dashed lines and the PMC channels as solid lines. Total supplied heat flux was 300 kW/m² and total coolant flow rate in the NiTi was 80 ml/min for all cases. When the PMC was cooled, the total flow rate in the PMC was 60 ml/min. Coolant was water.

Figure 1.1.24 shows the free surface temperature profiles from IR imaging. Active cooling was most effective when coolant was distributed through more channels, with the cooled PMC, four channel NiTi case performing the best. Cooling was least effective for the two channel NiTi without PMC cooling case, which was the only configuration where the interface temperature exceeded the Tg of the PMC. In all cases the NiTi temperature was maintained well below the 500 °C maximum service.

23

1.2 ACTIVELY COOLED POLYMER MATRIX COMPOSITES (AC-PMC)

RESEARCH TEAM MEMBERS
PIs: Prof. Scott R. White, Prof. Nancy R. Sottos, Prof. Philippe H. Geubelle
Graduate Students: Anthony M. Coppola, Ahmad R. Najafi, Marcus Tan, Dr. Piyush R. Thakre (post-doc, former), Dr. Soheil Soghrati (former)
Undergraduate Students: Sean Murray, Vignesh Vishwanathan, Luke Warpinski (former), Kevin Hughes, Jie Lin, Anthony S. Griffin (former)

COLLABORATORs:
Liangfa Hu (Texas A&M University), Prof. Miladin Radovic (Texas A&M University), Prof. Ibrahim Karaman (Texas A&M University),Dr. Alejandro Aragón (EPFL, Lausanne, Switzerland), Dr. Masoud Safdari (U. of Illinois)

OBJECTIVES:

(vi) Manufacture and characterize vascularized composites for multifunctionality
(vii) Study the effect of channels on the mechanical properties of the PMC
(viii) Experimentally evaluate thermal performance and thermomechanical behavior of actively cooled PMCs
(ix) Develop multi-disciplinary computational tool for the efficient and accurate modeling of the thermal impact of embedded microchannels in microvascular composites
(x) Combine the tool developed in Objective (iv) with optimization scheme to perform the computational design of microvascular composites

TECHNICAL ACCOMPLISHMENTS

1.2.1 Manufacture of Channels in PMCs by Vaporization of Sacrificial Components (VaSC)

VaSC was developed to manufacture channels in PMCs with minimal effect on composite processing. Figure 1.2.1 outlines the VaSC procedure. Sacrificial material composed of poly(lactic acid) treated with catalyst (*e.g.* tin(II) oxalate or tin(II) octoate) are integrated into the fiber preform prior to matrix solidification. The sacrificial material is designed to survive typical PMC manufacturing processes up to 177 °C then be removed during a 200 °C or above post-cure in a vacuum environment to create a hollow channel. SFs can be integrated directly into the textile manufacturing process to create complex, three-dimensional network architectures. In addition, the sacrificial material is a thermoplastic polymer and can be formed into complex shapes through melt or solvent processing. Vascular architectures have been created from sintered spheres, melt-spun fibers, laser cut hot-pressed sheets, and 3D printed structures (Figure 1.2.2).
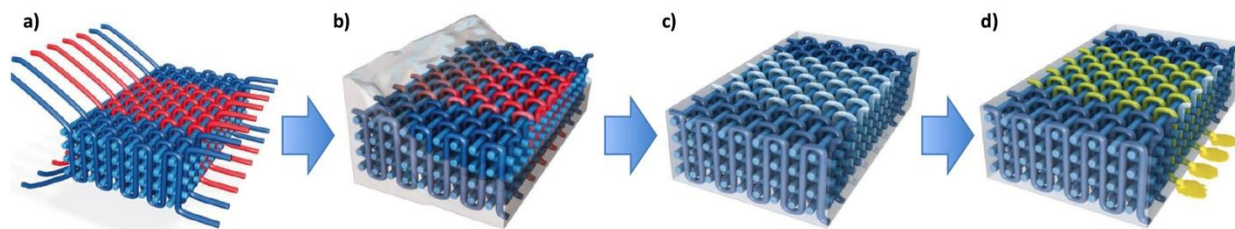

Figure 1.2.1: Outline of the VaSC process. The sacrificial material is first integrated into the fiber preform (a), the matrix is introduced (here using VARTM) (b), the composite is cured, and then the sacrificial material is removed at elevated temperature to create a hollow channel (c). In (d) a functional fluid is introduced.
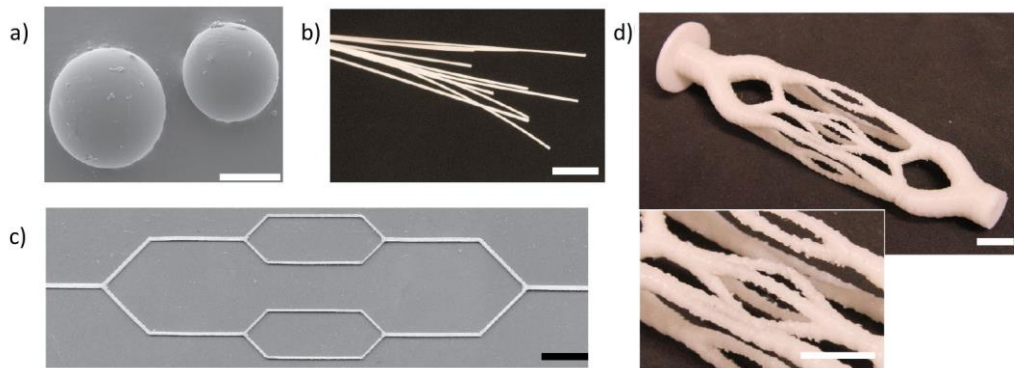
24

Figure 1.2.2: Examples of sacrificial templates that have been created for the VaSC process with dimensionality increasing from 0D-3D. a) SEM of sacrificial spheres (scale bar = 20 µm). b) 300 µm melt-spun fibers (scale bar = 5 µm). c) Network laser cut from a hot-pressed sheet (scale bar = 10 mm). d) 3D printed structure (scale bars = 10 mm).

1.2.2. Mechanical Behavior of Vascularized Composites

The effect of vascularization on the in-plane tensile properties and damage development for three-dimensional orthogonally woven glass fiber textile composite was examined (Figure 1.2.3). Two vascular architectures, straight and wave shaped, were tested in both longitudinal and transverse orientations. Non-vascular controls subject to the same post-cure conditions required for removal of sacrificial fibers (48 h at 200°C under vacuum) had no effect on the tensile properties of the composite material, despite the post-cure temperature being significantly higher than the composite's glass transition temperature. The results of tension testing confirm that vascular channels have negligible effect on composite tensile strength and modulus when integrated with the fiber architecture so that no disruption of the reinforcing fibers occurs (*i.e.* straight channels), regardless of orientation of loading. In contrast, when the vascular channels misalign the reinforcing fibers in the textile (*i.e.* wave channels), some reduction in strength occurred, especially when loaded in a transverse orientation.
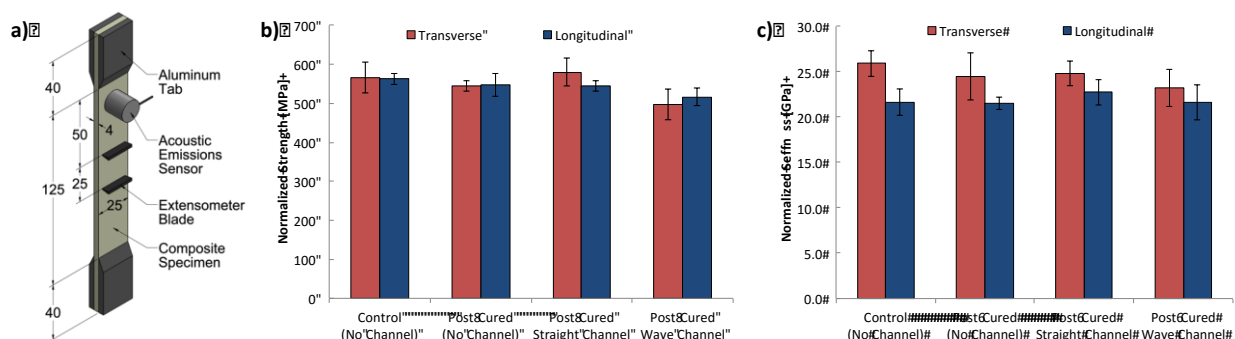
Figure 1.2.3: a) Sample setup for tensile testing. b) Test results for strength. c) Test results for stiffness. Strength and stiffness were normalized to equal fiber volume fractions.

Active Cooling Characterization of Vascularized PMCs

Active cooling performance of vascularized PMCs was characterized using the test setup shown schematically in Figure 1.2.4(a). The PMC sample was heated by a resistive heater on one face and imaged using an infrared camera on the opposite face while coolant was pumped through the channels. Several cooling configurations were evaluated by varying coolant flow

25

direction in each channel, channel architecture, and flow rate. Cooling efficiency was defined as the ratio of the heat extracted by the coolant to the heat supplied. Extracted heat was measured using the change in coolant temperature from inlet to outlet, as measured by thermocouples. Results are shown in Figure 1.2.4(b), which compares a non-cooled specimen to actively cooled specimens in several cooling configurations. Using counter flow, where the flow in each channel is in the opposite direction to its neighbor, provided a more uniform temperature field and higher cooling efficiency than using parallel flow. The straight channel specimen was more effective than the wave channel specimen, with a slightly higher cooling efficiency.
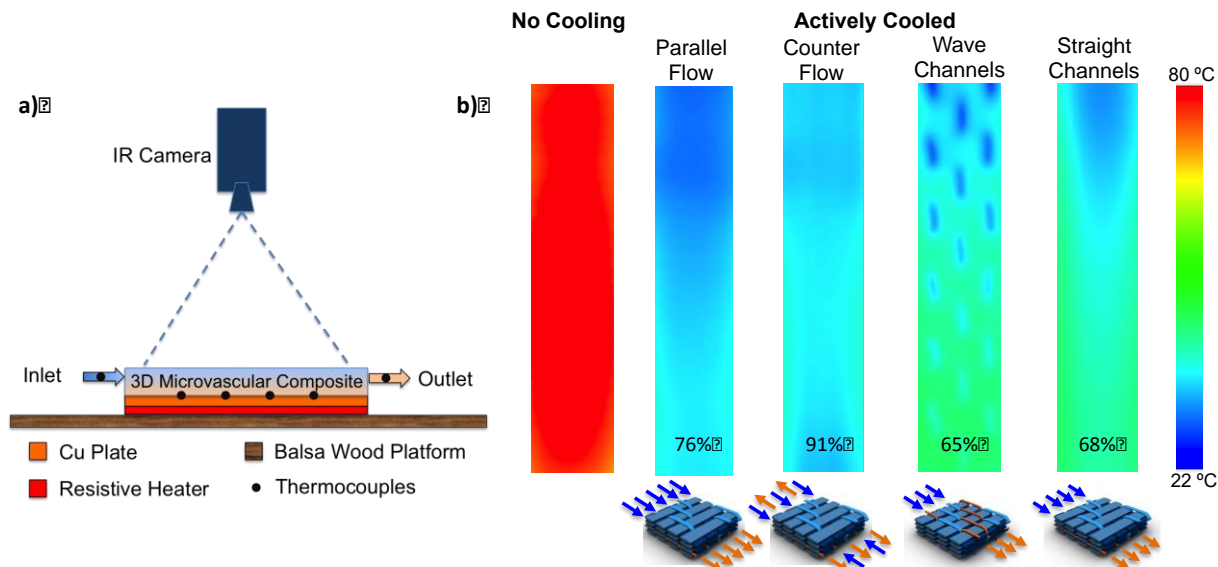
Figure 1.2.4: a) Schematic of the test setup for thermal characterization of actively cooled composites. b) Results from thermal testing comparing a non-cooled sample to actively cooled specimens. Parallel flow vs. counter flow and wave channels vs. straight channels are compared. Cooling efficiency is marked on each specimen. Supplied heat flux equaled 2.1 kW/m^2 and flow rate was 1 ml/min per channel. Coolant was water.

1.2.3. Thermomechanical Characterization of Actively Cooled Composites

Building on the results from thermal characterization of the actively cooled composite, thermomechanical behavior was studied. Two tests were performed to evaluated thermomechanical performance. In the first experiment, a four-point bending test was performed in a convectively heated environmental chamber while water was pumped through the channels at a fixed flow rate, shown schematically in Figure 1.2.5(a). Vascular composites were manufactured from the three-dimensional orthogonally woven glass fiber textile used for tensile testing. The effectiveness of two different channel architectures was evaluated, including specimens containing channels only at the mid-plane ("MPC") and specimens containing channels at the top and bottom surface ("SC"), containing four and eight channels, respectively. Stiffness retention was defined as the modulus at a given temperature (E_{HT}) divided by the stiffness of the composite at room temperature (E_{RT}). Actively cooled composites demonstrated vastly improved high temperature behavior compared to non-cooled composites. Actively cooled composites retained up to 90% of their modulus in a 325°C environment, a temperature that thermally degraded and destroyed the non-cooled composites (Figure 1.2.5(b)). These remarkable results were achieved by reducing the temperature of the composite by over 50% compared to the temperature of the environment. Comparison of MPC and SC specimens show

26

that placing the channels near the surface of the composite and distributing the coolant through more channels yielded improved cooling results.

The second experiment is currently on-going and examines the failure behavior of actively cooled PMCs during thermomechanical loading. The test shown in Figure 1.2.5(c) has been developed to study the failure behavior of actively cooled composites subjected to simultaneous compressive loading and one-sided heat flux. Straight channels are manufactured in an autoclave cured carbon fiber prepreg composite. Heat is provided using a radiative heater on one face, while the temperature of the opposite face is measured using an IR camera. The plate is loaded in a Boeing compression-after-impact style fixture, providing anti-buckling support at the edges. During a test, the plate is compressed at a constant load less than its room temperature strength, then heat is applied while the plate is cooled. Time-to-failure is then measured. Figure 1.2.5(d) shows the time-to-failure for non-cooled and actively cooled specimens as a function of supplied heat flux. Non-cooled composites failed rapidly at heat fluxes as low as 10 kW/m^2. However, actively cooled composites sustained 50 kW/m^2 for 30 minutes without failure and showed prolonged failure times at higher heat fluxes compared to what would be experienced by the non-cooled specimens.
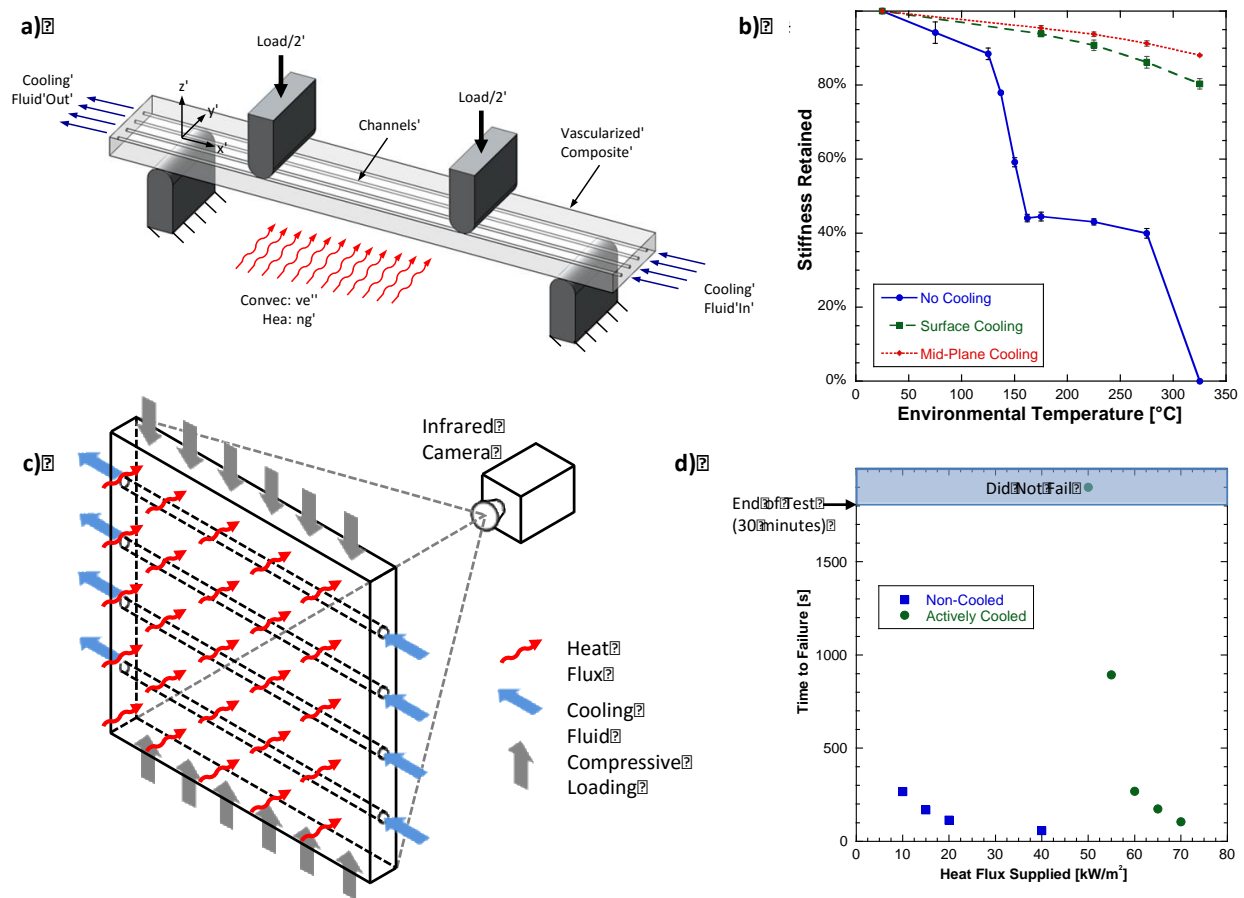
Figure 1.2.5: a) Schematic of the test setup for measuring flexural modulus retention as a function of heating and cooling parameters. b) The stiffness retained by a non-cooled specimen compared to actively cooled specimens. Total water flow rate equaled 160 ml/min. a) Schematic of the testing setup for studying failure behavior of actively cooled composites. d) Time-to-failure as a function of heat flux for non-cooled and actively cooled specimens (6 channels spaced 12 mm). Compressive load was 200 MPa and water flow rate was 15 ml/min per channel.

27

1.2.4. Active cooling of a bilayer nickel titanium (NiTi)-polymer matrix composite (PMC) hybrid containing microchannels fabricated by Vaporization of Sacrificial Components (VaSC)

Based on prior results, active cooling in the PMC alone is inadequate to remove heat fluxes in the hundreds of kW/m² range without temperatures exceeding the glass transition temperature of the PMC. Active cooling through channels manufactured into the NiTi layer was examined to enhance thermal performance by taking advantage of the high thermal conductivity of the metal. Channels were manufactured in both materials using VaSC. In the PMC, poly(lactic acid) fibers treated with tin(II) oxalate were used as the sacrificial material. These fibers were created using the previously reported solvent infiltration method. In the NiTi, our collaborators at Texas A&M developed a new method for creating channels in sintered metal using Mg Wire as the sacrificial material, which vaporize to form the channel during sintering. Channels formed by VaSC in each material are shown in Figure 1.2.6(a). A vascularized sample of the bilayer material was thermally characterized using the test setup schematically shown in Figure 1.2.6(b). Figure1.2.6(c) shows a comparison of the temperature in the hybrid system with and without active cooling. Without active cooling the maximum temperature of the PMC (T_g) was exceeded at just 10 kW/m². In contrast, the temperature of the PMC in the actively cooled system was maintained below this threshold through 300 kW/m².
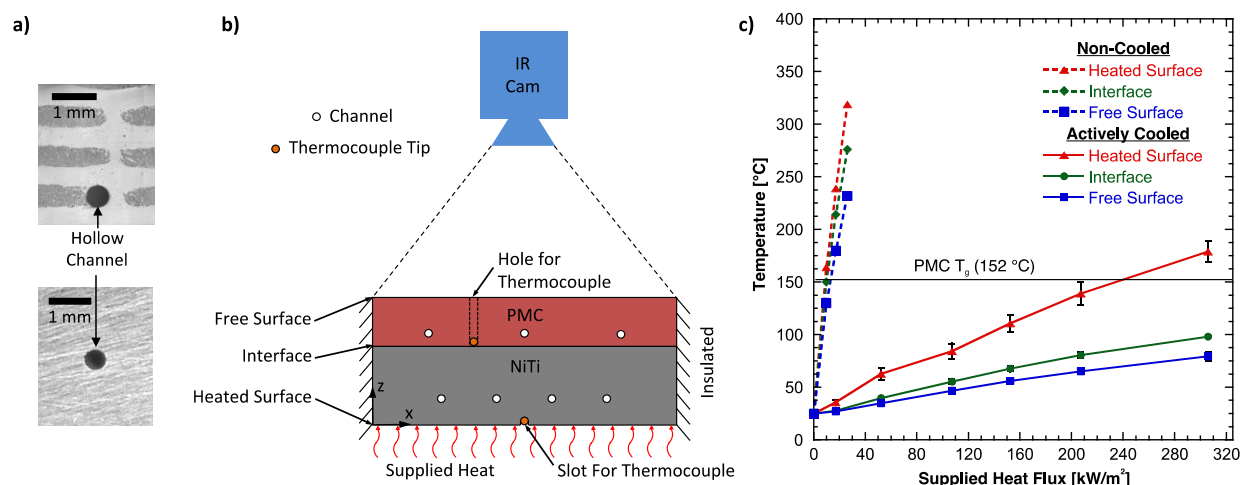
Figure 1.2.6: a) Image of 500 μm channels in the PMC (top) and NiTi (bottom). b) Schematic of the testing setup for thermal evaluation. A resistive heater supplied the heat. The sample measured 22 mm (x) by 27 mm (y, into the page). Straight 500 μm diameter channels were oriented along the y-direction and spaced as shown in the schematic. Thermocouple tips were inserted halfway along the y-direction in machined holes. c) Comparison of material temperatures with and without active cooling as a function of the supplied heat flux. The total flow rate of water during active cooling was 140 ml/min, with the flow equally distributed through each channel.

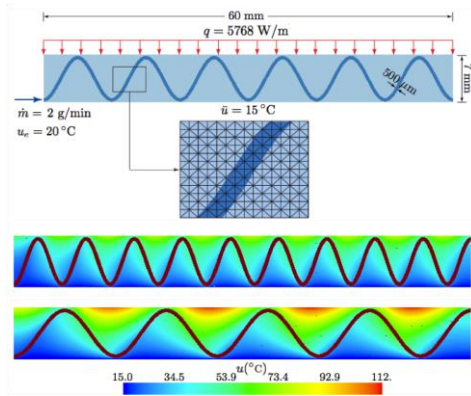## 1.2.5 Development of an interface-enriched generalized finite element method

Fig. 1.2.7: IGFEM thermal analysis of a microvascular plate with a sinusoidal-shape microchannel. The inset shows the non-conforming structured mesh used in the analysis.

To support these experimental developments and guide the design of embedded microchannels, a multidisciplinary computational method referred to as the Interface-enriched Generalized Finite Element Method (IGFEM) was developed. The introduction of this method was motivated by the need to simulate a large number of microchannel configurations due to the large number of design variables (channel shape and diameter, channel separation, flow rate of the coolant, applied heat flux, etc.) entering the design process. The creation of finite element meshes conforming to every configuration was a major bottleneck in this computational design process.

To address this challenge, the new numerical method was introduced to allow for the efficient and accurate simulation of the thermal impact of embedded microchannels containing a flowing coolant on the high-temperature composite component without the need for finite element discretizations that conform to
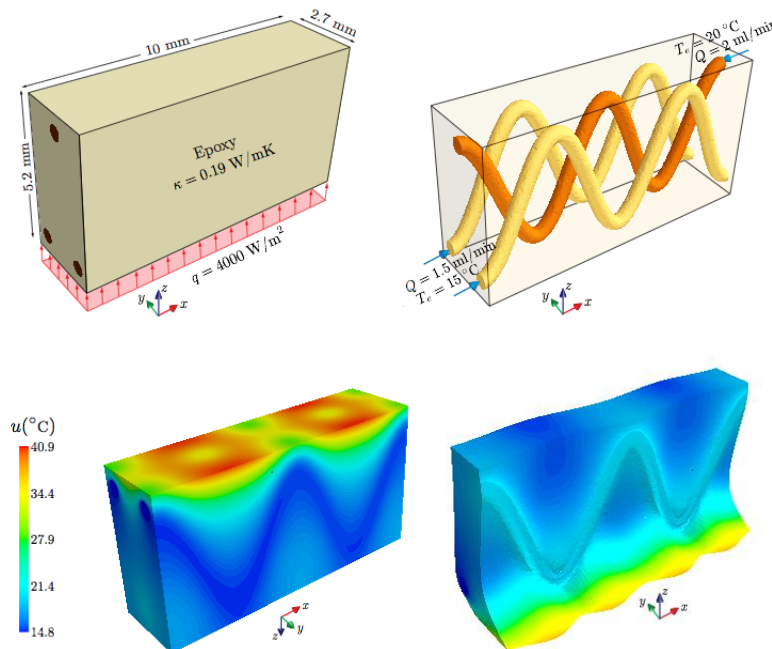
Fig. 1.2.8: 3D IGFEM thermal analysis of a microvascular epoxy fin with 3 counter-flowing microchannels. The thermal solution shown in the bottom figures clearly shows the thermal impact of the embedded microchannels.

29

the microchannel geometry, as illustrated in Figure 1.1.2.7.

As in conventional GFEM, the IGFEM relies on the enrichment of the finite element approximation in the element intersected by the material interfaces (i.e., the microchannel boundary in the case of microvascular, composites). For the thermal problem of interest, this enrichment aims at capturing the discontinuous gradient at the solid/fluid interface. However, in the IGFEM approach, the generalized degrees of freedom that define the enriched solution are associated with the nodes defined along the interface itself, not the nodes of the non-conforming mesh. This presents a set of important advantages in terms of the number of generalized degrees of freedom and the imposition of Dirichlet (essential) boundary conditions (Soghrati *et al.*, 2012).

Thermal and structural versions of the IGFEM were formulated, implemented, verified and validated in both 2D and 3D, showing excellent precision and convergence properties, similar to those of the classical finite element mesh, but without the need for conforming meshes. The IGFEM solver was further enhanced with a Streamline Upwind Petrov-Galerkin (SUPG) treatment of the convective term associated with the flowing coolant in the microchannels, thereby reducing the numerical oscillations associated with the conventional Galerkin treatment of the convective term. An example of the type of solution provided by the 3D IGFEM solver with a non-conforming tetrahedral finite element mesh is shown in Fig. 1.2.8.

It should be mentioned that, although the method was developed for the computational analysis and design of microvascular composites for high temperature, the IGFEM can be applied to model efficiently any heterogeneous materials, including particulate composites (Figure 1.2.9).
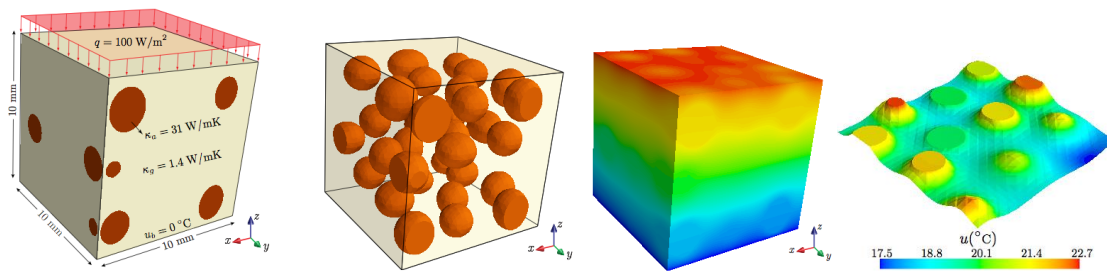

Fig. 1.2.9: IGFEM thermal analysis of a particulate composite. The right figure shows a slice of the thermal field, demonstrating the ability of the IGFEM solver to capture the sharp gradient discontinuities at the particle/matrix interfaces.

The ability to model complex heterogeneous materials without the need to generate finite element discretizations that conform to the material interfaces makes this method particularly attractive in the multiscale modeling of heterogeneous materials, in which multiple realizations of the microstructure need to be simulated to extract some of the statistics of the macroscopic (homogenized) response of interest (Aragón *et al.*, 2013). It should also be mentioned that the method can readily be extended to more complex enrichments, as was done recently using NURBS-based enrichment functions to model very accurately interfaces with very complex shapes (Safdari *et al.*, 2014).

1.2.6. Computational design of microvascular composite

Two types of computational design studies were conducted as part of this project. The first one (Sighrati, Najafi *et al.*, 2013) involved a parametric study for a microvascular composite panel subjected to a heat flux applied along its bottom face (Figure 1.2.10), for which the design parameters included the wavelength, amplitude and spacing of the wavy microchannels, the length of the panel, the applied heat flux and the flow rate and direction (parallel vs. counter-flow) of the coolant.
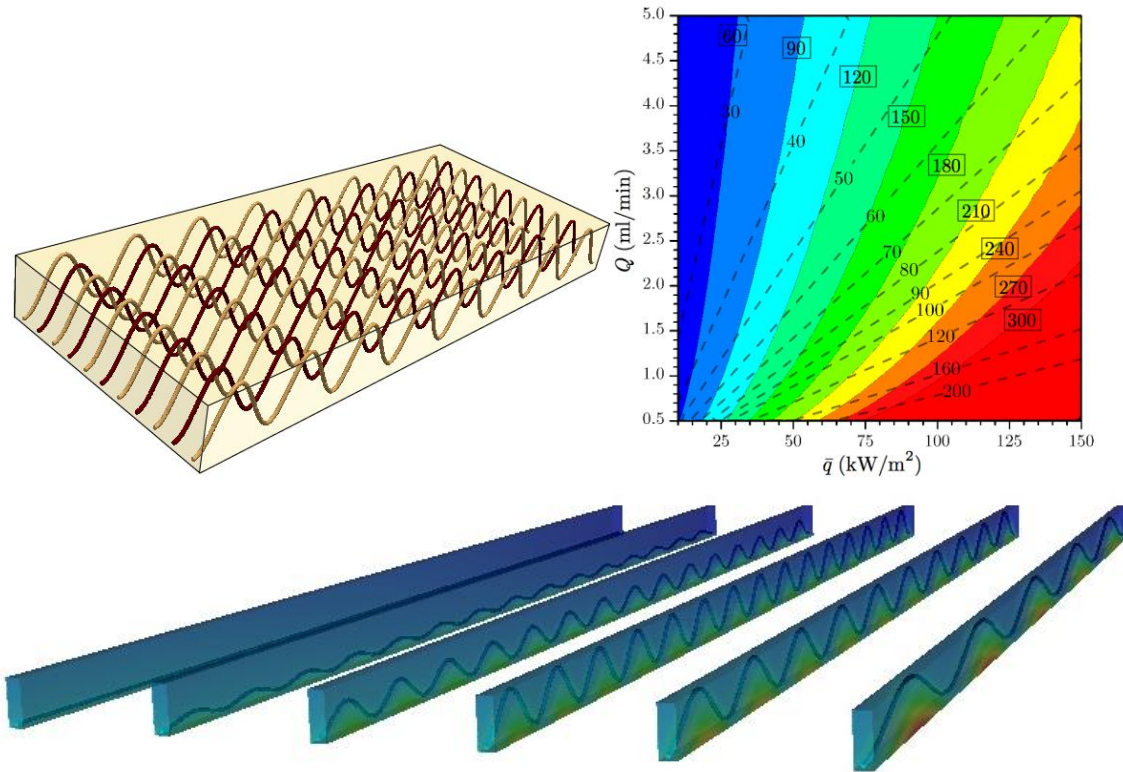
Fig. 1.2.10: Parametric design study of a composite panel with embedded parallel sinusoidal microchannels (top left fig.). The heat flux $\bar{q}$ is applied along the bottom face. Top right: design chart for a composite panel of length *L*=10cm. *Q* denotes the coolant flow rate (water). The contours (with boxed numbers) correspond to the maximum temperature (in °C) in the panel, the dashed lines to the outlet temperature of the coolant. The lower figure shows the thermal field in a periodic unit cell of the panel for size microchannel configurations. All these IGFEM results were obtained with a single non-conforming structured finite element mesh.

The second computational design method combines the IGFEM solver with a gradient-based optimization scheme and an adjoint sensitivity analysis, taking advantage of the stationary nature of the non-conforming mesh as the shape of the microchannel evolves during the optimization process. As illustrated in the simple examples shown in Fig. 1.2.11, while conventional finite-element-based shape optimization scheme suffers from issues associated with mesh distortion, the IGFEM-based shape optimization scheme alleviates these issues by using a stationary mesh that does not conform to the evolving geometry and thereby provides a more accurate solution. In the illustrative problem shown in Fig. 1.2.5, a circular inclusion (with thermal conductivity κ_1 and distributed heat source Q_1) is embedded in a square domain (with properties κ_2 and Q_2), as shown in Fig. 1.2.11(a), which also presents the boundary conditions. The illustrative design problem

31

aims at optimizing the particle diameter that maximizes the average temperature $\overline{T_b}$ along the bottom edge of the domain. The exact dependence of $\overline{T_b}$ on the inclusion radius R is shown in Fig. (g). Fig. (b) presents the outcome of the IGFEM-based study, with the smaller blue circle indicating the initial guess and the larger red circle the optimum inclusion size. Fig. (c) shows the thermal field corresponding to the optimal solution. The next row of figures (d-f) presents the same shape optimization study conducted with the conventional finite element method, showing substantial mesh distortion inside and outside of the inclusion. A direct comparison of the optimization process for these two approaches is shown in Fig. (h): both methods converge rapidly to the optimum temperature (left axis) and inclusion size (right axis); however, the mesh distortion associated with the conventional FEM approach leads to

Fig. 1.2.11: Illustrative comparative study between IGFEM- (b,c) and conventional FEM-based (d,e,f) shape optimization of a circular inclusion embedded in a square domain (a,g). See adjoining text for comments.

noticeable error in the predicted optimum value of $\overline{T_b}$ (indicated by the dash-dotted horizontal red line).

The method has been applied to the design of microvascular panels, allowing us to extend the results from the aforementioned parametric design study (Najafi *et al.*, 2014). The method is being applied to a wide range of material design problems, including the multiscale microstructural design of heterogeneous materials aimed at achieving a desired homogenized constitutive response.

1.3 INTERFACE DESIGN AND CHARACTERIZATION

RESEARCH TEAM MEMBERS
PIs: Ozden Ochoa, Dimitris Lagoudas
Graduate Student: Hieu Truong

COLLABORATORs:
Dr. Fu-Kuo Chang (Stanford University), Dr. Khalid Lafdi (University of Dayton), Dr. John Whitcomb and Dr. Ibrahim Karaman (Texas A&M University), Dr. GP Tandon (AFRL), Dr. Aaron Forster (NIST), Dr Jerome Tzeng (ARL)

OBJECTIVES:

(i) Create robust PMC-Metal interfaces that will sustain thermo-mechanical loads; Design, fabricate and test laminates with hybrid interfaces incorporating layers of carbon fabric with surface CNT growth
(ii) Integrate models and experiments to assist the design of hybrid interfaces that joins the PMC and metal/SMA layers

TECHNICAL ACCOMPLISHMENTS

1.3.1 Fuzzy interface fabrication and Fracture toughness test at room & elevated temp

Developing interfaces with CNTs grown on carbon fabric (fuzzy fabric denoted as FF) as well as on Ti foil (fuzzy Ti denoted as fTi) is of significant interest as a potential mechanism of joining GCMeC to PMCs. Both the fuzzy fabric and fTi were processed at UDRI (work done by Dr. Khalid Lafdi's group) and shipped to TAMU. Panels were fabricated with i. FF middle layer and ii. fTi middle layer at TAMU using the heated vacuum assisted resin transfer molding process (H-VARTM). The cross-section image of a typical panel with mid-plane Ti foil is depicted in Figure 1.3.1a and the fracture surface and crack path are shown in Figure 1.3.1b-c.

Extensive OM, SEM-EDS imaging indicated that CNTs i. are not firmly attached on the fabric tows, ii. form a "halo" around the fibers-tows, and iii. migrate to resin rich crimp sites.
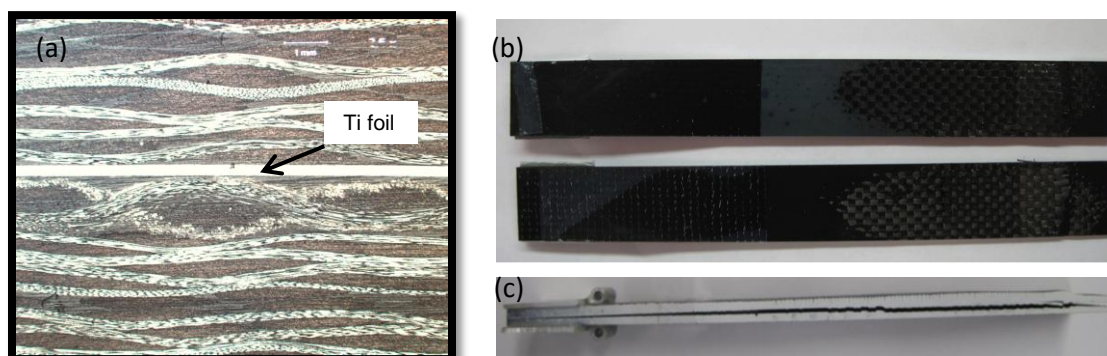
Figure 1.3.1 (a) Cross-section image of FF/Ti panel (b) Fracture Surface of T300_AM_FF/fTi_1 tested at 25 °C (c) Observed crack side of T300_AM_FF/fTi_6 tested at 25 °C

Furthermore, DMA and DSC tests were conducted on a single layer and two-layer fuzzy fabric laminate [T300/Ep862_AM_FF_1L and _2L] to assure that the presence of CNT had not altered the T_g of the resin. DCB tests were performed on specimens obtained from these panels at room temperature (25°C) and at 110°C. After testing, the fracture surface and microstructure of the laminate were evaluated microscopically. Results for T650-8HS/EPON862W showed that the Mode I Fracture Toughness FF/PMC interface increased by 2.5x at room temperature and it was insensitive to changes in temperature (about the same magnitude at 110°C and at RT). Clearly,

the crack propagation was different at high temperature tests where the crack growth path remained in the resin.

Herein, we present the laminate layup and description for the hybrid metal-PMC fracture toughness result in Figure 1.3.2b-c are as follows; FF/Ti: $[0/90]_4$/FF/Ti/FF/$[0/90]_4$ and FF/fTi: $[0/90]_4$/FF/fTi/FF/$[0/90]_4$ where FF: T300 with CNTs; Ti: plain Ti foil and fTi: Ti foil with CNTs. The red symbols identify tests conducted at 110°C and blue symbols are for 25°C data. Similarly, solid symbol refers to fuzzy fabric-fuzzy Ti foil interface (FF/fTi) whereas hollow symbols denote fuzzy fabric-plain Ti foil interface (FF/Ti) at the interface where the crack is located. It is noted that Mode I fracture toughness of FF/fTi laminates are almost twice as high as the FF/Ti samples. Figure 1.3.3a-b shows images of fracture surfaces of a fuzzy Ti DCB specimen, and schematic of crack jumping to weaker interfaces. Fracture of fiber tows is observed and scarp, riverline and cusp features shown in Figure 1.3.3c indicate a mixed mode I and II fracture.
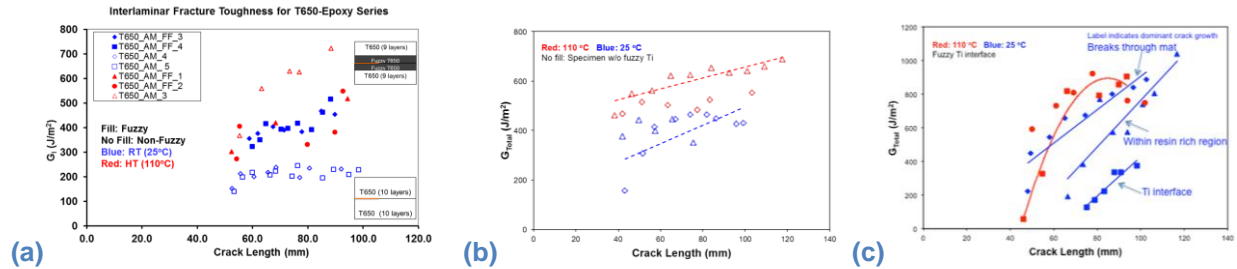
Figure 1.3.2: Mode I fracture toughness for (a) T650-8HS/EPON862 (b) Ti-T300pw/EPON862 of interface with Non-fuzzy Ti (c) Fuzzy Ti.
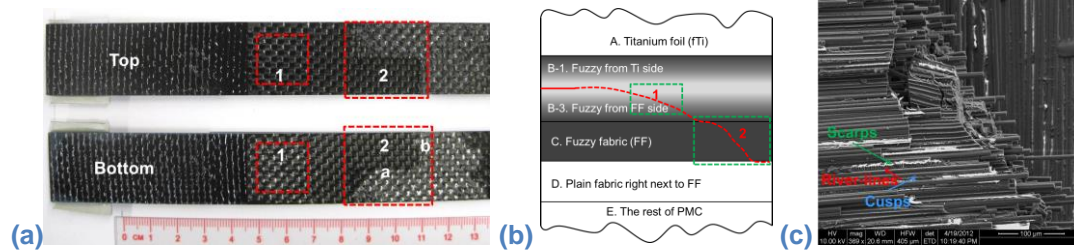
Figure 1.3.3: (a) Fracture surfaces of a fuzzy Ti DCB specimen (b) Schematic of crack jumping interfaces in a fuzzy Ti DCB specimen (c) Fracture of fiber tow at the fuzzy Ti interface.

1.3.2 Finite element models of DCB specimen

DCB specimen modeled in this study has an asymmetric configuration about the crack plane. Schematic of the layup contains PMC and a mid-layer of thin Titanium foil as shown in Figure 1.3.4a. The crack is located at the Ti-PMC bi-material interface. It is assumed that the crack stays on the same interface, i.e. between the Ti and PMC, as it advances. Given the geometry and layup, although the specimen is symmetric about the Ti foil, it is asymmetric about the crack. These models simulate the DCB experiments done on Ti-T300pw/EPON862 series for the case of non-fuzzy Ti foil. It should be noted that although there is no CNTs pre-grown on Ti surface, presence of CNTs at the interface in the real experiment still exists as CNTs come from the two fuzzy fabric layers adjacent to Ti foil. However, the models presented here do not take into account CNTs presence. Properties of the plain weave T300/EPON862 composite used in the DCB models are homogenized using Whitcomb's in-house FE code for textile composites, assuming an overall fiber volume fraction V_f is 57.15% and fiber volume fraction in a tow V_f is 81%. These homogenized properties are summarized in Table 1.3.1. Titanium foil used in this study is a Grade 2, annealed Ti with properties as follows: E = 102 GPa, G = 41.67 GPa, v = 0.34.

34

Table 1.3.1: Plain Weave T300/EPON 862

E_1(GPa)	E_2(GPa)	E_3(GPa)	v_{12}	v_{23}	v_{13}	G_{12}(GPa)	G_{23}(GPa)	G_{13}(GPa)
56.750	56.750	7.776	0.069	0.413	0.413	2.539	2.092	2.092

1.3.2.1 DCB models of crack propagation at Ti-PMC interface

2-D FE models of DCB specimen assuming plane strain is carried out. Quadratic traction criterion was used for damage initiation. BK law was used for mixed mode behavior of damage evolution with an exponent of 2.284 and mode I critical energy release rate G_{Ic}=150 J/m^2 (obtained from experiment). It is assumed that critical mode I, II, III strain energy release rates of this Ti-PMC interface have the same value, that is $G_{IC} = G_{IIC} = G_{IIIC}$. CPE4I elements were used. The mesh contains 150x1 for Ti foil and 150x8 elements for each PMC arm). Displacement was applied to the top arm while bottom armed is fixed. Maximum applied displacement is 25 mm. At first, the model was done for fully elastic Ti foil, using surface-based cohesive behaviors for both top and bottom Ti-PMC interfaces. The crack propagates along the bottom Ti-PMC interface. Cohesive zone parameters were obtained from literature and summarized in Table 1.3.2. The load-displacement results from this model is compared to experiment and shown on Figure 1.3.5a. The model was then run for the case where Ti foil has isotropic plastic hardening behavior, using built-in elasto-plastic material model in ABAQUS. Yield stress of Titanium is 268.1 MPa. Besides surface-based cohesive behaviors, virtual crack closure technique (VCCT) is also considered to model the Ti-PMC interface. Various interfacial behaviors were used, cases are as follows: (i) Both top and bottom Ti-PMC interfaces were modeled with surface-based cohesive zone, (ii) Top Ti-PMC was assumed perfect and modeled with tie constraint while bottom interface was modelled cohesive, (iii) Top Ti-PMC interface was modeled cohesive and bottom was modeled with VCCT, and (iv) Top interface was modeled as perfect interface and bottom was modeled with VCCT. Figure 1.3.5b shows load-displacement results from these models. Combinations of cohesive Ti-PMC interfaces and isotropic hardening behavior of Ti show higher energy dissipation as the crack first progresses from the initial crack. However, these models still do not capture closely the behavior observed in the experiment. It is suggested that the presence of CNTs and CNTs bridging as well as energy dissipation through damage of the PMC be considered.
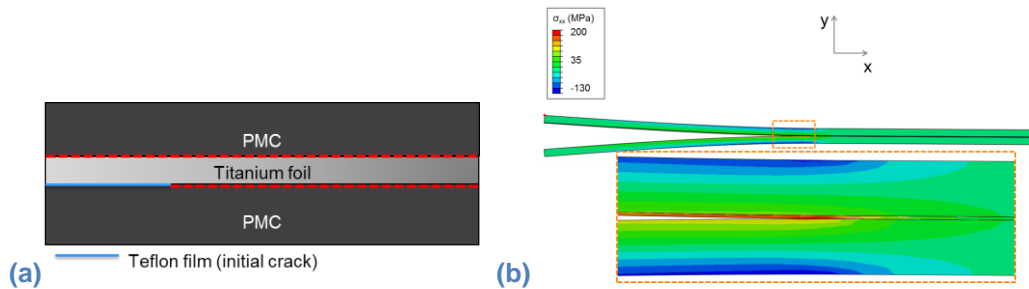
Figure 1.3.4: (a) Schematic of DCB finite element model (b) Sigma xx contours on DCB specimen.

Table 1.3.2: TiO₂/EPON 862 interface cohesive properties

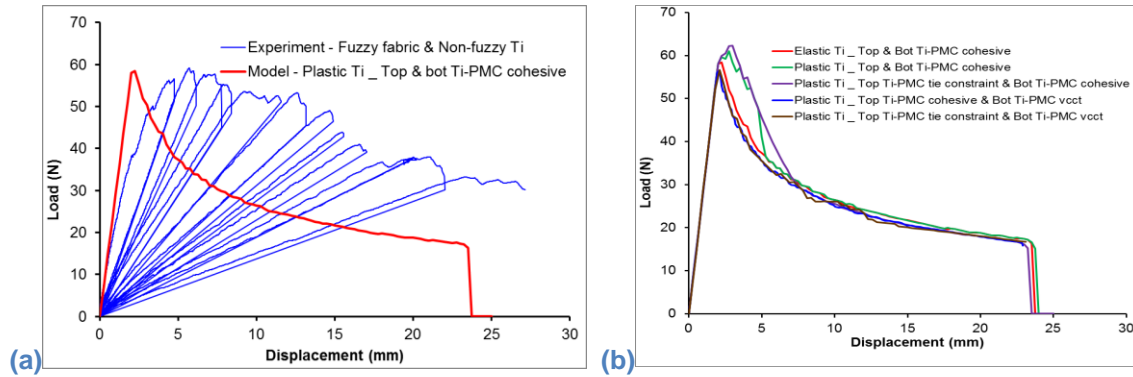| K_{nn} (GPa)	K_{ss} (GPa)	K_{tt} (GPa)	t_n (MPa)	t_s (MPa)	t_t (MPa)
3.438 x 10^6	1.021 x 10^6	1.021 x 10^6	23.8	18.6	18.6

Figure 1.3.5: (a) DCB load-displacement results from experiment and FE model (b) Comparisons of DCB finite element models of various interfacial behaviors and elastic/plastic behavior of Ti.

1.3.2.2 Analytical and FE models of asymmetric double cantilever beam (A-DCB) – strain energy release rate calculations of the Ti-PMC interface
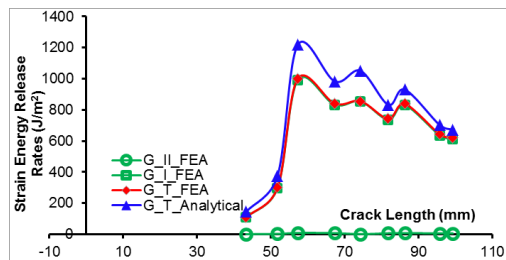

Figure 1.3.6 Comparison between analytical solution and FEA results

Due to the asymmetry about the crack plane, it is important to account for mode-mixity at the interface. Analytical and finite element models are carried out for the ADCB. Experimental values of crack length and the corresponding opening displacement are used as input for the models. The VCCT is utilized in the finite element model to compute different modes of strain energy release rate and the degree of mode-mixity. FE models are carried out using Whitcomb's in-house FE code. The results from analytical and FE models are summarized in Figure 1.3.4. The total strain energy release rate calculated from FEM is within 90% of the values obtained from analytical solution. Furthermore, FEA results suggest a low mode-mixity or G_{II}/G_{I} ratio of less than 1%.

1.3.3 Joining and characterization of interface between SMA to high temperature PMC
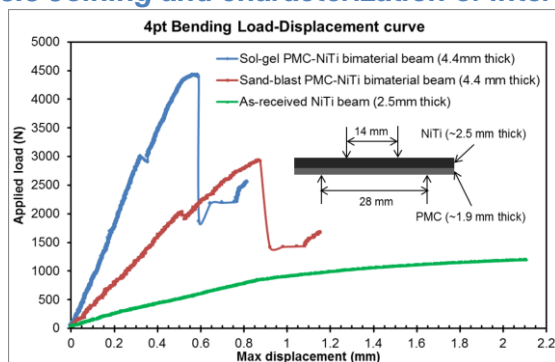
Figure 1.3.7 Load-Displacement data from 4-pt bending test

Four-point bending tests are undertaken with NiTi-T300pw/Matrimid5292 laminates (PMC) with the layup of $[0/90]_{2s}$ as well as monolithic equiatomic NiTi beam. These specimens were created by joining pre-cured PMC to NiTi using Matrimid 5292 as adhesive and curing with a hot-press. Surface treatments include sol-gel and sand-blasting methods. Load-displacement curves together with loading schematic for 4-point bending test are presented in Figure 1.3.7. SEM images of the delaminated sol-gel sample are shown in Figure 1.3.8 and 9. It is clearly observed that the interfacial separation evolves into typical 45° matrix cracks in the composite layers. Residual of PMC with imprints of fiber on delaminated NiTi surface, and fracture of fiber on delaminated PMC surface show evidence of a good interface.
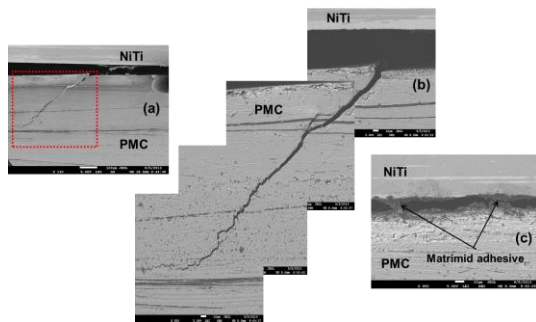
36

Figure 1.3.8: Cross-section view of a NiTi-T300pw/Matrimid5292 bimaterial beam after 4-point bending test.

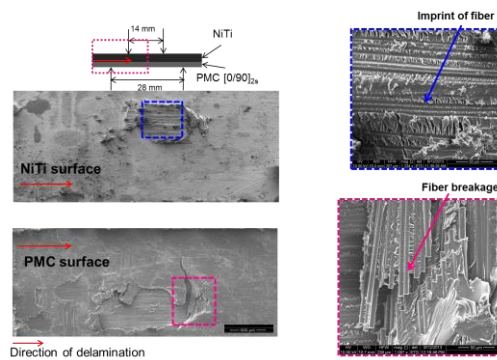**Figure 1.3.9: Delaminated surfaces of a NiTi-T300pw/Matrimid5292 bimaterial beam (NiTi treated with sol-gel method) after 4-point bending test.**

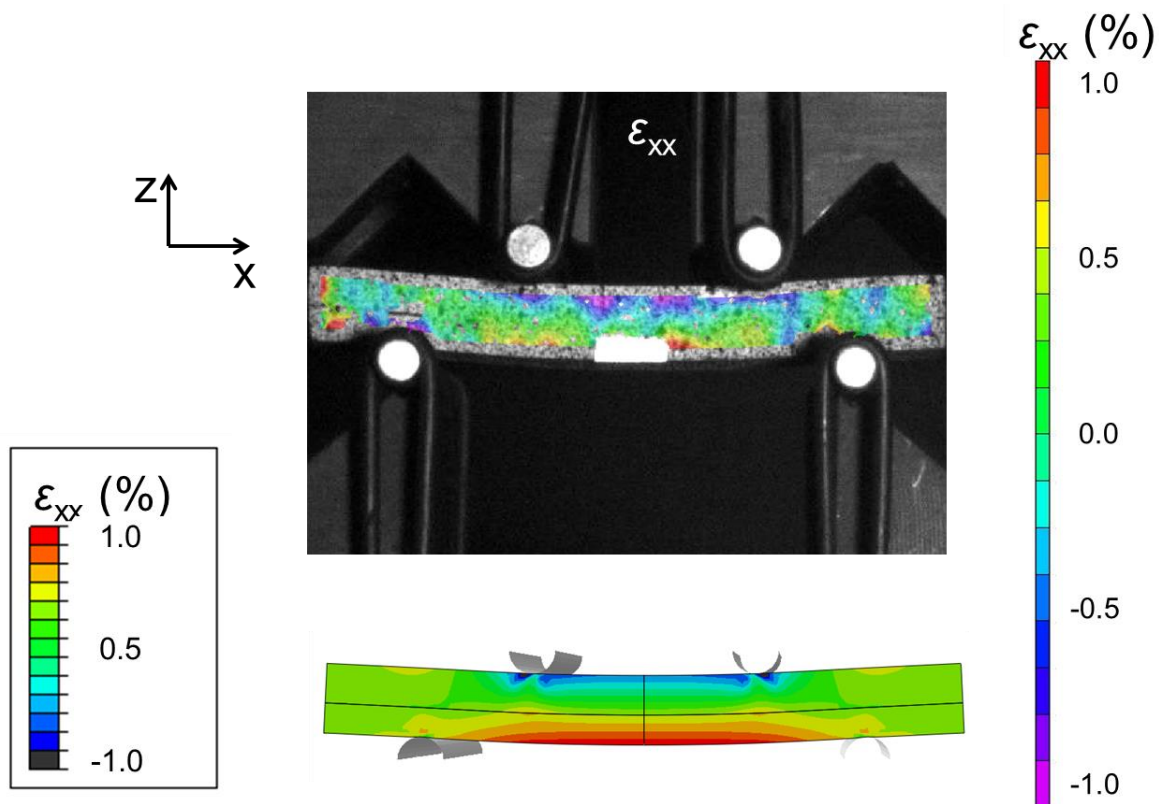### 1.3.4 Nonlinear finite element model of 4-point bending SMA-PMC bimaterial beam

Figure 1.3.10: Strain profile from 4-point bending test with DIC versus strain profile from FE model.

Finite element models of the 4-point bending bimaterial beam (NiTi-T300pw/Matrimid5292) are carried out using ABAQUS. Strain profile obtained from the model is verified with DIC experiment. Due to symmetry, only a quarter of the beam is modeled with symmetry about the x and y planes through the origin, placed at the center of the beam. Properties for T300pw/Matrimid5292 PMC are calculated using Whitcomb's FE code for textile, summarized in Table 1.3.3. Shape memory alloy behavior is captured using a UMAT user subroutine for SMA constitutive model Developed by Lagoudas *et al.* Properties of equiatomic NiTi used in this model are shown in Table 1.3.4.
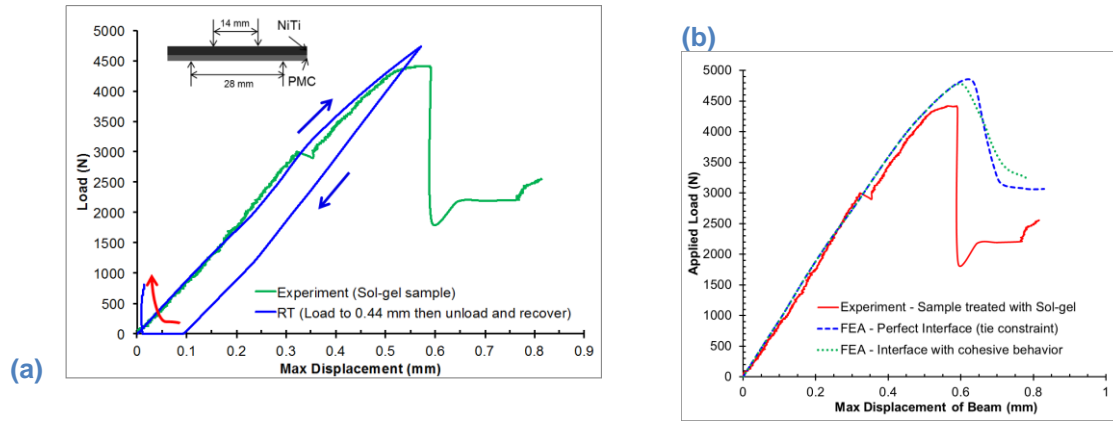
Figure 1.3.11: (a) SMA UMAT only loaded to 0.44mm, unloaded and then recovered by heating to temperature above A_f (b) 2 UMATs loaded to 0.56 mm.

Table 1.3.3: Thermal-Mechanical and damage initiation properties of PMC

$E_{11} = E_{22}$ (GPa)	56.5
E_{33} (GPa)	10.6
G_{12} (GPa)	4.13
$G_{23} = G_{13}$ (GPa)	3.13
v_{12}	0.148
$v_{23} = v_{13}$	0.392
$\alpha_{11} = \alpha_{22}$ (1/$^{\circ}$C)	2.17×10^{-5}
α_{33} (1/$^{\circ}$C)	-3.62×10^{-7}
$\sigma_{L,t} = \sigma_{T,t}$ (MPa)	610
$\sigma_{L,c} = \sigma_{T,c}$ (MPa)	420
τ_{LT} (MPa)	106

Table 1.3.4: Thermal-Mechanical properties of equiatomic NiTi

E^T (GPa)	24.50
E^D (GPa)	56.31
M_s ($^{\circ}$C)	23.06
M_f ($^{\circ}$C)	-31.50
A_s ($^{\circ}$C)	78.94
A_f ($^{\circ}$K)	108.14
$v_A = v_M$	0.33
$C_A = C_M$ (MPa/$^{\circ}$C)	11.41
α_M (1/$^{\circ}$C)	32×10^{-6}
α_A (1/$^{\circ}$C)	21×10^{-6}

38

Figure 1.3.11a shows schematic of the model and comparison of FE model with experimental data for a specimen with NiTi treated with sol-gel. In the model, displacement is applied on top the bimaterial beam, unloaded by releasing the applied displacement, and heated to temperature above Austenitic finished temperature of NiTi to recover the shape. The NiTi-PMC interface is assumed perfect using tie constraint. Nonlinearity in the FE model is then considered to include damage behavior of PMC. Figure 1.3.11b shows load-displacement predictions from a model with perfect interface assumption and cohesive interface. The models capture the large drop in load as observed in the experiment, however, still cannot capture the first small drop at about 3000N.

Interfacial stresses through thickness at the center of the beam for perfect interface and cohesive interface are shown in Figure 1.3.12. These values are obtained at the time step where the specimen is subjected to maximum load, i.e. before the large load drop.
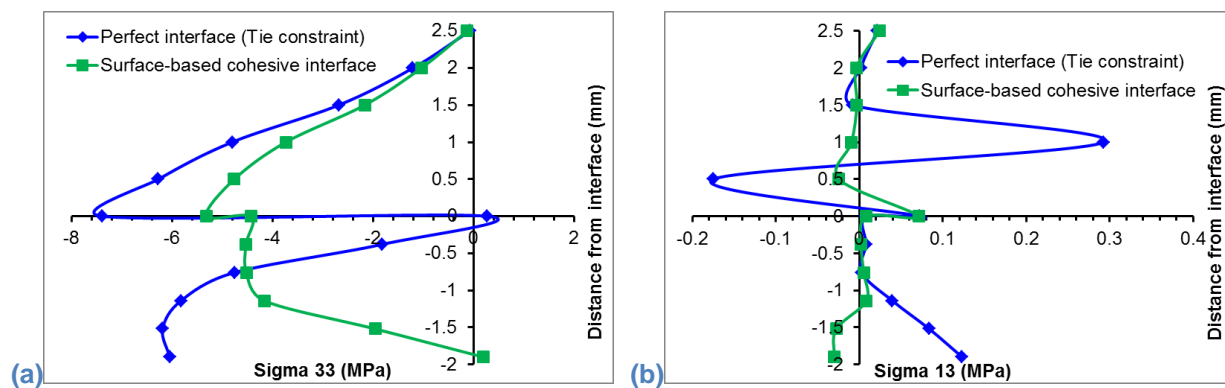
Figure 2.3.12: (a) Sigma 33 (b) Sigma 13.

Studies done in *1.3.3* and *1.3.4* provide insights on effects of different surface treatment techniques on quality of hybrid interfaces. The 4-pt bending test results of the bimaterial beams created using different surface treatments imply that the stronger the interface, the more load is transfer through that interface and the higher load the hybrid system can sustain. To further understand the observed behaviors from experiment, finite element models were performed. It is very important to consider nonlinear behaviors of both the SMA and PMC, and not just simply assume linear elastic behaviors. It is also important that cohesive zone was introduced to model the interface and to capture the flexure response when delamination occurs. If calibrated correctly, these models can be used to predict behaviors of similar hybrid systems and to predict responses when the hybrid system is subjected to different loading conditions.

Investigations will be carried out at elevated temperatures to study performance of this high temperature-hybrid interface in comparison with behaviors observed at room temperature.

1.3.5 Integration of piezoelectric sensors to interface between SMA to HT PMC

Piezoelectric sensors fabricated at Stanford University were integrated at the NiTi-PMC and PMC-PMC interfaces. PMC used here is also pre-cured T300pw/Matrimid5292. Matrimid 5292 is used as adhesive and the specimens were cured with a hot press. Preliminary results of the four-point bending tests at room temperature for samples with and without sensors suggest that the presence of a thin sensors layer does not significantly alter the mechanical behaviors of the hybrid composite beams in terms of effective stiffness of the beams and maximum load they can sustain. In addition, adding a thin sensor layer increases the flexibility of the hybrid system because samples with sensors deflect approximately 3.5 times more than those without sensors

39

before final failure occurs. Figure 1.3.13 shows sensor series on top of PMC prior to joining, delaminated surfaces after 4-point bending test and experimental load-displacement results.

An on-site lab visit/internal MURI collaboration took place in the Spring 2014 semester. PhD student Hieu Truong spent one week working with PhD student Yu-Hung Li at Dr Fu-Kuo Chang's laboratory, Stanford University. During this time, samples where piezoelectric sensors were sandwiched between two aluminum plates, and between two cured-neat Matrimid plates were fabricated. Matrimid 5292 was used as adhesive; and curing was done using a hot press. Measurements of the sensors' impedance were done before and after sample fabrication to ensure functionality of the sensors after being embedded between two plates and cured. Sensors in samples with Al plates did not give signals after being embedded due to electrical shortage when the sensors wires in contact with metal surfaces, while the sensors embedded between two insulating Matrimid plates still function after the curing cycle. Samples where sensors embedded between Matrimid plates were undergone 4-point bending tests at room temperature. Signals from the sensors were measured at different load applied until the specimens fail. Since the sensors were placed at the midplane, and only one sensor was presented in each 4-point bending specimen, located at the center of each specimen, zero stress was experienced at the location of the sensor. As a result, no change in signals was observed for different load applied. The sensors embedded between 2 Matrimid plates, however, could detect change in temperature. At zero applied load, signals was measured at 25°C and 90°C. The impedance peak in signals measured at 90°C shift to a lower frequency compared to that of the signals measured at 25°C. This suggests that the sensors could be used to detect temperature change when placed anywhere in the specimens, and should be placed off-neutral plane in order to detect displacement/deformation in bending.

Finite element analyses were carried out to study impedance response of piezoelectric sensor in the free and clamped configurations. Commercial APC-850 circular sensor of 3.175 mm diameter and 254 µm thickness was studied. Poling direction is through the thickness of the sensor. Direct steady-state dynamics analyses were carried out where zero potential was applied on one face of the sensor as the ground electrode and harmonic potential signal of magnitude 50mV was applied on the other side. Complex charges output from the model was used to the

frequency response of the sensor's impedance Z using the formula $\widehat{Z} = \dfrac{\widehat{V}}{j\omega\widehat{Q}}$, where V is the applied Voltage, Q is the complex charge output, and ω is the frequency at which the voltage was applied and charge calculated.

The impedance peaks obtained from the analyses occurred at the frequencies that agree with experimental observations. There are frequency shifts in the impedance peaks from the free to the clamped sensor as shown in Figure 1.3.13 (g). Electrical resonances are unique properties of piezoelectric materials. Upon any changes in the loads or boundary conditions of the sensor, impedance peaks shift to different frequencies. This behavior will be used to study how the applied thermal-mechanical load and how damage on the host structures affect the impedance response of piezoelectric sensor using FE analyses.

1.3.6 Molecular scale simulations

Hybrid interface behaviors are complex. Interfacial phenomena often occur at the atomistic and molecular scales that cannot yet be quantified experimentally. Thus, Molecular Dynamics (MD) simulation is used to facilitate understanding of fundamental physical and chemical phenomena at the interface between a crystalline metallic structure and a cross-linked amorphous polymeric structure. In this work, MD simulation is performed to obtain work of adhesion and traction-separation curve between cross-linked Epoxy or Matrimid and NiTi or Ti. The traction-separation behavior obtained from MD simulation will be used to calibrate cohesive zone parameters for FE

models at the continuum scale. Effects of temperature and silane coupling agents presence at the interface and any chemical reaction if occurs during processing steps can also be investigated by MD models. Furthermore, MD simulations can give more insight into the effect of oxide layer on metal side prior to and after joining to polymer. MD simulations can be performed in parallel with experiments to assist with processing methods in creating the interface. So far, MD models have been carried out to simulate interaction between TiO_2 and epoxy (section 1.3.6.1) as well as cross-linking reactions in Matrimid 5292 (section 1.3.6.2).
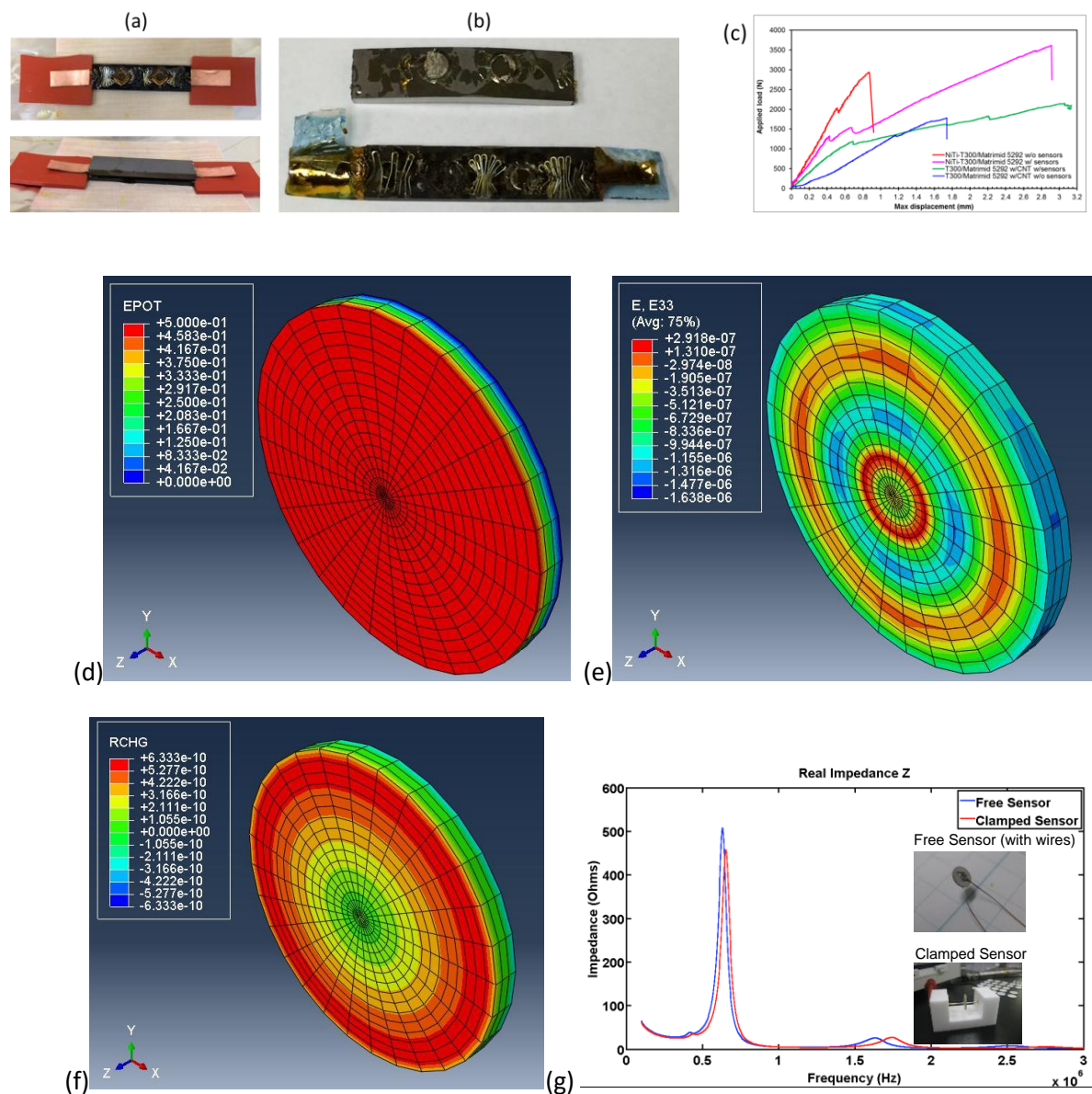
Figure 1.3.13: (a) Fabrication – Integration of sensors at the interface (b) Delaminated surface after 4-point bending test (c) Load-displacement results for 4-point bending tests (d) Applied potential in FE analysis of PZT sensor (e) Calculated strain field in the poling direction of PZT sensor (f) Real values of charges calculated from FE analysis (g) Real Impedance response of a free and clamped PZT sensor.

41

1.3.6.1 Interaction of TiO$_2$ and EPON862/W at the molecular scale
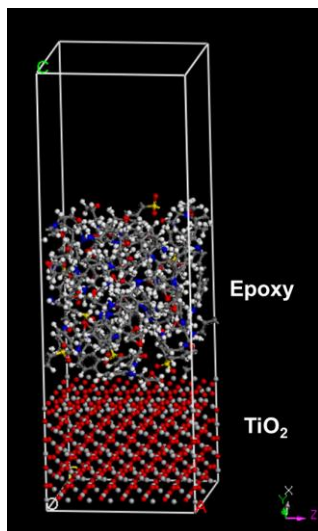
Figure 1.3.14 Molecular scaled TiO2 – Epoxy interface

Molecular dynamics simulation was done with TiO$_2$ and epoxy to obtain the work of adhesion value for this interface. More analyses will be performed to obtain traction-separation curve that will be used to calibrate cohesive zone parameters for DCB finite element models of Ti/Epoxy-matrix-PMC interface described in section 1.3.2.1. Rutile TiO$_2$ structure is used in this study. Because the (1 1 0) plane of rutile TiO$_2$ is the most active, the TiO$_2$ surface was constructed by cleaving the (1 1 0) plane and creating a supercell. EPON862/W monomers were packed into a confined layer. The epoxy-TiO$_2$ interface system has periodicity in the x and z directions. A vacuum slab is added on top of epoxy to eliminate periodicity in the y direction as shown in Figure 1.3.14. COMPASS forcefield and NVT ensemble were used for MD analyses in this study. Work of adhesion value obtained from this MD model is 1.15 J/m^2, which is consistent with values reported in literature.

1.3.6.2 Cross-linking simulation of Matrimid 5292 at molecular scale

Cross-linking simulation of Matrimid 5292 was carried out. This is done as the first step to understand behavior of Matrimid. Chemical structures of Matrimid 5292 part A and B are shown in Figures 1.3.15 and 1.3.16a-b. In the experiment, the ratio between part A and B is 100 to 113 part-by-weight, that yields molar ratio of A:B equals to 1:1. 20 molecules of Matrimid 5292A and 20 molecules of Matrimid 5292B were packed in a confined layer with periodic boundary. Dimensions of the simulated cell are 26.21 x 26.21 x 25.48 Å^3 with a density of 1.23 g/cm^3. COMPASS forcefield and NVT, NPT ensembles were used to simulate the cross-linking reactions of these molecules. At the end of the simulation, there are 34 cross-links formed, which yields an 85% cross-linked structure, shown in Figure 1.3.16c-d. Mechanical properties will be calculated and compared with experimental values reported for neat Matrimid 5292. This cross-linking model will be done for the case where the polymer molecules are packed in a cell on top of a crystalline metallic structure (TiO$_2$, Ti or NiTi) to determine if presence of this metal layer affects cross-linking behavior of the thermoset polymer. In addition, effect of Silane coupling agents, which are presented at the interface on degree of Matrimid cross-linking will be studied.

Results from models described in 1.3.6.1 and 1.3.6.2 provide preliminary understanding for behaviors at the molecular scale for the hybrid interfaces. Models will be carried out to study interactions of cross-linked Matrimid 5292 with metallic structure (TiO$_2$, Ti or NiTi) with and without presence of silanes at the interface. These models will be used to calibrate parameters for continuum scale models using finite element method.
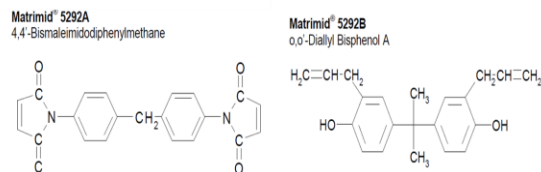

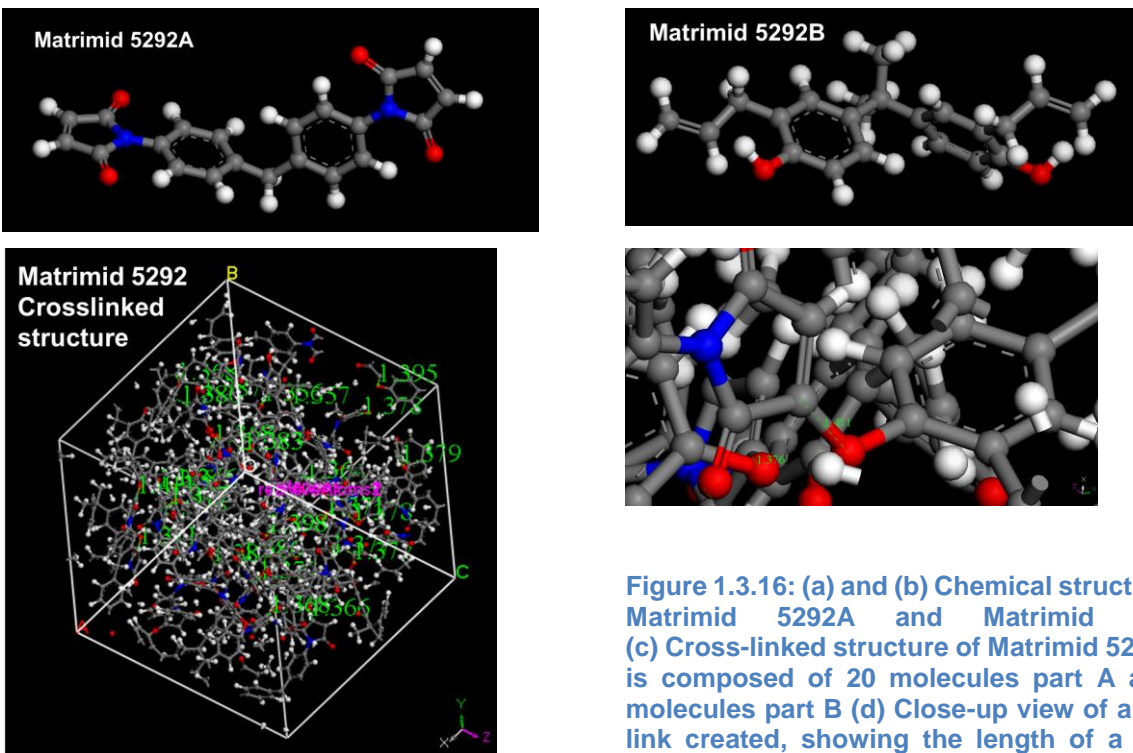**Figure 1.3.15: Chemical composition of Matrimid 5292 part A and part B.**

Figure 1.3.16: (a) and (b) Chemical structures of Matrimid 5292A and Matrimid 5292B. (c) Cross-linked structure of Matrimid 5292 that is composed of 20 molecules part A and 20 molecules part B (d) Close-up view of a cross-link created, showing the length of a newly-formed C-O bond.

1.3.7 External collaborations

Dr GP Tandon (AFRL) fabricated the composite laminates with Matrimid 5292 matrix and plain weave T300 carbon fabric reinforcement. These laminates were used to obtain tensile and flexure responses at room (25°C) and elevated (160°C) as well as used to create the SMA-NiTi bimaterial beams described in sections *1.3.3* and *1.3.5*. Dr Aaron Forster (NIST) helped obtain AFM images at the PMC-SMA interface of a bimaterial beam sample fabricated as described in section *1.3.3*. Figure 1.3.17 shows images of this interface obtained using tapping and peak force AFM modes. This effort, however, is not very successful due to the quality of polished surface as well as the different natures of shape memory alloy and polymer matrix composite.
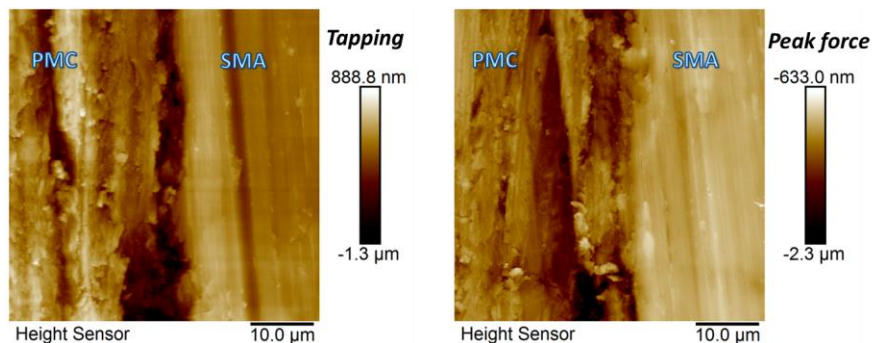
Figure 1.3.17: AFM images at the PMC-SMA interface

43

Dr Jerome Tzeng (ARL) helped obtain SEM images of the SMA-PMC interface as well as laser microscopic images on SMA surface and its 3D tomography as shown in Figure 1.3.18.

(a)   (b)
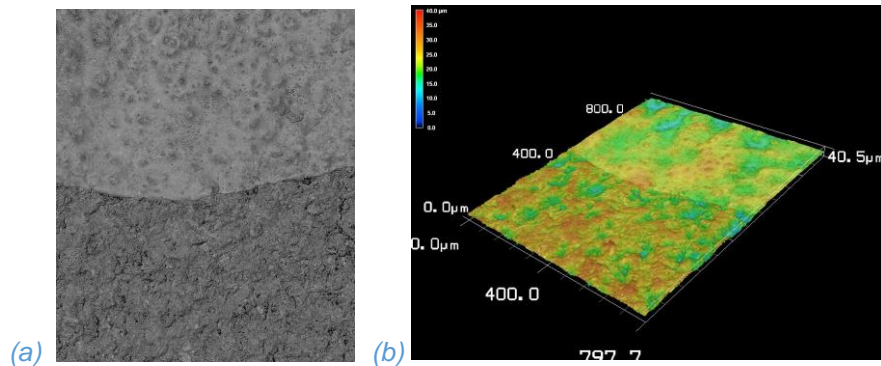
Figure 1.3.18: (a) Laser microscope image on metal surface (b) 3D tomography image of metal surface

1.3.8 Other accomplishments

1.3.8.1 Collaboration with TU Delft – The Netherlands

Research resulted from this MURI-funded project has enabled collaboration with Delft University of Technology (TU Delft), and a NASA Space Technology Research Fellowship (NSTRF) awarded to PhD student Hieu Truong to perform research needed to complete her dissertation. In the Fall 2014, Hieu Truong is doing research at the Structural Integrity & Composites laboratory at TU Delft, fabricating high temperature hybrid composite panels composed of Matrimid 5292 matrix, T300 plain weave carbon fabric and Ti/NiTi foil. In each of these panels, one single layer of metallic foil (either Ti or NiTi) will be sandwiched between eight layers of carbon fabric on the top, and eight layers of carbon fabric on the bottom. Double cantilever beam (DCB) specimens will be prepared from these panels, and mode I fracture toughness of the hybrid metal-PMC interface will be investigated via DCB tests at room and elevated temperatures with in-situ monitoring using fiber optics, DIC and acoustic emission techniques. Effects of different surface treatment techniques will be studied, and extensive investigation with microscopic imaging will be carried out on treated metal foil surfaces as well as fracture surfaces. Fiber metal laminates with alternating layers of metal foils and carbon fabric will also be fabricated for investigation of tensile and flexure response as well as fatigue behavior at room and elevated temperatures.

Current outcomes

Axial strain profiles along the DCB beam's length are obtained from FEA results at the top and bottom surfaces at different time steps during crack propagation as shown in Figure 1.3.19 (a) and (b). These strain predictions have been validated by comparing with strain data obtained from the experiment using fiber optics to perform the measurement. It is observed that the compression strain increases linearly from the delaminated end of the beam to the vicinity of the crack tip, then immediately jumps to a maximum value and exponentially decays to zero strain. This behavior repeats as the crack propagates to the end of the specimen and the maximum compressive strain near the crack tip location remains almost a constant value. Experimental observations reveal similar behavior as predicted from the FE model. However, fiber optic measurements can also capture the crack arresting behavior at the interface. Critical measured strain values are similar to FE predictions when the crack propagates. In the experiment, after the crack propagates for about 2-5 mm, the crack tip arrests at the new location for several seconds. Right after the crack jumps, the measured strain values reset back about 500 microstrains and gradually increases as the applied displacement increases until the critical strain value at the crack tip. The crack then propagates to the next location and the described behaviors repeat till the end of the specimen. This behavior, however, was not captured in the FE analysis.

44

Example of two adjacent crack tip locations is shown in Figure 1.3.19(d). The trend in strain increasing, resetting and re-increasing is illustrated by the black arrows on Figure 1.3.19(d).
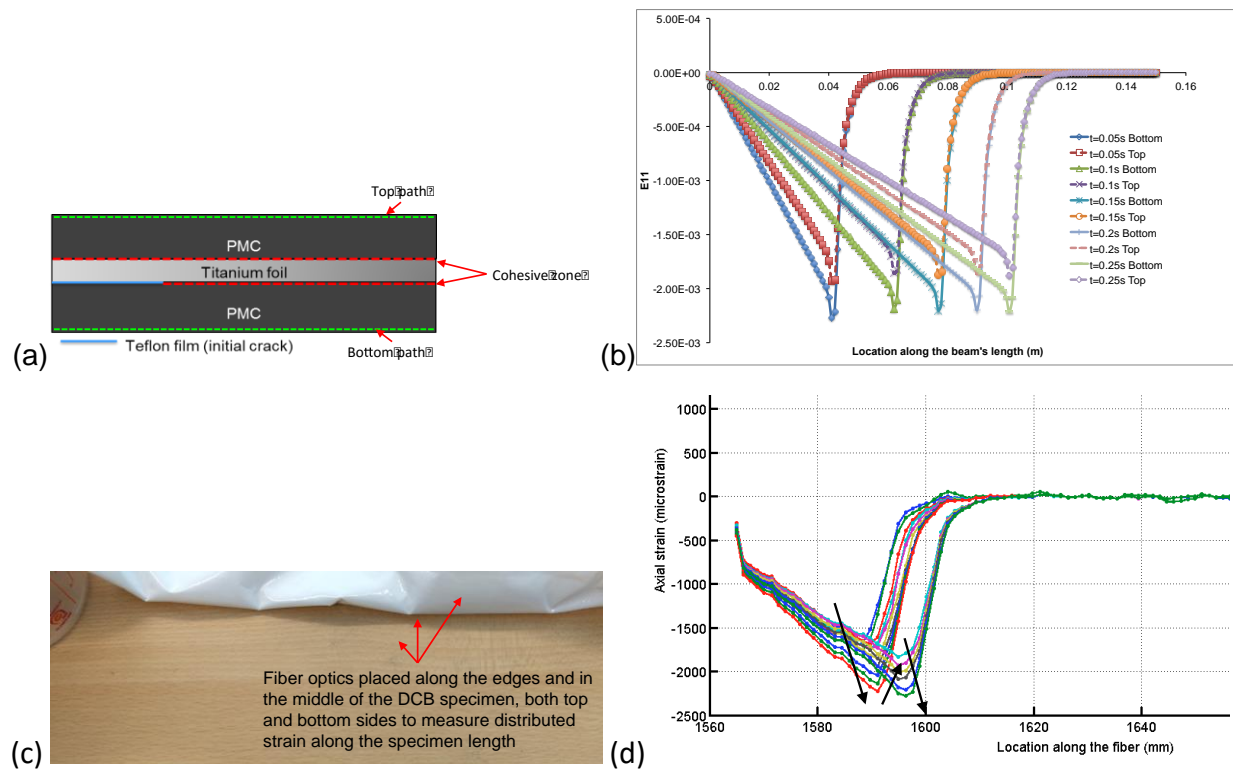

Figure 1.3.19: (a) Schematic of DCB model and where axial strain is obtained (b) Axial strain profiles along the length of the beam from FE model and (c) DCB specimen with fiber optic bonded for strain measurement (d) Axial strain profiles along the length of the beam from experiment with fiber optics

1.3.8.2 NASA NSTRF Fellowship and collaboration with NASA researchers at Langley Research Center

The NSTRF fellowship was granted for Hieu Truong's proposal titled "Creating and Understanding Hybrid Interfaces of Multifunctional Composite Laminates for Extreme Environments." The objectives of the proposed research are to (a) create and investigate hybrid interfaces between metal and shape memory alloy and polymer matrix composite for use in high temperature environment, and (b) develop computational models to provide more perspectives toward the understanding of hybrid interfaces and their thermo-mechanical performance and assist the design of these interfaces. To fulfill objective (a), continuation of experimental work from this MURI project as well as work done at TU Delft will be performed, where a new surface treatment technique for metal foils, i.e. laser ablation, will be introduced and compared with traditional treatments for the new Matrimid-matrix PMC and metal interface. Hybrid interface between high temperature polymer matrix (e.g. polyimides) composites and high temperature shape memory alloy (e.g. NiTiHf and NiTiZr) will also be created and investigated. This experimental effort will be done in collaboration with Dr. John Connel's group at NASA Langley Research Center and Dr. Ronald Noebe's group at NASA Glenn Research Center. Computational effort to fulfill objective (b) includes molecular dynamics modeling as well as finite element modeling.

Current outcomes

Laser ablation treatment on 127µm thick Ti and NiTi foils with depth of ablation less than 5µm was performed in collaboration with scientists at NASA Langley Research Center. It is observed that intense ablation causes minimal damage on the metal foils' surfaces. In addition, micro-roughness is created on the metallic surface in a regular pattern, which will yield uniform interfacial properties when the metal substrate is bonded to polymeric composite structures.
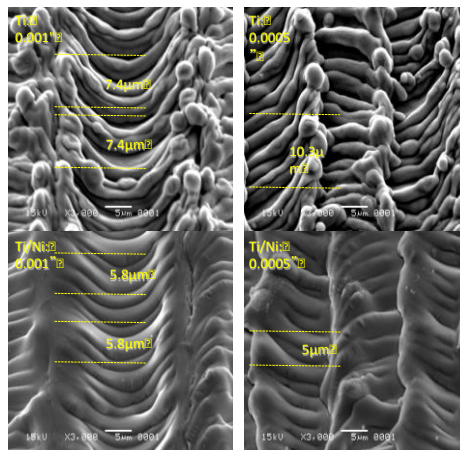

Figure 1.3.20. Laser-ablated Ti and NiTi foils' surface

1.4 CHARACTERIZATION OF IMPACT AND DYNAMIC RESPONSE OF MAX PHASE MATERIALS

RESEARCH TEAM MEMBERS

PI: Dr. Nakhiah Goulbourne, University of Michigan, Ann Arbor
Graduate Students: Riddhiman Bhattacharya

COLLABORATORs:

Dr. Miladin Radovic, Texas A&M University

OBJECTIVES:

Experimental characterization of high strain-rate response of Kinking Non-Linear Elastic (KNE) solids (Ti_2AlC and Ti_3SiC_2) and MAX phase based composites using Split Hopkinson Pressure Bar technique coupled with high speed imaging and microscopy; Identifying dominant deformation and damage propagation mechanisms as a function of material composition, grain size, and strain rate; Characterizing effect of thermal quench and rapid temperature gradients on dynamic deformation mechanisms; Developing a nanoscale continuum model for kink band kinematics in nano-layered solids.

TECHNICAL ACCOMPLISHMENTS

46

1.4.1 High strain-rate response of MAX Phases

In the first two years, first experiments on high strain rate response of MAX phases were performed along with development of an in-situ SHM experimental set-up for layered structural materials, and a fractional calculus based phenomenological model to capture temperature dependent hysteresis in MAX Phases. In the subsequent years, a refined experimental protocol for high strain rate testing of Ti_2AlC using Split Hopkinson Pressure Bar (SHPB) technique was established and characterized over a wide range of strain rates. The high strain-rate experiments were coupled with in-situ high speed imaging and Digital Image Correlation (DIC) to facilitate full field characterization of the strains. The in-situ imaging also facilitated us to a) delineate real strains in the material, and b) identify crack formation zones and paths in the sample.
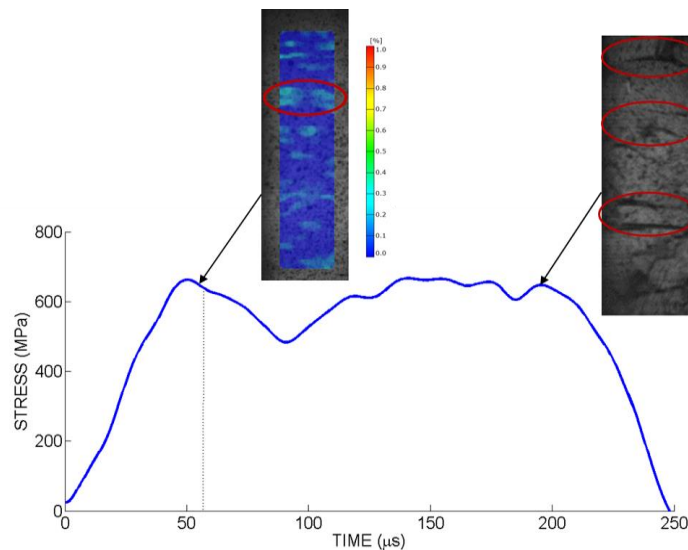
Figure 1.4.1: Stress versus time response of Ti_3SiC_2 at ~2500 s^{-1} with a) DIC strain field showing heterogeneous field and potential crack formation zone, and b) in-situ image from high speed camera showing cracks parallel to the loading axis

This characterization and analysis method was extended to Ti_3SiC_2 which revealed that a) Ti_3SiC_2 is damage tolerant under strain rates of ~2500 s^{-1} unlike conventional ceramics (Fig.1.4.1), b) Ti_3SiC_2 has lower strain to failure and higher maximum stresses as compared to Ti_2AlC, and c) mesoscopic mechanisms lead to a heterogeneous strain field evolution under static and dynamic loading conditions. Figure 1.4.1 shows a typical stress versus time response at 2500 s^{-1}, which indicates a yielding type behavior. There are three distinct regimes, an initially linear loading regime followed by a peak in the stress and a subsequent large softening regime that occurs before hardening and ultimate failure. The dotted vertical line on the plot indicates the point when cracking was first observed. It must be noted that the strain softening regime after attainment of the peak stress and before observation of macroscopic cracks is attributed to microcracking and delaminations at the microstructural scales (well below 0.1 mm). At relatively low (SEM) magnification levels, a lamellar structure with voids and cavity formations is observed along with the co-existence of smooth cleavage planes. At much higher magnifications, the lamellar regions reveal kink banding of the nano-layers within a grain, interlayer delamination and sliding, intergranular delaminations, translayer and transgranular cracking, grain cleavage and grain pullouts. Among these, kink bands, interlayer delamination, and void formation are the most extensive and unique features believed to be responsible for the observed pseudoductility and damage mitigation in MAX phase materials. Due to extensive formation of kink bands, the

47

fractured surface appears to have a more refined appearance compared to the intact microstructure. From the DIC strain field image, the location and orientation of macrosocopic cracks can be inferred as highlighted by the red circle in Fig 1.4.1. The localization of higher strain in the region is indicative of potential crack formation.

To establish a more direct connection between microstructure and macroscopic behavior, we performed micro CT scanning on as received MAX phase samples from TAMU. Fig 1.4.2 (a) shows the dynamic stress versus strain response of Ti_2AlC at 2600-4700 s^{-1}. Note that samples from the same batch do not conform to a strict dependence on strain-rate. We hypothesize that some amount of scatter in the peak stress values may be due to pre-existing micro-flaw concentrations that vary from sample to sample. The as-processed Ti_3SiC_2 samples were characterized using micro CT scanning. Subsequent image processing and density calculations were made using Avizio™ 3D rendering software to measure sample flaw concentration and spatial distribution.
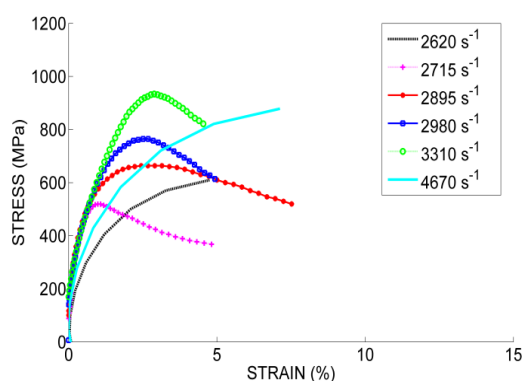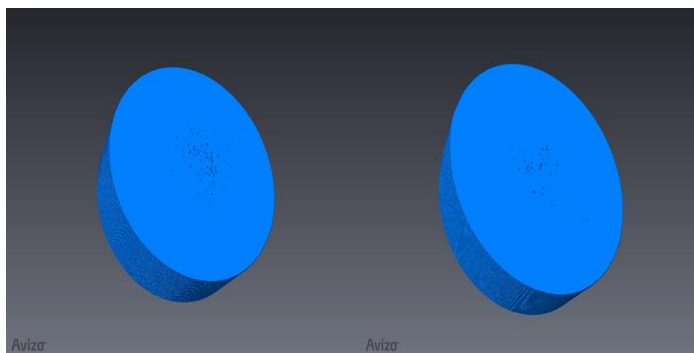
(a)   (b)

Figure 1.4.2: (a) Stress versus strain response of Ti_2AlC in the regime 2600-4700 s^{-1}, and (b) 3D rendering of CT scan of Ti_3SiC_2 samples with slightly different flaw concentrations. The distribution of flaws on the surface is indicated by the presence of black dots.

The results obtained from SHPB testing of Ti_3SiC_2 samples that were analyzed using CT scan, are summarized in Tables 1.4.1 and 1.4.2. Apart from the spatial distribution, relative volume fraction and absolute volume occupied by the voids were also calculated from CT scan measurement data. Although the relative void fraction varied between 3-9 %, a direct trend with respect to maximum stress values or strain to failure under high strain-rate loading was not observed (see Table 1.4.1). However, for a given sample size (and hence volume), the amount of time for which dynamic equilibrium was retained increased with decreasing void fraction for most of the samples (see Table 1.4.2). It must be noted that the response of Ti_3SiC_2 under high strain-rates is more typical of a ceramic in comparison to Ti_2AlC i.e. it is relatively more brittle. Therefore, attainment of dynamic equilibrium before fracture using the same experimental protocols was not possible. Hence, development of newer experimental protocols and techniques to circumvent these issues is currently underway.

48

Table 1.4.1: Void fraction, max. stress and strain values for Ti_3SiC_2 at strain rates 350-1500 s^{-1}

Void fraction (%)	Max. Stress (MPa)	Max. Strain (%) (based on wave analysis)
5; 4; 4.5	940; 940; 980	1.4; 1; 1.3
5; 3	780; 650	3.7; 3
8; 9	760; 700	2.5; 2

Table 1.4.2: Sample size, plateau times and void fraction for Ti3SiC2 tested under high strain-rates

L:D	D_s:D_b	Plateau Times (µs)	Void fraction (%)
0.4	0.7	40; 30; 40	5; 4; 4.5
0.5	0.7	55;70	5; 3
0.5	0.8	40;20	8; 9

1.4.2 Strain evolution in MAX phases

Our analysis of full-field measurements obtained from DIC show that the local strain fields are heterogeneous, which indicate an underlying *meso-structure* in the bulk material. Strain measurements were performed using 2D DIC to capture localized features of deformation and a validation of the method is also provided using a 3D DIC technique. The results show that heterogeneous strain fields are present under both static and dynamic loading conditions, beyond a certain stress level, underlying origins of which can be related to lower length scales. For Ti_2AlC, this value is found to lie between 200-300 MPa and for Ti_3SiC_2 this value is slightly higher and lies in the range 300-350 MPa, independent of the strain-rate.

Commercial MAXthal powders (Sandvik Technologies, Sweden) are processed into cylindrical discs using Spark Plasma Sintering (SPS) and pressureless sintering methods at temperatures of 1300°C (for Ti_2AlC) and 1325°C (for Ti_3SiC_2) at a heating rate of 50°C / min and load of 100 MPa. As-received discs were machined into smaller discs using Electrical Discharge Machining (EDM). For the majority of experimental data reported herein, 2D DIC was used to calculate strains in cylindrical specimens. This approach was validated by comparing 2D DIC results with 3D DIC. The validation tests were performed with three cylindrical Ti_3SiC_2 samples (7 mm (dia.) x 13 mm (length)) using two cameras under quasi-static loading conditions. Figure 1.4.3 shows a comparison between strains obtained using 2D and 3D DIC. The figure plots the average strain versus time response and strain fields at a given time instant during the test. It is observed that both the average strain calculations as well as the strain fields from the two methods have excellent agreement (average error < 5%) up to 1.5% strain.
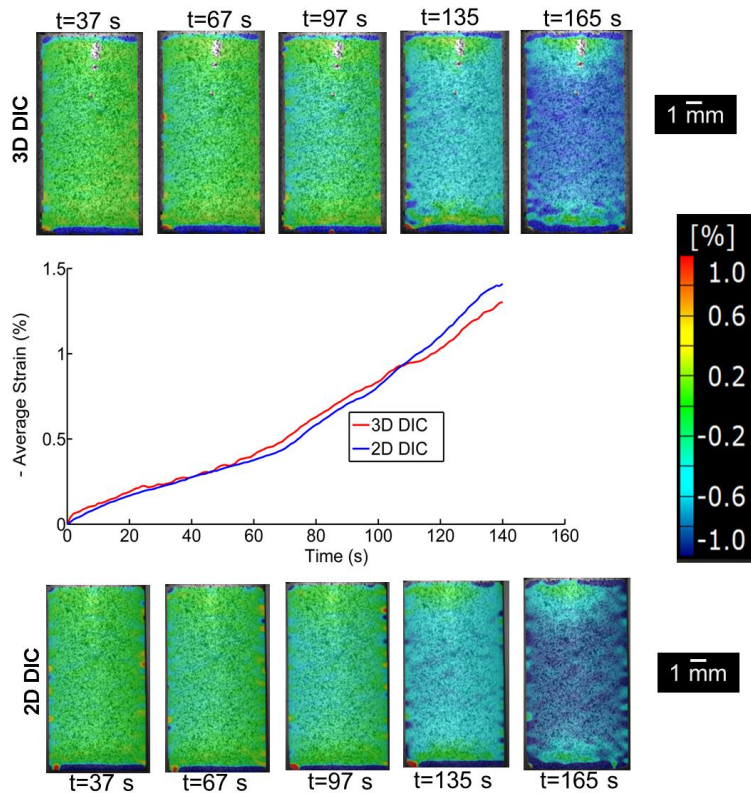
Figure 1.4.3: Characteristic plot of average strain versus time response. Field images at different times for Ti$_3$SiC$_2$ loaded quasi-statically using 2D and 3D DIC methods surround the plot.

Our experimental results show that the critical stress signals a transition from homogeneous to heterogeneous strain. In depth analysis of the strain fields reveal an underlying meso-structure comprised of soft and hard grain clusters. Strain field evolutions for Ti$_2$AlC and Ti$_3$SiC$_2$ in the range (10^{-3} – 10^{-5} s^{-1}) are presented below. Figure 1.4.4(i) shows typical stress and strain versus time responses for Ti$_2$AlC loaded at a strain rate of 2 x 10^{-3} s^{-1}. The response has an initial flat regime after which the strain increases non-linearly. The end point of the curve indicates the last frame without visible cracks. After this point, cracks propagate unsteadily leading to near catastrophic failure of the specimen, which is indicated by an arrow on the stress versus time curve. The full-field images ((a)-(g)) shown in this figure depict the axial strain fields i.e. along the compressive loading direction. It is observed that up to a certain stress level (~240 MPa, as indicated by (d)), strains remain nearly homogenous. Beyond this point, the field becomes increasingly inhomogeneous until the specimen fails. Overall, the stress versus time response has a near linear character without any significant visible transitions. Figure 1.4.4(ii) shows the average strain / stress versus time in Ti$_3$SiC$_2$ loaded at a strain rate of 1.2 x 10^{-4} s^{-1}. The most interesting highlight from analyzing the average stress and strain curves is that in both Ti$_2$AlC and Ti$_3$SiC$_2$, there is a transition stress that coincides with the initiation of strain heterogeneity in the material. We would expect this to be true for other MAX phases as well. Furthermore, this transition point is most certainly controlled by processing conditions. The dynamic average strain versus time response is similar in nature to the quasi-static response i.e. an initial near flat regime followed by a non-linear rise.

50
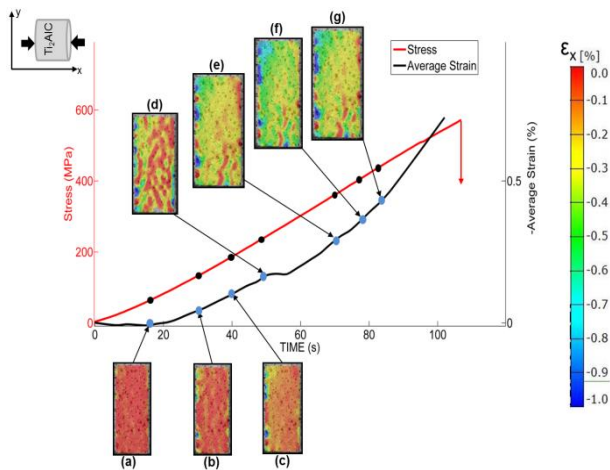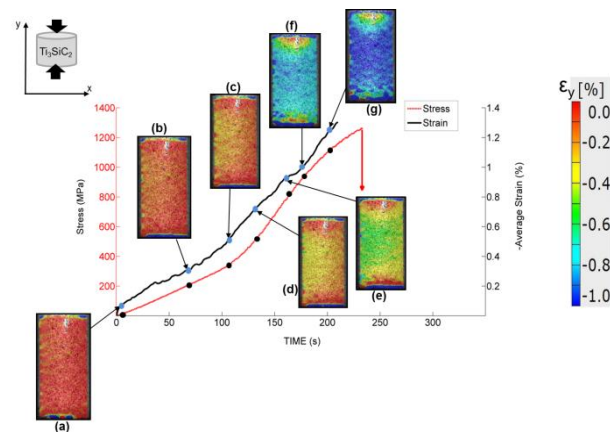
Figure 1.4.4: Characteristic stress / average axial strain versus time response, and strain field evolution in axial direction ((a)-(g)) for i) Ti$_2$AlC and ii) Ti$_3$SiC$_2$. The blue and black dots indicate the time instant at which the field images are taken taken on the average strain / stress versus time response, respectively.

We analyzed the inherent inhomogeneity in the strain field by considering points along and transverse to the compression axis and analyzing the strain evolution of individual points. Overall, for most of the points in both materials, the strain has two regimes: i) a collated shallow regime and ii) a splayed steep regime. Figure 1.4.5 shows the typical axial strain variations along and perpendicular to the axis of compression in Ti$_2$AlC. The transition from an initially slow rate of strain accumulation (indicated by a near flat regime) followed by a marked increase indicates a sudden change in the global dominant deformation mechanism. This occurs at a critical stress and is consistent across the sample. This change in slope is also approximately coincident with the splay or divergence of the different point strains. In other words, the critical stress signals a transition from relatively homogeneous strain in the sample to heterogeneous strain. The initial linear character is associated with coordinated elastic deformation mechanisms; subsequent heterogeneous strains are caused by multiple simultaneous deformation modes active within the material i.e. activation of slip systems and movement of dislocations. However, since the crystal structure is hcp, slip is limited to basal planes only. The mobile dislocations, on the other hand, are responsible for a multitude of competing mechanisms, the most significant of which is the KB formation. This is further supported by variations in point-wise strain accumulation slopes. The rates at which average strain accumulate in the two materials are similar (pointing to similar mechanisms) but the initial near flat regime is smaller for Ti$_2$AlC.

Herein, we provide a mechanistic correlation of the heterogeneities to the meso-structure, which essentially constitutes a cluster of grains in polycrystalline MAX phases. The results from the analysis presented here point to intergranular interactions and grain cluster deformation as the source of strain heterogeneity. Our results show that both intergranular and intragranular deformation mechanisms are responsible for the heterogeneous strain-fields resolved at the macro-scale. Furthermore, the wide distributions of grain sizes appear to be responsible for creating mesoscopic regimes of soft and hard grain clusters.
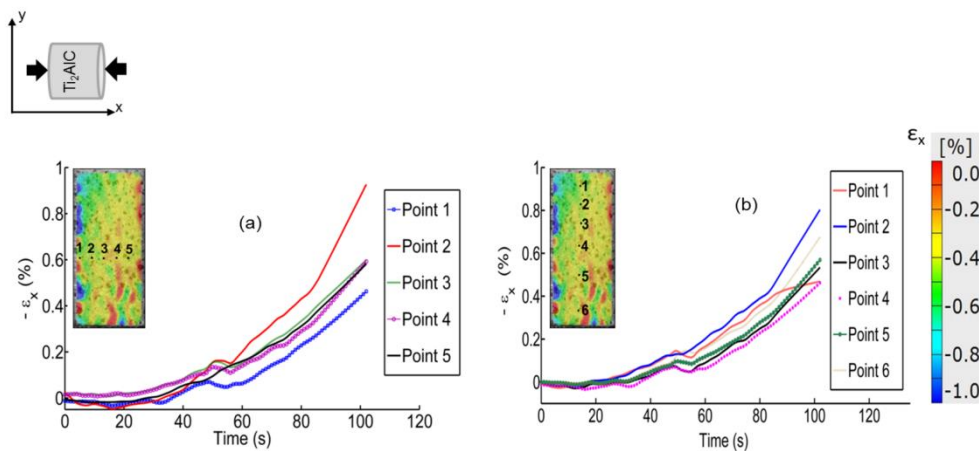
51

Figure 1.4.5: Representative point-wise axial strain evolution in Ti₂AlC for points taken along and perpendicular to the direction of applied compressive load.

Figures 1.4.6(a)-(i) show magnified versions of the strain fields at different time stamps (i.e. levels of average global strain) during the test. It is observed that regardless of the level of strain there are regions of low strain surrounded by regions of high strain. This identifiable pattern occurs at an acute angle with respect to the loading axis. There appears to be some rotation with increasing strain, though that is difficult to confirm without more fine-scale data to analyze. These patterned regions of low and high strain are on the order of a few hundred microns, which would represent a cluster of 5-8 grains or even one very large grain. Now kinking has been the primary focus of MAX Phase deformation mechanisms to date, which is a phenomenon occurring within a single grain and is an interesting mechanism because of its implied role in pseudo-ductility and potential for irreversible deformation. Here, we show that the current size/scale analysis of the strain data clearly point to mesoscopic mechanisms, as relevant. Given the scale of the heterogeneity, strain localization near grain boundaries is an unlikely source and we cannot resolve sub-grain strains. Therefore, based on the size of the resolved strain, grain cluster deformation dominates the response (it is also possible for very large single grain deformation to dominate in isolated regions). Overall, these regions of high and low strains can be associated with soft grain clusters and hard grain clusters. This means that grain size, geometry and microtexture are possible factors which influence heterogeneity significantly. By extension, inter-granular void formation and distribution play a role in accommodating grain deformation (according to their aspect ratio) and rotation. Higher resolution optics is required to resolve strain fields within grains, which will certainly shed even more light on this evolving picture of MAX phase deformation behavior. This is the subject of future work.

In summary, we have shown for the first time that grain-grain interactions play an important role in MAX phase deformation and that grain clusters are the source of strain heterogeneity. Since slip is limited and twin formation is not possible in these materials, the relatively soft grains can deform by nano-layer buckling, kinking and delamination. On the other hand, the relatively hard grains deform elastically and then by quasi-brittle modes. At the macroscale, the simultaneous coexistence of these deformation modes give rise to soft and hard grain clusters that manifest as heterogeneities in the strain field. These experimental data point to non-negligible grain-scale phenomena that should be considered in any theoretical formulations proposed and multi-scale models developed for MAX phases. Although these materials crystallize in a hexagonal (hcp) crystal structure that facilitates limited basal slip, deformation progresses via a

52

combination of several mechanisms at the microstructural scales, such as Kink Bands (KBs), delaminations, cavitation, grain boundary decohesion and sliding. Fractography studies point to a combination of ductile and brittle modes present at failure. The latter includes laminar fracture, transgranular cracking, grain pullout, and grain delaminations. The most interesting of these are the ductile modes that can be influenced through synthesis and processing and controlled to delay the onset of brittle failure and catastrophic fracture.
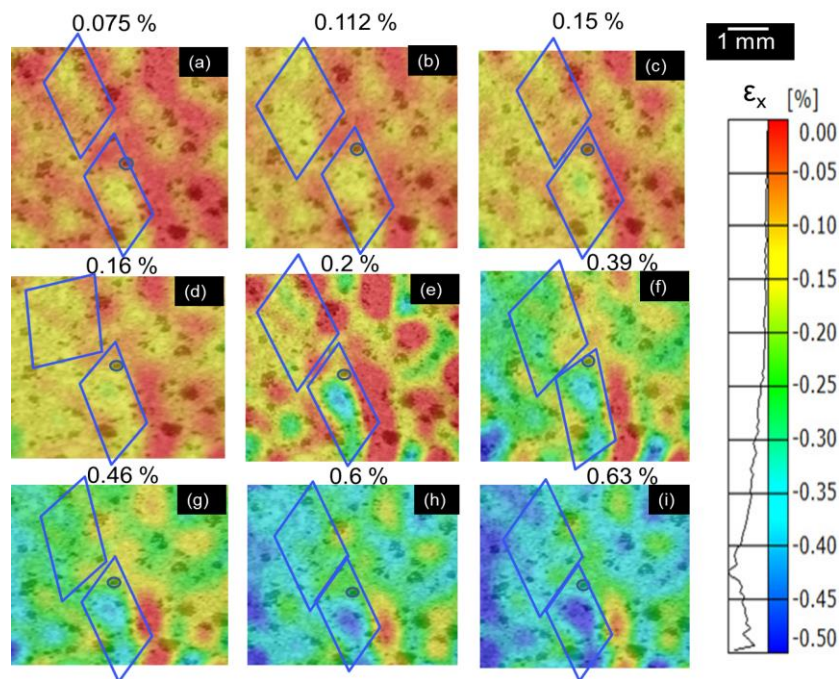
Figure 1.4.6(a)-(i): Magnified views of the axial strain field taken from the central portion of a Ti$_2$AlC sample tested under static conditions, at different instants. The values at the top of each image indicate the average axial strain accumulated, and the boxes highlight two regions where higher strains are bounded by lower strains.

1.4.3 Effect of rapid thermal gradients in MAX phases

To study the effect of rapid thermal gradients on MAX phases, Ti$_2$AlC samples were subjected to temperatures of up to ~900°C and subsequently quenched in water to induce rapid thermal gradients in the material. Contrary to typical ceramics, it was observed that the samples showed no signs of cracking and/or spalling. To assess the strength retention capabilities and hence determine thermal shock susceptibility of Ti$_2$AlC, these samples were subjected to loading under high strain rates using SHPB at strain-rates of ~3500 s^{-1}. Figure 1.4.7 shows the variation of retained strength with quenching temperatures. From the results, it is inferred that Ti$_2$AlC retains its strength post-quench and it is postulated that the ductile microstructural mechanisms (such as kink bands) operative in these materials dominates over the brittle modes to facilitate this response.
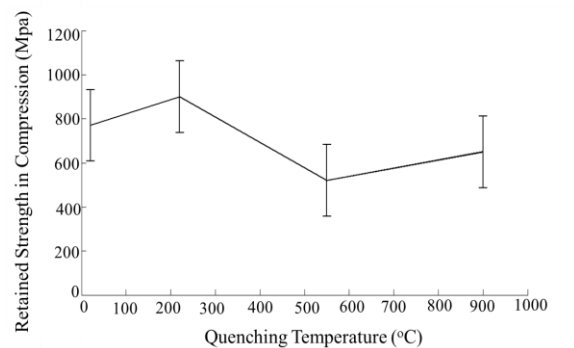
Figure 1.4.7: Retained strength versus quenching temperature for Ti$_2$AlC tested at 3500 s^{-1}(two samples were tested for each temperature).

Modeling of hysteresis in MAX phases and MAX-SMA Composites

A fractional calculus based model developed earlier (Year 2) for high temperature hysteresis in Ti$_3$SiC$_2$ was refined to capture the precise experimental phenomenology. In the first model, a sinusoidal input strain wave was assumed and the corresponding stress values were calculated by fitting to experimental stress-strain data. In the refined model, a triangular waveform for stress was an input to the fractional calculus model to calculate corresponding strain values by using a Monte Carlo fitting algorithm developed in house. In the earlier model, only the coarse grained response was captured effectively. New improvements allow us to capture the response of both coarse and fine grained materials using only three parameters over a temperature range from room temperature to 1200°C. Due to the low number of parameters required, the model is highly suitable for numerical implementation. Moreover, this model is first of its kind to capture high temperature response in KNE solids. The earlier developed modified Preisach model could only capture the room temperature response and is not directly implementable in a numerical formulation due to computational expense. Figures 1.4.8(a) and (b) show a typical comparison between experimental data and model calculations for coarse and fine grained materials respectively under higher temperatures. The high temperature hysteresis is different from the room temperature response, wherein the loops are closed and there is no residual strain. Figure 1.4.9 shows a typical comparison of experimental data and model calculations in MAX phase-SMA composites, capturing the response under room temperature and different stress levels.

54
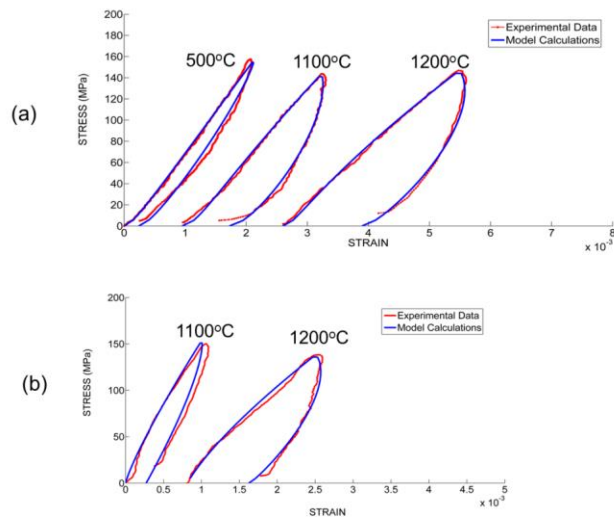
Figure 1.4.8: Stress strain response for (a) coarse-grained and (b) fine-grained Ti₃SiC₂, highlighting the capability of the model to capture high temperature hysteresis.
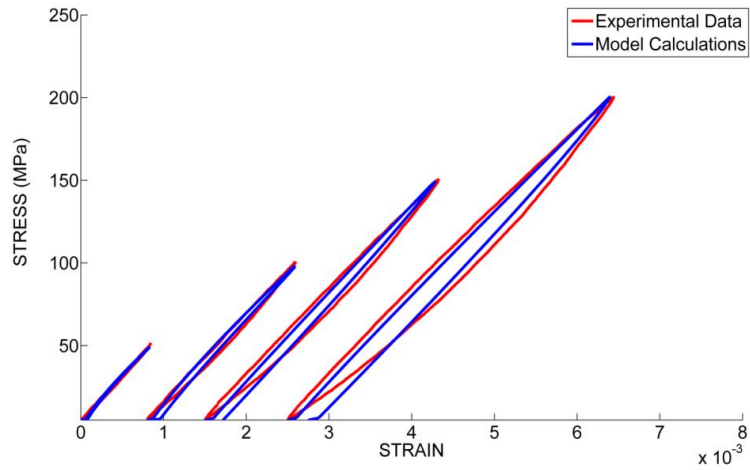
Figure 1.4.9: Stress strain response MAX phase-SMA composites, highlighting the capability of the model to capture the response at a given temperature and different maximum stresses.

2. RESEARCH THRUST AREA: MULTISCALE CHARACTERIZATION AND MODELING

2.1 Micromechanics-based modeling of GCMeC

RESEARCH TEAM MEMBERS
PI: Dimitris C. Lagoudas
Post docs: N/A
Graduate Students: Brian T. Lester and Babatunde Agboola
Undergraduate Students:

COLLABORATORs: Dr. I. Karaman, Dr. M. Radovic, A. Kothalkar, L. Hu, R. Benitez Texas A&M University; Drs. S. Qidwai and A. B. Geltmacher, U.S. Naval Research Laboratory (NRL)

OBJECTIVES:

(i)   Development of Micromechanical Models of GCMeC
(ii)   Image-based finite element analysis of GCMeC
(iii)   Development of MAX phase constitutive modeling
(iv)   Phase field modeling of interface development and constitutive SMA behavior

TECHNICAL ACCOMPLISHMENTS
To analyze the inelastic response of the GCMeC, a series of models have been constructed. These models incorporate a range of complexity in terms of microstructural detail and numerical complexity and have been used to analyze a series of model characteristics. The first model focused on the development of an efficient, micromechanical model based via an Eshelby, Mori-Tanaka model of the effective transformation characteristics of composites with SMA inhomogeneities. As a first step in studying the GCMeC of interest the developed model was used to identify the effective phase diagram of Ti_2AlC composites with NiTi inhomogeneities. Figure 2.1.1a shows an example of such a phase diagram and shows the large shift in effective transformation surfaces due to the impact on the nonlinear SMA response. This shift (especially in the M_f and A_s surfaces) is associated with the stress redistribution arising from SMA transformation while interacting with a stiff ceramic matrix and highlights the interaction of these two phases.

(a)"   (b)"   (c)"
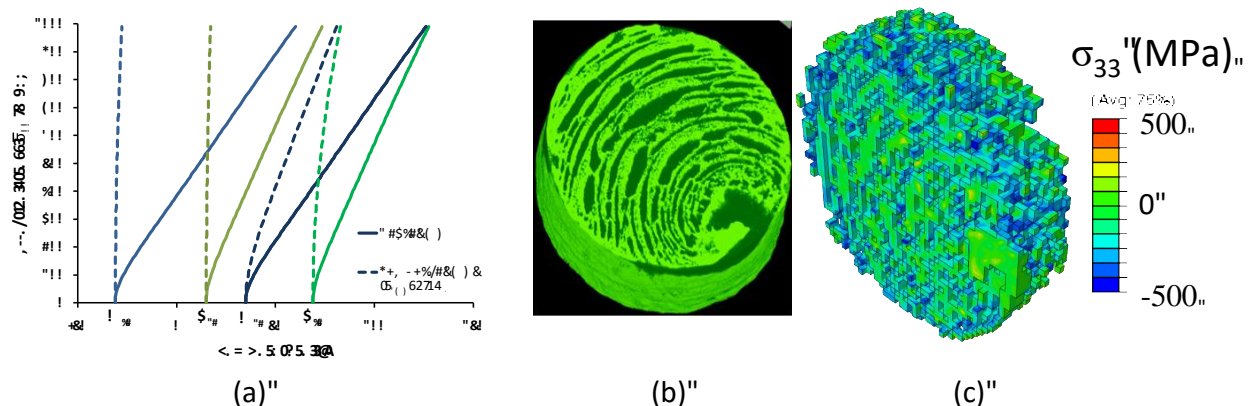
Figure 2.1.1: (a) Effective phase diagram of a Ti₂AlC containing 30% spherical SMA inhomogeneities; (b) Microstructure reconstruction of a porous SMA used for modeling representative GCMeC and (c) Residual stress in the ceramic phase of an example GCMeC after an actuation path.

56

In order to account for microstructural detail and explore the entire response of the GCMeC, a series of image-based FE models were constructed. Specifically, tomography (performed in collaboration with NRL) was first used to characterize the microstructure or a porous NiTi specimen with the porosity being treated as the Ti_2AlC phase. Finite element models constructed via this microstructure characterization were then used to study the interaction of the phases through the loading cycle and explore both the local response of the phases and that of the effective composite. Importantly, it was shown that through an isobaric thermal cycles (an actuation path) austenitic to martensitic transformation could be used to induce permanent deformations in the MAX phase material which upon heating back to austenite and unloading resulted in a residual, non-zero stress state – important for subsequent discussion of these materials. The reconstruction of the microstructure is shown in Fig. 2.1.1b while the final residual stress of the ceramic phase is presented in Fig. 2.1.1c. Additional studies with this set of model also focused on the impact of different hardening parameters and determined the effect of thermal expansion mismatch.

Figure 2.1.2: (a) Finite Element mesh of NiTi-Ti$_2$AlC composite model incorporating four phases (NiTi, non-transforming NiTi, Ti$_2$AlC, and porosity) (b) Simulated effective actuation response of the GCMeC under a variety of compressive loadings (c) Residual stress histogram of the ceramic phase along with the actual final stress state of the composite (insert) under an applied 350 MPa loading.

Actual GCMeC composite specimens were modeled via a similar approach. Specifically, a NiTi-Ti$_2$AlC composite specimen provided by the materials team was also characterized via x-ray microtomography approaches (in this case again with NRL). These resultant images along with measurements of the porosity and non-transforming SMA material determined by Profs. Radovic and Kaman's group were then used to produce a four-phase model (NiTi, non-transforming NiTi, Ti$_2$AlC, and porosity) as shown in Fig. 2.1.2a. The developed model was then used to explore the composite response through actuation loading paths. Specifically, Fig. 2.1.2b presents the effective, simulated actuation response of the composite under a variety of load levels. In comparison to experiments, the numerical results show good qualitative agreement with many of the important characteristics of the model. Such features may be seen in Fig. 2.1.2b in which initially a closed hysteresis (beginning and end points of the cycle are the same) loops are observed at lower applied stress levels while at higher load levels a more open nature (difference in the beginning and end points) of the composite response indicating the development of permanent deformations. Additionally, unique response characteristics such as the decrease in martensitic finish temperature (corresponding to the end of forward transformation) with applied stress. This runs counter to what is expected of bulk SMAs but agrees with experimental observations. The open nature of the hysteresis loops is indicative of the residual stress states previously referred to. Closer examination of these final ceramic conditions may be seen in Fig.

57

2.1.2c in which a histogram of the final distribution is presented clearly indicating a compressive state. Furthermore, by doing a multicycle simulation (at 450 MPa and then unloaded) it was demonstrated (in Fig. 2.1.3a) that the development of residual stresses in the composite leads to an effective two-way shape memory behavior. That is to say, without cycling when unloaded and subject to a thermal cycle a near thermoelastic response is noted. If, however, a thermal cycle with a large applied bias load is performed and then a no-load cycle is performed a hysteretic response is noted even under no load.

Additional simulations were also performed on this model (and others) to investigate the impact of different microstructural and constitutive parameters on the effective response. For instance, a series of finite element meshes were constructed with different porosities and the increased in permanent deformations and stresses with porosity may be seen in Fig. 2.1.3b. Similar observations were reported with the percentage of non-transforming SMA behavior and modulus of the non-transforming phase. Given much of the constitutive response of the reaction layer is unknown, various plastic constitutive responses were also considered which did change the magnitude but not the sign of Ti$_2$AlC residual stress. Although the image-based model gives plenty of detail on the complex effect of the microstructure, smaller RVEs of distinct reinforcement type were also considered to look at the various effects of these features on the material performance and aid in subsequent design. An example is given in Fig. 2.1.3c in which cylindrical reinforcement in all three directions was considered. As the reinforcement in the direction of loading versus the transverse (given by a/b) the average residual stress magnitude actually decreased due to the changes in the complex three-dimensional loading.

(a)$ (b)$ (c)$
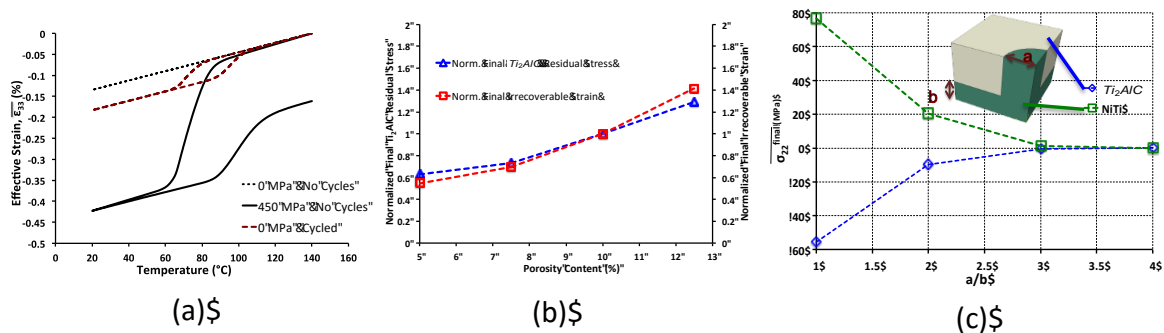
Figure 2.1.3: (a) Simulation showing the development of an effective two-way response due to the development of residual stress states (b) Dependence of final Ti$_2$AlC residual stress and irrecoverable strain on porosity of composite (c) Residual stress of the Ti$_2$AlC composite in a simple RVE for different reinforcement architectures.

One other emphasis in this effort was the development of mechanism based predictive models of the MAX phase response. Due to the lack of an existing MAX phase model of this type, prior results focused primarily on elastic-plastic or CDM based assumptions to emphasize the role of the permanent deformations that were primarily of interest. To address this issue, a model accounting for the deformations associated with the recoverable IKB mechanisms and permanent deformations and damage associated with kink band formation. Plastic deformation in non-aligned grains was also allowed to study the possible role in these other grains. For utilization in finite element simulations, a internal state variable, continuum thermodynamics based phenomenological approach was adopted. Results provided by Prof. Radovic were used to study these responses in detail and a model combining a recoverable mechanism similar in nature to the pseudoelastic response of SMAs for the IKB response with a CDM-analogous type damage model for the permanent deformation response was developed and implemented. Example results of this model are shown below in Fig. 2.1.4. A number of additional studies have been

58

performed looking at the interaction of the various mechanisms in the effective response and how tuning the relative hardening and other parameters manifests in the global response to understand the various couplings evident in the system.
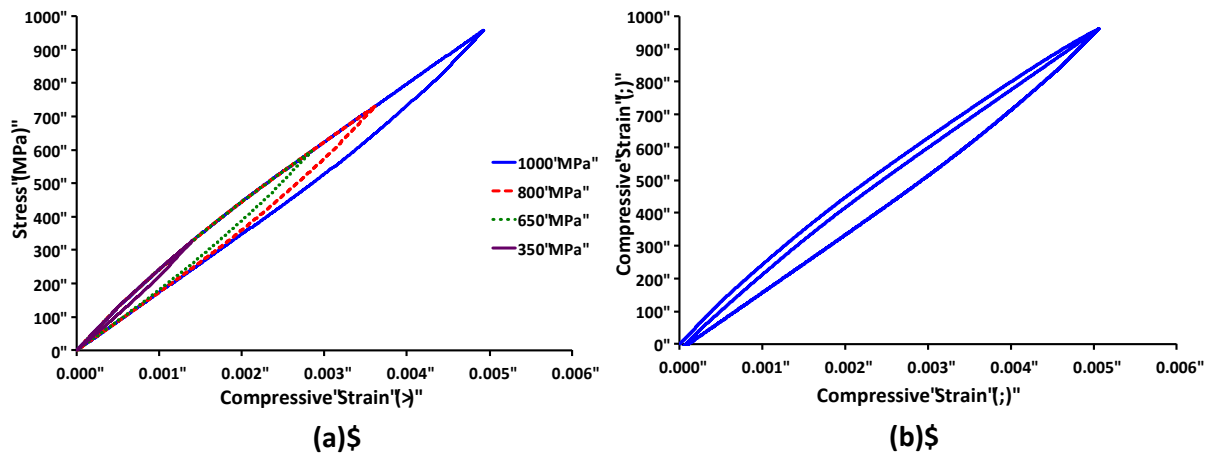

Figure 2.1.4: Numerical simulation using the developed MAX phase exhibiting (a) formation of recoverable kink bands and (b) multicycle response highlighting the formation of permanent deformations through permanent kink band formation.

A novel 3-D thermodynamically consistent, thermomechanical constitutive modeling of shape memory alloys (SMAs) is developed using the notion of configurational forces (or otherwise called material or chemical forces by other scientists). The model is based on the notion of a phase field (an order parameter for materials that involve symmetry breaking as they change from one phase to another – which is the case for shape memory alloys) to identify the two phases present in SMA. The order parameter is a macroscopic manifestation of atomic reconfiguration at the microscopic scale that leads to the transformation in SMAs from austenite to martensite. The two phases being a low temperature (martensitic) and a high temperature phase (austenite).

This model is a contribution to the state of the art in constitutive modeling of SMAs as it incorporates intrinsic rate dependency into the constitutive modeling of SMAs. The kinetics of the evolution of the phase field is used to capture the propagation, after nucleation of a new phase, of transformation front or interface in the SMA. Thermodynamic consistency of the model is ensured by using an approach classical in continuum thermodynamics following the rational mechanics school of thought. In particular, the Coleman-Noll entropy principle is employed on the Clasius-Duhem inequality (which is a popularly used form of the second law of thermodynamics) after combining it with the Legendre transformation and the first law of thermodynamics.

The inelastic strain during phase transformation is related to the primary order parameter in such a way that the primary order parameter is the sole kinematic contributor to the rate of dissipation during inelastic deformation of the SMA. This is also done to ensure that the thermodynamic consistency required for the model is not violated, which necessitated that the inelastic strain be related to the primary order parameter through their rates. Therefore, we employ an approach similar to the flow rule in plasticity and have been further shown to be true using the principle of maximum rate of dissipation. Another motivation for the choice of the particular form of the relationship between the inelastic strain and the primary order parameter is the need to capture the Luders-band like feature reported thin SMA strip under pseudoelastic loading as well as the domain pattern formation which is due to the deformation in the SMA.

The free energy (which is the energy available in the SMA to do work) is written in a form similar to the Landau–type free energy, and elastic energy as well as a gradient energy is also introduced to the free energy. The gradient energy is incorporated to capture the energy cost

59

associated with the formation of an interface, which is mathematically a penalization of a sharp interface (based on Gibbs-Thompson Idea). The chemical part of the free energy is made to look like the landau free energy by calibrating the model to the stress-temperature phase diagram. The parameters of interest being the clasius-clapeyron parameters for austenitic and martensitic transformation, the maximum transformation strain as well as the austenite and martensite start temperatures. This phase diagram can be determined from experiment using approach such as Differential Scanning Calorimetry (DSC) technique.
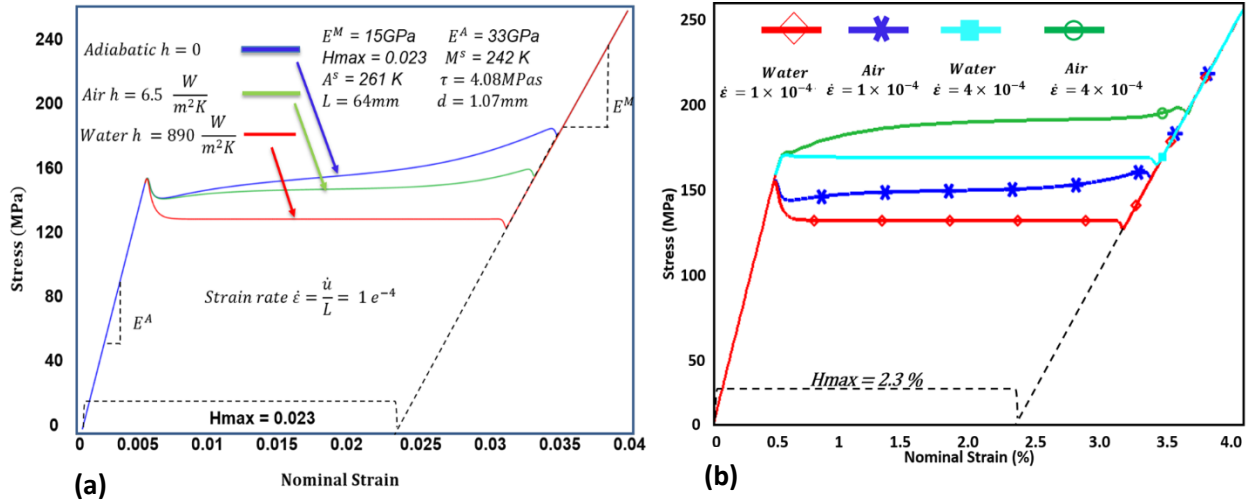
Figure 2.1.5: (a) Thermal hardening, effect of thermal boundary condition, strain softening and (b) Effect of loading rates on Shape Memory Alloys.

A new kinetic law similar to the Ginzburg-Landau equation is developed constitutively. Essentially, this kinetic law is a direct result of the second law of thermodynamics and a balance law for the configurational force system which is analogous to the standard balance of linear momentum in mechanics. Therefore, the kinetic law satisfies the thermodynamic consistency need of the model.

A length scale is present in the SMA model which means that the model should be able to phenomenological capture the effect of size on SMA response. An outstanding result of this model is its ability to capture seeming pseudo-viscoelastic behavior of SMAs (i.e. stress relaxation and creep). These phenomena have been known in polymeric materials and metals at high temperature and have been recently reported in SMAs as well by experimentalists. Using this model, a possible explanation has been proposed for the reported seeming viscoelastic behavior of SMA. We observed, based on our simulation, that this seeming viscoelastic response is a result of the motion of the transformation front after loading has been stopped due to stored energy and thermal conditions, which this model does capture constitutively.

The model is simplified to 1-D and implemented in COMSOL Multiphysics (a commercial finite element code). Some preliminary results generated that shows the capability of the model are presented in Figures 2.1.5 and 2.1.6. Figure 2.1.5a show three of the different features characteristic of pseudoelastic SMA reported in experiments. These include the thermal hardening observed in pseudoelastic SMA macroscopic response as well as the difference in the degree of hardening depending on the thermal boundary condition. Figure 2.1.5b is a plot of the effect of mechanical loading rates. Figure 2.1.6a on the other hand shows the effect of size (through an intrinsic length scale) on the pseudoelastic response of SMAs. Transformation induced stress relaxation is also simulated using the model as shown in Figure 2.1.6b. This stress relaxation behavior is one very important feature that, as mentioned earlier, could not be captured

60

by most existing SMA models that are useful for engineering design. These results are in good agreement with experimental observation and demonstrate the novelty and usefulness of this 3-D model for the design of SMAs for engineering application. So far the model has not been used to simulate load biased shape memory effect (SME), which is ideal for aerospace application of SMAs. However, the model should be able to simulate SME in SMAs and possibly give insight into new behavior of SMA undergoing temperature induced load biased transformation.
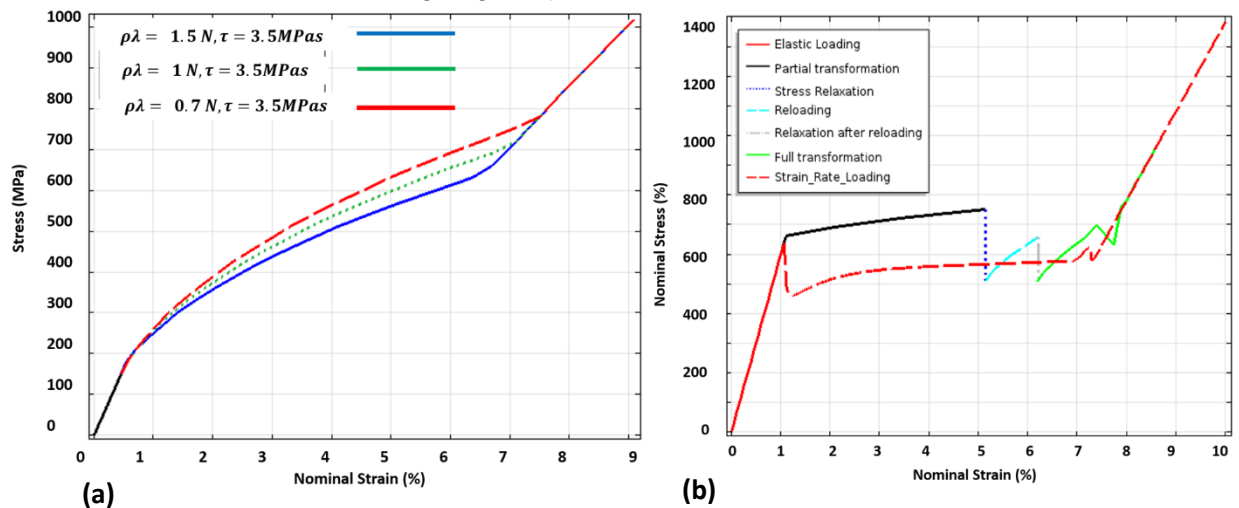
Figure 2.1.6: (a) Size effect in SMAs loaded at 30 MPa/s stress rate due to the intrinsic length scale (interface width) (b) Transformation induced stress relaxation

In conclusion, we report a novel 3-D continuum phase field model, which is capable of simulating SMA response. The model is novel in that it models the macroscopic response of SMAs as a result of evolution of macroscopic transformation front (or interface) subsequent to the nucleation of a second phase. Also, the model is thermodynamically consistent and is constitutively rate dependent. One important usefulness of the model would be in novel application of SMAs when interacting with fluids or solids wherein they are embedded or with their environment (especially thermally). GCMeC is a good example of such composite with embedded SMA and should benefit from the rate dependency incorporated into the new model. In general, this model is a contribution to the state of the art in SMA modeling as well as the field of continuum mechanics as it suggest very strongly (if not corroborate) the need for a new set of configurational or accretive forces (and their balance) to be basic concept of continuum modeling of materials with evolving interface.

2.2 Modelling of Progressive Damage in Complex Microstructures

RESEARCH TEAM MEMBERS
PI: John D. Whitcomb
Post doc: Kaushik Das
Graduate Students: W. Ross McLendon, and M. Keith Ballard
Undergraduate Students:

COLLABORATORs: Dr. Ibrahim Karaman,Dr. Ozden Ochoa, Dr. Dimitris Lagoudas, Hieu Truong, Ozgu Ozsoy, Ankush Kothalkar, Texas A&M University

61

(iii) Develop a computational inverse method that accounts for random arrangements of fibers to determine fiber moduli and the in-situ matrix strength, which cannot be directly measured

(iv) Develop a reduced order multiscale strategy for predicting progressive damage growth in complex microstructures

(v) Develop numerical models to guide the design of experiments and interpret the experimental data to obtain fracture properties

(vi) Explore potential of nanoporous material for thermal barrier coating

(vii) Develop transient nonlinear thermoelastic analysis for hypersonics aeroelasticity analysis framework

TECHNICAL ACCOMPLISHMENTS

2.2.1. Microscale Inverse Analyses
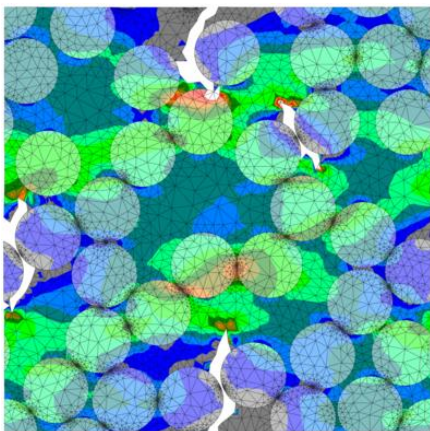
Figure 2.2.1 Stress contours from microscale progressive damage analysis

In the micromechanical analyses of fibrous polymer matrix composite (PMC) systems, one of the fundamental challenges is the determination of the constituents' properties. While it is possible to directly measure some of these properties (e.g. the engineering constants for the neat matrix and longitudinal Young's modulus of the fibers), other properties, such as engineering constants associated with transverse and shear deformation of the fibers, and failure properties of either constituent, are difficult or impossible to measure. The properties are often obtained through the solution of an inverse problem, which have in the past neglected randomness in the microstructure. A framework was developed to determine constituent properties for fiber-matrix material systems with randomly arranged fibers. Once the constituent properties are known, the framework allows the prediction of properties for other conditions for which experimental data is unavailable, such as for other temperatures or volume fractions.

This framework was used predict the elastic properties for AS4, IM7, T300, and T650-35 graphite fibers and compared to results using the Mori-Tanaka average scheme and FEA assuming a hexagonal fiber arrangement. It was observed that randomness in the arrangement of fibers results in significantly different predictions for the longitudinal shear modulus of the fiber, differing up to 6x for some material systems. The space between fibers was observed to have a significant impact on the longitudinal shear modulus with little effect on other elastic properties.

For hexagonal and a collection of random arrangements, the in-situ matrix strength was determined in an inverse fashion using a progressive failure analysis. The value (or values, depending on the local failure criterion) of the in-situ matrix strength was determined such that the predicted strength of micromechanics model matched the observed strength of the composite under some simple loading (e.g. transverse tension). Because of the random arrangement of

62

fibers, there is a distribution of the predicted lamina/tow strength. Figure 2.2. shows a typical distribution.
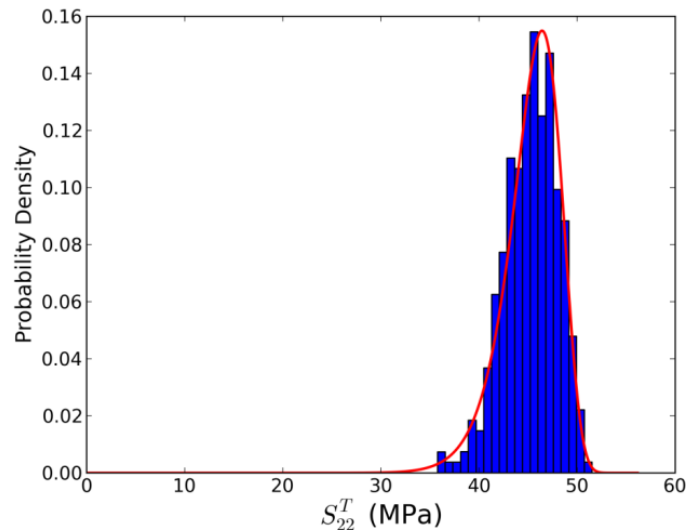
Figure 2.2.2 Distribution of transverse tensile strength

Using the matrix strength, the effect of cure and service thermal loads was predicted. Again, a collection of random microstructures were analyzed to determine the distribution of tow/lamina strengths. Interestingly, when the random arrangement of fibers is accounted for, the distribution of the normal strength for the tow/lamina increased as the ΔT (due to the curing process) decreased. This means that the curing process can actually strengthen the composite by inducing beneficial thermal stresses which counter-act the stresses due to tensile load. This is opposite of the behavior observed using a hexagonal arrangement of fibers for a ΔT lower than -90° C, as shown in Figure 2.2..

This demonstrates that assuming a hexagonal arrangement of fibers, which is often done in the literature, can lead to misleading predictions. The distribution of tow/lamina strengths and in-situ matrix strength were used as input for the progressive damage analyses at the mesoscale (i.e. the next larger scale).
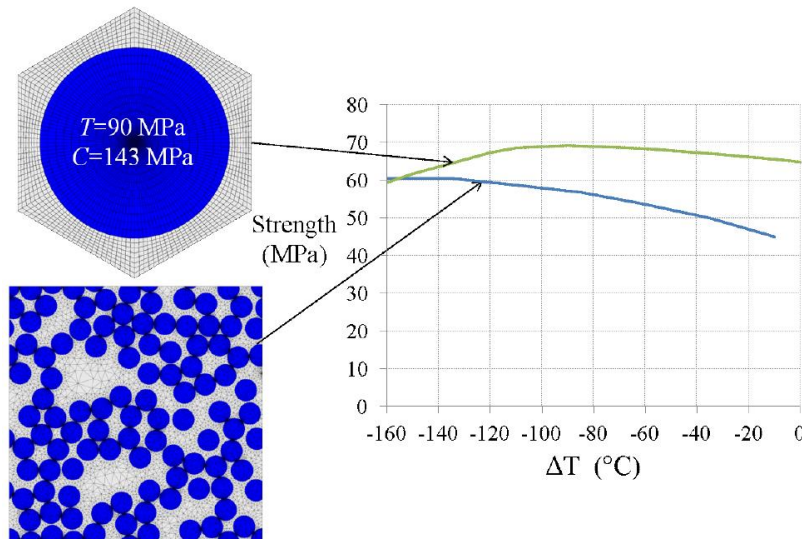
Figure 2.2.3 Variation of 5th % transverse normal tensile strength with ΔT from cure

2.2.2 Progressive Damage in Material Systems with Complex Microstructure

The proposed MURI hybrid material system has components that have complex microstructure, such as textile composite, interpenetrating max phase and SMA, and material with vascular cooling networks. Predicting damage initiation and growth in such materials is computationally very challenging because of the multiple scales that must be considered. Our focus has been on the textile composite component. The goal has been to develop a multiscale analysis that uses limited experimental data to create a reduced order analysis to predict structural performance under hypersonic service. This effort has involved a range of tasks, which will be described next.

Many types of progressive damage models have been proposed for finite element analysis of composite materials. Continuum damage models rely on various criteria to govern the initiation of damage and degrades the material at the quadrature points when local failure is predicted. Cohesive zones models use interfacial elements placed on the interfaces of solid continuum

63

elements to model discrete damage once a critical traction has been exceeded. Several continuum damage models, a cohesive zone model, and a combination of the two were compared for a [0/90]s laminated composite under uniaxial and shear loads. It was shown that the cohesive zone model considered offered clearer descriptions of discrete cracks, more accuracy due to the ability to place them in locations where damage is physically expected, and less sensitivity to mesh refinement. Unfortunately, the cohesive zone model suffered from poor computational efficiency and numerical instabilities under some situations. The underlying reasons for several cases of numerical instabilities were investigated and an adaptive strategy to improve the convergence behavior was identified.

At the mesoscale, a comprehensive study has been conducted to determine the failure initiation envelope of a plain-weave carbon-fiber polymer-matrix composite under multiaxial in-plane loading at a variety of temperatures. The stress field in the composite associated with a particular combination of mechanical and thermal loads was obtained using superposition. This stress field is then examined to determine how much the mechanical load can be scaled before failure occurs at some location in the textile unit cell. An in-house tool has been developed to enable tens of thousands of load cases to be examined in a matter of hours, which allows the development of a failure initiation envelope in stress space. This research builds on our previous findings (under this project) in which it was noted that there were a limited number of ways that failure was predicted to initiate in a textile composite, even when a broad range of multiaxial loadings are considered. Figure 2.2. shows the predicted failure initiation envelope for the composite material at one of the temperatures considered. The colors on the envelope correspond to the different modes of failure initiation in the composite…load combinations with the same color all cause failure initiation to occur at the same location in the textile architecture due to a similar local stress state.

Figure 2.2.4 Failure initiation envelope for ΔT = 50°

The determination of this failure envelope enables the prediction of failure initiation in the textile in analyses at larger scales in which the textile response is homogenized and tows are no longer modeled discretely. An approach has been developed for the prediction of failure initiation for a given stress state and temperature using the calculated envelope.

64

Stress Ratios in Database		
σ_{xx}	σ_{yy}	σ_{xy}
1	0	0
2	1	0
1	1	0
12	0	1
12	6	1
12	12	1
6	0	1
6	3	1
6	6	1
0	0	1

Simulate many load proportions — **Form database of results for the load proportions** — **Interpolate characteristic damage variables for arbitrary stress state and load proportion**
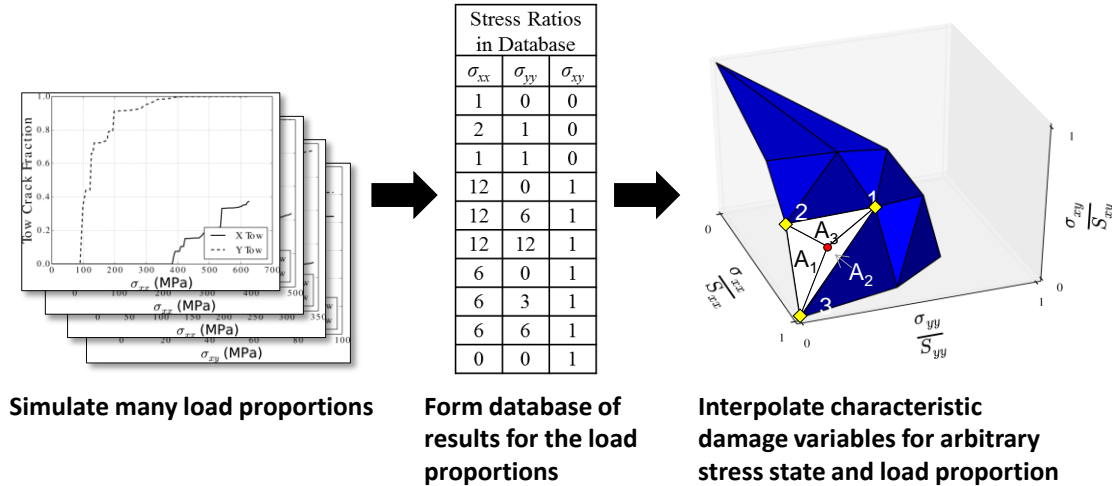
Figure 2.2.5 Reduced order model for predicting characteristic damage states
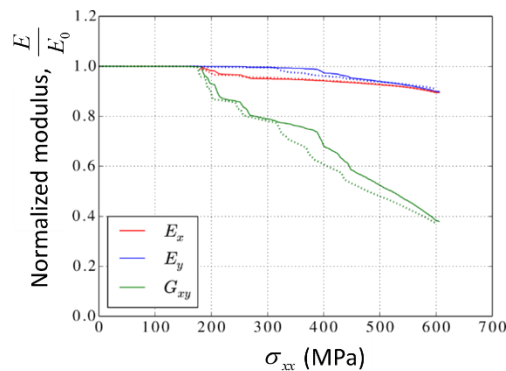
Figure 2.2.6 Comparison of degraded moduli using reduced order model and direct analysis

To predict the growth of damage at a larger scale, a reduced order model was developed. A textile unit cell was analyzed under a variety of mechanical loads at many different temperatures. As the mechanical loads were incremented, the homogenized properties of the unit cell were determined. The engineering constants of the homogenized response during the progressive failure analyses were fit to a polynomial function of the characteristic damage state variables, allowing the approximate moduli during damage growth to be calculated given an applied stress state. This allows the stress state in a macroscale analysis to be used to determine the microscopic damage and degradation of the homogenized material. A database of results was used to interpolate the damage state for a given stress state from the tabulated simulation results, as shown in Figure 2.2.. For proportional load paths, the degraded engineering constants using the reduced order model matches the actual results quite accurately, as shown in Figure 2.2..

2.2.3 MAX Phase/NiTi Interface Chacterization

The material system considered for the MURI project has a MAX phase/SMA composite. For the material to be modeled effectively, the interface between the MAX phase ceramic matrix and the SMA inclusions must be characterized. We have worked with Dr. Karaman to develop four-point bending test specimens for the characterization of the fracture properties of the interphase material that develops between the SMA and MAX phase in the metal ceramic composite. Parametric studies have allowed the experimentalists to choose specimen dimensions that will provide the most advantageous mode mix for characterizing the fracture properties of the

65

interphase and understand the sensitivity of the results to measured values, such as crack lengths. Figure 2.2.7 shows the specimen and load configuration.
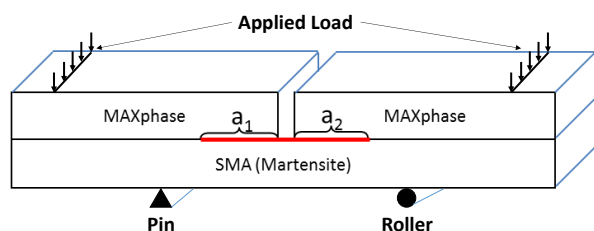
Figure 2.2.7 Four-point bending specimen configuration and boundary conditions
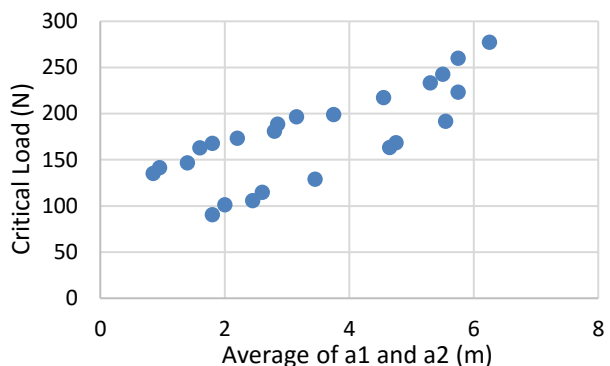
Figure 2.2.8 Critical load, the load at which crack growth is observed, vs. the average of the two crack lengths, a1 and a2

After the experiments were conducted, the virtual crack closure technique (VCCT) was employed to determine the strain energy release rates by mode. The initial analyses assumed that the material deformed elastically. However, residual deformation and unrealistic R-curve behavior suggested that detwinnning was occurring even away from the crack tip. The specimen design should result in crack growth at an approximately constant load. Figure 2.2.8 shows that there was a very large sensitivity to crack length. We are now performing further analyses that account for detwinning to see if that will explain the unexpected behavior.

2.2.4 Thermal Barrier Coating

The goal was to determine the potential of a multi-layer film for use as a highly reflective thermal barrier coating. The multi-layered film used a periodic microstructure consisting of cylindrical nanopores that acted as a photonic band gap (PBG) crystal. The film was constructed such that pores were arranged periodically along the in-plane directions and axes of the pores were parallel to the thickness direction (Figure 2.2. Figure 2.2.10). The pore diameter was varied periodically through the thickness to form a multi-layer film of alternating low and high porosities. The primary motivation behind considering this microstructure was that it can be potentially fabricated from aluminum dioxide, which remains stable at high temperatures. The reflectivity of a single layer with uniform porosity was computed by numerically solving Maxwell's equations, both by considering the microstructure explicitly and by considering a homogenized layer to gain insights into the effect of pore size on the reflectivity of the nanoporous layer. Based on the study of the single layer, two microstructures (Figure 2.2. Figure 2.2.10) with different arrangements of pores were designed to exploit the effect of microstructure to widen the band gap of the PBG crystal and to increase the reflectivity of the TRBC. Results of numerical simulations revealed (see Figure 2.2) that a wider band gap and higher reflectivity can be achieved by microstructure 2, in which the inter-pore distance of alternate layers of the multi-layer film was comparable to the wavelength of the incident thermal radiation.

A TRBC, which is made of a microstructure with a wider band gap and has increased reflectivity, will reflect a greater amount of incident heat energy over a wider range of frequencies. It was found that the presence of the TRBC, which reflected 70% of the incident radiative flux, could reduce the amount of heat the micro-vascular cooling channels had to carry from 390 kJ/m^{2}s to 300 kJ/m^{2}s.
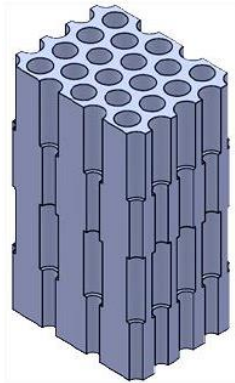
Figure 2.2.9 Microstructure 1 with concentric cylindrical nano-pores
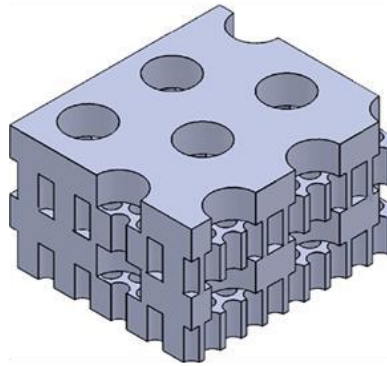
Figure 2.2.10 Microstructure 2 with nano-porous layers of different inter-pore distances
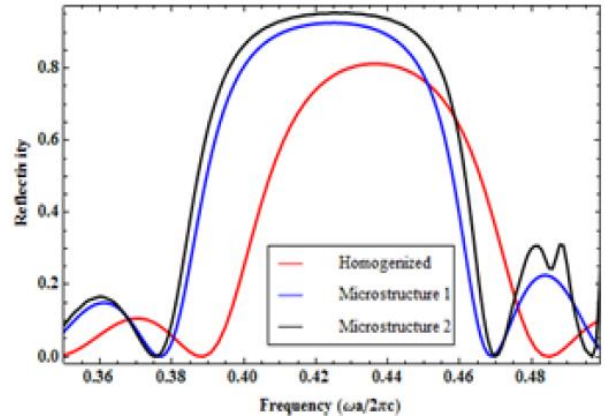
Figure 2.2.11 The variations of the reflectivity with the wavelength of the incident radiation for the TRBC

Framework for hypersonic aeroelastic analysis

At the largest scale considered, the interaction of the hypersonic flow and a wing was modelled through collaboration with Dr. Cizmas. Some of the recent improvements made in this work include an increased fidelity by developing an improved mesh generator, more efficient and flexible inter-process communication between the separate computational codes, additional validation cases, an improved time integration scheme, and accounting for geometrically nonlinear effects in the structural model. The results of the work are covered herein in a later section.

2.3 MECHANICAL RESPONSE OF STRUCTURAL ELEMENTS AND INTERFACES

RESEARCH TEAM MEMBERS
PI: *J. N. Reddy*
Institution: *Mechanical Engineering, Texas A&M University*
Graduate Students: *Feifei Cheng, Ö. Özgü Özsoy, Gregory Payette, Venkat Vallala, and J. Kim*

COLLABORATORs:
Liangfa Hu, Ibrahim Karaman, Miladin Radovic, and Ozden Ochoa.

- Viscoelastic failure analysis of adhesively bonded joints
- Multi-scale computational modeling of GCMEC with preexisting micro-damage
- Micromechanics based modeling of SMA/MAX phase composite
- Modeling of Plastic-damage behavior of porous MAX phase with Aligned Ellipsoid-like Pores
- A robust shell finite element for nonlinear analysis of laminated composite and functionally graded plate and shell structures.

OBJECTIVES:

- Viscoelastic and failure FE modeling of single lap-shear adhesive joints considering geometry nonlinearity and thermal expansion. Develop finite element model for bond failure analysis at viscoelastic adhesive-elastic adherend interfaces for a mixed-mode fracture problem in the framework of cohesive zone model (CZM).
- Estimation of the effective elastic moduli of two-phase functionally graded material with pre-existing damage using micromechanics based methods. Finite element analysis on mechanical response of a graded Ti_2AlC/Al rectangular plate with degraded effective moduli.
- Characterization of microstructure for SMA/MAX phase composite with porosity and interface layer using representative volume element (RVE) method. Predict the effective temperature-dependent thermal properties of the composites using finite element method and compare with experimental results.
- Computational modeling of plastic-damage response of MAX phase with open-cell foam structure. Implement proper constitutive model to characterize distinct tensile and compressive behaviors porous Ti_2AlC and investigate the damage mechanism under uniaxial compression.
- Prediction of interface properties in a double cantilever beam.
- Development of the theoretical formulation and numerical implementation of an efficient locking-free shell finite element that may be used to determine nonlinear response of structural components (plate and shell-like components) due to thermo-mechanical loads.

TECHNICAL ACCOMPLISHMENTS

During the past five years, we have developed computational frameworks for Adhesively Bonded System, Graded Ceramic Metal Composite (GCMEC) plate, SMA/MAX phase composite, and porous MAX phase.

2.3.1. Viscoelastic behavior of the adhesive and damage analysis of adhesive-adherend interfaces in adhesively bonded joints.

First, viscoelastic finite element analysis of a model joint with viscoelastic adhesive has been conducted while considering geometric nonlinearity as well as thermal expansion. Then a finite element model for bond failure analysis at the viscoelastic adhesive-elastic adherend interface for a mixed-mode fracture problem is proposed. In the framework of cohesive zone model, traction-separation law is used to define the constitutive response of the cohesive elements at the interface. Quadratic nominal stress criterion and mixed-mode energy criterion are used to determine the damage initiation and evolution at the interface, respectively. Fig. 2.3.1 shows the effect of thermal expansion on the viscoelastic adhesively bonded joint, and it is noted that CTE mismatch is a very important factor that influences the stress distribution in the high stress concentration arears of adhesive. The damaged configuration of the single lap joint is plotted in Fig. 2.3.2. It can be observed that the crack length different for top and bottom

interfaces, and the reason is due to the asymmetrical distributions of shear stress and peel stress along the overlap length which is shown in Fig. 2.3.3.
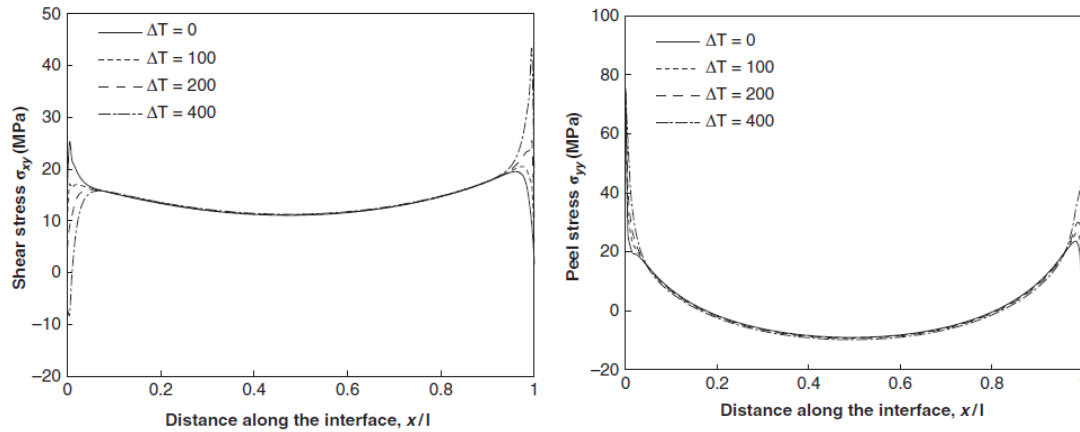
Fig. 2.3.1: Shear and Peel stress distribution along overlap length with various ΔT at t=50s.
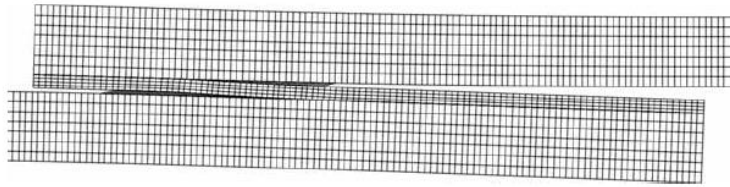
Fig. 2.3.2: Damaged configuration of the single lap joint obtained from FE model.
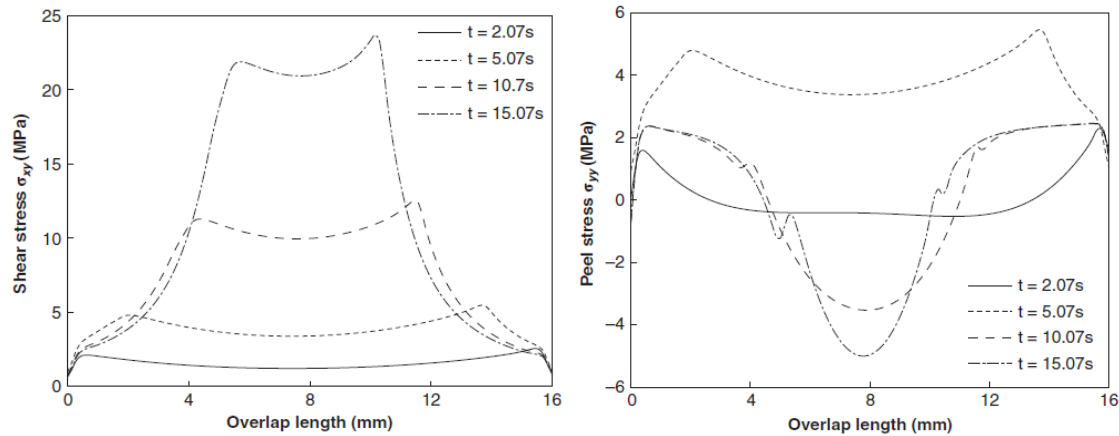
Fig. 2.3.3: Shear and Peel stress distributions along overlap length at different times.

2.3.2. Mechanical response of functionally graded Ti₂Al/Al rectangular plate with pre-existing micro-damage.

A micromechanics based unit cell model for interpenetrating phase composite, see in Fig. 2.3.4(a), is used in obtaining the effective elastic moduli along the graded direction of Ti$_2$Al/Al rectangular plate. The predicted elastic moduli are plotted in Fig. 2.3.4(b). Through thickness distributions of axial and transverse stresses of Ti$_2$Al/Al plate for various void volume fractions

69

obtained from FE analysis are shown in Fig. 2.3.5. It can be seen that the through thickness distributions of axial stress become slightly smaller with rising void volume fraction while the transverse shear stress altered significantly in the middle and lower part of plate in thickness direction for different void volume fractions.

(a)   (b)
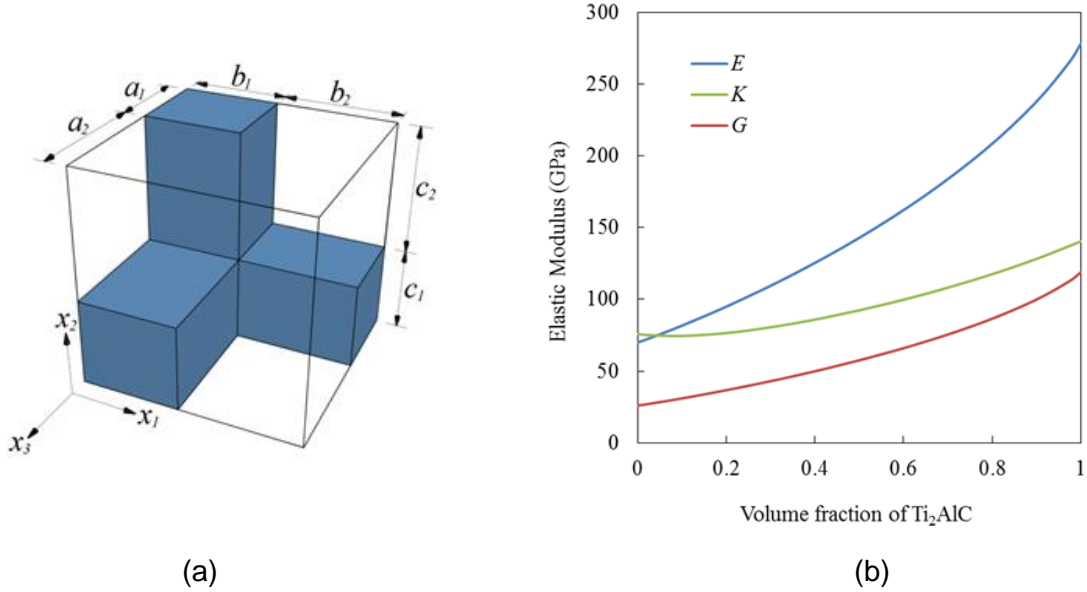
Fig. 2.3.4: (a) Unit cell method for two-phase interpenetrating phase composites. (b) Effective elastic moduli of Ti₂AlC/Al composite with varied volume fraction of Ti₂AlC obtained from unit cell method.
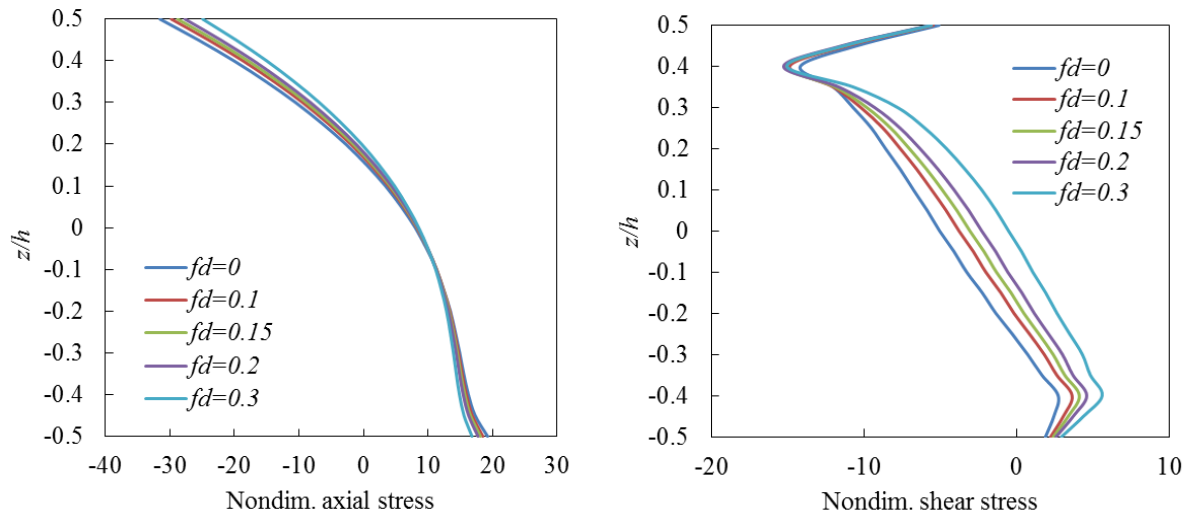
Fig. 2.3.5: Through-thickness distributions of non-dimensional axial stress (at x=a/2, y= a/2) and non-dimensional transvers shear stress (at x=a/2, y=0) of the graded Ti₂AlC/Al plate for various voids volume fraction values.

2.3.2 Temperature-dependent thermal properties of a SMA/MAX phase interpenetrating phase composite with porosity.

Detailed 3D Represented Volume Elements (RVEs) are created based on microstructures of the given composite. The effective thermal properties are predicted using finite element method. The effect of existence of porosity and interfacial reaction layer for SMA/MAX phase composite was investigated. Fig. 2.3.6 contains the plots of 3D RVEs created for SMA/MAX phase composite with porosity and/or interface. Fig. 2.3.7(a) shows a comparison between simulation and experimental results for both configuration A and B. For configuration A, the numerical simulation overestimates the effective thermal conductivity by 9-19% against measured data. The discrepancy indicates that the presence of interfaces, besides porosity, plays an important role in the thermal transport within the composite. Using configuration B, the predicted effective thermal conductivity of the interfaces is of 0.3-1.0Wm^{-1}K^{-1} for the temperature range 300-600K. Following the same procedure, the thermal conductivity of the interfaces in bilayer samples are also predicted and the results are very close to that of the composite, see in Fig. 2.3.7(b) which validates the computational framework developed in this study.
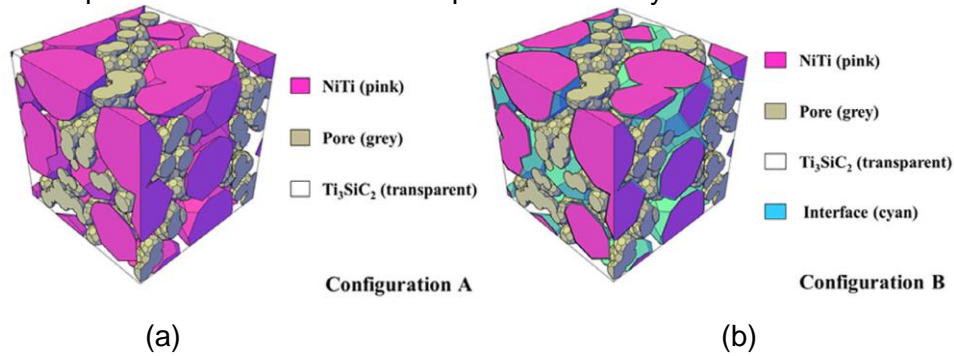
Fig. 2.3.6: 3-D RVEs of the NiTi/Ti$_3$SiC$_2$ composite: (a) in configuration A, grey represents pore,pink NiTi, and transparent Ti$_3$SiC$_2$; (b) in configuration B, grey represents pore, pink NiTi, transparent Ti$_3$SiC$_2$, and cyan interface.
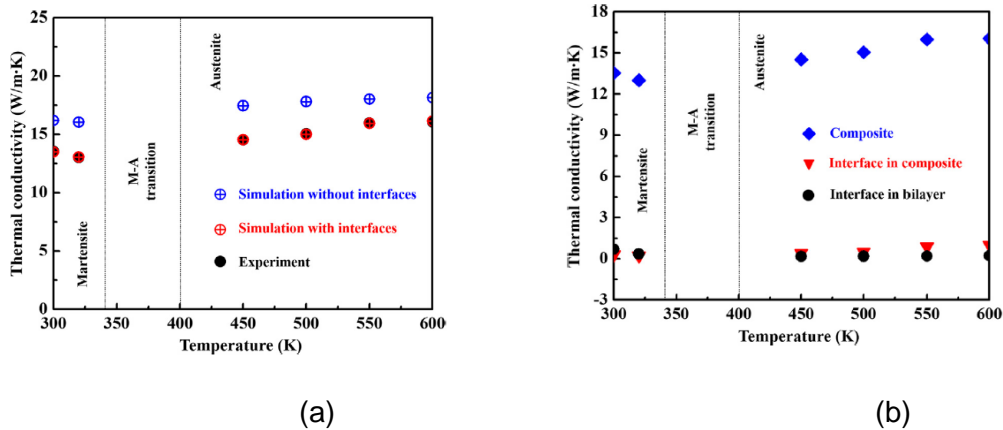
Fig. 2.3.7: Temperature-dependent thermal conductivity of the NiTi/Ti$_3$SiC$_2$ composite: (a) comparison between experiment and simulation results, (b) comparison between FE predicted thermal conductivity of interface in the composite and FE predicted thermal conductivity of interface in the bilayer.

71

2.3.3 Plastic-damage Behavior of Porous MAX phase with Aligned Ellipsoid-like Pores under Uniaxial Compression.

Micromechanics based representative element volume (RVE) and finite element (FE) method are adopted in modeling porous Ti_2AlC. A damage-plasticity coupled constitutive model considering different tensile and compressive behaviors is used in modeling the inelastic behavior of porous Ti_2AlC under uniaxial compression. Overall the given porous Ti_2AlC system fails in a quasi-brittle manner under uniaxial compressive as a result of combined effect induced by the local tensile and compressive damage accumulation. That is the stress-strain curve has the reversed narrow "V" shape, see in Fig. 2.3.9. The effects of loading direction and porosity volume fraction on compressive behavior of the porous Ti_2AlC systems are also investigated. Since the given porous MAX phase is transversely isotropic due to the ellipsoid-like shape of the aligned pores, the material system can sustain more loads in transverse directions (x-, and y-direction) than in longitudinal direction (z-direction), see in Fig. 2.3.9(a). It is shown in Fig. 2.3.9(b) that with porosity decreasing from 32.8% to 40.5%, the compressive strength of porous Ti_2AlC in longitudinal direction increases approximately 51%.

(a)   (b)   (c)
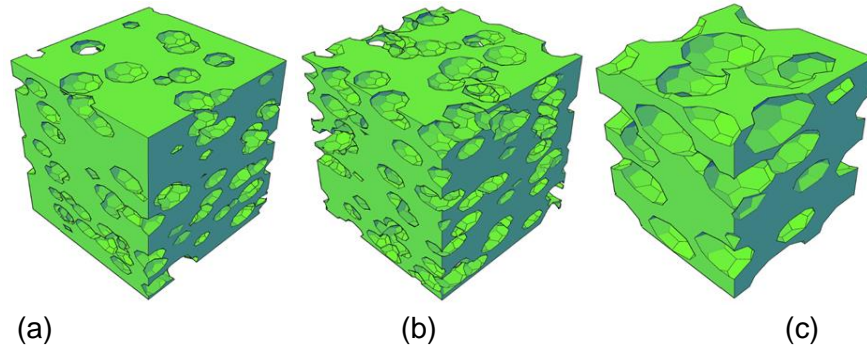
Fig. 2.3.8 RVEs (1000×1000×1000µm3) for (a) pore size 170-250µm, porosity volume fraction 32.8%, (b) pore size 170-250µm, porosity volume fraction 40.5%, (c) pore size 340-500µm, porosity volume fraction 33.5%.
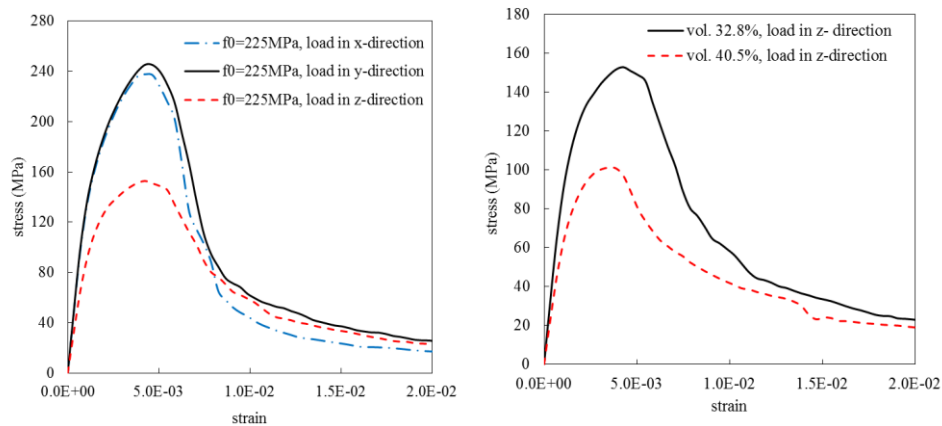
Fig. 2.3.9 (a) Stress-strain relation of porous Ti_2AlC with 32.8% vol. aligned 170-250µm ellipsoid-like pores for the cases: initial yield stress = 225MPa with load in y- and z-direction, (b) Stress-strain relation of porous Ti_2AlC with 32.8% vol. and 40.5% vol. aligned 170-250µm ellipsoid-like pores for the case: initial yield stress=225MPa with compressive load in longitudinal direction (z-direction);

The failure mechanism is successfully identified through implementation of Cicekli type constitutive model in the sophisticated 3D FE model. For damage evolution process, it is shown in Fig. 2.3.10 that initially the tensile damage occurs randomly in the porous Ti_2AlC at low strain

72

level. As strain level increases, the local damage accumulates and starts to form small cracks. Further, these small cracks grow, coalesce and become larger cracks. Also, it can be seen in Fig. 2.3.10 and Fig. 2.3.11 that at $\varepsilon = 1.0E\text{-}1$, considerable part of the given porous Ti$_2$AlC experiences tensile failure (i.e. tensile damage density approaches 1.0); whereas there is only small part of the porous system fails due to compressive failure. Therefore, it can be concluded that the damage mechanism of porous Ti$_2$AlC is dominated by localized tensile damage.
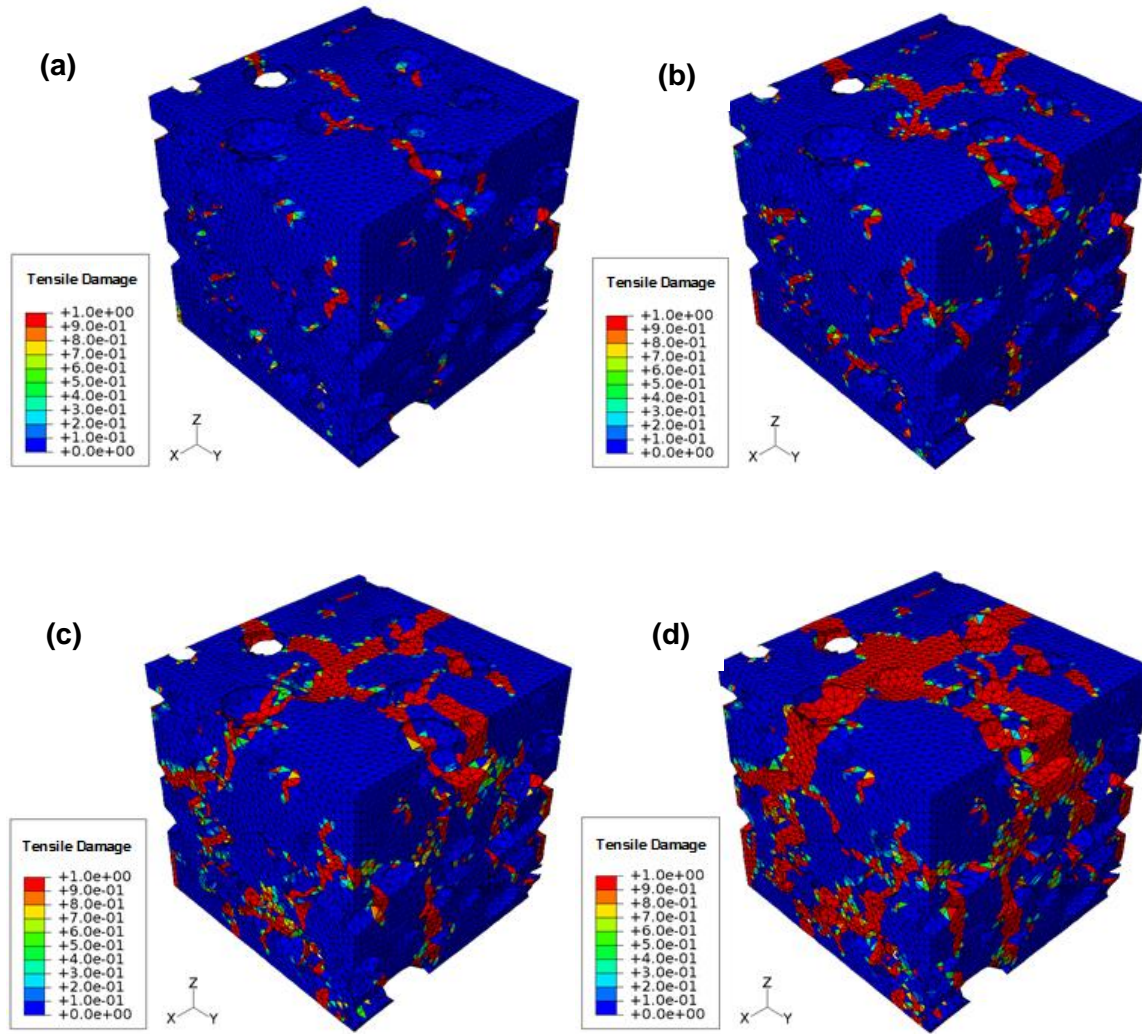
Fig. 2.3.10: Tensile damage density for porous Ti$_2$AlC with 32.8 vol. % aligned 170-250µm ellipsoid-like pores ($f_0^+ = f_0^- = 225$MPa case) with compressive load in z-direction at different strain level: (a) $\varepsilon = 3.0E\text{-}2$, (b) $\varepsilon = 5.0E\text{-}2$, (c) $\varepsilon = 7.0E\text{-}2$, (d) $\varepsilon = 1.0E\text{-}1$.

73
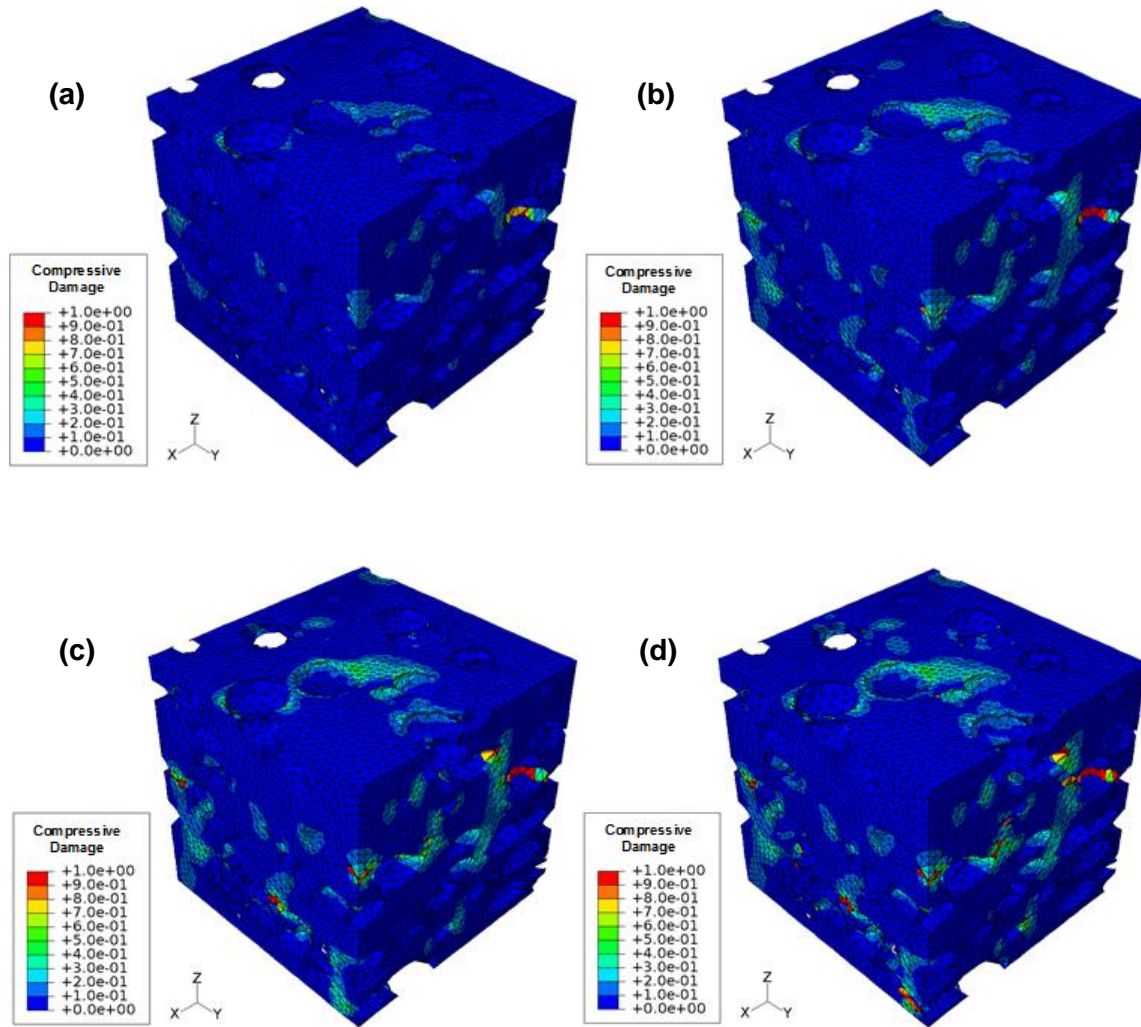
Fig. 2.3.11: Compressive damage density for porous Ti₂AlC with 32.8 vol. % aligned 170-250μm ellipsoid-like pores ($f_0^+ = f_0^- = 225$ MPa case) with compressive load in z-direction at different strain level: (a) $\varepsilon = 3.0$E-2, (b) $\varepsilon = 5.0$E-2, (c) $\varepsilon = 7.0$E-2, (d) $\varepsilon = 1.0$E-1.

2.3.4 Interface Design and Characterization: Prediction of Interface Properties in a Double Cantilever Beam.

Interface strength in a double cantilever beam (DCB) [T650 PMC and T300 PMC-Ti specimens; see Fig. 2.3.12] is investigated by using a potential based cohesive zone model (CZM), which is implemented through a user-element (UEL) in ABAQUS. The results of specimens analyzed are in good agreement with the test results (results here are given for T650 PMC). Fracture energy is identified using delamination resistance curves obtained by DCB tests (Fig. 2.3.13). Non- fuzzy and fuzzy DCB specimens test results are obtained by the applied cohesive zone model and interface strength is predicted (see Figs. 2.3.14 and 2.3.15). It is found to be ~60 MPa and ~100MPa for non-fuzzy and fuzzy interfaces, respectively.

74
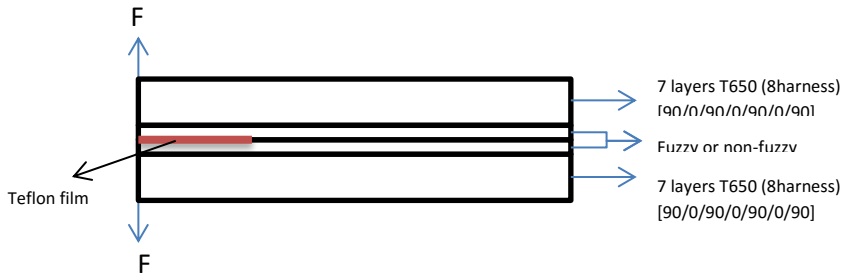
Fig. 2.3.12: Example schematic of a DCB specimen
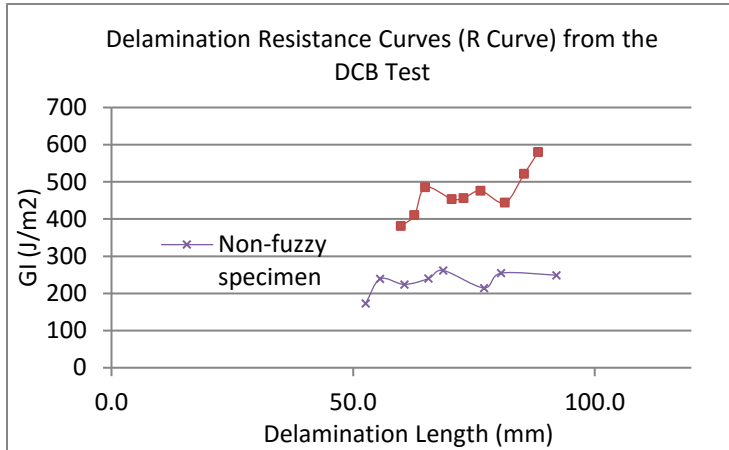
Fig. 2.3.13: Delamination resistance curves (R Curve) from DCB tests
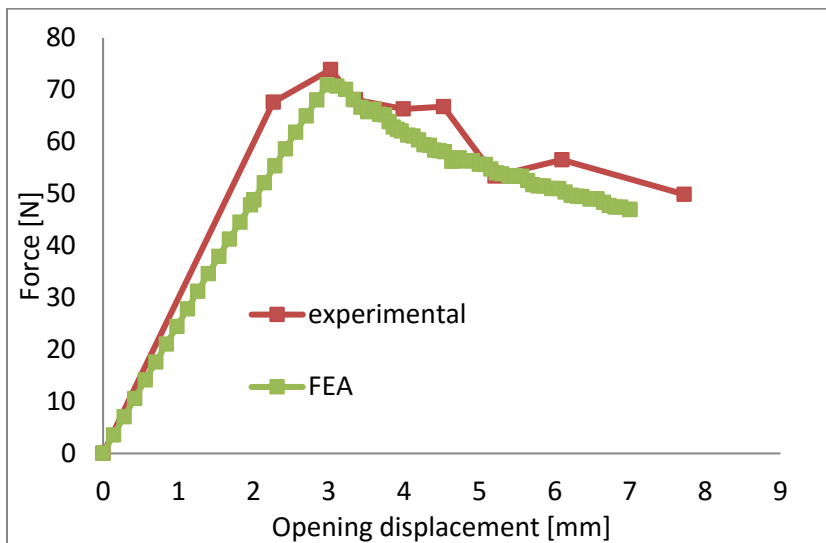
Fig. 2.3.14: Force vs. displacement curves for a non-fuzzy specimen
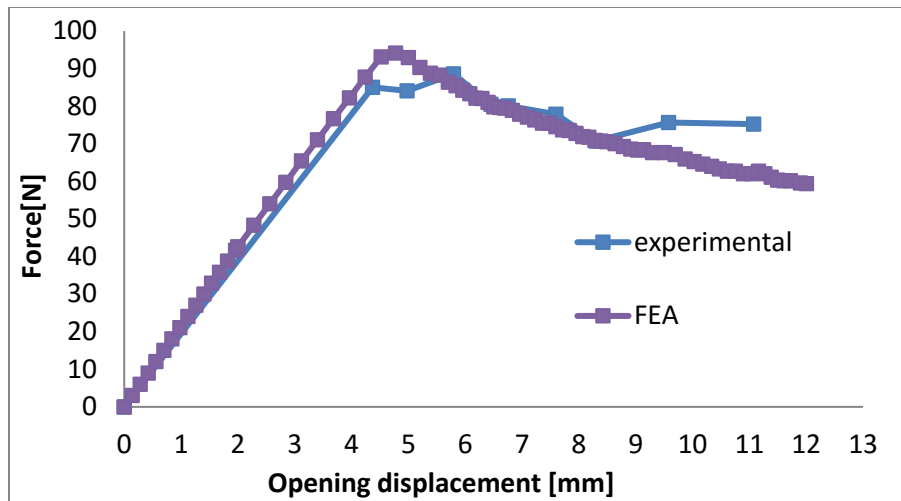
Fig. 2.3.15: Force versus displacement curves for a fuzzy specimen

2.3.5 Shell finite element for nonlinear analysis of laminated composite and functionally graded plate and shell structures

Shells constitute some of the most prevalent and significant of structural components employed in engineering design and, therefore, efficient and accurate procedures for their numerical simulation are of great importance. Robust algorithms are particularly crucial, as shells are widely recognized as the prima donnas of structures due to the fact that small changes in geometry and loading can culminate in large changes in the mechanical response. In this research we developed and numerically implemented an improved first-order shear deformation continuum shell finite element formulation for use in the analysis of the fully geometrically nonlinear mechanical response of thin and thick isotropic, composite, and functionally graded elastic shell structures. We adopted a seven-parameter formulation which naturally circumvents the need for a rotation tensor in the kinematical description and allows us to use fully three-dimensional constitutive equations in the numerical implementation. Also, we have utilized high-order spectral/hp type quadrilateral finite element technology in a purely displacement-based finite element setting which naturally allows us to obtain: (1) highly accurate approximations of arbitrary shell geometries and (2) reliable numerical results that are completely locking-free. In the computer implementation, the Schur complement method is adopted at the element level to statically condense out all degrees of freedom interior to each element in a given finite element discretization. This procedure vastly improves computer memory requirements in the numerical implementation of the resulting shell element and allows for significant parallelization of the global solver. The use of spectral/hp finite element technology provides an efficient mechanism for reducing errors associated with the isoparametric approximation of arbitrary shell geometries and no solution stabilization techniques are required (e.g., reduced integration, assumed natural or enhanced assumed strains, mixed interpolation, etc.). The formulation permits the use of skewed and/or arbitrarily curved elements in the actual finite element discretization. Numerical results are obtained for a variety of non-trivial finite deformation elastic benchmark problems taken from the literature to demonstrate the overall robustness of the shell finite element developed. Typical results are included in Figures 2.3.16-2.3.20. As a first example, we examine the mechanical response of a cylindrical, roof-like panel, subjected to a point force P at the apex (see Fig. 2.3.16). This is especially a popular problem on account of the snap-through behavior it exhibits. In the present example Isotropic, composite, and FGM shell panels are investigated.

76
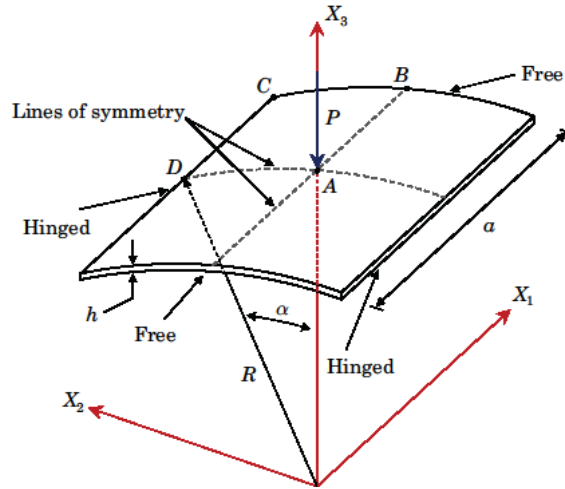
Fig. 2.3.16: Geometry of a cylindrical shell panel.

In Figures 2.3.17 and 2.3.18 we trace the center deflections vs. P for the isotropic and laminated composite panels for the cases where $h = 12.7$mm and $h = 6.35$ mm. Each numerical simulation has been conducted using the cylindrical arc-length method. The results are in excellent agreement with the tabulated values found in the literature for isotropic shells. It is evident that decreasing the shell thickness greatly increases the complexity of the equilibrium path associated with the arc-length based numerical solution. For example, we observe from Fig. 2.3.18 that laminates (0°/90°/0°), (-45°/45°/-45°/45°) and (30°/-60°/-60°/30°) exhibit highly involved equilibrium paths when shell is thin (i.e., $h = 6.35$ mm). Numerical results for metal-ceramic functionally graded panels, for the case where $h = 12.7$ mm are shown in Fig. 2.3.19. The metal (aluminum) is taken as the material at the bottom surface and the ceramic (zirconia) as the material at the top surface of the shell panel. The following properties are used:

$$E^{\text{bot}} = 70\,\text{Gpa}, \quad k^{\text{bot}} = 204\,\text{W/mK}, \quad a^{\text{bot}} = 23' \, 10^{-6}/\,^0\text{C}, \quad n^{\text{bot}} = 0.3$$

$$E^{\text{top}} = 151\,\text{Gpa}, \quad k^{\text{top}} = 2.09\,\text{W/mK}, \quad a^{\text{top}} = 10' \, 10^{-6}/\,^0\text{C}, \quad n^{\text{top}} = 0.3$$
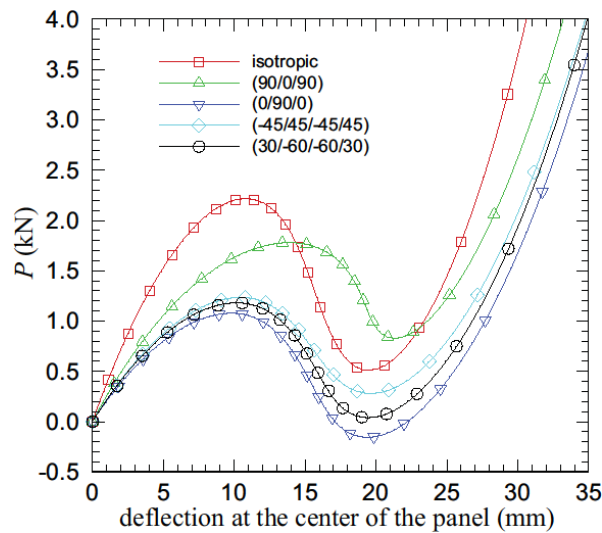
Fig. 2.3.17: Vertical deflection of an isotropic and laminated composite shallow cylindrical panels under point load (cases shown are for h = 12.7mm).

77
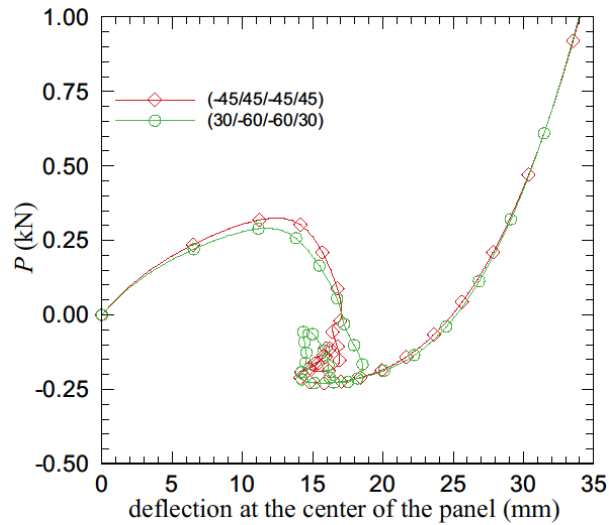
Fig. 2.3.18: Vertical deflection of an isotropic and a laminated composite shallow cylindrical panel under point load (cases shown are for h = 6.35 mm).
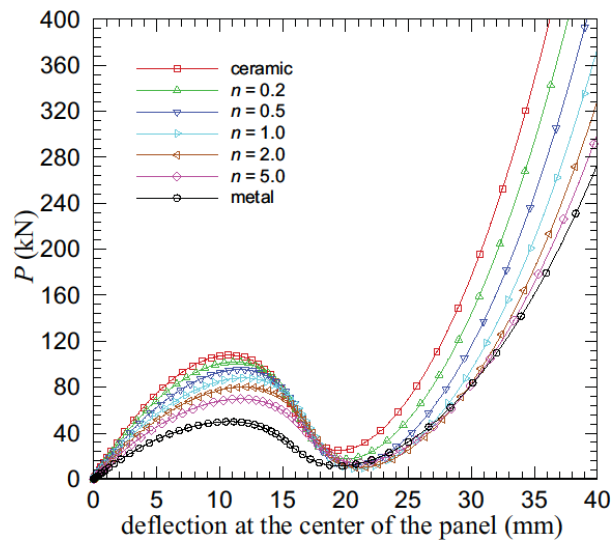
Fig. 2.3.19: Vertical deflection of functionally graded metal-ceramic shallow cylindrical panels under point load (cases shown are for h = 12.7mm).

The second example deals with a FGM shell panel (geometry is the same as that shown in Fig. 2.3.16) subjected to only mechanical load (as before) and mechanical and thermal loads (a temperature difference on two sides of the shell is specified). The top surface is ceramic and bottom is aluminum with the properties given earlier. The top and bottom faces are have specified temperatures as follows $T^{\text{bot}} = 293\text{K}$ and $T^{\text{top}} = 393\text{K}$. The material properties of two-constituent FGM are based on the power-law (with index n). Fig. 2.3.20 shows load-deflection curves for the problem. In the case of thermal load, there is a clear indication of thermal buckling.

78

In the coming months, thermal buckling a three-material FGM shell will be investigated using the material properties provided by the materials group.
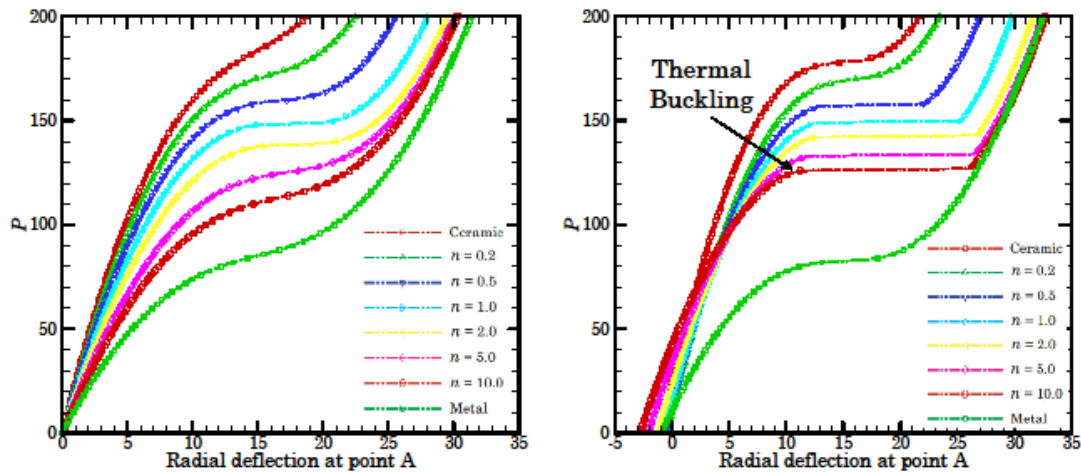
Fig. 2.3.20: Radial deflections at the apex vs. force P (a) Pure mechanical load and (b) Under combined mechanical and thermal load.

2.4 MULTISCALE CHARACTERIZATION OF FGHCS - DETERMINATION OF MODULUS AND DAMPING PARAMETERS OF FGHCS

RESEARCH TEAM MEMBERS
PIs: Daniel J. Inman
Post Doctoral Students: Cassio Faria, Ya Wang,
Graduate Students: Mohamad Bonakdar, Nick Konchuba
Undergraduate Students: Heloise Lephay, Matthias Petitdemange,

COLLABORATORs:
Dr. Gary Seidel (Virginia Tech), Dr. Scott White (University of Illinois), Dr. Nancy Sottas (University of Illinois), J N Reddy (Texas A&M), Fu-Kuo Chang (Stanford), Nakhiah Goulbourne (University of Michigan).

OBJECTIVES:

(viii) First objective: Understand the dynamic characteristics (effective modulus and damping properties) and their effect on vibration response of Ti_2AIC,
(ix) Determination of impact damage by a Structural Health Monitoring method.
(x) Second objective: Understand the dynamic characteristics (effective modulus and damping properties) of hybrid composites and their effect in vibration response.
(xi) Third objective: Develop a surrogate model of the layered FGHC system and understand its dynamic response and determine its vibration properties.
(xii) Fourth Objective: Investigate the effects of fluid filled vascular channels on damping properties of the surrogate model
(xiii) Fifth Objective: Experimentally validate all theoretical, modeling and numerical results of i-iv.

TECHNICAL ACCOMPLISHMENTS

2.4.1 Vibration Properties of Ti₂AIC

A sample of Ti_2ACI was purchased and tested for its modulus and damping using the "Oberst Beam Method". Figure 2.4.1 shows the testing set up. The method involved comparing a known beam to an unknown material, in this case Ti_2AIC. The plain aluminum beam is measured for comparison with an identical aluminum beam epoxied to the Ti_2AIC sample.
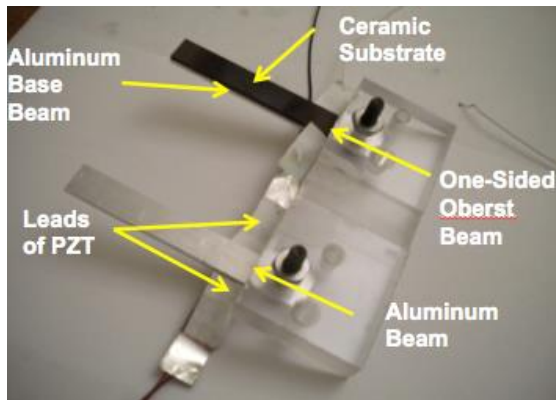
Figure 2.4.1: The experimental set up for measuring damping properties of an unknown material, in this case Ti₂AIC, mounted on an identical beam.

The results show clearly that Ti_2AC has twice the damping of plain aluminum. The change in modulus also caused the first natural frequency to shift. Comparing to a theoretical analysis based on layered beam theory, the frequencies agree to within 0.7% and the damping ratio agrees to within 12%. More advanced methods of measuring the damping are used in the out years.

2.4.2. Vibration Properties Damping of FGHC

Based on the experiments do in the first year, it's apparent that the damping measurements contain hysteresis. Hence an internal variable method is employed to model and measure the damping. For our initial efforts we used a 3 layer beam consisting of aluminum with a viscoelastic layer. These methods once validated with experimental data are then use in later years to examine the surrogate multilayer beam. Figure 2.4.2 illustrates the success of our modeling efforts and its ability to successfully predict the loss and storage modulus (not shown).
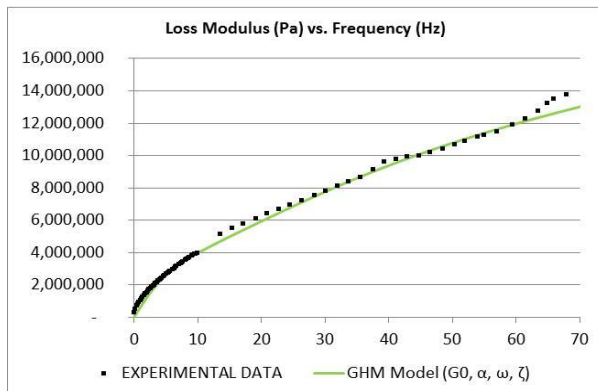
Figure 2.4.2: A comparison of theory and experimental data for using the internal variable method of modeling viscoelastic hysteresis.

The mathematical details of the modeling require adding degrees of freedom to the model to account for the hysteresis induced by the viscoelastic behavior. These details can be found in the published papers listed below and in previous reports.

2.4.3 Surrogate Model Development

Figure 2.4.3 illustrates the configuration of the constrained layer surrogate model of the FGHC sandwich beam being used in our modeling and experimental validation efforts. There are

five component layers: a oxide ceramic outer layer capable of withstanding high temperatures, a functionally graded ceramic layer combining shape memory alloy (SMA) properties of NiTi together with Ti_2AlC (called Graded Ceramic/Metal Composite, or GCMeC), a high temperature sensor patch, followed by a polymer matrix composite (PMC) laced with vascular cooling channels all held together with various epoxies, and then a layer of a piezoelectric actuator. Matrices and vectors associated with each layer are denoted with subscripts c, v, s, b and p, respectively. Nodes in the cross section are denoted using the global coordinate system located at the center of the left end of the base beam, and relative coordinate systems located at the bottom of each constraint, viscoelastic, sensor base and piezoelectric actuator layer.
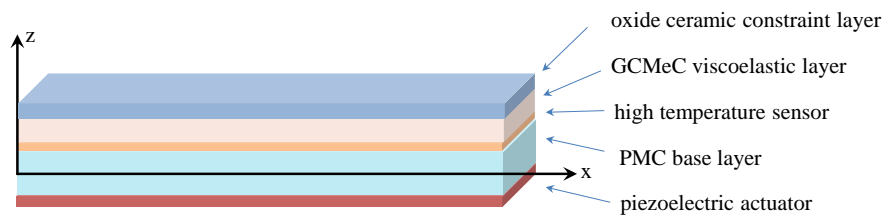
Figure 2.4.3: The surrogate model used to emulate the FGHC dynamically scaled and made with 3D printing.

One discovery made here is the great difference between a static modulus measured in a traditional DTM and modulus and damping measure dynamically in structure sized tests. These differ and Figure 2.4.4 shows the agreement between a measured frequency response function and a numerical simulation using GHM based on a dynamic measurement of the modulus.
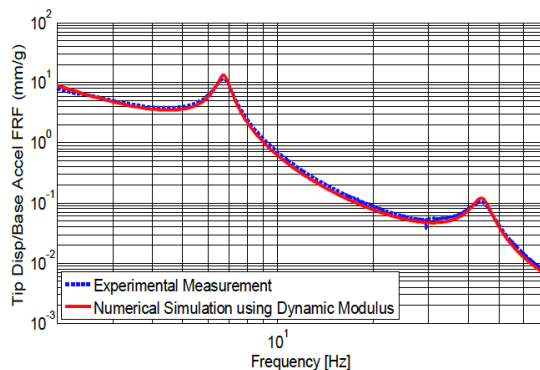
Figure 2.4.4: A comparison between the frequency response function (FRF) measured experimentally and a FRF computed via our modeling, showing excellent agreement.

2.4.4 Damping Effects of Vascular Channels

The vascular channels have the potential to add damping to the FGHC structure. Damping to due flow in a pipe has been studied, however damping due to flow through a channel embedded in a solid has not previously been considered. A multifunctional structure with vascular channels and investigate how the fluid in the channels provides damping to the system. While the vibration and stability of flow through a pipe has been extensively examined, internal fluid induced passive damping has not been well investigated in literature. Motivated by research in using vascular channels to provide self-cooling and autonomous healing of multifunctional composites, here we investigate the material and mechanical parameter dependence effects of internal fluid damping using an experimental study, modeling and numerical analysis of the dynamics of flexible

81

cantilever beam conveying three types of internal vascular fluid flows. Figure 2.4.5 illustrates the system under consideration.
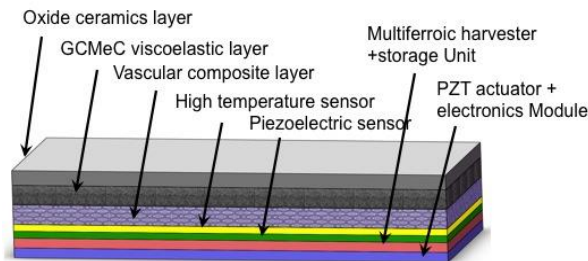
Figure 2.4.5: Surrogate with Vascular Channels used to investigate the damping properties over a range of temperatures and frequencies.

Figure 2.4.6 summarizes the results in tabular form. Basically temperature and frequency are modeled using the internal variable method described in years 1 and 2. The model agrees well with the theoretical/numerical predictions. The table shows how well the model predicts experimental data for various fluids of different viscosity (sCt).

Beam	Channel	Mode	Damping ratio		
			Theory	Experiment	Error (%)
Beam A	Empty	First mode	0.0312	0.0312	0.00
		Second mode	0.0236	0.0226	-4.42
	Filled with Silicone 10,000 cSt	First mode	0.0338	0.0339	0.29
		Second mode	0.0243	0.0242	-0.41
Beam B	Empty	First mode	0.0322	0.0320	-0.62
		Second mode	0.0217	0.0216	-0.46
	Filled with Silicone 30,000 cSt	First mode	0.0351	0.0351	0.01
		Second mode	0.0246	0.0240	-2.5
Beam C	Empty	First mode	0.0280	0.0279	-0.36
		Second mode	0.0200	0.0201	0.5
	Filled with Silicone 100,000 cSt	First mode	0.0324	0.0326	0.61
		Second mode	0.0230	0.0226	-1.7

Table 2.4.1. The effect of increasing viscosity (from low to high moving from top to bottom) and the agreement between theory and measured values.

The increasing effectiveness of damping is addressed by investigating the material and mechanical parameter dependence of internal fluid damping using experimental study, modeling and numerical analysis of dynamics of flexible cantilever beams conveying three types of internal vascular fluid flows. Details can be found in the journal and conference papers referenced below

.

82
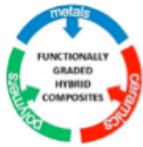
2.5 Aeroelastic Modeling of Functionally Graded Hybrid Composites

RESEARCH TEAM MEMBERS

Texas A&M University
Graduate Students: Robert Brown and Keith Ballard
Collaborators: Prof. John Whitcomb

RESEARCH

The work on the aerothermoelastic modeling for the evaluation of functionally graded hybrid composites (FGHC) during the fourth year was focused on the following topics: (i) expanding the simulations using the coupled aerodynamic and thermal structural solvers, (ii) assessing the aerothermoelastic response of a representative fin subjected to high temperatures caused by hypersonic flow at various Mach numbers, altitudes, and cooling profiles, and (iii) increasing the parallelization potential of the aerodynamic and coupled solvers.

OBJECTIVES

The objectives of this period consisted of: (1) the simulation of the hypersonic airfoil using more efficient and realistic cooling profiles, (2) the simulation of a typical hypersonic fin geometry subjected to hypersonic flow conditions and allowed to respond to forces and heat loads based on structural parameters, material properties, and imposed cooling profile, and (3) the improvement in simulation speed by updating the parallelization methodology in the aerodynamic solver.

TECHNICAL ACCOMPLISHMENTS

2.5.1 Extension of simulation regime for aerothermal response to hypersonic loading

Last year, a number of runs had been completed using only the aerodynamic solver to determine an appropriate flight regime for further analysis. Simulations using the coupled aerodynamic and thermal solvers were in preliminary stages, and only cases with simple applied heat flux profiles had been performed.

These results have been augmented by coupled aerodynamic-thermal analyses performed at a speed of Mach 5 at an altitude of 45 km and at a speed of Mach 8 at an altitude of 25 km with several chordwise-position-dependent cooling distributions on the interior of the airfoil. Augmented cooling near the leading edge was needed to adequately cool the entire airfoil, but created large chordwise temperature gradients. Cooling with chordwise constant heat flux is inefficient because of the localized high temperature at the leading edge. Simultaneous reduction of both the maximum temperature and the temperature gradient requires further optimization studies.

2.5.2 Upgrade of parallelization and coupling methodology

As the size of the computational domain increases due to simulation of the full three-dimensional fin, there is a much larger potential for simulation speedup through the use of parallelization on large computing clusters. For this reason, the flow solver was parallelized using

a domain decomposition paradigm, allowing more than an order of magnitude reduction in simulation times.

This modification also required a change in the coupling implementation from shared memory, which has limited utility on large supercomputing clusters, to the Message Passing Interface (MPI) paradigm. This paradigm has support on all large parallel computers, and allows for much more straightforward usage.
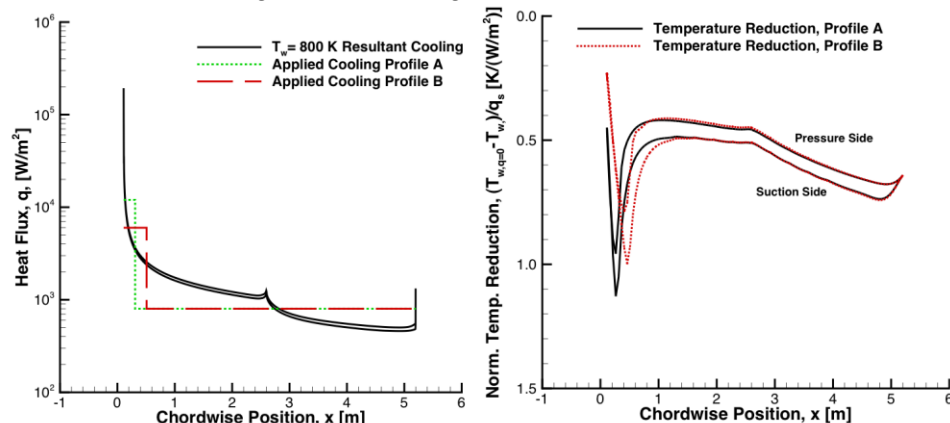

Figure 2.5.1: Chordwise variation of: (a) two applied heat flux profiles, A and B, compared to the cooling required to maintain a constant temperature of 800 K, (b) normalized temperature reduction due to the two applied heat flux profiles at Mach 5 and 45 km
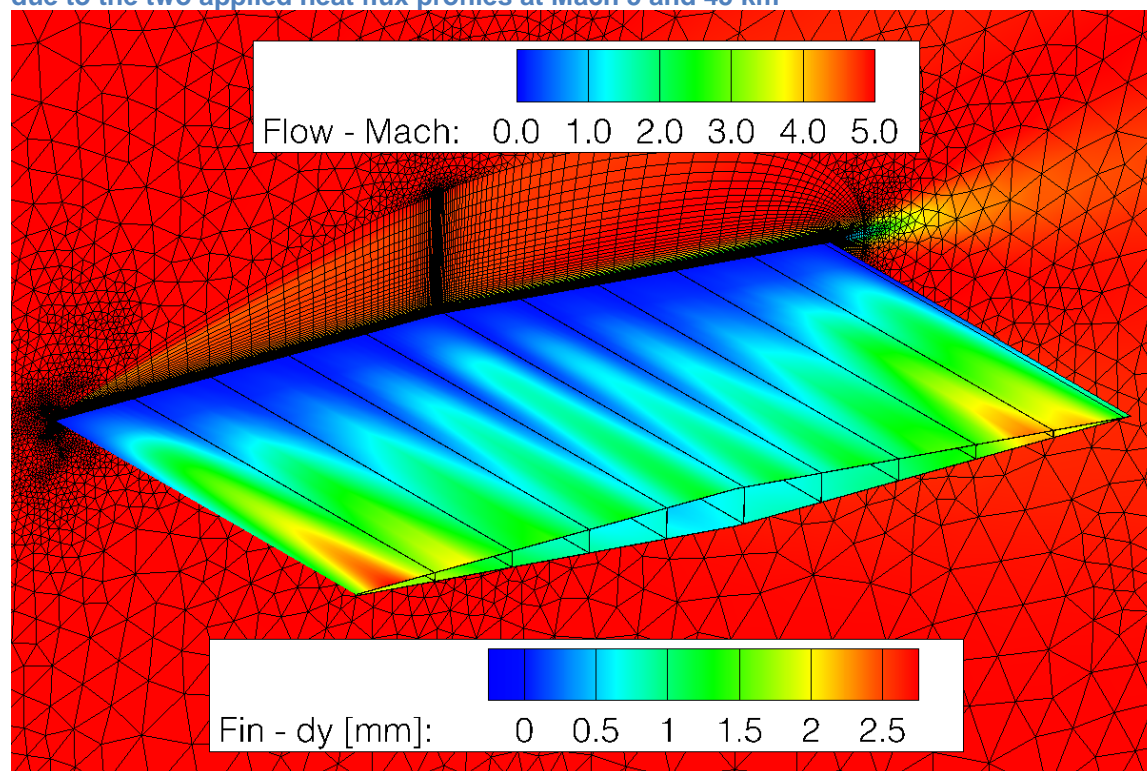
Figure 2.5.2: Contour plot of the steady-state y-displacement of the fin due to aerodynamic loading and the Mach number of the surrounding flow. Simulation was performed at Mach 5 and an altitude of 45 km.

82

2.5.3 Prediction of transient dynamic and thermal response to hypersonic loading

Last year, we had used the coupled aerodynamic and structural codes to simulate the steady-state behavior of the thermal response to hypersonic loading. We have now focused on the dynamic aerothermoelastic response to forces and heat loads experienced at high Mach numbers. Simulations have been completed for a limited number of cases using coupling between aerodynamic and a structural elastic solver. These cases represent the aeroelastic response for a structure that has sufficient cooling to maintain a constant wall temperature, and therefore has no adverse effects due to thermal expansion or material property degradation.

3 RESEARCH THRUST: IN SITU NDE/SHM
3.1 FUZZY FIBER SENSOR DEVELOPMENT

RESEARCH TEAM MEMBERS
PI_Institution : Khalid Lafdi, University of Dayton
Graduate Students: M. Chao, M. Boehle, O. Memon, H. Muneaki, Q. Jiang
Undergraduate Students: P. Bianca, I. Lenfant, D. salomon, L. Funke
Collaborators: Drs. O. Oohoa , G. Seidel, and C. Fu-Kuo (MURI) and NDE branch, AFRL/RXLP, Charles Buynak and Eric Lindgren

OBJECTIVE(S)
Growth of carbon nanotubes as fuzzy surface to
(i) Use of fuzzy fibers as SHM sensor.
(ii) Reduce thermal interface and
(iii) Increase structural properties of PMC composites.

TECHNICAL ACCOMPLISHMENTS
Growth of carbon nanotubes on fiber surface and use (1) As a strain sensor (collaboration with Dr. C. Fu-Kuo and C. Buynak and E. Lindgren, NDE branch, AFRL/RXLP). (2) To enhance fracture toughness (Collaboration with Dr. O. Ochoa). However, the aligned nanotubes on Ti surface were proven to be great thermal interface in which it reduces the contact resistance between two surfaces (Collaboration with Dr. O. Ochoa). (3) May enhance the overall sensing and mechanical properties of the fuzzy fibers (Collaboration with G. Seidel and Dr. C. Fu-Kuo).

TECHNICAL ACCOMPLISHMENTS
3.1.1 Use of the fuzzy as a strain sensor
The efforts presented here highlight the feasibility of incorporating carbon nanomaterials into structural composites as sensors. Carbon nanotube (CNT) covered fiberglass has been shown to be a viable alternative to conventional metal foil strain gages. The fuzzy fiber sensors (Figure 3.1.1), created using a conventional chemical vapor deposition process, exhibit similar sensitivity to metal foil strain gages and are more easily integrated into composite structures as the sensor itself is a composite. The fuzzy fiber strain gages can be used to sense strain within composite structures and can be readily integrated into the structural laminate to provide sensing over large sections and in locations not accessible to conventional strain gaging techniques. The unique properties of the CNT covered fuzzy fiber lends itself to application in a wide range of sensing tasks within a structural composite including strain, temperature, degradation, etc.

The fabricated and machined specimen is shown in Figure 3.1.2. Figure 3.1.3 shows the specimen loaded into the hydraulic test machine used for testing.
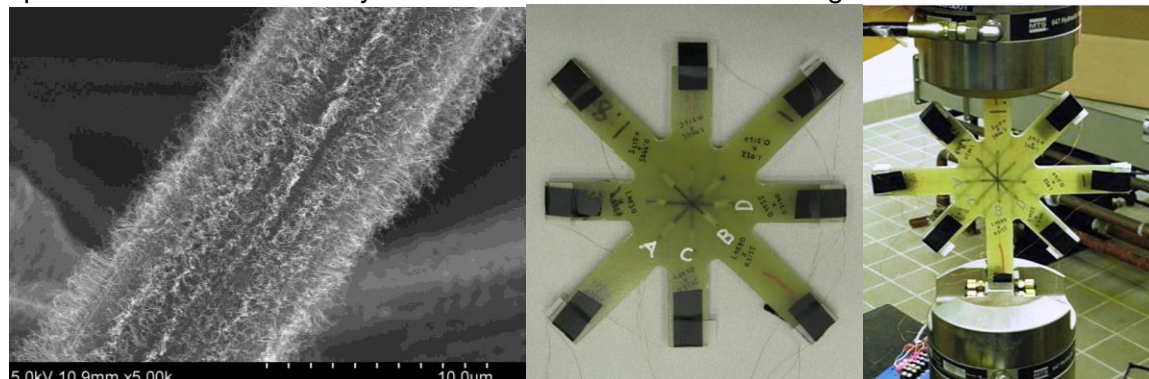

Figure 3.1.1. SEM micrograph of low density CNT growth on glass fiber. Figure 3.1.2. Sensor-orientation specimen. Figure 3.1.3. Specimen loaded into test machine.

The sensors were monitored with a Wheatstone bridge, much the same as a commercial strain gage. Figure 3.1.4 shows the data from one test, where the specimen was loaded along axis "A". The sensor aligned with the loading had the highest response, the sensor at 45° to the loading had a lower positive response, and the sensor at 90° to the loading showed a negative response because of Poisson effects. Due to the lack of a reference strain measurement, the magnitude of these sensitivities cannot be compared directly with results from previous sensors.
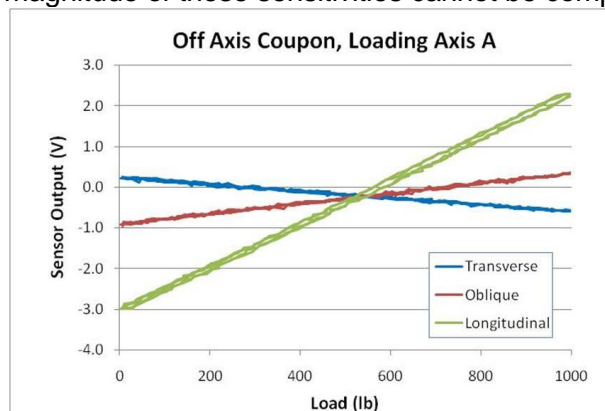
Figure 3.1.4. Typical off-axis sensor response.
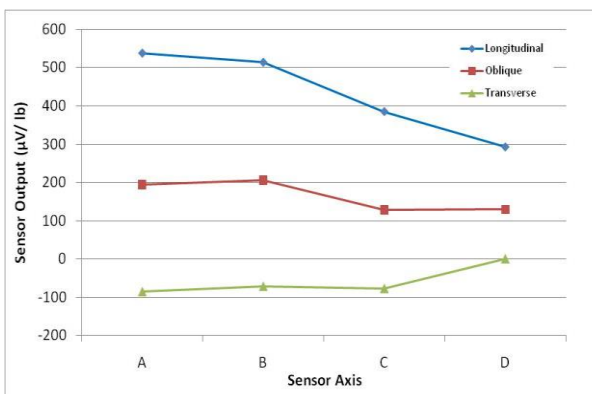
Figure 3.1.5. Off-axis sensitivity data.

Figure 3.1.5 is a compilation of the sensitivity results from all tests on this specimen, with each data point representing the average of six, twelve, or twenty-four tests, depending on the sensor and the sensing mode. Data from all sensors was recorded with loading along all axes. In every case, the strongest response was in the longitudinal mode, followed by the oblique mode, and, finally, by the transverse mode, which was negative (or zero for sensor D). These tests confirmed the behavior or the fuzzy fiber sensors in an orthotropic composite.

A finite element model was constructed to corroborate the experimental data. Abaqus/CAE was used to construct the model, which is shown in Figure 3.1.6. Due to limitations on the number of elements the model could contain, only half of the thickness of the specimen was modeled. The boundary conditions and material properties were set to mimic those of the experimental test. As is evident from the model in Figure 3.1.6, the six legs of the specimen which are not loaded are under very little stress. In order to simplify the model and refine the mesh near the sensors, the model was trimmed to focus on the part of the model where the stresses were highest. Figure
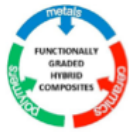
84

3.1.7 shows this modified model with inactive arms removed and a fine mesh around the sensor areas.
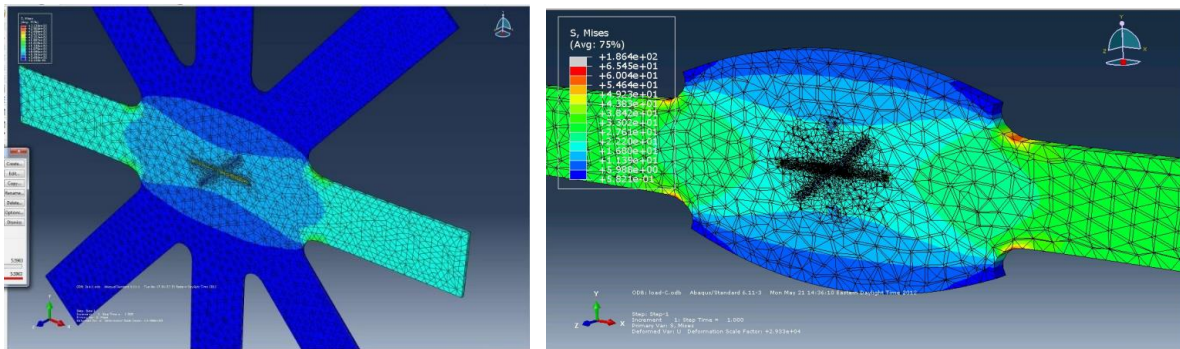

Figure 3.1.6. Finite element model of "star specimen". Figure 3.1.7. Refined finite element model with inactive areas omitted and refined mesh around sensor locations.

The exact mechanism for the strain sensitivity of the fuzzy fiber is not known, however previous tests have shown that the change in resistance is linearly related to strain. Data was extracted from the finite element analysis in order to obtain the strain along the fiber in the model. Using this strain data and previous results, the expected resistance change and Wheatstone bridge output for the model were calculated. Figure 3.1.8 shows the results of a single cycle mechanical test, and the corresponding test computing using the finite element model. The model prediction of longitudinal sensor output matches nearly perfectly with the mechanical test results. The transverse and off-axis tests follow the correct trends; however the magnitude of the output does not match well with the experimental data.

The model is currently being enhanced to account for shear sensitivity, which would correct the small error in the off-axis fiber response. The experimental transverse response is much smaller than the model predicts. It is suspected that the response of the fuzzy fiber to transverse loading is governed by a different mechanism than the longitudinal result. Further testing is underway to quantify the perceived difference in sensitivity and use the knowledge gained to enhance the accuracy of the model and its ability to predict sensor response based on a known strain field in a component.
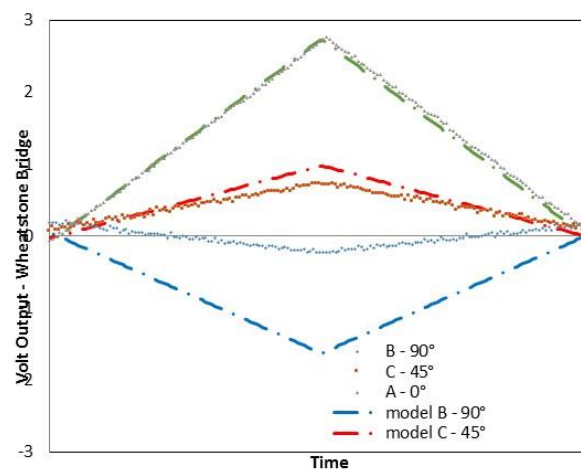
Figure 3.1.8. Experimental Data vs. Model Output

3.1.2 Use of the fuzzy morphology as thermal and electrical interface to reduce the contact resistance

As surfaces are never perfectly flat, the interface comprises point contacts at asperities and air pockets. Some heat is conducted through the physical contact points, but much more is transmitted through the air gaps. Since air is a poor conductor of heat, it should be replaced by a more conductive material to increase the joint conductivity and thus improve heat flow across the thermal interface. Use of suitable interface materials can thus have a significant role in lowering thermal contact resistance. The focus of this study is first, to study the effect of thermal contact resistance on heat transfer capability of high thermal conductivity materials and second is to demonstrate the effectiveness of Carbon nanotubes CNT as thermal interface materials. We managed to grow aligned CNTs with thickness ranging from several micrometers to about 200 um with a narrow diameter distribution around 10 nm (Fig. 3.1.9a and 3.1.9b).
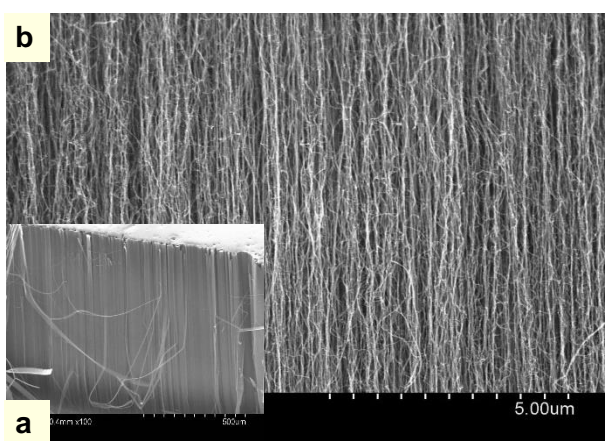
Product	Thermal Impedance [$°C\ in^2/W$]
Dry Test	0.160
Arctic Silver	0.013
Aremco 640	0.060
Circuit Works Grease	0.018
Omegatherm 201	0.054
PowerFilm 51	0.474
Aligned CNT (11%)	0.0092
Aligned CNT (36%)	0.0054

Figure 3.1.9. (a) SEM image of Aligned Carbon Nanotubes. (b) Higher magnification image showing the size and the orientation of carbon nanotubes.
Table 3.1.1. Results of TIMs tested Materials.

A variety of thermal interface materials were tested to establish a baseline of current technology. The testing was done on an ASTM D5470 compliant test. The materials tested are listed in Table 3.1.1. They were tested at three power levels and loadings.
For all processed materials based nanotube, the test measurement was set using optimized conditions with a pressure of 300lb/inch and input current of 1 Amp. We used different concentrations of nano-additives (low, medium and high). The results show that as concentration of nano-additives increases the thermal impedance decreases (Table 3.1.1). Significant improvement was observed in the case of aligned carbon nanotubes with denser nanotube growth (Table 3.1.1).

The arrangement of CNTs in an aligned manner and the quality of the CNT array produced using the CVD method could be the key factors responsible for lowering the thermal impedance value. The above study will be extended for increased volume fraction of CNTs in the TIM film and also for the case CNT film TIM used with other materials like aluminum and graphite with different values of surface roughness.

3.1.3 Use of the fuzzy morphology as an interface to increase structural properties of PMC composites (effort was leveraged by ONR contract N00014-13-1-0110).

Earlier efforts focused on enhancing the fracture toughness of PMCs. Dr. O. Ochoa have recorded 100% improvement in fracture toughness with a CNT growth of 20 weight %. However,

other structural properties need to be examined. In order to establish a baseline understanding of the influence of the CNT growth process on the mechanical strength, a series of tests were done to quantify the strength degradation at each step in the growth process. Figure 3.1.10 shows the results of the first series of testing comparing the tensile strength after each process step. This work proved that the fiber properties can be drastically affected by the growth processing. The next step was to select the key parameters responsible for influencing the fiber properties. The high temperatures present in the surface conditioning and growth steps were suspected to be the largest contributors to the strength reduction. The catalyst composition and application can also have a significant effect, as it may catalyze an unintended reaction which may attack the surface of the fiber. The temperature, time at temperature and catalyst were therefore chosen as the three parameters to study in this project.

T300 fiber was selected and studied through the entire growth process. This process requires the remove of seizing by oxidation, catalyst deposition and then CNT growth. As shown in the figure below that the oxidation temperature to remove seizing is important and it should not exceed 300 ℃ otherwise the fiber starts to degrade (Figure 3.1.10).
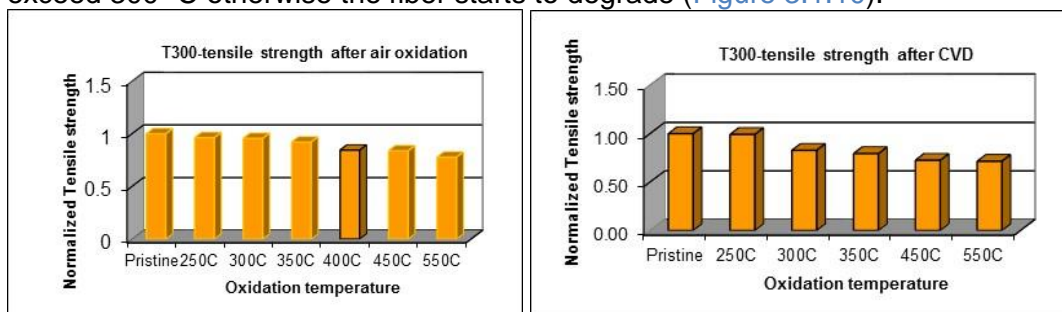
Figure 3.1.10a &b. T300 tensile vs oxidation temperature.

The fiber degradation is caused either high oxidation temperature to remove the fiber seizing or by chemical reaction of various contaminant present in the seizing mixture. If the latters are remind they will activate during CNT growth forming catalytic carbons (diffraction of yellow circled area, Figure 3.1.11) which leads to the formation of porosities (yellow circled area, Figure 3.1.11). Conversely, standard PAN based carbon fibers is made of turbostratic carbons (diffraction of red circled area, Figure 3.1.11), the fiber cross section should not exhibit any preferential orientation.
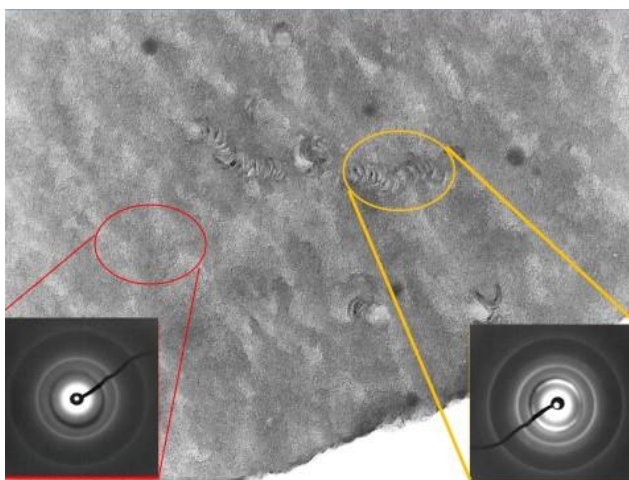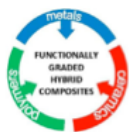

Figure 3.1.11. Image of fibers showing the effect of contaminants on carbon microstructure.

Based on prior experience, the growth process parameters were adjusted to reduce degradation of the fiber and favor mechanical property improvement. The temperature of the surface conditioning furnace was reduced, the catalyst deposition was adjusted and the growth furnace temperature and time of growth were both reduced to prevent fiber degradation while still being conducive to CNT growth. It is clear that we have established the growth condition at various CNT weight gain ranging from 1%, 2%, 20%. Composite panels were made and tested using short beam shear test (ASTM D2344) and flat tension test (ASTM D7291). Results show that low % of CNT leads to a significant improvement in composite properties (Table 3.1.2 & 3.1.3). However, at higher % of CNT the fabricated composites were very porous (Figure 3.1.12). The resin was not able to permeate through the fiber preform and thus results were not good. It might be a critical CNT % in which the physical properties are optimized.

Table 3.1.2. Results of Short bean shear strength test. Table 3.1.3. Results of flatwise tensile strength test.

Specimen	~ % CNT	Short Beam Shear Strength (psi)	Standard Deviation
T300-Bseline	0	5172.08	108.2
T300-1	1	6123.11	179.23
T300-2	2	6714.02	218.36
T300-20	20	7625.17	146.15

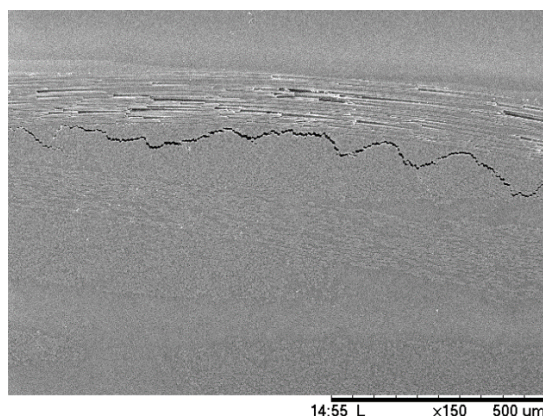| Specimen	~ % CNT	Flatwise Tensile Strength (psi)	Standard Deviation
T300-Bseline	0	2143.56	231.81
T300-1	1	2753.66	189.07
T300-2	2	3236.84	111.23
T300-20	20	1864.23	176.54

14:55 L   ×150   500 um

Figure 3.1.12. Image showing voids at the interface CNT forest and resin.

3.2 IN-SITU NDE/SHM FOR FUNCTIONAL GRADED HYBRID COMPOSITES
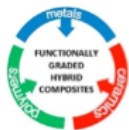
RESEARCH TEAM MEMBERS
PIs: Fu-Kuo Chang
Graduate Students: Yu-Hung Li
Post Docs: Nathan Salowitz

COLLABORATORS:
Dr. Ozden Ochoa (Texas A&M University)
Dr. Dimitris Lagoudas (Texas A&M University)

OBJECTIVES:

Developing an embedded high-temperature SHM sensor network for the proposed functionally graded hybrid composites:

(xiv) Development of high-temperature piezoelectric sensor network which can maintain functionality over 350°C

(xv) Verification of the SHM capabilities of the sensor network at elevated temperatures

(xvi) Fabrication integration of the miniaturized high-temperature SHM sensor network

(xvii) Validation of the miniaturized sensor network

TECHNICAL ACCOMPLISHMENTS

3.2.1 Development of High-Temperature Piezoelectric Sensors

Ultrasonic SHM techniques for high-temperature applications have been desirable yet challenging because most of the PZT-based ultrasonic transducers cannot survive the thermal depoling process when temperatures exceed 250°C. Based on the knowledge about the high-temperature piezoelectric material system, $(1-x)$ BiScO$_3$ - x PbTiO$_3$ (BS-PT), we investigated how to enhance the performance of the intrinsic BS-PT with different stoichiometry of BS-PT solid solutions to create suitable replacement materials for PZT in high-temperature SHM systems. We found that controlling the PbO deficiency in the BS-PT material system can substantially enhance the piezoelectric responses because the PbO deficiency improves the current leakage characteristics in the materials. This improvement is suggested by the higher remnant polarizations and smaller coercive fields of the PbO deficient samples (BS-PT#3 and BS-PT#4) in the polarization-electric field (P-E) curves shown in Figure 3.2.1.
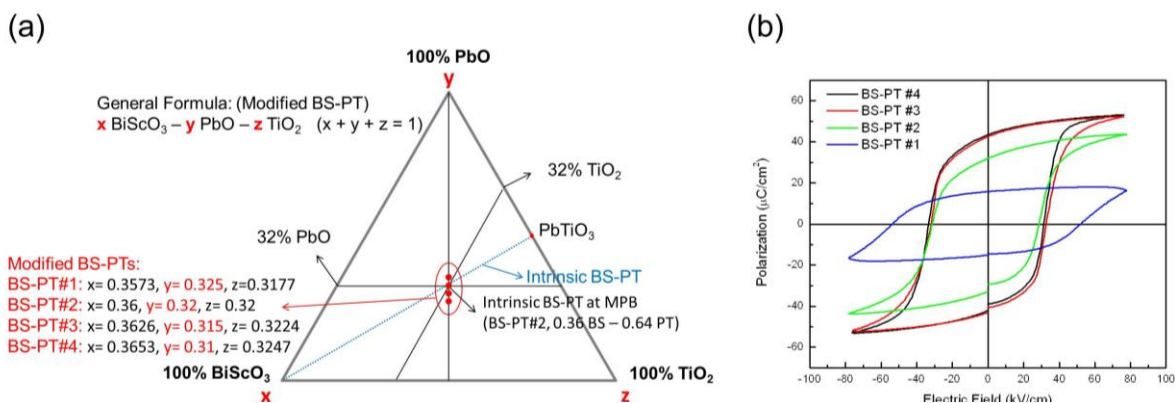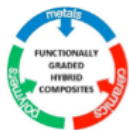

Figure 3.2.1: (a) The ternary phase diagram of the BS-PT solid solution system. The blue dotted line represents the intrinsic $(1-x)$ BiScO$_3$ - x PbTiO$_3$ with different composition ratios. In our study, we controlled different amounts of PbO in the solid solution system to form BS-PT#1 to #4, which are marked in red dots in the diagram. (b) The P-E curves of BS-PT#1~BS-PT#4. Excess PbO in BS-PT#1 aggravates the leaky nature of the intrinsic BS-PT (BS-PT#2) while PbO deficiency in BS-PT#3 and #4 leads to a less leaky characteristic and a higher remnant polarization.

In the thermal depoling tests (shown in Figure 3.2.2), we demonstrated that the newly developed BS-PT#3 transducers exhibit a high d$_{33}$ piezoelectric coefficient up to 350°C and remain over 80% of their original d$_{33}$ values after being exposed at 350°C for two hours. These results show that our new BS-PT#3 transducers do have superior piezoelectric responses over a wide temperature range, and the thermal tolerance is not compromised by the enhancement of the piezoelectric responses.
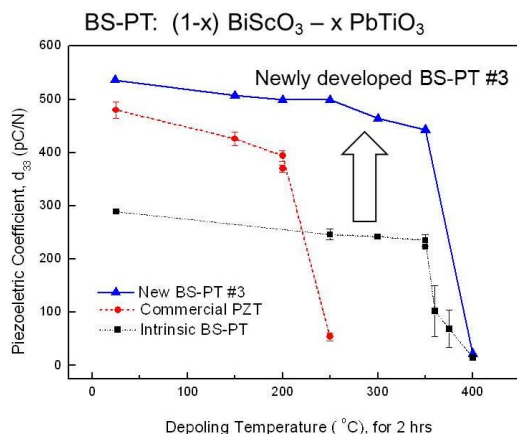
Figure 3.2.2: Results of thermal depoling tests for commercial PZT (PZT-5A), intrinsic BS-PT and our newly developed BS-PT (BS-PT#3) bulk transducers.

3.2.2 SHM Signal Study at High-Temperatures

In addition to material characterizations, we also tested the new BS-PT#3 transducers on simple metallic structures to see whether typical SHM signals (5-peak tone burst) can be actuated, conveyed, and sensed properly at different temperatures. As shown in Figure 3.2.3, the signal strength of the BS-PT#3 transducers exhibits an increasing trend at higher temperatures while the commercial PZT transducers show a decreasing trend as the temperature increases. The pitch-and-catch test results not only confirm the good thermal and piezoelectric properties of our in-house fabricated BS-PT#3 transducers but these results also show that our new BS-PT based transducers have a great potential to perform SHM techniques in the target temperature range of 300~400°C between GCMeC and PMC layers in the functionally graded hybrid composites (FGHCs)
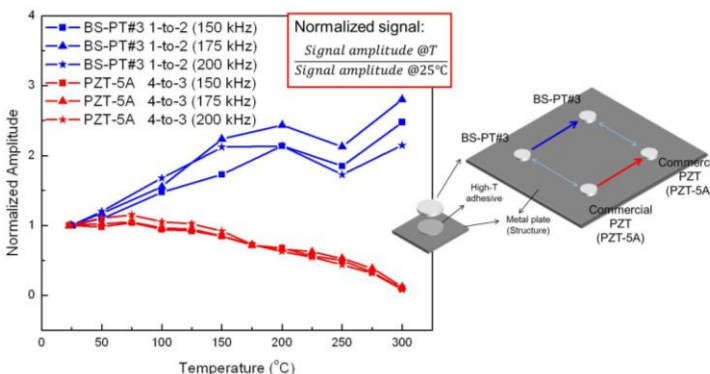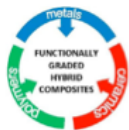

Figure 3.2.3: The comparison of signal strength between BS-PT#3 and commercial PZT (PZT-5A) transducers using different actuation frequencies at different temperatures. Normalized amplitude values are obtained by comparing the maximum signal amplitude measured in the Hilbert transform of the first wave packet at room temperature with the ones measured at different testing points from the same actuator-sensor pair.

3.2.3 Sensor Miniaturization and Fabrication Integration

To fully exploit the good properties of the BS-PT based piezoelectric transducers in embedded SHM systems, we have developed a microfabrication process with screen-printing techniques to fabricate thick-film BS-PT transducer arrays. The main advantage of using the screen-printing techniques is that these techniques enable mass-production of thinner piezoelectric transducers with more complex shapes at a lower cost, compared to the traditional

solid-state reaction method .Screen printing was applied to fabricate miniaturized BS-PT#3 transducers. Printing and sintering conditions were optimized to obtain good ferroelectric properties. As shown in Figure 3.2.4, a saturating hysteresis curve with a fairly high remnant polarization indicates that the screen-printed BS-PT#3 transducers are successfully functionalized and are ready to be integrated with the en masse network fabrication processes.
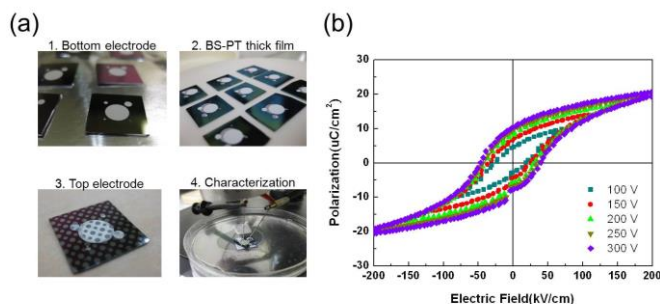

Figure 3.2.4: The optimization process of sintering conditions. (a) Process flow to fabricate the test specimens (b) The P-E curve of the optimized condition – a saturating hysteresis curve with the highest remnant polarization.

A novel microfabrication process was developed to integrate the screen-printed piezoelectric transducers with thin polyimide substrates. Polyimide is a high-temperature polymer with a glass transition temperature range close to 400°C. The inert and robust nature of polyimide makes it a perfect candidate to be integrated with screen-printed BS-PT transducers for high-temperature SHM applications. An overview of the integrated process is described in Figure 3.2.5. With our flexible and stretchable designs, we can fabricate a piezoelectric transducer array from a small wafer and deploy the transducer arrays to cover a larger area or a complex-shaped structure.
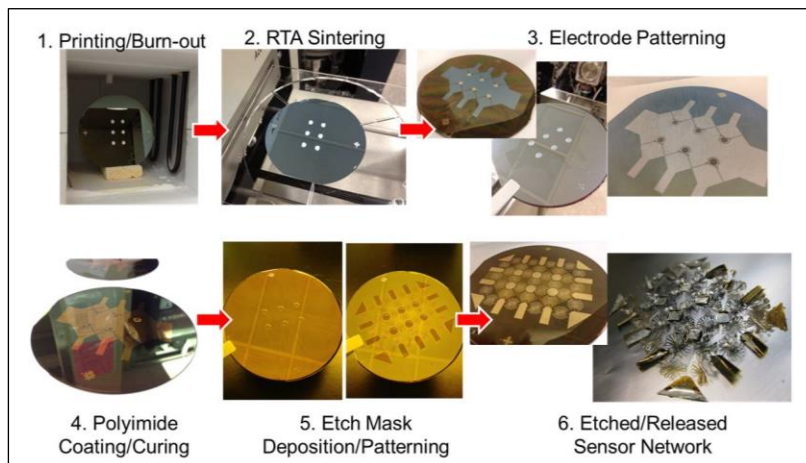

Figure 3.2.5: An overview of the integrated microfabrication process to transfer the screen-printed piezoelectric transducers on a polyimide-based flexible substrate.

3.2.4 Verification of SHM Capabilities

For testing the SHM capabilities of the screen-printed BS-PT#3 transducers, similarly, we used the 5-peak Gaussian windowed tone burst as the input actuation signal to see whether the screen-printed transducer was able to have both sensing and actuating capabilities on a simple structure. Figure 3.2.6 (a) and (b) show the raw signals sensed by the screen-printed BS-PT#3 transducer and the bulk commercial transducer respectively. From both signals, obvious wave packets are observed; the screen-printed BS-PT#3 transducer can differentiate different levels of vibrations initiated by the bulk commercial transducers and can create different levels of vibrations itself. This indicates that the screen-printed BS-PT#3 transducers can not only sense the
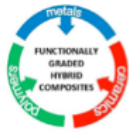
vibrations of different magnitudes sent from the other transducer but also actuate Lamb waves with different amplitudes.
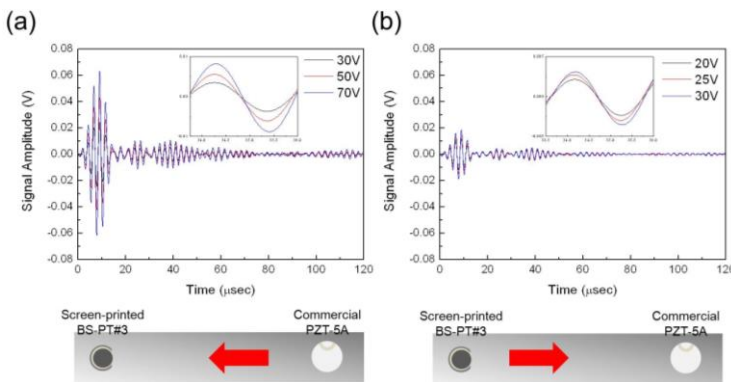

Figure 3.2.6: Demonstration of SHM capabilities of the screen-printed BS-PT#3 transducers – raw signal data at 400 kHz for (a) sensing and (b) actuation

Our final goal for this thin transducer array is to achieve embedded SHM application for the functionally graded hybrid composites (FGHCs) in harsh environments. Characterization of the released transducers and the interaction between the embedded transducer layer and the host structure are still under investigation. Ongoing work focuses on the structural influence of the transducer layer and the temperature dependence of the performance of the screen-printed BS-PT#3 transducers.

3.3 MULTISCALE MODELING OF NANOCOMPOSITES-BASED SHM

RESEARCH TEAM MEMBERS
PIs: Gary D. Seidel, Virginia Tech
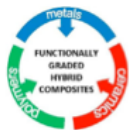Graduate Students: Xiang Ren, Adarsh Chaurasia, Yumeng Li, Josh Burton
Undergraduate Students: Josh Burton, Nick Janssens, Stefan Povolny

COLLABORATORs:
Dr. Khalid Lafdi (University of Dayton Research Institute), Dr. Dan Inman (University of Michigan), Dr. Dimitris Lagoudas (Texas A&M University), Francis Aviles Cetina (Centro de Investigacion Scientifica de Yucatan)

OBJECTIVES:

(xviii) Develop a multiscale model correlating changes in nanocomposite electromechanical properties with damage evolution within the nanocomposite interphase surrounding structural fibers (i.e. the fuzzy fiber)

(xix) Explore the design space for fuzzy fibers as structural health monitoring sensors through correlation of fuzzy fiber design parameters with sensing properties

(xx) Integrate multiscale model for fuzzy fibers with higher length scale models for application in full multiscale model for the FGHC

(xxi) Assessment of modeling approach with comparison of predicted piezoresistive response with fuzzy fiber (UDRI) and single fuzzy fiber fragmentation testing (VT)

TECHNICAL ACCOMPLISHMENTS

3.3.1 Identification of Influence of Cylindrically Orthotropic Material Symmetry
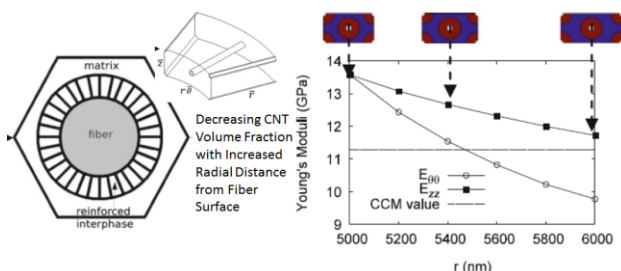

Figure 3.3.1: Demonstration of the change in interphase properties as a function of radial distance associated with the cylindrically orthotropic material symmetry of fuzzy fibers (Analytic CCM, FEA, and average nominal interphase properties).

By taking advantage of the cylindrical orthotropic symmetry, analytic hierarchical mechanical and electrostatic composite cylinder models were developed to obtain the effective mechanical and electrostatic properties of the nanocomposites with well dispersed and aligned fuzzy fibers. As a comparison, an asymptotic expansion homogenization approach for the mechanical and a FEM model for the electrostatic case were developed, which explicitly account for the anisotropic material properties of the fuzzy fiber interphase region to obtain the material response. It was found that the effective mechanical and electrostatic properties as obtained from the CCM models and the numerical methods were in good agreement, which verified the accuracy of the hierarchical CCM models. In addition, the Mori–Tanaka model was used to obtain the effective mechanical and electrostatic properties of the nanocomposites with randomly dispersed fuzzy fibers or with mixtures of aligned fuzzy fibers and structural fibers. From these cases the importance of controlling alignment was observed as in Figure 3.3.1 in the sensitivity of the aligned direction properties to the presence and properties of the nanocomposite interphase, particularly in terms of effective electrical conductivity. It was further noted that controlling glass/fuzzy fiber mixture ratio can offer a means to achieving desired unidirectional ply properties for stiffening and sensing applications. The analytic hierarchical CCM models therefore show promise as relatively inexpensive preliminary design tools for fuzzy fiber enriched composite laminates.

3.3.2 Development of 2-Scale Computational Micromechanics Approach for CNT Inherent Piezoresistivity Effects

An analytic micromechanics approach to modeling the piezoresistive response of fuzzy fibers was explored using the composite cylinder method. While the model was able to demonstrate the piezoresistive response for a two-phase fiber-matrix system, the exercise demonstrated that there are great difficulties in determining analytic solutions even for relatively simple composite microstructures. These difficulties center around the determination of the potential solution for the electrostatics problem in the presence of non-uniform strain fields in piezoresistive materials due to the increase in electrical resistivity material symmetry from transversely isotropic to orthotropic, or even fully anisotropic with off-diagonal contributions. These difficulties can be mitigated for cases involving homogeneous circular cylinders with judicious selection of piezoresistive coefficients in conjunction with the applied mechanical boundary conditions. However, such cases are not representative of actual composite microstructure and constituent material response, and therefore relegated to being used as verification problems in computational micromechanics code development.
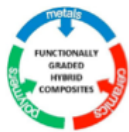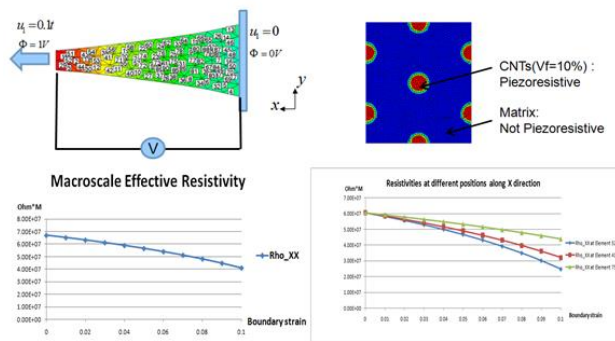
Figure 3.3.2: Demonstration of the influence of CNT inherent piezoresistivity on the macroscale piezoresistive response due to the macroscale strain distribution in the 2-scale computational micromechanics approach.

As such, a computational multiscale piezoresistive algorithm was developed and a corresponding 2D multiscale finite element approach was constructed to model the piezoresistive effects of the fuzzy fiber material. The piezoresistive effects of the fuzzy fiber material mainly come from its nanocomposite interphase, in which there are dense radially oriented carbon nanotubes. In the initial model, effective mechanical properties of CNTs were obtained and internal piezoresistive effects of CNTs are incorporated into the multiscale algorithm for calculating the electric response of the fuzzy fiber material as a whole under different kinds of strains. In this multis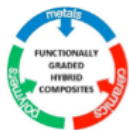cale approach there is an underlying nanoscale representative volume element (RVE) associated with macroscale element integration points which have met some criteria that calls for more detailed information at the fine scale, e.g. a volumetric or von Mises strain criterion. As the nanoscale piezoresistive response is dependent on the RVE boundary conditions (i.e. it is load dependent, but reversible, and therefore not path dependent), the macroscale strain and electric potential are passed to the nanoscale. The nanoscale response to the applied load increments is then passed back up to the macroscale in the form of updated element constitutive properties, and therefore used in the subsequent macroscale load increment.

For illustration purposes of the multiscale piezoresistive algorithm, the piezoresistive response of a tapered bar was considered where the tapered bar contained numerous homogeneous transversely isotropic CNTs extruding in the out-of-plane direction, each of which has internal piezoresistive effects that can be characterized with the constitutive equation of $\Delta\rho_{ij} = g_{ijkl}\varepsilon_{kl}$ where g_{ijkl} are internal inherent piezoresistive strain coefficients for CNTs. For every element of the macroscale material, effective mechanical and electric material properties are used. The effective material properties are obtained through homogenization in the microscale RVEs, which are chosen to represent every element of the macroscale, and in which are applied macroscale displacement field boundary conditions. Due to the piezoresistive effects of CNTs, the resistivities of CNTs change with strains, causing the macroscale effective resistivities change with applied strains, as seen in Figure 3.3.2.

3.3.3 Integration of Continuum Damage Modeling in 2-Scale Computational Micromechanics Approach for Polymer Damage Effects on Nanocomposite Piezoresistivity

Matrix damage effects have been incorporated into the multiscale strategy in order to be able to assess how damage at the nanoscale would affect the macroscale mechanical response, i.e. resulting in non-reversible path and load dependent response. A continuum damage formulation in which local matrix stiffness within the nanoscale representative volume element was adjusted according to the damage state resulting from either a volumetric or von Mises type criterion. The damage model was implemented within the 2-scale multiscale model for piezoresistivity resulting in the ability to capture both deformation and damage at the macroscale. Before introducing the geometric complexities of the fuzzy fiber composite, a model problem was proposed consisting of a tapered bar (so that the stress varies at the macroscale) having a hexagonal CNT arrangement at the nanoscale. The resulting macroscale and microscale piezoresistive

94

responses with and without damage are provided in Figure 3.3.3, as are contour plots of the macroscale stress and the microscale stiffness and conductivity distribution. It is observed that the piezoresistive response has a good correspondence with the stress-strain response, and is able to distinguish between the two damage models used. The stress contours demonstrate how the stress varies with the applied damage model. The microscale contours show the damage distribution in the matrix, and how that influences the inherent piezoresistivity of the CNTs. The model provides a good first step for integrated sensing of deformation and damage.

3.3.4 Development of 2-Scale Computational Micromechanics Approach for Electron Hopping Induced Piezoresistivity in CNT-Polymer Nanocomposites
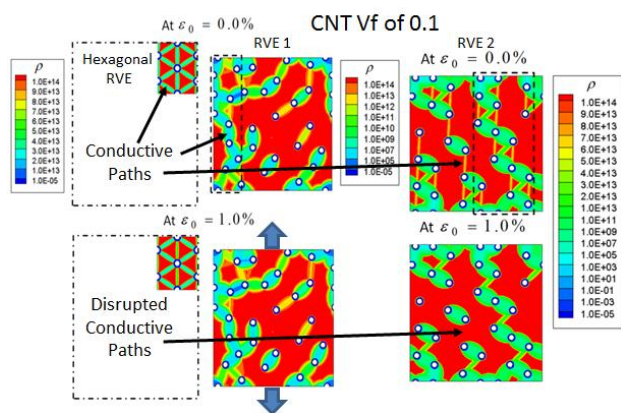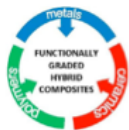

Figure 3.3.4: Demonstration of the disruption of conductive paths in well-dispersed and random 2D nanocomposite RVEs under tension.

Piezoresistive Response of a Sample Nanocomposite with Inherent Piezoresistivity and Damage Evolution at the Microscale.

A key focus was the incorporation of electron hopping into the multiscale modeling efforts for fuzzy fiber piezoresistivity. As part of this effort, initial studies of CNT dispersion effects on the piezoresistive response were undertaken. It was observed that while the well-dispersed (hexagonal RVE) has the largest number of conductive paths, the random CNT dispersions can have fewer but more conductive paths. Further, it was observed that on the application of strains on the order of 1%, that some of these conductive paths in the randomly dispersed CNTs could be disrupted as shown in Figure 3.3.4. As a result, the random dispersion CNT cases can display gauge factors which are both higher and lower than the well-dispersed case. For example, the ratio of the 1% strained resistivity to the zero strain resistivity, the key factor governing gauge factor in nanocomposites, is 1.19 for the for the well-dispersed case where as it is 1.48 for random RVE 1 and 1.07 for random RVE 2 (it is 1 for a standard strain gauge). The electron hopping was integrated into the two-scale modeling approach where it was demonstrated that well-dispersed low volume fraction (0.01) nanocomposites yield gauge factors on the order of 1.6 which is the value obtained for purely geometric response and therefore indicates that inherent piezoresistivity of CNTs is not a significant factor at such volume fractions and strain levels. In contrast, with randomly dispersed CNTs the locally high concentrations of CNTs allowed electron hopping to take place and were therefore observed to yield gauge factors of 2.8 which is comparable to experimental observations at those global volume fractions. Thus, controlling the global and local volume fractions of CNTs within the nanocomposite interphase region of the fuzzy fibers will strongly influence the fuzzy fiber gauge factor.

The electron hopping modeling approach was integrated with the continuum damage technique such that the effects of hopping through a damaged region (partially void) vs. hopping through the undamaged matrix where taken into account. Comparison of the response of the hexagonal RVE to the Random RVEs demonstrated not only the aforementioned large differences in resistivity and piezoresistive response to deformation, but also demonstrated large differences in where damage formed and to what degree, thereby resulting in large differences in the observed piezoresistive response in terms of damage sensing. The influence of electron hopping disruption due to matrix damage evolution was demonstrated in a 2-scale model for a plate with

a hole. As shown in Figure 3.3.5, the location of the macroscale element relative to the hole was able to influence where damage initiated and evolved at the microscale, and therefore which electron hopping pathways were disrupted and to what degree. The evolution of damage at the microscale was in turn able to influence the evolution of damage at the macroscale which is noticeable to some degree in the

Figure 3.3.5: Demonstration of macroscale damage detection in 2-scale computational micromechanics model.

macroscale C_{22} stiffness distribution, but is more so observed in the macroscale conductivity κ_{22} distribution. However, in order to be useful in applications, the damage should be detectable in an average sense. From the average stress and average resistivity as a function of applied strain, it was observed that indeed the resistivity was detecting the initiation and evolution of damage prior to being able to be observed in the stress-strain response.
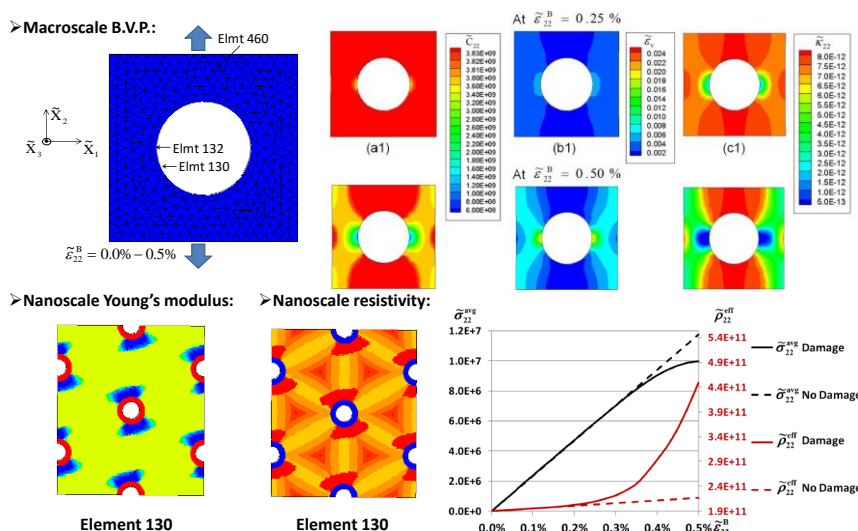
3.3.5 Development of Electromechanical Cohesive Zone and Integration into 2-Scale Computational Micromechanics for Interface Damage Effects on Nanocomposite Piezoresistivity

In terms of modeling damage sensing from fuzzy fibers, efforts were focused on introducing an electromechanical cohesive zone for coupling interface damage and electron hopping and integration of electron hopping effects with the continuum damage models applied in the 2-Scale concurrent models which previously only captured inherent CNT piezoresistivity. In the former, cohesive zones were placed at the CNT-polymer interface within nanoscale RVEs (at present the well-dispersed hexagonal RVE for demonstration purposes) which, as damage evolved within them, allowed for larger distances between CNTs to open up and therefore to reduce and even disrupt the electron hopping conductive paths between neighboring CNTs. As shown in Figure 3.3.6, the effective relative change in resistivity for the damaged interfaces with applied strain is appreciably larger than the perfect interface cases in tension indicating the significance of interfacial debonding on the macroscale gauge factors. In contrast, in compression, the damaged and undamaged interfaces behave the same as the interface remains in contact (so that CNT separation distances are the same), and therefore provides an additional source of tension-compression asymmetry which has been observed experimentally in nanocomposites.
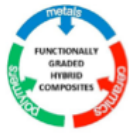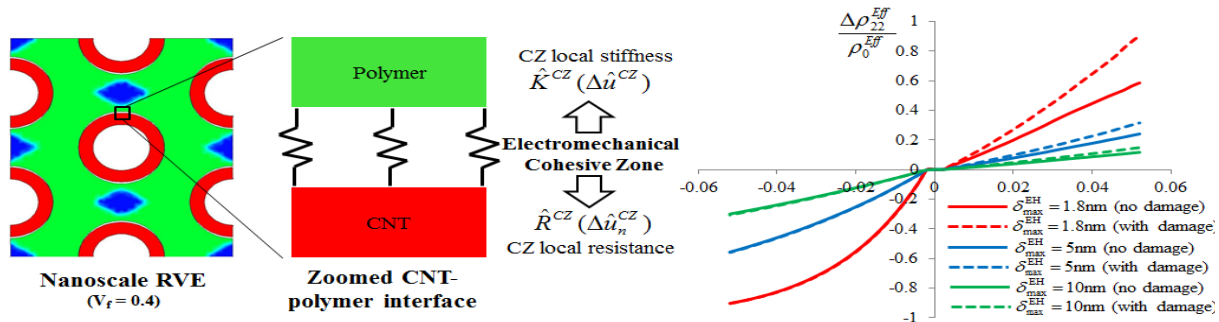
Figure 3.3.6: Introduction of interface damage modeling at the nanoscale and correlation with electron hopping through the development of an electromechanical cohesive zone. Comparison of relative change in resistivity as a function of applied strain for undamaged and damaged interface conditions.

The 2-Scale concurrent model test problem of a tapered bar with nanocomposite hexagonal RVE sub-elements was revisited in terms of introducing the electron hopping effects at the nanoscale to work in conjunction with the inherent CNT piezoresistivity and matrix continuum damage models at the nanoscale. It is recalled that for the inherent piezoresistivity cases, the relative change in resistivity directly followed the stress reduction with damage as the reduced load carrying capacity in the matrix led to less strain transfer to the CNTs. In contrast, as observed in Figure 3.3.7, the increase in matrix damage at the

Figure 3.3.7: Macroscale damage sensing achieved with interface influenced electron hopping effects included at the nanoscale.

nanoscale leads to larger separation distances between CNTs and therefore greatly reduces and even disrupts electron hopping conductive paths at the nanoscale such that the macroscale relative change in resistivity increases as the overall stress reduces with damage. Further, the magnitude of this observed response is observed to be significantly larger at up to 325% change in relative resistance when electron hopping is considered compared to the 2% change observed for inherent CNT piezoresistivity. This indicates that critical importance of electron hopping connectivity within the fuzzy fiber nanocomposite interphase for both strain and damage sensing, and therefore, that the high local CNT concentrations obtained from the CVD growth process are critical and perhaps a tunable feature of fuzzy fibers.

3.3.6 Application of Multiscale Modeling Approach towards Understanding Nanocomposite and Fuzzy Fiber Composite Piezoresistive Response

The electron hopping approach was also implemented within a 3-scale concurrent multiscale model of the piezoresistive single fiber fragmentation testing of fuzzy fiber tows as shown in Figure 3.3.8. From these simulations it was observed that the electron hopping barrier height at the nanoscale could have significant impact on the macroscale gauge factors
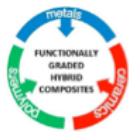
.

In addition to the modeling efforts, we have been working towards obtaining piezoresistive response data from fuzzy fiber samples obtained from UDRI which can be used to assess the multiscale model results. At VT we have embedded fuzzy fibers received from UDRI within an

Figure 3.3.8: 3-Scale Concurrent Multiscale Model of Piezoresistive Fuzzy Fiber Tow Fragmentation Testing. (a) macroscale test coupon (b) sub-element within fuzzy fiber tow demonstrating a high local fuzzy fiber concentration and denoting the nanocomposite fuzzy interphase (c) sub-element from within the nanocomposite interphase for a specific radial orientation and high local CNT volume fraction such that electron hopping is taking place. Relative change in resistivity at the macroscale as a function of applied macroscale strain for two different electron hopping barrier heights at the nanoscale.

epoxy matrix in order to fabricate single fiber fragmentation test samples. Figure 3.3.9 demonstrates the piezoresistive response obtained from the fuzzy fiber samples having a good correspondence with the stress-strain response in both monotonic and tension-tension cyclic loading. However, the gauge factors obtained from these specimens was much lower (0.07) than the gauge factors obtained from the modeling efforts (9-30) and those obtained by UDRI (31) for the fuzzy fiber tow in the absence of matrix material. Several microstructural features were identified as potentially being the source of the difference between modeling predictions and experimental measurements. These included the random dispersion of fuzzy fibers within the matrix infused tow, the asymmetric distribution of CNTs around the glass fibers, the orientation of the CNTs within the nanocomposite (random vs radially oriented), the clustering and impurities in the fuzzy nanocomposite region, curvature and distribution of CNT type, and non-fuzzy segments along the fuzzy fiber length (bare or sparse regions), all of this which were observed in SEM studies of single fiber fragmentation fuzzy fiber samples.
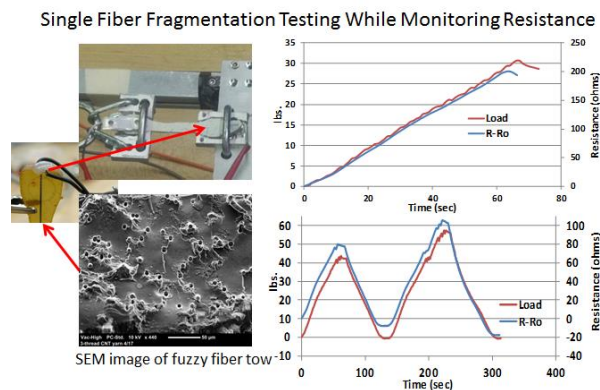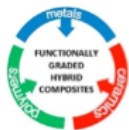

Figure 3.3.9: Microtensile fragmentation testing of single fuzzy fiber tows in an epoxy matrix.

98

In order to understand distribution effects, a detailed multiscale study of the effects of microscale dispersion of local CNT orientaitons was conducted. This study led to the observation that radially oriented moderately dense packed CNT distributions which would take full advantage of the electron hopping induced piezoresistive response would yield the largest gauge factors whereas random oriented, densely packed distributions led to staturation of the conductivity such that the piezoresistive response of the nanocomposites was attributed to inherent piezoresistivity of the CNTs or nominal geometric effects as observed in non-piezoresistive conductors. In the case of the former, it was further observed that finite aspect ratio effects meant that there was poor strain transfer to CNTs not alligned with the local stretching direction, and hence, small gauge factors were likely, though still larger than those observed for fuzzy fiber samples experimentally.
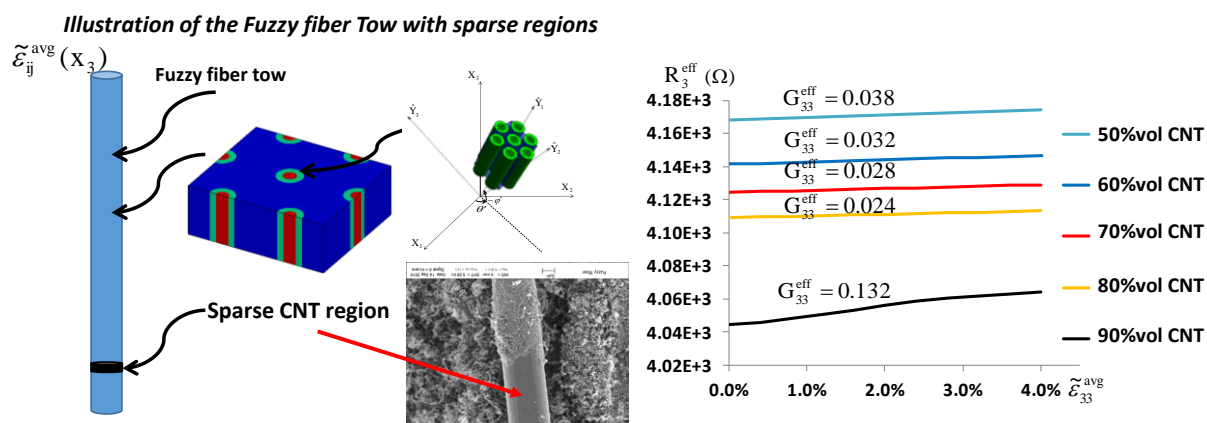

Figure 3.3.10: A simple model was developed to demonstrate the influence of the sparse regions on the effective gauge fiber of the fuzzy fiber composite samples.

A simple model was developed to demonstrate the influence of the sparse regions on the effective gauge fiber of the fuzzy fiber composite samples from which it was observed that gauge factors on the same order as those observed in experiments could be obtained with the fuzzy fibers having less than 1% of the length considered to be bare. Thus the combination of densely packed randomly oriented CNTs and bare regions were deemed to be the primary reasons for the small gauge factors observed experimentally for the singel fiber fragmentation fuzzy fiber samples.

Summary

Through multiscale modeling and characterization efforts in this project we have developed understanding of the key parameters which influence the deformation and damage detection capabilities of nanocomposites and fuzzy fiber composites. The next steps would be to refine this understanding through more rigorous validation procedures and subsequently to apply multiscale modeling of nanocomposite sensing towards exploring the design space for the development of full scale deformation and damage sensing composites.
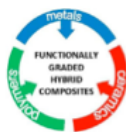
STUDENTS AND POSTDOCTORAL FELLOWS
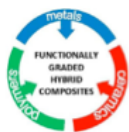
TAMU

Postdoctoral fellows

First and last name	Starting Date	End Date	Supervisor (s)
Kaushik Das	Fall 2009	Spring 2012	J. Whitcomb, D. Lagoudas
Sandip Basu	Spring 2010	Fall 2011	I. Karaman, M. Radovic

Graduate students:

First and last name	Degree	Graduation Date	Supervisor (s)
Keith Ballard	M.S.	Summer 2014	J. Whitcomb
O. Ozgu Ozsoy	PhD	Spring 2014	J.N. Reddy
Robert Brown	PhD	Spring 2014	P. Cizmas
Feifei Cheng	PhD	Fall 2013	J.N. Reddy
Venkat Vallala	PhD	Summer 2013	J.N. Reddy
W. Ross McLendon	PhD	Spring 2013	J. Whitcomb
Wesley McLendon	PhD	Spring 2013	J. Whitcomb
Hieu Truong	M.S.	Fall 2012	O. Ochoa
Gregory S. Payette	PhD	Spring 2012	J.N. Reddy
Liangfa Hu	PhD	Spring 2015	I. Karaman, M. Radovic
Babatunde Agboola	PhD	Fall 2015	D. Lagoudas
Rogelio Benitez	PhD	Fall 2015	M. Radovic
Ankush Kothalkar	PhD	Fall 2015	I. Karaman
Brian Lester	PhD	Fall 2015	D. Lagoudas
Huili Gao	PhD	Spring 2016	M. Radovic
Hieu Truong	Ph.D.	Spring 2016	O. Ochoa
Miguel Gutierrez Rivera	PhD	Fall 2016	J.N. Reddy

Undergraduate students:

First and last name	Starting Date	Graduation Date	Supervisor (s)
Keith Ballard	Fall 2010	Speing 2012	J. Whitcomb
Morgan O'Neil	J. Whitcomb	J. Whitcomb	J. Whitcomb
Philip Koelpin	Fall 2012	Spring 2014	J. Whitcomb

Virginia Tech

Graduate students:

First and last name	Degree	Graduation Date	Supervisor (s)
Mohammad Bonakdar	MS	Fall 2011	G. Seidel, D. Inman
Xiang Ren	PhD	Spring 2015	G. Seidel
Adarsh Chaurasia	PhD	Fall 2015	G. Seidel
Yumeng Li	PhD	Spring 2015	G. Seidel
Josh Burton	MS	-	G. Seidel

Undergraduate students:

First and last name	Starting Date	Graduation Date	Supervisor (s)
Josh Burton	Summer 2011	Spring 2012	G. Seidel
Nick Janssens	Summer 2014	-	G. Seidel
Stefan Povolny	Summer 2014	-	G. Seidel

University of Dayton

Postdoctoral fellows

First and last name	Starting Date	End Date	Supervisor (s)
L. Li	-	-	K. Lafdi

Graduate students:

First and last name	Degree	Graduation Date	Supervisor (s)
Hikita Muneaki	PhD	Spring 2015	K. Lafdi
Qiong Jiang	MS	Fall 2013	K. Lafdi
Meng Chao	MS	Fall 2012	K. Lafdi
Omar Memon	MS	Spring 2012	K. Lafdi
Matthew Boehle	MS	-	K. Lafdi

Undergraduate students:

First and last name	Starting Date	Graduation Date	Supervisor (s)
Daniel Salomon	Spring 2013	-	K. Lafdi
Ian Lenfant	Fall 2013	Spring 2014	K. Lafdi
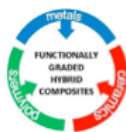
Paul Bianca	Spring 2012	Spring 2013	K. Lafdi
Larry Funke	Spring 2010	Spring 2012	K. Lafdi

Stanford

Postdoctoral fellows

First and last name	Starting Date	End Date	Supervisor (s)
Sang Jong Kim	Fall 2009	Summer 2013	F.-K. Cheng

Graduate students:

First and last name	Degree	Graduation Date	Supervisor (s)
Nathan Salowitz,	Ph.D	Spring 2013	F.-K. Cheng
Kuldeep Lonkar	Ph.D	Fall 2013	F.-K. Cheng
Yu-Hung Li	PhD	-	F.-K. Cheng

University of Illinois Urbana-Champaign

Postdoctoral fellows

First and last name	Starting Date	End Date	Supervisor (s)
Piyush Thakre	Spring 2010	Spring 2013	S. White, N. Sottos
Masoud Safdari	Spring 2013	Spring 2013	P. Geubelle

Graduate students:

First and last name	Degree	Graduation Date	Supervisor (s)
Jason Patrick	PhD	Fall 2014	S. White, N. Sottos
Soheil Soghrati	PhD	Spring 2013	P. Geubelle
Anthony Coppola	PhD	-	S. White
Ahmad Najafi	PhD	-	P. Geubelle
Marcus Tan	PhD	-	P. Geubelle

Undergraduate students:

First and last name	Starting Date	Graduation Date	Supervisor (s)
Anthony Griffin	Spring 2013	Fall 2013	S. White, N. Sottos
Luke Warpinski	Spring 2014	Fall 2014	S. White, N. Sottos
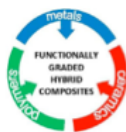
Vignesh Vishwanathan	Fall 2014	-	S. White, N. Sottos
Sean Murray	Fall 2014	-	S. White, N. Sottos
Kevin Hughes	Spring 2011	Fall 2012	P. Geubelle
Jie Hua Lin	Summer 2010	Spring 2011	P. Geubelle
Carrington Watkins	-	Spring 2015	N. Sottos

University of Michigan

Postdoctoral fellows

First and last name	*Starting Date*	*End Date*	*Supervisor (s)*
Ya Wan	Summer 2012	Summer 2014	D. Inman

Graduate students:

First and last name	*Degree*	*Graduation Date*	*Supervisor (s)*
Nick Konchuba	MS	Fall 2013	D. Inman
Riddhiman Bhattacharya	PhD	Fall 2015	N. Goulbourne

Undergraduate students:

First and last name	*Starting Date*	*Graduation Date*	*Supervisor (s)*
Alex Briand	Fall 2012	Spring 2013	D. Inman
Matthias Gaucher-Petitde	-	Spring 2013	D. Inman

PUBLICATIONS

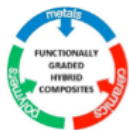## *PEER REVIEWED JOURNAL PUBLICATIONS*

Published:
Year 5

1. Kothalkar A, Cerit A, Proust G, Basu S, Radovic M, Karaman I. "Interfacial study of NiTi-Ti3SiC2 solid state diffusion bonded joints," *Materials Science and Engineering A,* 2015, 622:168-177.

2. Parrikar PN, Gao H, RadovicM, Shukla A. "Static and dynamic therm-mechanical behaviour of Ti2AlC MAX phase and fiber reniforced Ti2AlC composites," *Dynamic Beahviour of Materials* 2015, 162: F14-F22.

3. Hu L, Kothalkar A, Karaman I, Proust G, Radovic M. "Fabrication and characterization of NiTi/Ti$_2$AlC and NiTi/Ti$_3$SiC$_2$ composites," *Journal of Alloys and Compounds* 2014, 610: 635-44.

4. Cheng F, Hu L (*Cheng and Hu equally contributed*), Reddy JN, Karaman I, Hoffman E, Radovic M. "Temperature-dependent thermal properties of a shape memory alloy/MAX phase composite: Experiments," *Acta Materialia* 2014, 68: 267-78.

5. Kothalkar A, Benitez R, Hu L, Radovic M, Karaman I. "Thermo-mechanical response and damping behavior of shape memory alloy/MAX phase composites," *Metallurgical and Materials Transactions A* 2014, 45: 2646-58.and modeling.

6. Hu L, Kothalkar A, O'Neil M, Karaman I, Radovic M. "Current-activated, pressure-assisted infiltration: a novel, versatile route for producing interpenetrating ceramic-metal composites," *Materials Research Letters* 2014, 2(3): 124-30.

7. Salowitz, N., Guo, Z., Kim, K., Li, Y.-H., Lanzara, G., and Chang, F.-K, "Microfabricated Expandable Sensor Networks for Intelligent Sensing Materials," IEEE Sensors Journal, Vol. 14, No. 7, 2014

8. Bhattacharya, R., Benitez, R., Radovic, M., and Goulbourne N.C., "High strain-rate response and deformation mechanisms in polycrystalline Ti$_2$AlC", *Materials Science and Engineering A*, Vol. 598, pp. 319-326, 2014

9. J. Sebastian, N. Schehl, M. Bouchard, M. Boehle, L. Li, A. Lagounov, K. Lafdi, "Health monitoring of structural composites with embedded carbon nanotube coated glass fiber sensors," *Carbon* Volume: 66, pages: 191-200, Jan 2014.

10. Cheng, F., Kim, S., Reddy, J.N. and Abu Al-Rub, R.K., "Modeling of Elastoplastic Behavior of Stainless-steel/Bronze Interpenetrating Phase Composites with Damage Evolution", *International Journal of Plasticity*, Vol. 61, 2014, pp. 94-111.

11. Payette, G. S. and Reddy, J. N., "A seven-parameter spectral/hp finite element formulation for isotropic, laminated composite and functionally graded shell structures," *Computer Methods in Applied Mechanics and Engineering*, Vol. 278, 2014, pp. 664-704.

12. Gary Don Seidel, George Chatzigeorgiou, Xiang Ren, Dimitris C. Lagoudas, "Multiscale Modeling of Multifunctional Fuzzy Fibers Based on Multi-Walled Carbon Nanotubes," *Modeling of Carbon Nanotubes, Graphene and their Composites, Springer Series in Materials Science*, Volume 188, pp. 135-176, 2014.

Year 4

1. Truong, H. T. X., Lagoudas, D. C., Ochoa, O. O., Lafdi, K., "Fracture Toughness of Fiber Metal Laminates: Carbon Nanotube Modified Ti-Polymer Matrix Composite Interface," *Journal of Composite Materials*, (2014) vol. 48 no. 22.
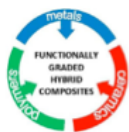
104

2. Wang, Y. and Inman, D. J., "Finite Element Analysis and Experimental Study on Dynamic Properties of a Composite Beam with Viscoelastic Damping", *Journal of Sound and Vibration,* Vol. 332, Issue 23, pp. 6177-6191, 2013.

3. Hu, L., Karaman, I., and Radovic, M., "Simple, inexpensive synthesis of damage tolerant MAX phase foams," *American Ceramic Society Bulletin,* vol. 92, 2013, pp. 31-32.

4. Radovic, M. and Barsoum, M.W., "The MAX Phases: Bridging the Gap Between Metals and Ceramics" *invited feature article in the American Ceramic Society Bulletin*, April, 2013.

5. Reddy, J. N. and Kim, J., "A nonlinear modified couple stress-based third-order theory of functionally graded plates," *Composite Structures*, Vol. 94, 2012, pp. 1128-1143.

6. Payette, G. S., Nakshatrala, K. B., and Reddy, J. N., "On the performance of high-order finite elements with respect to maximum principles and the nonnegative constraint for diffusion-type equations," *International Journal for Numerical Methods in Engineering*, Vol. 91, 2012, pp. 742-771.

7. Kiyono, C. Y., Silva, E. C. N., and Reddy, J. N., "Design of laminated piezocomposite shell transducers with arbitrary fiber orientation using topology optimization approach," *International Journal for Numerical Methods in Engineering*, Vol. 90, No. 12, 2012, pp. 1452–1484.

8. Xiang Ren and Gary D. Seidel, "Computational micromechanics modeling of inherent piezoresistivity in carbon nanotube-polymer nanocomposites," *Journal of Intelligent Material Systems and Structures*, vol. 24, No. 12, 2013, pp. 1459-1483.

9. Xiang Ren and Gary D Seidel, "Computational micromechanics modeling of piezoresistivity in carbon nanotube-polymer nanocomposites," *Composite Interfaces*, In Press, first published on-line July 9, 2013 as doi:10.1080/15685543.2013.813199.

10. S. Soghrati, A.R. Najafi, K. M. Hughes, J. H. Lin, S. R. White, N. R.Sottos, and P. H. Geubelle. "Computational analysis of actively-cooled 3D woven microvascular composites using a stabilized interface-enriched generalized finite element method." *International Journal of Heat and Mass Transfer*, vol. 65, 2013, pp. 153-164.

11. A. M. Aragón, S. Soghrati, and P. H. Geubelle. "Effect of in-plane deformation on the cohesive failure of heterogeneous adhesives." *Journal of the Mechanics and Physics of Solids*, vol. 61 no.7, 2013, pp. 1600-1611.

12. S. Soghrati, A. M. Aragón, C. A. Duarte, and P. H. Geubelle. "An interface-enriched generalized finite element method for problems with discontinuous gradient fields." *International Journal for Numerical Methods in Engineering*, vol. 89 no. 8, 2012, pp 991-1008.

Year 3

1. Salowitz, N., Guo, Z., Li, Y. H., Kim, K., Lanzara, G., and Chang, F .K, "Bio-Inspired Stretchable Network-Based Intelligent Composites," *Journal of Composite Materials*, *Journal of Composite Materials*, Vol. 47, No. 1, pp97-105, 2013.

1. Vallala,V., Ruimi, A., and Reddy, J.N., "Nonlinear viscoelastic analysis of orthotropic beams using a general third-order theory," *Composite Structures*, Vol. 94, 2012, pp. 3759-3768.

2. Vallala, V. P., Payette, G. S., and Reddy, J. N., "Spectral/hp finite element formulation for viscoelastic beams based on an higher-order beam theory," *International Journal of Applied Mechanics*, Vol. 4, No. 1, 2012, pp. 1250010-1 to 28.

3. Cheng, F., Ozsoy, O. O., and Reddy, J. N., "Finite element modeling of viscoelastic behavior and interface damage in adhesively bonded joints", In: *S. Kumar and K.L. Mittal (Eds.) Advances in Modeling and Design of Adhesively Bonded Systems*, (23–46), 2013, Scrivener Publishing LLC.

4. Payette, G. S., and Reddy, J. N., "A nonlinear finite element framework for viscoelastic beams based on the high-order Reddy beam theory," *Journal of Engineering Materials and Technology*, Vol. 135, No. 1, 2013, pp. 011005-1 to 011005-11.
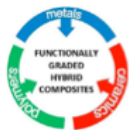
5. Boehle, M., Jiang, Q., Li, L., Lagounov A., and Lafdi, K, "Carbon nanotubes grown on glass fiber as a strain sensor for real time structural health monitoring," *International Journal of Smart and Nano Materials*, 2012 (in press).

6. Soghrati S., and Geubelle, P. H., "A 3D interface-enriched generalized finite element method for weakly-discontinuous problems with complex internal geometries," *Computer Methods in Applied Mechanics and Engineering*, No. 217-220, 2012, pp. 46-57.

7. Soghrati, S. Thakre, P. R., White, S. R., Sottos, N. R., and Geubelle, P. H., "Computational design of actively-cooled microvascular materials". *International Journal of Heat and Mass Transfer*, Vol. 55, No.19-20, 2012, pp. 5309-5321.

8. Esser-Kahn, A., Thakre, P. R., Dong, H., Patrick, J. F., Sottos, N. R., Moore, J. S., and White. S. R., "Three-Dimensional Microvascular Fiber-Reinforced Composites," *Advanced Materials*, Vol. 23, No. 32, 2011, pp. 3654-3658.

9. McLendon, W. R. and Whitcomb, J. D., "Characteristic Failure Initiation Sites in Plain Weave Textile Composites", *Journal of Composite Materials*, online December 2012.

10. Chatzigeorgiou, G., Seidel, G. D., and Lagoudas, D. C., "Effective mechanical properties of 'fuzzy fiber' composites" *Composites Part B: Engineering*, Vol. 43, No. 6, 2012, pp. 2577-2593.

11. Hu, L., Benitez, R., Basu, S., Karaman, I., and Radovic, M., "Processing and Characterization of Porous Ti_2AlC with Controlled Porosity and Pore Size", *Acta Materialia*, Vol. 60, 2012, pp. 6266-6277.

12. Basu, S., Obando, N., Gowdy, A, Karaman, I, and Radovic, M., "Long-Term Oxidation of Ti_2AlC in Air and Water Vapor at 1000-1300 °C Temperature Range", *Journal of the Electrochemical Society*, Vol. 159, 2012, pp. C90-C96.

Year 2

1. Das, K., Lagoudas, D.C. and Whitcomb, J., "Analysis of a Nano-Porous Multi-Layer Film for Thermal Radiation Barrier Coatings". *Applied Nanoscience*, Vol. 1, 2011.

2. Lester, B. T., Chemisky, Y., and Lagoudas, D. C., 2011, "Transformation Characteristics of Shape Memory Alloy Composites", *Smart Materials and Structures*, 20 (2011) 094002.

3. Payette, G.S. and Reddy, J.N., "On the Roles of Minimization and Linearization in Least-Squares Finite Element Models of Nonlinear Boundary Value Problems," *Journal of Computational Physics* 2011; 230(9): 3589-3613.

4. Wang, X. and Gao, X.-L. (2011). "On the Uniform Stress State inside an Inclusion of Arbitrary Shape in a Three-Phase Composite." *Z. angew. Math. Phys.* (published on-line in June 2011) (DOI: 10.1007/s00033-011-0134-3).

5. Basu, S., Ozaydin, M.F., Kothalkar, A., Karaman, I., and Radovic, M., "Phase and morphology evolution in high temperature Ti_3SiC_2-NiTi diffusion bonded joints", *Scripta Mat.*, Vol. 65, pp. 237-240, 2011.

6. Barsoum, M. and Radovic, M., "The Elastic and Mechanical Properties of the MAX Phases", *Ann. Rev. Mater. Res.*, Vol.41, pp. 9:1-9:33, 2011.

7. Spencer, C.B., Córdobad, J.M., Obando, N., Sakulich, A., Radovic, M., Odénc, M., Hultman, L. and Barsoum, M., "The Reactivity of Ti_2AlC and Ti_3SiC_2 with SiC Fibers and Powders up to Temperatures of 1550°C", *J. Amer. Ceram. Soc.*, 94 [6], p – 1737 - 1743, 2011.

8. Seidel, G. D. and Puydupin-Jamin, A.-S. "Analysis of Clustering, Interphase Region, and Orientation Effects on the Electrical Conductivity of Carbon Nanotube-Polymer Nanocomposites Via Computational Micromechanics", *Mechanics of Materials*, 2011, 43, p 755-774.

9. Gao, X.-L., Liu, M. Q., "Strain Gradient Solution for the Eshelby-Type Polyhedral Inclusion Problem." *Journal of Mechanics and Physics of Solids*, 2011, Vol. 60, Issue 2, 2012, p-261-276.
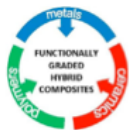
10. Spencer, C.B., Córdobad, J.M., Obando, N., Sakulich, A., Radovic, M., Odénc, M., Hultman, L. and Barsoum, M., "Phase Evaluation in Al2O3 Fiber-Reinforced Ti2AlC During Sintering in the 1300°C–1500°C Temperature Range", J. Am. Ceram. Soc., 94 [10], p-3327–3334, 2011.

Accepted:
1. S. Soghrati, A. M. Aragón, and P. H. Geubelle. "Design of actively-cooled microvascular materials: A genetic algorithm inspired network optimization." To appear in *Structural and Multidisciplinary Optimization*, 2013.
2. Wang, Y., Masoumi, M., Gaucher-Petitdemange, M., 2014, Vascular Fluid Damping of Flexible Cantilevers Under Varied Temperatures: Experiment, Modeling and Analysis, *Journal of Sound and Vibration*, Accepted
3. Cheng, F. Kim, S., Reddy, J.N, "Computational Modeling of the Plastic-damage Behavior of Porous MAX phase with aligned ellipsoid-like Pores", *International Journal of Solids and Structures,* accepted with revisions.
4. Ballard, K, McLendon, R., Whitcomb, J., "The Influence of Microstructure Randomness on Prediction of Fiber Properties in Composites". Accepted for publication in Journal of Composite Materials, 12/2013.
5. M. Tan, M. Safdari, A.R. Najafi, and P.H. Geubelle. (2014) "A NURBS-based interface-enriched generalized finite element scheme for the thermal analysis and design of microvascular composites." *CMAME*.

Submitted/In Review
1. Brown, R. L., Das, K., Cizmas, P. G. A., Whitcomb, J. D., 2013. "A Numerical Investigation of Actively Cooled Structures in Hypersonic Flow", Submitted to Journal of Aircraft on April 21, 2013.
2. Lester, B. T., Kothalkar, A., Karaman, I. Radovic, M., and Lagoudas, D. C., "Modeling of Shape Memory Alloy – Ceramic Composites," *Composites: Part B*, 2013, Submitted.
3. Thakre P.R., Sottos N.R., White S.R., "Active Cooling of Biomimetic Vascular Composites", 2013.
4. Hu L, O'Neil M, Erturun V, Benitez R, Proust G, Karaman I, Radovic M. "An infiltration approach for producing high-performance metal/ternary carbide composites with controlled microstructures," Submitted to *Advanced Functional Materials.*
5. Hu L, O'Neil M, Erturun V, Karaman I, Radovic M.On the energy dissipation in metal/Ti$_2$AlC composites under cyclic, compressive loading. Submitted to *Scripta Materialia.*
6. Coppola AM, Hu L, Thakre PR, Radovic M, Karaman I, Sottos NR, White SR. "Active cooling of a bilayer nickel titanium (NiTi)-polymer matrix composite (PMC) hybrid containing microchannels fabricated by replication of sacrificial components," Submitted to *Advanced Functional Materials.*
7. Benitez R, Proust G, Radovic M. "Hysteretic stress-strain behaviour of Ti2AlC revisited," *Acta Materialia* 2014.
8. Bhattacharya R., and Goulbourne N.C, "*Heterogeneous strain evolution representative polycrystalline MAX phases*", in submission.
9. Masoumi, M., Wang, Y**.,** Inman, D.J.. Gaucher-Petitdemange, M., 2014, Effect of Temperature Gradient on the Vibration Characteristics of Fluid-Filled Cantilever Beams: *Experimental Mechanics*, In Review.
10. K. Lafdi, I. Lenfant, C. Chao, M. Boehle, C. Chinesta, *"Degradation Mechanism of Fuzzy fibers during CNT Growth"* Carbon (to be submitted, 2014).

11. M. Boehle, P. Pianca, , K. Lafdi, Chinesta, *"Modeling of an Embedded CNT Based Composite Strain Sensor"* Advances in Aircraft and Aerospace Science (submitted July , 2014)

12. X. Ren, J. Burton, G.D. Seidel, K. Lafdi, "*Computational Multiscale Modeling and Characterization of Piezoresistivity in Fuzzy Fiber Reinforced Polymer Composites*", Submitted to International Journal of Solids and Structures.

13. X. Ren, A. Chaurasia, G.D. Seidel, "*Concurrent Multiscale Modeling of Coupling between Continuum Damage and Piezoresistivity in CNT-Polymer Nanocomposites*", Submitted to Mechanics of Materials.

14. X. Ren, A. Chaurasia, A.I. Oliva-Aviles, J.J. Ku-Herrera, G.D. Seidel, F. Aviles, "*Modeling of Mesoscale Dispersion Effect on the Piezoresistivity of Carbon Nanotube-Polymer Nanocomposites via 3D Computational Multiscale Methods*", Submitted to Composites Science and Technology.

15. S. Soghrati, C.A. Duarte and P.H. Geubelle. (2013) "An adaptive interface-enriched generalized finite element method for the treatment of problems with curved interfaces." Submitted to *CMAME*.

16. A. R. Najafi, M. Safdari, D. Tortorelli and P.H. Geubelle. (2014) "A gradient-based shape optimization scheme using an interface-enriched GFEM." Submitted to *Structural and Multidisciplinary Optimization*.

17. M. Safdari, A. Najafi, N.R. Sottos and P.H. Geubelle. (2014) "An NURBS-based interface-enriched generalized finite element method for problems with complex discontinuous gradient field." Submitted to *IJNME*.
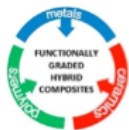

PATENTS:

1. Li, Y.-H., Kim, S. J., and Chang, F.-K., "Development of High Piezoelectric Response BiScO₃-PbTiO₃ Ceramics by Controlling PbO deficiency," US Provisional Patent Application, submitted August 2012.

CONFERENCE PROCEEDINGS:

Year 5

1. Li, Y.-H., Kim, S. J., Salowitz, N., Chang, F.-K.,. " Development of High-Performance BS-PT Based Piezoelectric Transducers for High-Temperature Applications," Proceedings of the 7th European Workshop on Structural Health Monitoring, La Cité, Nantes, France, July 8-11, 2014

2. Brown, R. L., Ballard, K., Cizmas, P. G. A., Whitcomb, J. D., 2013. "Simulation of Actively Cooled Deformable Structures in Hypersonic Flow", Accepted for AIAA SciTech Conference, January 13-17, 2014.

3. Masoumi, M., Wang, Y., Gaucher-Petitdemange, M., Inman, D., 2014, Damping Behaviors of Flexible Cantilevers Conveying Vascular Flow under Varied Temperatures: Theoretical and Experimental Analysis, ASME 2014 Dynamic Systems and Control Conference, Oct. 22-24, 2014, San Antonio, Texas, USA.

4. Masoumi, M., Wang, Y., Vibration Characteristics of Magnetic Nano Fluids-filled Flexible Cantilevers under Varied Temperatures and Magnetic Fields, Proceedings of ASME 2014 Conference on Smart Materials, Adaptive Structures and Intelligent Systems SMASIS, Newport, Roald Island, USA, 8-10 September 2014.
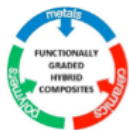
5. Gaucher-Petitdemange, M., Wang, Y., Masoumi, M., Inman, D., Vascular Fluid Damping of Flexible Multifunctional Composite Cantilevers: Experiment, Modeling and Analysis, Proceedings of the ASME 2013 International Design Engineering Technical Conferences & Computers and Information in Engineering Conference, Buffalo, NY, USA, 17-20, August 2014.
6. Wang, Y., 2014, Vascular Fluid Damping of Flexible Multifunctional Composite Cantilevers, Experiment, Model and Analysis, The 1st International Conference on Mechanics of Composites, Stony Brook, NY, USA, 8-12 June 2014.
7. Wang, Y., Inman, D.J., 2014, Damping in Hybrid Layered Composites, The 1st International Conference on Mechanics of Composites, Stony Brook, NY, USA, 8-12 June 2014.
8. Adarsh Chaurasia, Xiang Ren, and Gary D. Seidel, "*Computational Micromechanics Model to Study the Effective Macroscale Piezoresitivity of Carbon Nanotube-Polymer Nanocomposites for Strain and Damage Sensing*", Proceedings Paper for the ASME 2013 Conference on Smart Materials, Adaptive Structures and Intelligent Systems, Snowbird, Utah, USA, 16-18 September, 2013 (SMASIS2013-3223)
9. Adarsh K. Chaurasia, Xiang Ren, Yumeng Li, Engin C. Sengezer, Josh Burton and G. D. Seidel, "*Computational Modeling and Experimental Characterization of Macroscale Piezoresistivity in Aligned Carbon Nanotube and Fuzzy Fiber Nanocomposites*", Proceedings Paper for the 55th AIAA/ASME/ASCE/AHS/ASC Structures, Structural Dynamics and Materials Conference at AIAA SciTech 2014, National Harbor, Maryland, USA 13-17 January 2014 (AIAA 2014-1168).
10. Ballard, K., Whitcomb, J., "A Comparison of Approaches for Modeling Damage Initiation and Growth in Composites", ASC/US-J16/D30 Conference, UC San Diego, September 8-10, 2014.
11. A. Najafi, A.M. Coppola, S. Soghrati, N.R. Sottos, S.R. White and P.H. Geubelle. "Microvascular composite skin panels for hypersonic aircraft." Paper AIAA-2014-0630, AIAA SciTech 2014 Meeting, National Harbor, MD, January 2014.

Year 4

1. Li, Y.-H., Kim, S. J., Nardari, R., Oropeza, D., Chang, F.-K., 2013. " Development of High Performance BS-PT Based Piezoelectric Transducer for Structural Health Monitoring of High-Temperature Polymer-Matrix Composite Structures," Proceedings of the 9th International Workshop on Structural Health Monitoring, Stanford, CA, 2013.
2. Bhattacharya R., and Goulbourne N.C., 2013 "Characterization of Damage Evolution in Ti_2AlC and Ti_3SiC_2 under Compressive Loading", *Dynamic Behavior of Materials: Proceedings of the 2013 Annual Conference on Experimental and Applied Mechanics*, June 3-5, 2013, Lombard, IL, p. 1-11.
3. Wang, Y. and Inman, D. J., "A Finite Element Modeling of a Multifunctional Hybrid Composite Beam with Viscoelastic Materials", Proceedings SPIE's Smart Structures and NDE Conference, March 10-15, 2013, San Diego, CA paper number 8689-46.
4. Wang, Y. and Inman, D.J., 2013, "Viscoelastic Behavior of a Composite Beam Using Finite Element Method: Experimental and Numerical Assessment", Proceedings 19th International Conference on Composite Materials, July 29 – August 2, 2013, Montreal, Canada, pp. 310-328.
5. Wang, Y., and Inman, D. J., "Adaptive Multifunctional Composites" Proceedings SPIE Defense, Security and Sensing Conference, Baltimore, MD, April 2013, 9 pages.
6. Wang, Y. and Inman, D. J., "Experimental and Finite Element Analysis for a Multifunctional Beam with Frequency-Dependent Viscoelastic Behavior", Proceedings of the 54th
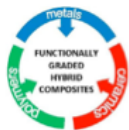
AIAA/ASME/ASCE/AHS/ASC Structures, Structural Dynamics and Materials Conference, Boston, MA USA, Paper No. AIAA-2013-1640.

7. Wang, Y. and Inman, D. J., "A Finite Element Modeling of a Multifunctional Hybrid Composite Beam with Viscoelastic Materials", Proceedings SPIE's Smart Structures and NDE Conference, San Diego, CA March 10-15, 2013, on CD, paper number 8689-46.

8. Lester, B. T., and Lagoudas, D. C., 2013, "Modeling of Residual Stresses in Shape Memory Alloy – Ceramic Composites", *Proceedings of the 54th AIA Conference on Structures, Structural Dynamics and Materials*, April 8-11, Boston, MA, USA.

9. Lester, B. T., and Lagoudas, D. C., 2013, "Modeling of the Effective Actuation Response of SMA-MAX Phase Composites with Partially Transforming NiTi", Proceedings of the ASME 2013 Conference on Smart Materials, Adaptive Structures and Intelligent Systems, September 16-18, Snowbird, UT, USA.

10. Truong, H. T. X., Kothalkar, A., Lagoudas, D. C. , Karaman, I., Ochoa, O. O. , "Joining Shape Memory Alloy to Carbon Fiber Reinforced Laminate: An interfacial perspective," *Proceedings of the 24th International Conference on Adaptive Structures Technologies*, October 7-9, 2013, Aruba.

11. Ochoa, O. O., Truong, H. T. X., Lagoudas, D. C., Lafdi, K. "Towards Understanding CNT Modified Metal-PMC Interfaces", *Proceedings of Composites Week @ Leuven And Texcomp-11 Conference*, September 16-20, 2013, Leuven, Belgium.

12. A. M. Coppola, N. R. Sottos, S. R. White. "Thermal-Mechanical Behavior of Actively Cooled Vascularized Composites." *The 19th International Conference on Composite Materials*, Montreal, Quebec, Canada, July 29- August 2, 2013.

13. S. Soghrati, A. Najafi, N. R. Sottos, S. R. White, and P. H. Geubelle. "Computational design of actively-cooled microvascular composite skin panels for hypersonic aircraft." Proceedings of AIAA SDM Meeting, Boston, MA, April 2013.
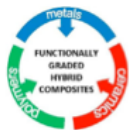
Year 3

1. Wang, Y. and Inman, D. J., "Vibration Properties of Multfunctional Hybrid Composites using Finite Elements", Proceedings of the International Conference on Adaptive Structures Technology, October 18-20, 2012, Nanjing, China.

2. Bonakdar, M., Seidel, G. and Inman, D. J., "Effect of Nanoscale Fillers on the Viscoelasticity of Polymer Nanocomposites", Proceedings AIAA 53rd Structures, Structural Dynamics and Materials Conference, 23-26 April, Honolulu, Hawaii, AIAA-2012-1825.

3. Bonakdar, M., Seidel, G. D., and Inman, D.J., "Damping Identification of Viscoelastic Composites using Micromechanical Approaches," SPIE Conference on Smart Materials and Structures/NDE, March 6-10, San Diego, California, 7978-48.

4. Lester, B. T**.,** Chemisky, Y., Geltmacher, A. B., Qidwai, S. M., Everett, R. K., and Lagoudas, D. C., "Hybrid Shape Memory Alloy Composites for Extreme Environments", Proceedings of the 22nd International Conference on Adaptive Structures and Technology, October 10-12, 2011, Corfu, Greece.

5. Lester, B. T**.,** and Lagoudas, D. C., 2012. "Computational Micromechanical Modeling of Ceramic-SMA Composites", Proceedings of the 53rd AIAA/ASME/ASCE/AHS/ASC Conference on Structures, Structural Dynamics and Materials, April 23-25, 2012, Honolulu, HI, USA.

6. Lester, B. T**.,** and Lagoudas, D. C., 2012. "Modeling of Hybrid Shape Memory Alloy Composites Incorporating MAX Phase Ceramics", Proceedings of the ASME 2012 Conference on Smart Materials, Adaptive Structures and Intelligent Systems, September 19-21, 2012, Stone Mountain, GA, USA.

7. Soghrati, S., Najafi, A., Hughes, K., Thakre, P. R., Duarte, C. A., Sottos, N. R., White, S. R., and Geubelle, P. H., "Computational design of actively-cooled microvascular composites for high temperature applications", Proceedings of the 53rd AIAA/ASME/ASCE/AHS/ASC Conference on Structures, Structural Dynamics and Materials, April 23-25, 2012, Honolulu, HI, USA, AIAA 2012-1494.

8. Coppola, A., Thakre, P. R., Sottos, N. R., and White S. R., "The effect of vascularization on the in-plane tensile properties and damage accumulation of 3D orthogonally woven glass fiber composites", Proceedings of the American Society for Composites 27th Technical Conference, October 1-3, 2012, Arlington, TX.

9. McLendon, W. R., and Whitcomb, J. D., "Failure Initiation Prediction in Textile Composite Under Complex Thero-Mechanical Loading Based on Meso-scale Analysis", Proceedings of the 53rd AIAA/ASME/ASCE/AHS/ASC Conference on Structures, Structural Dynamics and Materials, April 23-25, 2012, Honolulu, HI, USA.

10. McLendon, W. R., and Whitcomb, J. D., "Micro-scale Analysis for the Prediction of Strength under Biaxial Thermomechanical Load", Proceedings of the American Society for Composites 27th Technical Conference, October 1-3, 2012, Arlington, TX.

11. Truong, H., Ochoa, O., Klein, P., Lagoudas, D., and Lafdi, K., "Nano-Composite Materials for the Construction of Space Probes – An Investigation on Fracture Toughness of Hybrid Interfaces", Proceedings of the 9th International Planetary Probes Workshop, June 18-22, 2012, Toulouse, France.

12. Ren, X. and Seidel, G. D., "Computational Micromechanics Modeling of Piezoresistivity of Carbon Nanotube Polymer Nanocomposites", Proceedings of ECCM15 - 15TH European Conference on Composite Materials, June 24-28, 2012, Venice, Italy, ECCM15-914.

13. Bonakdar, M., Seidel, G. D., and Inman, D. J. 2012 "Effect of nanoscale fillers on the viscoelasticity of polymer nanocomposites" Proceedings of 53rd AIAA/ASME/ASCE/AHS/ASC Structures, Structural Dynamics and Materials Conference, April 23-26, 2012, Honolulu, HI, USA, AIAA 2012-1825.

14. Ren, X. and Seidel, G .D. 2012 "Computational Micromechanics Modeling of Axial Piezoresistivity of Polymer Nanocomposites with Well Dispersed and Aligned Carbon Nanotubes" Proceedings of 53rd AIAA/ASME/ASCE/AHS/ASC Structures, Structural Dynamics and Materials Conference, April 23-26, 2012, Honolulu, HI, USA, AIAA 2012-1496.

15. Ren, X. and Seidel, G. D., "Computational Modeling of Piezoresistivity of Carbon Nanotube Polymer Nanocomposites" Proceedings of SPIE Smart Structures and Materials & Nondestructive Evaluation and Health Monitoring Conference, March 11-15, 2012, San Diego, CA, USA, 8342-49

16. Ren, X. and Seidel, G. D., "Analytic and computational multi-scale micromechanics models for mechanical and electrical properties of fuzzy fiber composites" Proceedings of 52nd AIAA/ASME/ASCE/AHS/ASC Structures, Structural Dynamics and Materials Conference, April 4-7, 2011, Denver, CO, USA, AIAA 2011-1923

17. Bonakdar, M., Seidel, G. D., and Inman, D. J., "Damping characterization of viscoelastic composites using micromechanical approach" Proceedings of 2011 SPIE Smart Structures/NDE Conference, March 6-10, 2011, San Diego, CA, USA, 7978-48

18. Bhattacharya, R. and Goulbourne, N. C., "Deformation Mechanisms in $M_{n+1}AX_n$ Phase Ternary Ceramics at High Strain Rates", Dynamic Behavior of Materials, Volume 1: Proceedings of the 2012 Annual Conference on Experimental and Applied Mechanics, June 11-14, 2012, Costa Mesa, CA, p. 483-497.
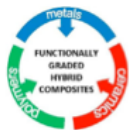
19. Bhattacharya R. and Goulbourne N. C., "Thermal shock effects on dynamic deformation mechanisms in Ti_2AlC", Proceedings of ASME International Mechanical Engineering Congress and Exposition (IMECE), November, 12-15, 2012, Houston, TX.

20. Brown, R. L., Das, K., Whitcomb, J. D., Cizmas, P. G. A., 2012. "Aeroelastic Simulation of Structures in Hypersonic Flow", Proceedings of AIAA SDM 2012 Conference, April 23-26, 2012, Honolulu, HI, USA

Year 2

1. Bonakdar, M., Seidel, G. D., Inman, D.J., "Damping Characterization of Viscoelastic Composites Using Micromechanical Approach," Proc. SPIE 7978, 797810 (2011); doi: 10.1117/12.880481, March 7-9, 2011.

2. Lester, B. T., Chemisky, Y., Geltmacher, A., Qidwai, S. M., and Lagoudas, D. C., "Virtual Processing of Hybrid SMA Composites Through Martensitic Transformation," Proceedings of SPIE: Smart Structures and Materials & Nondestructive Evaluation & Health Monitoring, March 7-9, 2011, San Diego, CA.

3. W. R. McLendon and J. D. Whitcomb, "Characterization of Damage Initiation in Textile Composites for Various Loadings and Architectures" Proceedings of 52nd AIAA SDM, April 4-7, 2011, Denver, CO.

4. K. Das, J. Whitcomb, and D. Lagoudas, "Analysis and Design of Microstructure for a Highly Reflective Thermal Barrier Coating of Nano-Porous Aluminum Oxide", 52nd AIAA/ASME/ASCE/AHS/ASC Structures, Structural Dynamics, and Materials, April 4-11, 2011, Denver, CO.

5. McLendon, W. R., Whitcomb, J. D., "Identification of Characteristic Failure Initiation Sites in Plain Weave Textile Composites," 52nd AIAA/ASME/ASCE/AHS/ASC Structures, Structural Dynamics and Materials Conference, Denver, CO, 4 - 7 April, 2011.

6. Ren, X. and Seidel, G.D., "Analytic and Computational Multi-Scale Micro-Mechanics Models for Mechanical and Electrical Properties of Fuzzy Fiber Composites," 52nd AIAA/ASME/ASCE/AHS/ASC Structures, Structural Dynamics and Materials Conference, Denver, CO, 4 - 7 April, 2011.

7. Bonakdar, M., Seidel, G.D., Inman, J., "Effect of Interphase on Damping Properties of Viscoelastic Nanocomposites," Presented at ASME McMat, May30- June 1, 2011, Chicago, IL.

8. Soghrati S., Aragón A.M., and Geubelle P.H., "Design of Actively-Cooled Microvascular Materials: Genetic Algorithms Inspired Topology and Shape Optimization", Applied Mechanics and Materials Conference, Chicago, Illinois, May 30-June 1, 2011.

9. Soghrati S., Lin J.H., Thakre P.R., Sottos N.R., White S.R., Geubelle P.H., "Design of Microvascular Networks in Actively-Cooled Polymer Matrix Composites", Applied Mechanics and Materials Conference, Chicago, Illinois, May 30-June 1, 2011.

10. Thakre P.R., Soghrati S., Sottos N.R., Geubelle P.H., White S.R., "Active Cooling of Three-Dimensional Microvascular Composites", Applied Mechanics and Materials Conference, Chicago, Illinois, May 30-June 1, 2011.

11. Geubelle, P. H., and Soghrati, S. "An Interface-enriched Generalized Finite Element Method (GFEM) for Thermal and Structural Modeling of Heterogeneous Materials." The Boeing Company, Seattle, June 2, 2011.

12. Dong H., et. al., "Microvascular Composites Fabricated from Sacrificial Fibers Made by Fiber Spinning", 3rd International Conference on Self-Healing Materials, Bath, U.K., June 27-29, 2011.

13. Geubelle P.H., Soghrati S., Lin J.H., Thakre P.R., Sottos N.R., White S.R., "An Interface-based Generalized Finite Element Method for Meso-scale Design of Microvascular High-
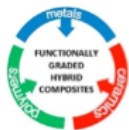
Temperature Composites", 3rd International Conference on Self-healing Materials, Bristol, UK, June 27-29, 2011.

14. Thakre P.R., et. al., "Thermal and Mechanical Behavior of Three-Dimensional Microvascular Composites", 3rd International Conference on Self-healing Materials, Bristol, UK, June 27-29, 2011.

15. Soghrati S., Geubelle P.H., "An Interface-based Generalized Finite Element Method for Problems with Discontinuous Graduateients", 11th US National Congress on Computational Mechanics, Minneapolis, Minnesota, July 25-29, 2011.

16. Li, Y.-H. , Kim, S. J., Salowitz, N., Roy, S., Larrosa, C., Janapati, V., Chang, F.-K., "High-Temperature Intelligent Composites," 18th International Conference on Composite Materials, August 21-26, 2011, Jeju, South Korea.

17. Lester, B. T., Chemisky, Y., Geltmacher, A. B., Qidwai, S. M., Everett, R. K., and Lagoudas, D. C., "Virtual Processing of Hybrid SMA Composites," ASME 2011 Conference on Smart Materials, Adaptive Structures and Intelligent Systems, September 19-21, 2011, Scottsdale, AZ.

18. Lester, B. T., Chemisky, Y., Geltmacher, A. B., Qidwai, S. M., Everett, R. K., and Lagoudas, D. C., "Virtual Processing of Hybrid SMA Composites," 22nd International Conference on Adaptive Structures and Technology, October, 10-12, 2011, Corfu, Greece.

19. S. Basu, L. Hu, E. Ormond, A. Kohalkar, K. Driedger, M. Radovic, I. Karaman, "Processing and Structural Characterization of MAX phase/metal Composts", 2011 ASME International Mechanical Engineering Congress and Exposition, Denver, Colorado, 2011.

Year 1

1. H. Dong, A. P. Esser-Kahn, P. R. Thakre, J. Patrick, M. L. Cale, N. R. Sottos, S. R. White, J. S. Moore, "Microvascular Composites Fabricated from Sacrificial Fibers", 8th National Graduate Research Polymer Conference (NGRPC), Chapel Hill, NC, June 7-9, 2010.

A. M. Aragón, P. H. Geubelle, S. Soghrati, B. Kozola, S. R. White, "Modeling and Design of Microvascular Materials for Active Cooling Applications", USNCTAM, 16th Conference on Theoretical and Applied Mechanics, Columbus, OH, June 27 - July 2, 2010.

2. M. Q. Liu and X. –L. Gao, "A micromechanics model for interpenetrating phase composites," Presented at the 16th U.S. National Congress of Theoretical and Applied Mechanics, State College, PA, June 27-July 2, 2010.

3. J. N. Reddy and G. S. Payette, "Least-squares finite element technology in fluid dynamics and structural mechanics," Opening Plenary Lecture, 4th International Conference on Advanced Computational Engineering and Experimenting(ACE-X2010) July 8-9, 2010, Hotel Concordia La Fayette, Paris, France.

4. J. N. Reddy, K. S. Surana, and G. S. Payette, "Least-Squares Finite Element Models and the k_version FEM: an Overview and Recent Developments," Semi-Plenary Lecture, 9th World Congress on Computational Mechanics and 4th Asian Pacific Congress on Computational Mechanics (WCCM/APCOM 2010), Sydney, Australia, July 9 – 23, 2010.

5. O.O. Ochoa and O.O. Ozsoy, "Joining Metal Laminates to CFRP Composites: Interfacial Study", American Society for Composites 25th Annual Technical Conference, Dayton, OH, September 20-22, 2010.

6. P. R. Thakre, H. Dong, A. P. Esser-Kahn, J. S. Moore, N. R. Sottos, S. R. White, "Development of Actively-Cooled Polymer Matrix Composites Using Sacrificial Fibers", American Society for Composites, 25th Annual Technical Conference, Dayton, OH, September 21-23, 2010.

7. Lester, B., Chemisky, Y., and Lagoudas, D., 2010. "Numerical Prediction of Effective Transformation Properties of Hybrid SMA-Ceramic Composites", Proceedings of ASME 2010 Conference on Smart Materials, Adaptive Structures and Intelligent Systems, September 28-October 1, 2010, Philadelphia, PA, p.1-8.
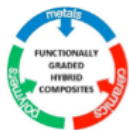
8. S. Soghrati, A. M. Aragón, J. F. Patrick, P. R. Thakre, P. H. Geubelle, S. R. White, and N. R. Sottos, "Design of Microvascular Materials in Actively-Cooled High-Temperature Composites", Society of Engineering Science, 47th Annual Conference, Iowa State University, October 4-6, 2010.
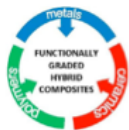
CONFERENCE PRESENTATIONS:

Year 5

1. Gao H, Tallman D, O'Neil M, Barsoum M, Radovic M. Fabrication and mechanical properties of fiber-reinforced Ti_2AlC and Ti_3SiC_2. TMS 2014, San Diego, Feb. 2014

2. Kothalkar A, Benitez R, Hu L, Radovic M, Karaman I. Thermo-mechanical response and damping behavior of Shape Memory Alloy/MAX phase composites. TMS 2014, San Diego, Feb. 2014

3. Gao H, O'Neil M, Karama I, Radovic I. Reaction Spark Plasma Sintering of Ti_2AlC from Ti, Al and TiC powders. 38th International Conference & Exposition on Advanced Ceramics & Composites, Daytona Beach, Jan. 2014

4. Gao H, Bandyopadhyay A, Karama I, Radovic M. Synthesis and characterization of bulk $(Cr_{1-x}Mn_x)_2AlC$ (0<x<0.2). 38th International Conference & Exposition on Advanced Ceramics & Composites, Daytona Beach, Jan. 2014

5. Hu L, O'Neil M, Benitez R, Kothalkar A, Proust G, Karaman I, Radovic M. Aluminum alloy/ti2alc composites prepared by infiltration of Ti_2AlC foam with molten aluminum alloy. 2014 Materials Research Society Spring Meeting, San Francisco, CA, Apr. 2014.

6. Hu L, O'Neil M, Benitez R, Kothalkar A, Proust G, Karaman I, Radovic M. Compressive properties and damping behavior of aluminum alloy/Ti_2AlC composites with controlled microstructures. 38th International Conference and Exposition on Advanced Ceramics and Composites (ICACC'14), Daytona Beach, FL, Jan. 2014.

7. Hu L, Kothalkar A, Karaman I, Proust G, Radovic M, Interfaces Between Shape memory alloys and max phases: A comparison study of interpenetrating and bilayer composites. 38th International Conference and Exposition on Advanced Ceramics and Composites (ICACC'14), Daytona Beach, FL, Jan. 2014.

8. Hu L, Kothalkar A, Benitez R, Radovic M, Karaman I. Shape memory alloy/max phase composites: High-temperature thermal and mechanical properties. 38th International Conference and Exposition on Advanced Ceramics and Composites (ICACC'14), Daytona Beach, FL, Jan. 2014.

9. Inman, D. J., 2014, "Adaptive Structures Applications: Smart Materials to Metastructures", 2014 Canadian Society of Mechanical Engineers Congress, **Keynote Address**, Toronto, Ontario, Canada, 3-7 June, 2014.

10. Inman, D. J., 2014, "Adaptive Structures, Multifunctional Structures and Metastructures for Improved Performance", **keynote Address,** Sixth World Conference on Structural Control and Monitoring, 15-17 JULY 2014, Barcelona, Spain.

11. Inman, D. J., 2014, "Smart Structures and Metastructures in Vibration Problems**",** **Keynote Address**, 4th International Conference on Dynamics, Vibration, and Control, Shanghai, China, August 22-25, 2014.

12. K.Lafdi, "Nano/Graphene, a new Player in the Aircraft Industry": ACMA 2014 International Symposium, (Marrakech, Morocco April 23-26th, 2014)

13. K.Lafdi, "Nanotechnology: Paving the Way": The 4th Federation of African Societies of Chemistry, (Marrakech, Morocco May 7-9th, 2013)

14. K.Lafdi, "Nano: The Interfacial Technology for Multifunctional Composites": 18èmes Journées Nationales sur les Composites, (Nantes, France, June 12-14th, 2013)

15. B. T. Lester and D. C. Lagoudas, "Modeling of the Effective Actuation Response of SMA-MAX Phase Composites", 24th International Conference on Adaptive Structures and Technologies, *Aruba,* October *7th, 2013*

16. B. T. Lester and D. C. Lagoudas, "Micromechanical Modeling of the Thermomechanical Response of Shape Memory Alloy – MAX Phase Composites", ASME 2013 International Mechanical Engineering Congress & Exposition, *San Diego, CA, November 20th, 2013*

17. Truong, H., Li, Y.H., Zhuang, Y., Ochoa, O., Chang, F.K., Lagoudas, D., "Integrating Thin Piezoelectric Sensors Network into Hybrid Interfaces between Shape Memory Alloy – Woven Fabric Polymer Matrix Composites and Experimental Investigations," ASME International Mechanical Engineering Congress and Exposition, Montreal, Canada, November 2014.

18. Ochoa, O. O., Truong, H. T., "Fiber Metal Laminates: An Interfacial Perspective", ASC 29th Annual Technical Conference (joint with US-Japan and ASTM Committee D30), San Diego, September 2014.

19. Truong, H., Ochoa, O., Lagoudas, D., "Hybrid Interfaces in High Temperature Multifunctional Hybrid Composites," The 25th International Conference on Adaptive Structures and Technology, The Hague, The Netherlands, October 6-8, 2014.

20. Truong, H., Ochoa, O., Lagoudas, D., "SMA Enriched High Temperature Polymer Matrix Composites: An Interfacial Study from Experimental and Computational Perspectives," The 25th International Conference on Adaptive Structures and Technology, The Hague, The Netherlands, October 6-8, 2014.

21. Truong, H., Ochoa, O., Lagoudas, D., "Joining Shape Memory Alloys to Bismaleimide-based Polymer Matrix Composites: An Interfacial Study," SPIE Smart Structures/NDE 2014, March 2014, San Diego, CA.

22. Reddy, J.N., "The Role of Computational Mechanics in Addressing Materials Challenges," **Keynote Lecture**, *Materials Science and Engineering Symposium 2014*, Qatar University, Doha, Qatar, 18 February 2014.

23. Reddy, J.N., "Computational Modeling of Complex Engineering Systems," **Keynote Lecture and Chief Guest** at *the Second International Conference on Innovation in Automation and Mechatronics Engineering* 2014, GH Patel College of Engineering and Technology, Vallabh Vidyanagar, Gujarat, INDIA, March 7-8, 2014.

24. Reddy, J. N., "Nonlinear Theories of FGM Beams and Plates with Nonlocal and Strain Gradient Effects," **Keynote Lecture**, *13th International Symposium on Multiscale, Multifunctional and Functionally Graded Materials,* Oct. 19-22, 2014, Taua Resort, SP, Brazil.

25. Reddy, J. N., "Non-classical Theories of Beams and Plates with Nonlocal and Strain Gradient Effects," **Plenary Lecture**, *International Conference on Multifunctional Materials and Structures and Applications (ICMMSA-2014),* National Institute of Technology (NIT), Dec 22-24, 2014, Allahabad, India.

26. Reddy, J. N., "Recent Developments in Computational Solid Mechanics with Particular Reference to Local and Nonlocal Theories of Structures," **Opening Plenary Speaker and Guest of Hono**r, *Sixth International Conference on Theoretical, Applied, Computational and Experimental Mechanics* (ICTACEM 2014), Dec. 29-31, 2014, IIT Kharagpur, India.

27. G.D. Seidel "Multiscale Modeling of Macroscale Piezoresistivity in Carbon Nanotube-Polymer Nanocomposites and Fuzzy Fibers" Seminar in the Engineering Science and
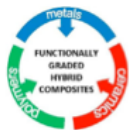
Mechanics Department at Virginia Tech Blacksburg, Va 22 - January 2014 (Invited by Dr. Romesh Batra)

28. A. M. Coppola, N. R. Sottos, S. R. White. *Thermomechanical Characterization of Actively Cooled Vascularized Composites.* 51st Annual Society of Engineering Science Technical Meeting, West Lafayette, IN, October 1-3, 2014.

29. A.R. Najafi, M. Safdari, D. Tortorelli and P.H. Geubelle. "Microstructural design of a microvascular composite: a gradient-based shape optimization scheme using Interface-enriched GFEM." 17th USNCTAM, Michigan State U., East Lansing, MI, June 16-20, 2014.

30. M.H. Tan, M. Safdari, A.R. Najafi and P.H. Geubelle. "A NURBS-based interface-enriched generalized finite element scheme for the thermal analysis and design of microvascular composites." 17th USNCTAM, Michigan State U., East Lansing, MI, June 16-20, 2014.

Year 4

1. Inman, D. J., *"Genomics of Multifunctional Structures and Materials for Flight",* Structures, Structural Dynamics and Materials (SDM) Conference Lecture (Keynote), 54th AIAA/ASME/ASCE/AHS/ASC Structures, Structural Dynamics and Materials Conference, Boston, MA USA April, 2013.

2. A. Kothalkar, B. T. Lester, L. Hu, M. Radovic, I. Karaman, and D. C. Lagoudas, "Experimental and Numerical Characterization of Hybrid Shape Memory Alloy (SMA) – MAX Phase Composites", TMS 2013 142nd Annual Meeting and Exhibition, *San Antonio, Texas, March 7th, 2013*

3. D. C. Lagoudas, "Perspectives on the Characterization and Modeling of Shape Memory Alloys for Smart Structure Applications", SPIE 2013 Conference on Smart Structures/NDE, Invited Keynote, *San Diego, California, March 11th, 2013*

4. B. T. Lester and D. C. Lagoudas, "Modeing of Residual Stresses in Shape Memory Alloy – Ceramic Composites", 54th AIAA Conference on Structures, Structural Dynamics and Materials, *Boston, Massachusetts, April 10th, 2013*

5. D. C. Lagoudas and B. T. Lester, "Modeling of Multifunctional Shape Memory Alloy – MAX Phase Ceramic Composites", 8th Japanese – Mediterranean Workshop on Applied Electromagnetic Engineering for Magnetic, Superconducting, Multifunctional and Nano Material, *Athens, Greece, June 24th, 2013*

6. D. C. Lagoudas, B. T. Lester, A. Cox, and T. Baxevanis, "Micromechanical Modeling and Analysis of Shape Memory Alloy Composite Materials at Different Scales", SES 50th Annual Technical Meeting, *Providence, Rhode Island, July 29th, 2013*

7. B. T. Lester and D. C. Lagoudas, "Modeling of the Effective Actuation Response of SMA-MAX Phase Composites with Partially Transforming NiTi", ASME 2013 Conference on Smart Materials, Adaptive Structures and Intelligent Systems*, Snowbird, Utah, September 18th, 2013*

8. A. Kothalkar, B. Lester, L. Hu, M. Radovic, I. Karaman, D. Lagoudas, "Experimental and Numerical Characterization of Hybrid Shape Memory Alloy (SMA) - MAX Phase Composites," *2013 TMS Annual Meeting & Exhibition, San Antonio, Texas*

9. L. Hu, A. Kothalkar, I. Karaman, G. Proust, M. Radovic, "Morphology Evolution and Phase Evaluation in Shape Memory Alloy/MAX Phase Composites," *2013 TMS Annual Meeting & Exhibition, San Antonio, Texas*

10. L. Hu, A. Kothalkar, I. Karaman, G. Proust, M. Radovic, Morphology Evolution and Phase Evaluation in Shape Memory Alloy/MAX Phase Composites, 37th International Conference and Exposition on Advanced Ceramics and Composites (ICACC'13), Daytona Beach, FL, Jan 2013.

11. Kothalkar, R. Benitez, L. Hu, M. Radovic, Ibrahim Karaman, Thermo-mechanical Response and Damping Behavior of Shape Memory Alloy/MAX Phase Composites, 37th
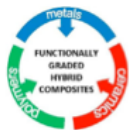
International Conference and Exposition on Advanced Ceramics and Composites (ICACC'13), Daytona Beach, FL, Jan 2013.

12. Reddy, J. N., "Modified couple stress theories of functionally graded shear deformable beams and plates," **Plenary Lecture**, *Fourth International Conference on Structural Stability and Dynamics*, Malavia National Institute of Technology, Jaipur, India, 4-6 January 2012.

13. Payette, G. S. and Reddy, J. N., "A general shell element with thickness stretch for large deformation analysis of composite structures," **Plenary Lecture**, SOMIM Conference, Salamanca, Mexico, 19-21 September 2012.

14. Payette, G. S. and Reddy, J. N., "A General Shell Finite Element for Large Deformation Analysis of Composite Structures," **Pleanry Lecture**, International Congress on Computational Mechanics and Simulation (ICCMS2012), Indian Institute of Technology, Hyderabad, 10-12, December 2012.

15. Reddy, J. N., "Spectral finite element technology for large deformation analysis of composite shells," **Keynote Lecture**, *Indo-US Workshop on Recent Developments in Composite Materials and Structures*, JFWTC- GE Global Tech. Center, Bangalore, India, March 18-20, 2013.

16. Reddy, J. N. Payette, G. S., and Vallala, V. P., "A spectral/hp shell finite element for the nonlinear analysis of laminated composites and functionally graded elastic structures," **Opening Guest and Plenary Lecture**, *the Fourth International Symposium on Solid Mechanics* - MecSol 2013, Porto Alegre, Rio Grande do Sul, Brazil, 18-19 April 2013.

17. Reddy, J. N., Payette, G. S., and Vallala, V. P., "Spectral/hp approximations in the finite element analysis of solid and fluid mechanics problems," **Plenary Lecture**, *Fourth International Conference on Mathematical and Computational Applications* (ICMCA 2013), June 11-13, 2013, Manisa, Turkey.

18. Reddy, J. N., "Refined theories and computational models of composite beams, plates, and shells," **Plenary Lecture**, *the 17th International Conference on Composite Structures* (ICCS/17), the University of Porto, Porto, Portugal, 17-21 June 2013.

19. Payette, G. S., Vallala, V. P., and Reddy, J. N., "Higher-order spectral/hp finite element technology for large deformation analysis of shell structures," **Plenary Lecture**, *the 2nd International Conference on Advances in Computational Modeling and Simulation,* 17-19 July 2013, Kunming, China.

20. S. Soghrati, A. Najafi, M. Safdari, and P. H. Geubelle. "An interface-enriched generalized finite element method for the computational analysis and design of microvascular composites." Keynote presentation. USNCCM XII, Raleigh, NC, July 21-25, 2013.

21. Multiscale Analysis of Textile Composites under Thermomechanical Loads, *19th International Conference on Composite Materials*, August 2013, Montreal, Canada.

22. McLendon, W.R. & Whitcomb, J.D., Progressive Failure of Plain Weave Textiles Under Multiaxial Loading, *54th AIAA SDM*, April 2013, Boston, MA.
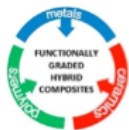
Year 3

1. D. J. Inman, "Smart Materials for Aerospace Structures: Harvesting and Morphing", 52nd Israel Annual Conference on Aerospace Sciences, Keynote Address, Tel Aviv and Haifa, Israel, February 29-March 1, 2012.

2. D. J. Inman, "Harvesting Energy from Vibrations: Making the Most of Nonlinearity," Belfer Symposium, The Technion, Haifa, Israel, February 27, 2012.

3. D. J. Inman, **"**Active Composites in Morphing, Monitoring and Harvesting**",** 26th ASC Annual Technical Conference/2nd US-Canada Conference on Composites, Plenary Lecture, Montreal, Canada, September 26-28, 2011.
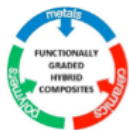
117

4. D. J. Inman, "Damping and Vibration Mitigation: Critical Issues", 2nd Multifunctional Materials for Defense Workshop, Invited Lecture, Arlington, VA, July 30-August 1, 2012.

5. B. T. Lester, Y. Chemisky, A. B. Geltmacher, S. M. Qidwai, R. K. Everett, and D. C. Lagoudas, "Hybrid Shape Memory Alloy Composites for Extreme Environments", 22nd International Conference on Adaptive Structures and Technologies, Corfu, Greece, October 10-12, 2012.

6. D. C. Lagoudas, B. T. Lester, and Y. Chemisky, "Modeling of Hybrid SMA-MAX Phase Composites for Extreme Environments", ASME 2011 International Mechanical Engineering Congress & Exposition, Denver, CO, November 2011.

7. B. T. Lester, and D. C. Lagoudas, "Computational Micromechanical Modeling of Ceramic-SMA Composites", 53rd AIAA Conference on Structures, Structural Dynamics and Materials, Honolulu, HI, USA, April 2012.

8. A. F. Parrinello, B. T. Lester, and D. C. Lagoudas, "Computational Modeling of Hybrid SMA-Ceramic Composites", 4th International Conference on Smart Materials, Structures and Systems (CIMTEC), Montecatini Terme, Italy, June 2012.

9. B. T. Lester, A. B. Geltmacher, S. M. Qidwai, R. K. Everett, and D. C. Lagoudas, "3D Image-based Modeling of Residual Stresses in Hybrid Shape Memory Alloy/Ceramic Composites", 1st International Conference on 3D Materials Science, Seven Springs, PA, July 2012.

10. B. T. Lester, S. M. Qidwai, A. B. Geltmacher, R. K. Everett, and D. C. Lagoudas, "Image-based Modeling of Hybrid Shape Memory Alloy – MAX Phase Ceramic Composites", 10th World Congress on Computational Mechanics, Sao Paulo, Brazil, July 2012.

11. D. C. Lagoudas, and B. T. Lester, "Micromechanical Modeling of Hybrid SMA Composites", 23rd International Congress on Theoretical and Applied Mechanics, Beijing, China, August 2012.

12. B. T. Lester, and D. C. Lagoudas, "Modeling of Hybrid Shape Memory Alloy Composites Incorporating MAX Phase Ceramics", ASME 2012 Conference on Smart Materials, Adaptive Structures and Intelligent Systems, Stone Mountain, GA, USA, September 2012

13. S. Soghrati, and P. H. Geubelle, "An interface-based generalized finite element method for problems with discontinuous gradients" 11th US National Congress on Computational Mechanics, Minneapolis, MN, 2011.

14. S. Soghrati, P. H. Geubelle, P. R. Thakre, N. R., Sottos, and S. R. White, "An interface-based generalized finite element method for the meso-scale design of high-temperature composites", 3rd International Conference on Self-Healing Materials, Bristol, UK, 2011.

15. S. Soghrati, A. M. Aragón, and P. H. Geubelle, "Design of actively-cooled micro-vascular materials: Genetic algorithms inspired topology and shape optimization", ASME Applied Mechanics and Materials Conference, Chicago, IL, 2011.

16. S. Soghrati, P. R. Thakre, J. H. Lin, N. R. Sottos, S. R. White, and P. H. Geubelle. "Design of microvascular networks in actively-cooled polymer matrix composites", ASME Applied Mechanics and Materials Conference, Chicago, IL, 2011.

17. S. Soghrati, A. R. Najafi, C. A. Duarte, N. R. Sottos, S. R. White, and P. H. Geubelle, "Computational modeling and design of actively-cooled microvascular 3D woven glass/epoxy composites". SES 49th Annual Technical Meeting, Atlanta, GA, October, 2012.

18. H. Truong, O. Ochoa, W. McLendon, J. Whitcomb, and K. Lafdi, "Fracture Toughness of Fuzzy Interfaces in Hybrid Composites," 2012 ASME International Mechanical Engineering Congress and Exposition, Houston, TX, November 20, 2012.

19. X. Ren and G. D. Seidel, "Computational Micromechanics Modeling of Piezoresistivity of Carbon Nanotube Polymer Nanocomposites", ECCM15 - 15TH European Conference on Composite Materials, Venice, Italy, 24-28 June, 2012, ECCM15-914.

20. G. D. Seidel, "Multiscale Modeling of the Multifunctional Properties of CNT-Polymer Nanocomposites via Analytic and Computational Micromechanics", Invited Talk, National Institute of Aerospace Research Seminar, NASA Langley Research Center (LaRC), Hampton,
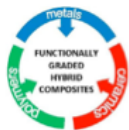
VA, June 18, 2012. (Invited by Dr. Douglas Stanley)

21. G. D. Seidel, "Computational Micromechanics Models for Multifunctional Nanocomposites", Invited Talk, Seminario de la Unidad de Materiales (Materials Department Seminar); Centro de Investigacion Cientifica de Yucatan (CICY) (Yucatan Scientific Investigation Center) Merida, Yucatan, Mexico May 14-16, 2012 (Invited by Dr. Francis Aviles).

22. M. Bonakdar, G. D. Seidel, and D. J. Inman, "Effect of nanoscale fillers on the viscoelasticity of polymer nanocomposites", 53rd AIAA/ASME/ASCE/AHS/ASC Structures, Structural Dynamics and Materials Conference, Honolulu, HI, April 23-26, 2012, AIAA 2012-1825.

23. X. Ren and G. D. Seidel, "Computational Micromechanics Modeling of Axial Piezoresistivity of Polymer Nanocomposites with Well Dispersed and Aligned Carbon Nanotubes", 53rd AIAA/ASME/ASCE/AHS/ASC Structures, Structural Dynamics and Materials Conference, Honolulu, HI, April 23-26, 2012, AIAA 2012-1496.

24. A. Kothalkar, S. Basu, P. Mchaffey, I. Karaman, and M. Radovic, "Diffusion Bonding between Ti_3SiC_2 and NiTi Shape Memory Alloy", 2012 TMS Meeting, Orlando, FL, 2012.

25. L. Hu, A. Kothalkar, S. Basu, F. Schaff, I. Karaman, and M. Radovic, "Processing and Characterization of NiTi-Ti_3SiC_2 Composite Prepared by Spark Plasma Sintering", 2012 TMS Meeting, Orlando, FL, 2012.

26. K. Jeon, S. Basu, F. Schaff, M. Barsoum, and M. Radovic, "Processing and Mechanical Properties of Ti_2AlC Reinforced with Alumina Fibers", 36th International Conference on Advanced Ceramics and Composites, Daytona Beach, FL, 2012.

27. L. Hu, S. Basu, R. Benitez, I. Karaman, and M. Radovic, "Effects of Porosity and Pore Size on Room Temperature Thermal Conductivity and Mechanical Properties of Porous Ti_2AlC", 36th International Conference on Advanced Ceramics and Composites, Daytona Beach, FL, 2012.

28. S. Aboutula, S. Basu, M. Radovic, and A. Shukla, "High Strain Rate Deformation Behavior of Nanolaminated Titanium Aluminum Carbide", 36th International Conference on Advanced Ceramics and Composites, Daytona Beach, FL, 2012.

29. A. Kothalkar, S. Basu, P. Mchaffey, I. Karaman, and M. Radovic, "Interfacial study between Ti_3SiC_2 and NiTi Shape Memory Alloy via Diffusion Bonding", 36th International Conference on Advanced Ceramics and Composites, Daytona Beach, FL, 2012.

30. A. Kothalkar, L. Hu, S. Basu, F. Schaff, I. Karaman, and M. Radovic, "Study of NiTi-MAX Phase Composites Prepared via Spark Plasma Sintering", 36th International Conference on Advanced Ceramics and Composites, Daytona Beach, FL, 2012.

31. L. Hu, R. Benitez, I. Karaman, M. Radovic, Development of porous Ti_2AlC with controlled porosity and pore size, Materials Science & Technology 2012 (MS&T 2012), Pittsburgh, Pennsylvania, USA, October 2012.

32. L. Hu, R. Benitez, S Basu, I. Karaman, M. Radovic, Processing and characterization of porous Ti_2AlC with controlled porosity and pore size, 4th International Congress on Ceramics (ICC4), Chicago, Illinois, USA, July 2012.

33. G. Payette and J. N. Reddy, "Recent Developmets in Shell Finite Elements for Large Deformation Analysis," Semi-Plenary Speaker, Third International Symposium on Computational Mechanics (ISCM III) in conjunction with the Second Symposium on Computational Structural Engineering (CSE II), Taipei, Taiwan, 5-7 December 2011.

34. G. S. Payette and J. N. Reddy "A General Shell Finite Element for Large Deformation Analysis of Composite Structures," Pleanry Lecture, International Congress on Computational Mechanics and Simulation (ICCMS2012), Indian Institute of Technology, Hyderabad, 10-12, December 2012 (to be presented).

Year 2

1. Ma, H. M. and Gao, X.-L. (2011). "A Homogenization Method for Multiphase Composites Using Strain Graduateient Elasticity-Based Eshelby Tensors." ASME Applied Mechanics and Materials Conference, Chicago, IL, May 31-June 2, 2011.
2. Lagoudas, D. C., Lester, B. T., and Chemisky, Y. "Hybrid SMA Composites for Extreme Environments", Micromechanics & Modeling of Multifunctional Materials, July 14-15, 2011, Thessaloniki, Greece.
3. Lester, B. T., Chemisky, Y., Geltmacher, A. B., Qidwai, S. M., Everett, R. K., and Lagoudas, D. C. "Finite Element Modeling of Hybrid SMA Composites", US National Congress on Computational   Mechanics, July 25-28,2011, Minneapolis, MN.
4. Das, K., Lagoudas, D.C. and Whitcomb, J.D., "Analysis of a Photonic Band Gap Film for Thermal Radiation Barrier Coatings", 2011 ASME International Mechanical Engineering Congress and Exposition, Denver, CO, November 11-17, 2011.
5. Lester, B. T., Chemisky, Y, and Lagoudas, D. C., "Virtual Processing of Hybrid Shape Memory Alloy – MAX Phase Ceramic Composites Utilizing Martensitic Transformation", 2011 ASME International Mechanical Engineering Congress and Exposition, Denver, CO, November 11-17, 2011.
6. Liu, M. Q. and Gao, X.-L., "Micromechanical Modeling of Interpenetrating Phase Composites", 2011   ASME International Mechanical Engineering Congress and Exposition, Denver, CO, November 11-17, 2011.
7. Ochoa, O., O., Truong, H., Klein, P., Lafdi, K.,"Fracture Toughness Study of Fuzzy Fabric Interface", 2011   ASME International Mechanical Engineering Congress and Exposition, Denver, CO, November 11-17, 2011.
8. Salowitz, N., Li, Y.-H., Kim, S. J., Roy, S., Chang, F.-K., "Structural Health Monitoring of High Temperature Composites", 2011 ASME International Mechanical Engineering Congress and Exposition, Denver, CO, November 11-17, 2011.
9. Su, Y.-Y. and Gao, X.-L. (2011). "Modeling of Peeling Test of an Adhesively Bonded Joint Using a Viscoelastic Bernoulli-Euler Beam Theory", 2011 ASME International Mechanical Engineering Congress and Exposition, Denver, CO, November 11-17, 2011.
10. Wang, X. and Gao, X.-L. (2011). "Achieving the Uniform Stress State inside an Inclusion of Arbitrary Shape in a Three-Phase Composite Through Interfacial Design", 2011 ASME International Mechanical Engineering Congress and Exposition, Denver, CO, November 11-17, 2011.
11. Mohammad Bonakdar, G.D. Seidel, and D. Inman, "Effect of Interphase on Damping Properties of Viscoelastic Nanocomposites," ASME 2011 Applied Mechanics and Materials Conference, Chicago, Illinois, 30 May - 1 June 2011 (McMat2011-4537).
12. Xiang Ren, Skylar Stephens and G.D. Seidel, "Nanocomposites as Structural Health Monitors: Multiscale Modeling of Piezoresistivity in Carbon Nanotube Polymer Nanocomposites," ASME 2011 Applied Mechanics and Materials Conference, Chicago, Illinois, 30 May - 1 June 2011 (McMat2011-4532).
13. X. Ren and G. D. Seidel, "Computational Modeling of Piezoresistivity of Carbon Nanotube Polymer Nanocomposites" SPIE Smart Structures and Materials & Nondestructive Evaluation and Health Monitoring Conference, San Diego, CA, March 11-15, 2012, 8342-49.
14. M. Bonakdar, G. D. Seidel, and D. Inman "Effect of Interphase on Damping Properties of Viscoelastic Nanocomposites " ASME 2011 International Mechanical Engineering Congress and Exposition, Denver, CO, November 11-17, 2011 (IMECE2011-64591).
15. X. Ren and G. D. Seidel, "Multiscale Modeling of Damage in the Carbon Nanotube-Polymer Interphase of Fuzzy Fibers Subjected to Quasi-static Mechanical Loading", ASME 2011 International Mechanical Engineering Congress and Exposition, Denver, CO, November 11-17, 2011 (IMECE2011-64567).
16. X. Ren, S. Stephens, G. D. Seidel and Francis Aviles "Nanocomposites as Structural Health
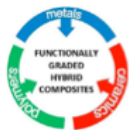
Monitors: Multiscale Modeling of Piezoresistivity in Carbon Nanotube Polymer Nanocomposites", ASME 2011 International Mechanical Engineering Congress and Exposition Denver, CO, November 11-17, 2011 (IMECE2011-64531).

17. G. D. Seidel, "Multiscale Modeling of Mechanical, Thermal, and Electrical Properties of Carbon Nanotube-Polymer Nanocomposites", Invited Talk, COMS 2011: Commercialization of Micro-Nano Systems Conference; Nanocomposite Manufacturing Initiatives and Challenges Panel Session, Greensboro, NC, August 28-31, 2011 (Invited by Mr. Raymond Jones).

18. G. D. Seidel, "Multiscale Modeling of Mechanical, Thermal, and Electrical Properties of Carbon Nanotube-Polymer Nanocomposites", Invited Talk, Seminario de la Unidad de Materiales (Materials Department Seminar); Centro de Investigacion Cientifica de Yucatan (CICY) (Yucatan Scientific Investigation Center) Merida, Yucatan, Mexico, June 20-23, 2011 (Invited by Dr. Francis Aviles).

19. X. Ren and G. D. Seidel, "Analytic and computational multi-scale micromechanics models for mechanical and electrical properties of fuzzy fiber composites", 52nd AIAA/ASME/ASCE/AHS/ASC Structures, Structural Dynamics and Materials Conference, Denver, CO, April 4-7, 2011 (AIAA 2011-1923).

20. M. Bonakdar, G. D. Seidel, and D. J. Inman, "Damping characterization of viscoelastic composites using micromechanical approach", 2011 SPIE Smart Structures/NDE Conference, San Diego, CA, March 6-10, 2011 (7978-48).

21. S. Basu, A. Kohalkar, M. Radovic, I. Karaman, "Diffusion Bonding between Ti_3SiC_2 and NiTi Shape Memory Alloy, 2011 ASME International Mechanical Engineering Congress and Exposition, Denver, Colorado, 2011.

22. S. Basu, L. Hu, E. Ormond, A. Kohalkar, K. Driedger, M. Radovic, I. Karaman, "Processing and Structural Characterization of MAX phase/metal Composts", 2011 ASME International Mechanical Engineering Congress and Exposition, Denver, Colorado, 2011.

23. E. Ormond, S. Basu, K. Driedger, I. Karaman, M. Radovic, "On the Diffusivity and Reactivity in Ti_2AlC - Ti system at 800-1400°C Temperature Range, submitted to 35th International Conference on Advanced Ceramics and Composites, Daytona Beach, FL, January 2011.

24. A. Kothalkar, M. F. Ozaydin, S. Basu, S. M. Razzavi, M. Radovic and I. Karaman, Interfacial Reactions in NiTi-Ti_3SiC_2 Diffusion Bonded Joints, ASME 2011 International Mechanical Engineering Congress and Exposition, Denver, Colorado, USA.

Year 1

1. Das, K., Whitcomb, J. and Lagoudas, D.C., "Electromagnetic Radiation Through a TiO2 Nanotube Membrane Used as a Thermal Barrier Coating," Proceedings of USNCTAM2010, 16th US National Congress of Theoretical and Applied Mechanics, June 27 - July 2, 2010, State College, PA.

2. Xiang Ren and G.D. Seidel, "Multiscale Modeling of the Elastic Properties of Fuzzy Fibers", ASME 2010 International Mechanical Engineering Congress and Exposition, Track 12: Mechanics of Solids, Structures, and Fluids, Topic 12-17: Multifunctional and Nanostructured Materials: Modeling and Characterization, Session 12-17-3: Multifunctional and Nanostructured Materials III Vancouver, British Columbia, Canada 12 -18 November 2010.

3. R. Avinash, S. Basu, E. Ormond, R. Arroyave, M. Radovic, "On thermodynamic stability of the crystal structure and morphology in Ti_3AlC", 2010 MS&T, Houston, TX, October 2010.

4. N. Lane, S. Vogel, M. Radovic, M. Barsoum, "Damping, High Temperature Neutron Diffraction and Rietveld Analysis of Selected MAX Phases", 2010 MS&T, Houston, TX, 2010.

5. S. Basu, E. Ormond, I. Karaman, M. Radovic, "Microstructure development and reactions in Ti and Ti_2AlC composites co-sintered at 1000°C – 1200°C", 2010 MS&T, Houston, TX, Oct., 2010.

6. S. Basu, E. Ormond, I. Karaman, R. Arroyave, M. Radovic, "Microstructure Development and Reactions in Ti – Ti_2AlC Sytem in 800- 1400°C Temperature Range," 2010 MS&T Conference, Houston, TX, 2010.

7. M.F. Ozaydin, S. Basu; S. Razavi, M. Radovic, I. Karaman, "Interfacial reactions in binary NiTi Shape Memory Alloy / Ti_3SiC_2, Ti_2AlC MAX-phase Ceramic Joints", 2010 MS&T, Houston, TX, 2010.

8. N. Obando and M. Radovic, "Effect of the water vapor on the oxidation of Ti2AlC in 1000- 1300°C temperature range", 34th International Conference on Advanced Ceramics and Composites, Daytona Beach, FL, January 2010.

9. M. Radovic, I. Karaman, "Fabrication and Characterization of Bulk MAX Phases and MAX-Metal Composites", Composite and Hybrid Materials Workshop, AFRL, Dayton, OH, May 2010.